University of Southampton

Side-Scan Sonar Observations of Upper Ocean Processes

by Marco Julio Ulloa, Ocean., M.Sc.

Submitted for the degree of
Doctor of Philosophy

School of Ocean and Earth Sciences
Southampton Oceanography Centre
Faculty of Science

December, 2002

UNIVERSITY OF SOUTHAMPTON

ABSTRACT

FACULTY OF SCIENCE

OCEANOGRAPHY

Doctor of Philosophy

Side-Scan Sonar Observations of Upper Ocean Processes

by Marco Julio Ulloa

This thesis describes a study of near-surface ocean processes based upon observations made with a novel acoustic remote sensing instrument, ARIES II. This is a streamlined body, designed to become orientated with the mean flow, with acoustic beams pointing forward and to starboard relative to the upstream direction. The observations have been carried out on August 1995 as part of the LOIS-SES programme at a position on the Malin Shelf. ARIES II has been deployed on a 'U-mooring' at a mean transducer depth of 34.6 m, at about 4 km East from the 200 m isobath and into 146 m water depth. High-resolution observations in a deep ocean environment reveal a wide range of acoustic signatures: the tide, non-linear internal waves of depression, rain squalls, Langmuir circulation, wind-sea in the spectral band (0.1882-0.3106) Hz, swell [(0.0938-0.1016) Hz], wave groups (0.0078 Hz), breaking surface waves, bubble plumes and biological activity. The main focus is on the uncertainties, assumptions and errors accompanying the performance of ARIES II, the interpretation of acoustic images and the derivation of formulations utilised to obtain detailed quantitative information about concurrent upper ocean processes.

ARIES II was operating continuously and unattended in a zone remote from shore, and it has proven to be a reasonably stable working framework with mean pitch and roll of 5.1° and 1.0°, respectively. Maximal pitching and rolling of 10° have been caused by both groups of surface waves and non-linear internal waves. ARIES II is capable of aligning within (6 ± 4)°T from the direction of mean currents, however, the rms scatter of points for the best alignment with internal-wave induced flows is 45°T. The yawing of ARIES H is attributed to the poor sampling rate of currents rather than instrumental imperfections or the dynamics of the study site. The current investigation has revealed many novel acoustic signatures of small-scale processes. Furthermore, the main factors affecting the appearance of signatures in acoustic images are the instrument heading and the orbital motions of surface waves. Specific formulations to describe these effects have been developed. Side-scan sonar images show a hierarchy of coexisting scales of bubble bands which appear to merge with larger bands. Pairs of bands also appear to merge with each other to form new bands between older ones. The spacing of bubble bands has been observed to increase with wind speed. An important gap in knowledge filled by ARIES II regards its capability to provide detailed measurements of internal wave straining. Variations in the orientation of bubble bands correlate with straining, which suggest the active modification of Langmuir circulation by solitary-like waveforms. The implication of these results is that acoustic devices are suitable to examine a series of interactions among different forms of turbulence within the upper ocean, provided that proper error bars are well-established.

Acknowledgements

I am indebted to Prof. Ian Robinson, for patience and advise, the well needed encouragement and the very considerable support afforded to completing the current research. It is also more than appropriated to express my sincere gratitude to my supervisor, Prof. Steve Thorpe, FRS for invaluable suggestions and for sharing his excitement to unravelling complex physical processes using simple ideas in his very particular enthusiastic manner. I remain very grateful to Prof. Pedro Ripa† for having pointed me towards Prof. Thorpe. Many thanks to both Dr. John Scott and Dr. Simon Boxall for the minor amendments that have improved this work. Financial support has come from CONACYT.

Alongside the trials and tribulations of the work, I owe a debt to David Baldwin, Alan Hall, Alex Nimmo-Smith, Angus Graham and Justin Small for assistance, guidance and very helpful discussions. Alex Nimmo-Smith, at very short notice and with the highest skill and enthusiasm, has examined most of the chapters providing many helpful comments and suggestions, and I am extremely grateful to them all. Also, suggestions kindly offered by Prof. Ching-Sang Chiu on the early chapters are highly appreciated.

I wish to thank John Hughes (BODC) and Lisa Carlin (POL) for supplying in respective order data from the LOIS-SES S140 study zone and tidal predictions. Wind data and a mean CTD cast were kindly provided by John Scott and Justin Small from DERA, as part of the NERC/MOD 'CAROS' agreement to SOC. The elusive Challenger Cruise Reports are acknowledged to Laura Carrillo (UCES, Bangor).

Thanks are due to Emma Mattey and David Baldwin, Matt Burrows and Paula, Alex Nimmo-Smith, Angus Graham, Luca Centurioni, Andreas Thurnherr, Jeff Blundel, Arigueri Protopapas, Popova Ekaterina, Michael Koch, Jens Larsen and Cristina Alfonsin, Asdrubal Martinez and Ernestina Castro, Luis Navarro and Lus Lopez, Miguel Tenorio and Brigitte Ale, Marco Salas and Tatiana Santander, Daniel Ballestero and Sandra Frech, Susana, Alberto and Sergio, and many others impossible to identify and to name who have contributed significantly to preserve my sanity through dinners, golf and squash matches, CD's, pub meetings, barbecues and parties. I am also deeply appreciative of the efficient and sympathetic help of Jane Atkins, Jackie Mayo, Amanda Tyler, Rachel Mills, Kate Davis, Pauline Simpson, Romayne Knight, Marion Raaymakers, Brenda Bagust and Diane Buckley. I owe a renewed debt to Guido Marinone, Isabel Ramirez, Jose Luis Ochoa, Roberto Soto, Joaquin Garcia and Emilio Palacios from CICESE for workstation time, disk space, and computer software granted. I am also most grateful to Roberto Millan, Rigoberto Guardado, Eliseo Almanza, Rene Pinet, Ruben Castro and Manuel Moreno from FCM-UABC, who generously gave the opportunity of a part-time teaching job that helped me with my expenses and to buy a personal computer.

This work is dedicated to my dearest auntie Aurora Buchanan†, my grandmother Imelda Procelle†, my mother Maria Martha Torres†, my wife Maria Francisca Fernandez and to my daughter and son, Maria Martha and Juan Pablo.

CONTENTS

Part I Background 1

Part I

BACKGROUND

1. INTRODUCTION

This thesis deals with the applicability of a novel instrument utilised to investigate, remotely from beneath the sea surface, physical processes occurring in the upper ocean boundary layer (see section 1.1 below). ARIES II, an acronym for **A**utonomously **R**ecording **I**nverted **E**cho **S**ounder, is the successor of a single vertically upward-looking narrow beam instrument, ARIES, devised by Hall (1986) and applied by Thorpe (1986b) to sample and record sound scattered from subsurface bubble clouds produced by breaking waves in either shelf edge or shallow water environments. The improved version of ARIES was designed by Packwood (1995), in a joint development with the Department of Oceanography, University of Southampton and The George Deacon Division of the Institute of Oceanographic Sciences (IOSDL), now both based in the Southampton Oceanography Centre (SOC). Electronics were developed by A. Hall and J. Campbell, whilst software by D. Baldwin (see Thorpe and Baldwin, 1995). ARIES II has a larger capacity to store data, a two-beam side-scan sonar tilted at 20° above the horizontal from which the speed of subsurface targets leaving some structure in high-resolution acoustic images or sonographs (see section 6.1 for a clear definition) is estimated, sensors to measure pressure and temperature, plus compass and inclinometers to record the heading, pitch and sideways tilt of the instrument. In addition, ARIES II is streamlined to let mean currents orientate it to minimise drag, is moored on a swivel from its lowest point about which it can rotate and it is capable of operation to depths of 200 m (see Fig. 3.1).

ARIES II was deployed in August 1995 in the Malin-Hebrides shelf break (Sherwin and Simpson, 1996) as part of the UK programme **L**and **O**cean **I**nteraction **S**tudy-**S**helf **E**dge **S**tudy (LOIS-SES), a region of both active fishing and soliton-type internal waves. The author's role in the ARIES II project was the testing of software, the analysis of acoustic images and the collection of acoustic data in the surf zone at Tunstall (at the Holderness area, East Yorkshire; see Baldwin and Thorpe, 1996).

Three main parts comprise the current research. Part I (chapters 1-2) defines the objectives of the research and gives the relevant background necessary for the physical interpretation of acoustic images obtained from ARIES II. Part II (chapters 3-6) is a critical description of ARIES II and its performance, whilst Part III (chapters 7-8) describes and interprets the most striking features observed in sonographs during the LOIS-SES experiment, plus a summary of results and suggestions for future areas of research.

The rest of this chapter gives the rationale (section 1.1), the objectives (section 1.2), and the structure of the dissertation (section 1.3).

1.1 Rationale

Oceanographers have long been enthralled by large-scale phenomena, but in recent years some shift towards small-scale physical processes has arisen, motivated by the development of innovative acoustic methods. The region of interest is the upper ocean boundary layer (hereinafter, for brevity, referred to as UOBL), a zone of transition between the atmosphere and the deep ocean with a thickness of typically 5 to 200 m (Thorpe, 1988, 1992b). It is bounded from above by the sea surface and from below by the thermocline. The current research focus attention on the motions of the sea surface produced at temporal scales in the range 3 s to 12 h and at spatial scales of surface waves generated by the wind (O(10-200 m)), and those of Langmuir circulations (O(10-20 m)), and on the near-surface manifestations of buoyancy-induced motions in the thermocline (e.g. internal waves) with vertical and horizontal scales of some 40 m and 400 m, respectively. These are scales of small-scale processes. Only those physical processes in the upper ocean at other scales of motion which impact on our observations (e.g. tides) are considered here. The scales of interest here lie between those of microstructure (from millimetres to centimetres) where molecular viscosity and diffusion are important (Osborn, 1998), although clouds of small bubbles are implicitly included in the study, commonly being acoustic targets; and those of large-scale flows for which the Coriolis acceleration is important (Pedlosky, 1987; Métais, 1997) or those large-scale motions in a stratified fluid affected by Earth's rotation and comparable to the Rossby radius of deformation in scale (Pedlosky, 1987; Thorpe, 1998).

Investigating small-scale processes in the upper ocean is not only important for the understanding of the exchange of heat, energy, momentum, and gases between the ocean and the atmosphere, but also because their dynamics have a direct impact on the motion of neutrally buoyant and buoyant particulate material such as both motile and non-motile live organisms, oil droplets, and air bubbles. The motions beneath the sea surface determine the horizontal and vertical dispersion of such material, and may be divided into those responding directly to surface and internal waves (the wave orbital velocities) and those which have a random or chaotic nature, characteristic of turbulence. Of the latter, a distinction may be drawn between the (smaller scale) motions leading to viscous dissipation and the larger scale motions which remain coherent for several minutes. Langmuir circulation (see sections 2.4 and 6.4) constitutes a remarkable example of a coherent flow, but turbulent, in the UOBL which affects the distribution of plankton and of *Sargassum sp*, an important free-floating brown algae in the food cycle and primary productivity of tropical areas (Woodcock, 1993). Further, there is evidence (Sutcliffe *et al.*, 1971; Dyke and Barstow, 1983; Malinen *et al.*, 2001) that plankton is carried upwards, to the sea surface, in upwelling flows associated with Langmuir circulation (hereafter referred to as LC) and accumulated in streaks by horizontally converging surface flows.

In situ measurements of planktonic distributions, with a vertical variability of $O(< 1\ \mathrm{m})$ within a water column of $O(10\ \mathrm{m})$, and the detailed structure of LC, which is in conformance with the coexistence of cells of many different scales with alternating sense (e.g. converging and diverging) of circulation, are limited by both the sampling resolution and by the vertical spacing of conventional instrumentation; for instance, vertical scales typically 5-15 m for biological samplers (Cowles *et al.*, 1998) and 2-30 m for physical observations using current meters (Weller and Plueddemann, 1996). Langmuir cells are particularly difficult to detect because visible markers, debris or foam, floating on the surface of the sea are not always present. Numerical models (Evans and Taylor, 1980; Li and Garrett, 1993) have been utilised as tools to unveil the physical structure of the cells; however, field measurements seem not to completely agree with existing theories. This, for example, is the case for the downwind jet-like surface current at the streaks which is significantly underestimated by the numerical model of Li and Garrett (1993).

The action of breaking surface gravity waves (section 2.2) in strong winds can break floating oil spilled after a major accident into fragments composed of many droplets of different sizes, some of which will form linear bands in the surface convergences of Langmuir cells (Thorpe, 1995b). Other oil droplets can become invisible to the unaided eye after being entrained into the water column by downwelling flows, where they might be trapped and redistributed beneath the bands in homogeneous regions of oil concentration (Leibovich and Lumley, 1982; Farmer and Li, 1994).

Internal gravity waves (section 2.3) play a significant role in modulating the distribution of particulate material at the surface and bottom of the sea. Whilst most phytoplankton suspended in motionless water sink because their density is larger than water, cyanobacteria are able to regulate their own buoyancy (Wallace and Hamilton, 1999); nevertheless both are subject to the vertical and horizontal movements of the surrounding water. Internal waves produce intense vertical excursions of phytoplankton (Kamykowski, 1979; Haury *et al.*, 1983; Lennert-Cody and Franks, 1999) and, by shear instability and associated mixing, enough turbulent energy is generated for an intermittent nutrient supply to the upper ocean (Sandstrom and Elliot, 1984; Holligan *et al.*, 1985). This is important because the intensity of solar radiation and the availability of nutrients are factors which affect the primary productivity and the chemical composition of planktonic organisms (e.g. Lande and Yentsch, 1988). Passive zooplankton, on the other hand, are susceptible to horizontal excursions and, together with the larvae of fishes, might be conveyed in solitary-type internal wave troughs for distances in the range 2-15 km (Lamb, 1997). A net transport of water itself (Kinder, 1984; Lamb, 2003), the organisation of phytoplankton in thin layers (Franks, 1995) and the resuspension of bottom sediments (Bogucki *et al.*, 1997; Bogucki and Redekopp, 1999) are also potentially linked to internal waves.

The breaking of surface waves, through jet and subsequent splashing by drop impact on the face of breaking waves themselves (Deane and Stokes, 2002), also constitutes the major mechanism introducing air bubbles (bubble clouds) into the near-surface ocean. The size of bubbles can be larger than 1 mm (Deane and Stokes, 2002), but it seems that most of them have a radius less than 30 μm (Medwin and Brertz, 1989). Following Thorpe (1992b), large bubbles of O(500 μm) tend to rise rapidly at speeds of about 7 cms^{-1}. They may contribute to form floating foam or burst, projecting air and aerosols into the atmosphere once reaching the sea surface. The role of these bubbles in the air-sea gas exchange appears, however, to be substantially unquantified (Thorpe, 1992b; Melville, 1996; Woolf, 1997). Small bubbles O(50 μm), on the other hand, rise at some 0.5 cms^{-1}, much less than the reported speeds of surface and downwelling flows of LC, of about 8-17 cms^{-1} (Weller *et al.*, 1985) and 5-30 cms^{-1} (Smith *et al.*, 1987) respectively. Large bubbles, therefore, need greater downwelling flows to remain beneath the surface, while small bubbles are transported down to tens of metres by convergent flows in Langmuir cells where they experience a significant hydrostatic overpressure and probably dissolve entirely, passing gases into solution in the surrounding water (Leighton, 1994). Upwelling flows in Langmuir cells can also bring and concentrate nutrients in the sea surface, thereby causing a local patch with enriched nutrients at horizontal scales comparable to the mean distance between adjacent streaks (spacing). Although there is evidence suggesting that LC and bubbles are unlikely to be a major source of observed nutrient enrichment of the sea surface (Haury and Shulenberger, 1998), the small sizes of air bubbles indicate the need for instrumentation capable of both detecting them and, from a general point of view, of performing high-resolution measurements of subsurface physical processes where *in situ* observations are difficult. As a consequence, numerous designs of specific equipment to cope with very dynamic environments have been proposed, for instance, streamlined tubular tow bodies (Proni *et al.*, 1978; Thorpe *et al.*, 1985) or streamlined spars suspended from catamarans towed horizontally from ships (Thorpe and Hall, 1987).

Small bubbles form a continuous 'stratus' layer at the surface in winds larger than 7 ms^{-1} (Fig.1.1c), whereas bubble clouds are separated in lower wind speeds as breaking waves are infrequent (Fig. 1.1b, see Thorpe, 1982). Many individual bubbles clustered

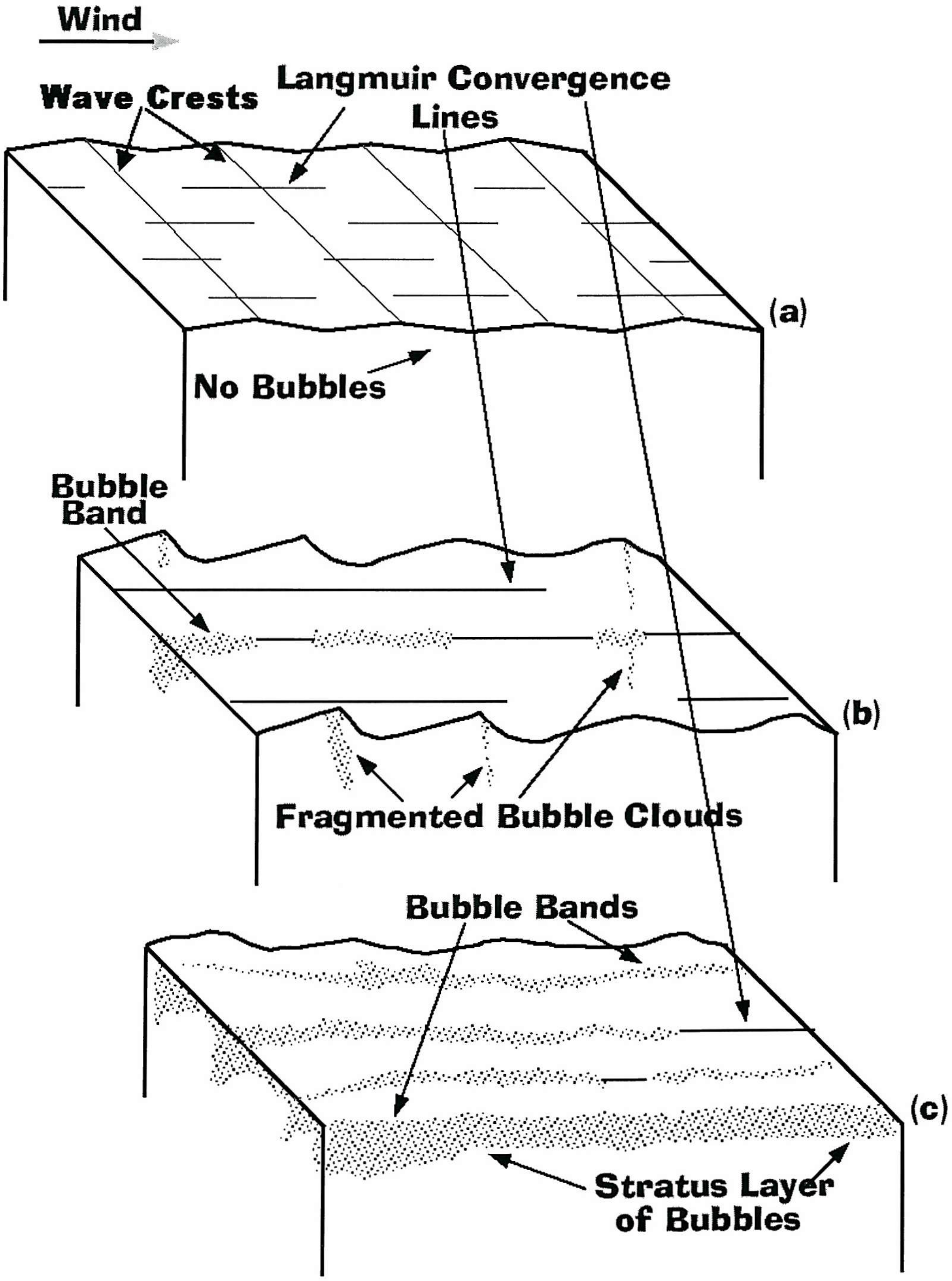

Fig. 1.1: *Schematic showing the development of a layer of bubble clouds as a function of wind speed. (a) For winds < 2 ms*$^{-1}$*, wind waves seldom break and few bubbles are created. (b) For winds > 2 ms*$^{-1}$ *but < 7 ms*$^{-1}$*, wind waves break more frequently and bubble clouds appear fragmented. Some bubbles may occasionally fill Langmuir convergence lines forming isolated bubble bands, some not. (c) For winds > 7 ms*$^{-1}$*, the fraction of the sea surface covered by breaking waves increases. Wind waves break more uniformly, a thin and variable stratus layer of bubbles is present near the surface, and a supply of bubbles is therefore available for all bubble bands. These bands now appear as long streaks or windrows.*

in clouds, and those created by rainfall, execute oscillatory motions when excited by sonar. Besides, bubble clouds can resonate naturally, radiating sound which contributes to the ambient noise in the ocean. Such noise and cloud resonance affects acoustic communications undersea (Leighton, 1994), but may be useful in imaging subsurface objects (Buckingham *et al.*, 1992; Liu *et al.*, 2003). Although bubble clouds represent a barrier to sound transmission by scattering and attenuation (Medwin and Clay, 1998), they have important oceanographic applications concerning the detection and the tracking of organised turbulent motions beneath the sea surface. When bubble clouds are ensonified by sonars (section 2.1) with a frequency similar to their natural frequency of oscillation (which depends mainly on the bubbles' radii), acoustic energy is scattered most efficiently. Then bubbles are useful as quasi-passive tracers (since they rise and dissolve) because their scattering can be registered remotely by sonars. In addition, bubbles are not merely sound scatterers and sources, but mediators between acoustic instrumentation and small-scale processes and, in consequence, cannot be ignored at all in studies of the UOBL.

The rationale for studying small-scale processes is to obtain information about the physical nature of the UOBL (poorly parametrised in numerical models), biological productivity, marine pollution and climate. The studies mentioned above help to identify some of the processes that are important to upper ocean dynamics, specifically Langmuir circulation, wind waves and internal gravity waves. These processes can be captured in acoustic images which, for instance, might be applied to provide insight into the effect of wind waves on the roughness of the sea surface (important in estimating the wind speed 10 m above the sea surface), the variability of LC in relation to both the wind direction and the direction of propagation of surface waves (an issue not properly addressed in most of numerical models of LC), and to illustrate how streaks or windrows may deform in response to non-linear internal waves (which may have a determinant impact on the dispersion of particulates). Here however, it should be emphasised that the role of measurement reliability in any serious investigation of such processes is of paramount importance.

1.2 Objectives

It has been remarked that progress into the understanding of physical processes occurring in the upper ocean depends upon the development of novel apparatus such as ARIES II. Acoustic instrumentation in particular have proved to be suitable for the detailed study of the UOBL. While the variety of acoustic devices developed up until now is ample, evolving from conventional inverted sonars (e.g. Aleksandrov and Vaindruk, 1974) towards the sophistication of coded-pulse Doppler sonars (e.g. Pinkel and

Smith, 1992; Alford and Pinkel, 2000), their effective utilisation seems greatly limited by the lack of long-life power supplies and by the incapacity to record large amounts of data. Thus, sonars have commonly been installed on fixed frameworks onto the sea bottom and connected through long cables with some electrical power unit located at a convenient 'high-point'. In the littoral zone (Thorpe and Hall, 1993), the deployment of sonar transducers near the breakers is done during spring tides and the high-point is usually a cliff to allow constant vigilance in stormy weather. In the coastal zone, say 40 m water depth, the high-point can be an hydrocarbon tower (Graham and Hall, 1997) or a ship (Thorpe *et al.*, 1996) which needs to remain riding at anchor during the whole measurements campaign even in extreme conditions! In the open sea, acoustic measurements collected by FLIP have particularly proved to be valuable in studies of the horizontal variability of LC during a storm (Smith, 1998). Nevertheless, there is interest into investigate the interaction of LC with several upper ocean phenomena in the open sea where, as a first step ahead in the right direction, a mooring equipped with acoustic instrumentation offers an exciting alternative to FLIP. To carry out a measurements programme in a zone remote from shore would require of autonomous acoustic systems capable of: (i) performing long-period measurements, (ii) operating continuously and unattended; (iii) withstanding all kinds of oceanic weather or hydrodynamic forces to which it will be subjected, and (iv) subsurface mooring deployment in order to minimise the effects of frequently violent sea-air interface. ARIES II is a robust novel acoustic instrument that complies with all the preceding requirements.

The general aim of this thesis is to demonstrate the potential, versatility and value of ARIES II into detecting acoustic signatures of physical processes arising at and beneath the sea surface in the open ocean. Although some of the ARIES II data have been interpreted already and published by Thorpe *et al.* (1998), it is nonetheless important to remove any doubt about interpretation. What emerges is to revisit the performance of the instrument itself, with a cautious and critical approach to establish the proper error bars and uncertainties which attach to ARIES II data. Hence the specific objectives are listed as follows:

- To describe the response of the streamlined instrument to fluid motions.
- To determine pitfalls which may affect the quantification of small-scale processes.
- To describe the instrument motions which may influence the appearance of features seen in acoustic images.
- To provide relationships to obtaining quantitative data in the near-surface ocean.
- To identify acoustic signatures caused by near-surface targets organising into patterns.

- To document and describe which novel acoustic features has the instrument captured.

This thesis adds new knowledge and understanding of how acoustic remote sensing techniques can be used underwater. Although the current work does not focus towards the sonar technology that ARIES II utilises, it is mainly about a critique of a new approach to acoustic underwater oceanography sensing. Its contribution lies in the use of a novel acoustic instrument and applying it in a new area, in the careful, detailed and critical analysis of the instrument's performance and methodology to be presented that has not been done before, in the approach to interpretation of high-resolution acoustic images, in the instrument's potential to measure upper ocean variables, and in the new simultaneous occurrence of phenomena captured in the data and not achieved by using other sonars, bringing evidence of its interaction.

1.3 Outline

The rest of the thesis is organised as follows. Chapter 2 reviews critically some of the advantanges and disadvantages involved in the use of acoustic technology and provides further fundamental information on the upper ocean processes detected by ARIES II.

Chapter 3 presents a detailed description of ARIES II and chapter 4 gives a critical account of the deployment site, a brief description of the non-linear internal waves on the basis of temperature records and highlights the need for better log accounts of physical events coming about during scientific cruises to aid in the interpretation of acoustic imagery. Chapter 5 comprises a critical description of the orientation of ARIES II in relation to mean currents and those induced by non-linear internal waves. In addition, it provides a simple method by which the vertical excursion of the instrument caused by the tilting of the mooring line is estimated. Chapter 6 tackles the problem of the distortion of the features captured in sonographs and resulting from the instrument motions. Specific formulations for estimating the phase speed and direction of surface waves, the orientation and lateral drift of bubble bands are given.

Chapter 7 focuses on what this novel instrument has revealed. Here observations consisting of novel acoustic signatures of upper ocean small-scale processes are documented, and the instrument's potential to obtaining quantitative information is demonstrated. Finally, chapter 8 completes the thesis with a summary and conclusions of main results, plus suggestions for future lines of research.

2. ACOUSTIC INSTRUMENTATION AND UPPER OCEAN SMALL-SCALE PROCESSES

Both the acquisition of quantitative estimates and physical interpretation of features appearing in sonographs (see also section 6.1) gathered using ARIES II, draw on the basic understanding of sonar transducers, surface and internal waves, Langmuir circulation and on their possible interactions. The purpose of the present chapter is to provide a brief yet critical review of the development of acoustic instrumentation and the above small-scale processes. It gives a theoretical basis of the methods and provides the detailed analysis of the processes to be referring later, drawing attention to uncertainties in the interpretation of acoustic imagery, and pointing to the gaps in knowledge that because of a lack of observations can potentially be filled by means of ARIES II.

2.1 The application of sonars to investigate the upper ocean boundary layer

The violence of motions generated by wind waves, notably in inhospitable oceanic regions, results in unavoidable and undesirable displacements of conventional instrumentation which is recording and sampling near the sea surface. The time scale of surface currents is only resolved by measurements of the velocity at fixed points, hence providing Eulerian observations. Aside from acoustic Doppler current meters, the horizontal scale is only resolved by means of arrays of moorings and the vertical scale through arrays of current meters suspended below a surface buoy on individual moorings. While surface drifters can minimise problems inherent in the stability of current meters, they are rather designed to cover large areas over significant periods of time. Reliable continuous measurements of processes in the top 20 m of the ocean are hence lacking; the region is under sampled. Sonars represent a tool that can resolve both the time and spatial scales of targets, passive tracers advected by near-surface currents and can therefore provide Lagrangian observations.

Acoustic instrumentation is advantageous over conventional instrumentation as a detector of turbulent motions for a number of reasons. First, short or far regions are ensonified, depending upon the pulse length and frequency of operation of sonar transducers, without interference with the flow field. Second, the velocity of near-surface scattered features that organise into patterns in sonographs can be estimated from, for example, the intersection of two beams corresponding to fixed sonars deployed in two different positions. Third, sonars provide continuous records of processes such as surface and internal gravity waves, breaking groups of waves, rainfall, fronts and Langmuir circulation (Fig. 2.1). Single targets could be detected with a very short pulse length in an environment with low concentration of scatterers. In order to gain insights into aspects of a complex environment, the utilisation of sonars, however, must be complemented with conventional measurements of wind, currents and water properties. When the above upper ocean processes coexist and when recorded simultaneously by sonars and conventional instrumentation, a source of exciting physical elucidation is available.

The development of acoustic instrumentation is here divided in four basic classes: echo sounders, inverted sonars, side-scan sonars and Doppler sonars. Some studies are briefly described below to emphasise the utility of acoustic devices in the gathering of information about turbulent processes in the upper ocean. An account of the sources of scattering is first made.

2.1.1 Sources of scattering

Several causes of acoustic scattering are summarised in Brown and Scott (1987) and Orr *et al.* (2000) (see also Pinkel, 2000). Here we refer only to those which are related to our observations, that is, bubble clouds and biological scatterers.

As mentioned earlier, bubble clouds also cause the scattering of sound beams, and sometimes they are associated with internal waves. Thorpe and Hall (1983) and Thorpe *et al.* (1987) have described strong echoes over internal wave troughs produced by both the roughening of the surface water and the breaking of surface waves in response to the currents induced by the internal waves as sketched in Fig. 2.1.

It is known (Medwin and Clay, 1998; Stanton *et al.*, 1998) that the swim-bladder of fish and the body structure of zooplankton (e.g. *Pteropods*, a group of shelled zooplankton which swim throughout the water column; see Stanton *et al.*, 2000) are acoustic scatterers. Fish and zooplankton often congregate at or within the thermocline over the continental shelf and in the open ocean, with fish yielding isolated targets and patch-like structures (e.g. schools) [sonars are sensitive to fish in the range 1-500 kHz; large fish are detected at frequencies less than 12 kHz and small fish at frequencies larger than 100 kHz (e.g. Cochrane *et al.*, 1991; Pedersen and Trevorrow, 1999)], or

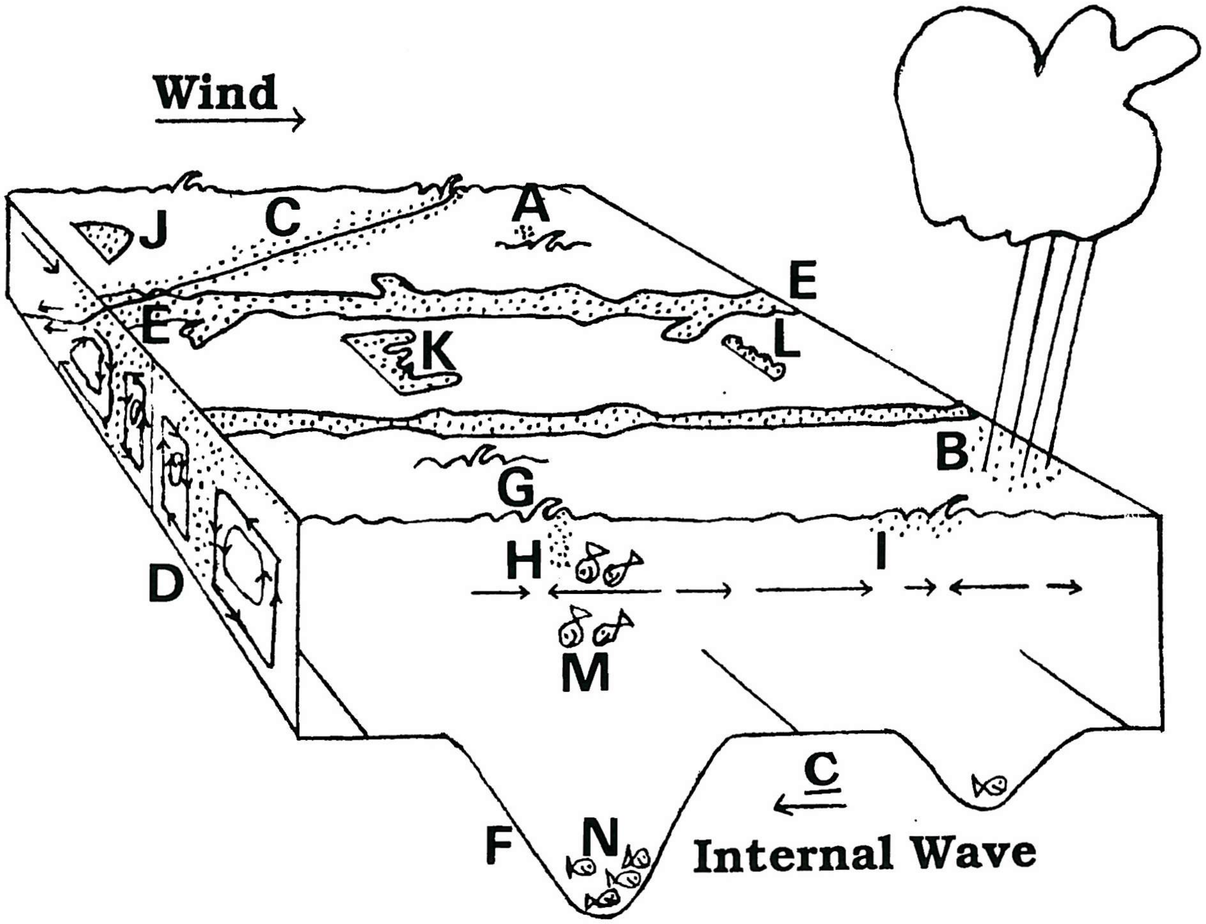

Fig. 2.1: *Schematic illustrating some small-scale processes occurring in the UOBL. Bubbles produced by breaking waves (A) and rain (B) are liable to accumulate into streaks and then redistribute below the sea surface by the flows associated with fronts (C) and Langmuir cells (D). Langmuir streaks (E-E) orient roughly parallel to the wind direction. Internal waves passing through (F), in this case, do not alter the spacing of Langmuir streaks but induce the breaking of surface waves over the forward flank of the internal wave trough (G). Two types of bubble clouds form during the process of wave breaking: vertical plumes of bubbles below the breaking wave (H) and accumulations of bubble clouds below the surface wave crests (I). Surface waves may also break and leave a classical near-surface horizontal plume of bubbles (J), but other structures have been detected by ARIES II (e.g. K and L). Internal waves may advect biological scatterers swimming around in the wave trough, most probably near the surface (M) or small fish may maintain position after the passage of the wave by opposing the flow at the orbital wave speed (N).*

zooplankton forming layers or regions of relatively homogeneous scattering. Plankton, commonly detected at 10^2-10^4 kHz, may form scattering layers with vertical scales between 10 and 50 cm and horizontal scales for tens of kilometres; some persisting for at least 4-6 h (Cowles *et al.*, 1998; Holliday *et al.*, 1998).

2.1.2 Echo sounders

Although knowledge that internal waves cause oscillations of scattering layers and that affect the sound transmission in the ocean can probably be traced back to Valdez (1960) and Lee (1961), respectively, it appears that oceanographers realised the potential use of (e.g. 5-25 kHz) echo sounders to observe internal waves only after the work of Proni and Apel (1975). They compared oscillating acoustic layers with simultaneous temperature recordings and found that layer troughs corresponded to troughs in the temperature signals which contained internal wave modulations. What Proni and Apel's (1975) work prompted was that echo sounders mounted on the hull of ships could both locate and provide Doppler shifted observations of internal waves through thermal inhomogeneities which change the acoustic impedance of the water, without having to rely on the presence of biological scatterers.

Typical graphical examples displaying the modulation of scattered layers by high-frequency internal waves are found elsewhere, for example, in Sandstrom and Elliot (1984), Brown and Scott (1987), and in Gasparovic and Apel (1988). Echo sounders operating at 100-200 kHz have provided vivid images (e.g. oscillations growing into billows) of different interactions between sills and tidal-driven flows of stratified water (Farmer and Smith, 1980; Wesson and Gregg, 1994; Farmer and Armi, 1999). There are also images of overturning events associated with both naturally occurring shear instabilities (Seim and Gregg, 1994) and internal waves (Haury *et al.*, 1979). The details of the preceding works are, unfortunately, beyond the scope of the current research.

Other common uses of echo sounders are related to the assessment of fish abundance and to the determination of vertical migrations of planktonic layers, both seasonal and diurnal (Szczucka and Klusek, 1996). Typical sonographs have shown that zooplankton ascends from depths of about 80 m and congregates near the sea surface at sunset, and that an intense downward migration, with a duration of a few minutes, takes place immediately after sunrise.

Ship-mounted acoustic instrumentation suffer from the drawback that measurements to some 3 to 5 m below the water surface are affected by the ship draft, wake turbulence and bubbles produced by the bow waves. However, inverted sonars, mounted on fixed platforms resting on the sea bottom or deployed on subsurface moorings, can easily obtain detailed acoustic data from this range of depths.

2.1.3 Inverted sonars

The application of inverted (i.e. upward-pointing) echo sounders to record wave heights was discussed by Tucker and Stubbs (1963), but Kanwisher (1963) was apparently the first into observe foam being swept down to 20 m by a breaking wave by means of an inverted sonar floating at a depth of 30 m. Thorpe (1982) has estimated that a minimum vertical speed of O(10 cms^{-1}) is needed to transport bubbles downwards to the above reported depth. The pioneers in the oceanographic use of upward-looking sonars, however, appear to be Aleksandrov and Vaindruk (1974). They suggested that the depth of bubble clouds responds to the orbital speeds of surface waves and the thickness to the turbulent motions of the water column, the latter carrying bubbles down to the observed depths and upwards to the surface, with speeds of O(10 cms^{-1}). The depth of the bubble clouds increased with the wave height and with the wind speed. These observations were obtained from an inverted narrow-beam sonar fixed on the sea floor at a depth of 20 m and at a distance of about 1 km from the shore. Using a mid-water inverted 248 kHz echo sounder in a freshwater lake, moored at 27 m beneath the surface in a water depth of 166 m, Thorpe and Stubbs (1979) found an empirical relation for the mean depth of bubble clouds ($\mathcal{D}$ in m) and the wind speed measured at 10 m ($\mathcal{U}_{10}$ in ms^{-1}). It is given by $\mathcal{D} = 0.4(\mathcal{U}_{10} - 2.5)$ for $0 \leq \mathcal{U}_{10} < 14$. Since individual tilted bubble clouds penetrating at depths larger than the wave height were observed in sonographs, a billow-like structure was suggested. The analysis of additional acoustic data, collected and reviewed by Thorpe (1982, 1986a), has shown that $\mathcal{D}$ also depends on the temperature difference ($\Delta\theta$ in K, which is the absolute temperature in Kelvins) between air and water as $\mathcal{D}_\theta = 0.31(1 - 0.1\Delta\theta)(\mathcal{U}_{10} - 2.5)$ for $0 \leq |\Delta\theta| < 4$. Billow-like clouds were found mainly in stable conditions ($\Delta\theta > 0$), whereas in unstable conditions ($\Delta\theta < 0$) the bubbles were vertical with a finger-like appearance (Fig. 2.2). It is worth mentioning how the mean depth of bubble clouds has been estimated. Whilst Thorpe and Stubbs (1979) considered a mean based on several estimates of the maximum depth (ignoring spaces in between) to which the bubble clouds observed in 30-min-sonographs penetrate, Thorpe (1982, 1986a) determined an average depth (measured from sonographs of over 60 min) to which bubble clouds can be detected according to the acoustic scattering cross section per unit volume of a cloud of bubbles, an integral measure of the effective area with which a density of bubbles scatter sound. Both $\mathcal{D}$ and $\mathcal{D}_\theta$ showed a general increase with $\mathcal{U}_{10}$.

Another relation for $\mathcal{D}$ now expressed as the relative depth $\frac{\mathcal{D}}{\lambda}$, where λ is the wavelength of surface waves, was found from measurements performed by ARIES (Thorpe, 1986b) in terms of the parameter $\frac{\mathcal{U}_{10}}{c}$. [Some ambiguity is here present as c can be the phase speed of the dominant waves (c_p), those with frequencies near the spectral peak, or the phase speed (c_z) estimated from the zero-crossing period in pressure records. In

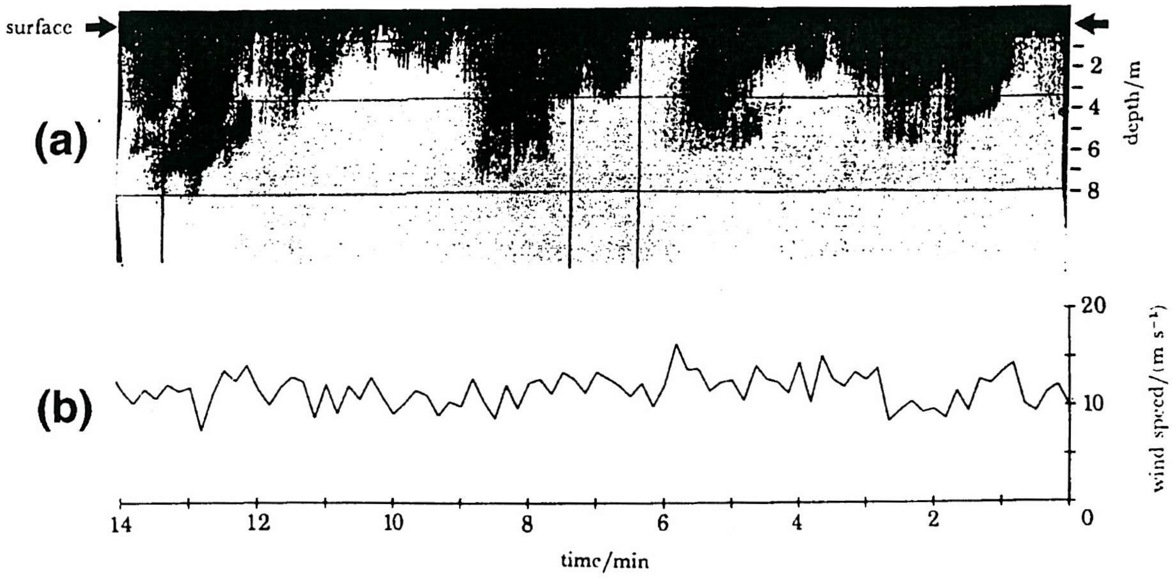

Fig. 2.2: *(a) Sonograph and (b) wind records from Oban (Scotland) in southwesterly winds for $\Delta\theta = -1.8$ K. (Taken from Thorpe, 1982).*

open ocean both are related as $\frac{c_p}{c_z} \sim 0.8$ (Longuet-Higgins, 1983)]. The parameter $\frac{\mathcal{U}_{10}}{c}$ gives information about the degree of development of surface waves, that is, whether or not the waves are receiving energy from the wind. Wind stress is effectively transmitted to water for large $\frac{\mathcal{U}_{10}}{c}$, that is, in conditions dominated by growing wind-waves. Plunging breakers and whitecaps are frequent, thus energy is available to, for instance, generate vorticity. Swell dominated or decaying wind-wave conditions occur for low values of $\frac{\mathcal{U}_{10}}{c}$ (low forcing) where spilling breakers are typical. Under these circumstances, breaking waves are less frequent and bubble clouds are intermittent. Although there is no empirical relation reported, bounds are given as $\frac{\mathcal{D}}{\lambda} = 0.04$ when $\frac{\mathcal{U}_{10}}{c} = 0.6$ and $\frac{\mathcal{D}}{\lambda} = 0.2$ when $\frac{\mathcal{U}_{10}}{c} = 2$ (Thorpe, 1992b, 1995a).

Vertical-looking sonars provide information regarding the vertical distribution of bubbles and the variation of the bubble layer depth with wind speed. Because such sonars are generally deployed in a fixed position, it is not possible to determine unambiguously whether changes in the bubble cloud's depth are caused by advection through the beam pattern or by local growth as bubble clouds deepen or thin (e.g. Thorpe, 1982). The latter depends upon the relative magnitudes of vertical flows and bubble rising speeds. Thorpe and Hall (1982) have taken photographs of foam streaks drifting slowly at speeds of 2-4 cms^{-1} and crossing simultaneously the acoustic field of an inverted echo sounder. A classification of windrows and a discrimination of signatures of bubble clouds located below Langmuir streaks from those located beneath breaking waves was devised in this manner. Without the guidance of observations of floating indicators of windrows on the sea surface, side-scan sonars represent an obvious alternative.

2.1.4 Side-scan sonars

Side-scan sonars provide information about the horizontal distribution and persistence of near-surface bubble clouds, and more importantly, they provide estimates of the speed and direction of propagation of scattered targets. When the targets are linear features depicting bubble clouds agglomerated into bands advected by mean currents, their azimuthal orientation and their lateral drift can be estimated from the geometry of orthogonal side-scan sonars. When targets are moving at speeds close to the phase speed of surface waves, they appear as quasi-vertical streaks in sonographs and both the phase speed and direction of propagation can similarly be estimated (see section 6.4.1). As for the speed of mean currents, the estimation is based upon the drift of a cloud of bubbles produced by surface waves breaking along the sea surface. The vertical structure of these bubbles can be inferred from their acoustic scattering cross section per unit volume.

A comprehensive description of the capabilities of this sort of sonars is given by Thorpe and Hall (1983). Their measurements were restricted to a coastal environment with a water depth of about 35 m because a power source, via a cable of some 700 m length onshore, is needed to operate the 248 kHz transducers mounted on a quadripod resting onto the sea floor. An effective range of about 150 m was attained with a pulse length of 0.12 m. The detection of individual wave breaking events and bubble bands through the presence of, respectively, sudden short-range quasi-vertical streaks and more persistent scattered linear features (Fig. 2.3), is of particular relevance. In fact, the orientation of near-surface bubble bands is assessed from the linear features appearing in orthogonal sonographs. Thorpe and Hall (1983) found bubble bands closely aligned in the wind direction and, helped by a 16-mm ciné camera, identified the bands as convergent streaks resulting from Langmuir circulation. The important point here is that side-scan sonars cannot only be used for revealing Langmuir circulation, but also to associate different types of features appearing in sonographs with breaking surface waves, fronts and internal waves. Moreover, Thorpe *et al.* (1998) have recently shown evidence that biological scatterers provide a link between subsurface zones of increased scattering and internal waves in dual-beam inverted side-scan sonars (see section 2.3).

The combination of side-scan and inverted sonars in a freely drifting instrument, with capacity to record 80 hrs of acoustic data, has also been utilised to successfully match Langmuir bubble bands and vertical bubble plumes (Fig. 2.3) depicting downwelling flows in convergent Langmuir cells (Zedel and Farmer, 1991). From side-scan

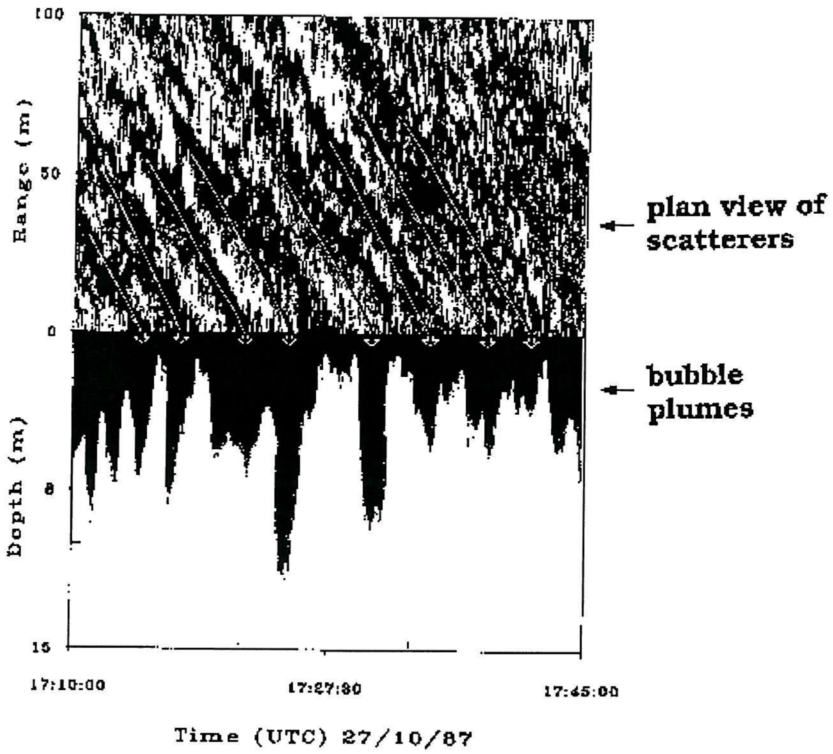

Fig. 2.3: *Linear features (mean slope marked by arrows) approaching a side-scan sonar and bubble plumes detected by a vertical-looking sonar. Both sonographs were recorded simultaneously. The linear features are interpreted as bands of scatterers arriving at about the same time than the plumes of bubbles, suggesting that the plumes are associated with particular bands and not just advected clouds. (Taken from Zedel and Farmer, 1991).*

sonars mounted on a submarine and photographs taken from an helicopter, Osborn *et al.* (1992) have demonstrated that, even if there is no visible manifestation of windrows on the sea surface, a pattern of Langmuir bubble bands may still be detected by the sonars. Besides, the detailed structure of bubble bands has become apparent from high-resolution side-scan sonographs (Thorpe, 1992a; Farmer and Li, 1995; Graham and Hall, 1997). In particular, bands converging (diverging) and merging into (splitting apart from) one another to form (inverted) Y-junctions have been found, particularly with the narrow end pointing dominantly downwind (A model for studying the formation of Y-junctions has recently been developed by Bhaskaran and Leibovich (2002)).

The conversion of scattered features with Y-like shapes in sonographs into two-dimensional features with a definite geometrical form in real space deserves caution (Farmer and Li, 1995) because of advection. One source of difficulty, similarly to that described earlier (section 2.1.3) in relation to inverted sonars, is that Y-junctions drifting in a direction normal to a single sonar beam would produce the same Y-like shape structure in a time-space frame of reference as the merging of parallel bubble bands (or of a bubble cloud into a bubble band) within the acoustic beam pattern. This ambiguity has partially been solved by means of current meter measurements (Zedel and Farmer, 1991) and by mechanically rotating Doppler sonars into several directions for each transmission to scan some area and produce two-dimensional spatial images (Farmer and Li, 1995). These junctions also arise in numerical models (Cox and Leibovich, 1997; McWilliams *et al.*, 1997) and reflect the three-dimensional character of Langmuir circulation.

Another ambiguity results from the geometrical interpretation of linear features approaching or receding from orthogonal side-scan sonars because, for quantitative and practical purposes, they can be reduced to simple lines (e.g. Fig. 2.3) or skeletons (see Fig. 2.4 and also Thorpe and Curé, 1994; Farmer and Li, 1995; Graham and Hall, 1997). Should lines or skeletons with, for example, a similar mean slope be connected so as to form a continuous straight line? What do such straight lines represent, bubble bands or bubble patches? Has the feature discontinuity originated from the absence of bubbles (e.g. low $\frac{u_{10}}{c}$) or from the instability and breaking up of the local circulation pattern (e.g. a changing wind direction)? By using sector-scanning Doppler sonars, Farmer (1997) has shown that continuous bubble bands indeed persist in some quadrants of acoustic images covering full 360° sectors (Fig. 2.5). Further the linear features shown in Fig. 2.3 and 2.5 emphasise the variation of scattering intensity along bubble bands. Then delineating straight bubble bands in sectors of 90°, continuous or quasi-continuous, from linear features observed in orthogonal sonographs is reasonable (see also chapter 6).

Whilst ARIES II can be deployed on subsurface moorings or fixed quadripods, unmanned autonomous underwater vehicles (e.g. AutoSub) can be steered to approach some steady pattern of windrows and oriented in a convenient direction to collect data of acoustic scatterers. Turbulence induced by the breaking of wind waves could also be recorded. Hence the next step forward in the development of acoustic instrumentation has recently been achieved in Loch Linnhe, Scotland (see Thorpe *et al.*, 2003) utilising AutoSub equipped with ARIES II instrumentation (e.g. side-scan and inverted sonars) and other sensors to measure near-surface turbulence. The aim of the trials was to establish sources of interference, that is the effect of the AutoSub propulsion system on acoustic devices and turbulence probes. The level of noise produced by AutoSub was detected, but at a level well beneath the normal signal in turbulent patches. The turbulence probes were also insensitive to interference from the ADCP and the collision avoidance sonar. An important development, in comparison with ARIES II (see chapter 3), is a modified logger with an ETHERNET output enabling down load data in situ; ARIES II mounted on AutoSub produced many good quality sonograms. The stability and performance of such vehicle within a region of intense non-linear wave

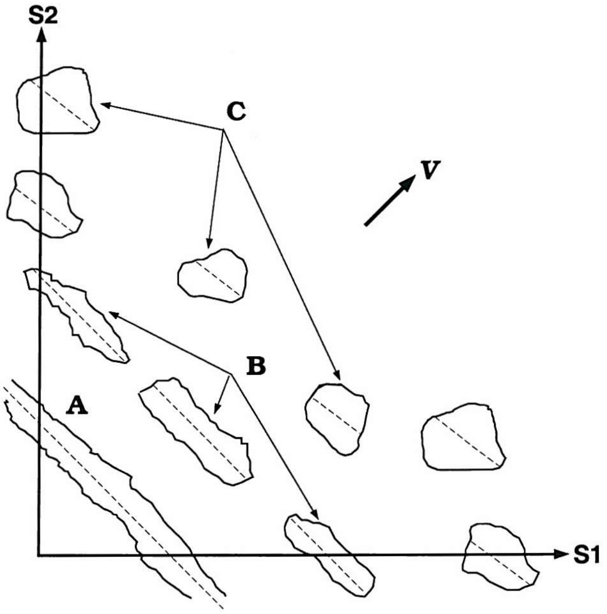

Fig. 2.4: *Plan view of features advected in a steady mean flow V and passing through the acoustic field of the orthogonal side-scan sonars S1 and S2. The features outlined here are: a bubble band (A), a fragmented bubble band (B) and patches of bubble clouds (C). The dashed lines represent mean slopes of the features (e.g. skeletons).*

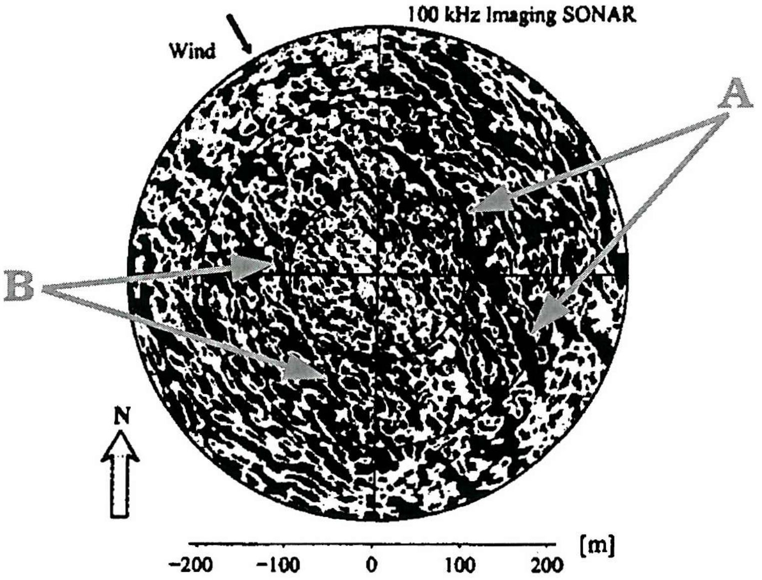

Fig. 2.5: *Scanning sonograph, obtained from a sonar suspended 25 m beneath the surface, showing bubble bands (e.g. those labelled A and B) aligned in the wind direction (wind speed is 15 ms^{-1}). A 360° image is obtained every 30 s. (From Farmer, 1997).*

activity during spring tides remains, however, uncertain.

2.1.5 Doppler sonars

In contrast to conventional sonars, Doppler sonars can measure the velocity field from discrete scatterers such as air bubbles and live organisms (Aleksandrov *et al.*, 1975; Pinkel, 1979). The component of velocity parallel to the sonar beam (radial velocity) is estimated from the Doppler shift of the returning echo as a function of range (Pinkel, 1981). Doppler tracking systems are useful for monitoring the motion of ocean moorings (e.g. Spindel *et al.*, 1978). Acoustic Doppler Current Profilers are also useful to estimate abundance and biomass of zooplankton (e.g. Flagg and Smith, 1989; Heywood *et al.*, 1991; Ashjian *et al.*, 1998) and wind direction (e.g. Zedel *et al.*, 1996, 1999), whereas the propagation of internal wave groups and the speed of diel migrations, typically O(1-4 cms^{-1}), have been assessed from multi-beam Doppler sonars (e.g. Pinkel, 1983; Plueddemann and Pinkel, 1989) and from Doppler sonars mounted on ships (Pinkel, 2000). Such sonars have also shown that diel migrations occur from depths as great as 300 m (Plueddemann and Pinkel, 1989; Fisher and Visbeck, 1993).

Several problems arise in the use of shipborne Doppler sonars which can degrade acoustic signals (Pinkel, 1981; García-Górriz *et al.*, 1997). These are connected with the speed and motions of the ship, and with the passive or random movement of scatterers within the sonar beams. Acoustic measurements are also affected by different levels of flow noise, depending on whether the ship is on station or steaming at full speed, by propeller cavitation noise and by the interference with other acoustic devices. It is perhaps for the above reasons that much of the research of the upper ocean using Doppler sonars has been carried out from the Research Platform FLIP. Also, it provides stability since the propagation of swell causes sonars mounted on FLIP to oscillate. According to Smith *et al.* (1987), vertical and horizontal tilts of sonars beams driven by swell have a root mean square of typically less than 5°.

Pinkel and Smith (1987) and Smith and Pinkel (1987) pioneered the application of Doppler sonars to study Langmuir circulation and wind waves, particularly over scales of 500-1400 m reached with frequencies between 75 and 80 kHz and a range resolution of roughly 20 m (a little too high to resolve all the LC patterns). Alternatively, sector-scanning Doppler technology has the advantage of removing ambiguities in the interpretation of the shape of scattered features because continuous spatial sectors are imaged (see section 2.1.4). For instance, Doppler sonars operating at 195 kHz can reach scales of O(200-400 m) with a range resolution of some 2.7 m over 45° sectors scanned in 2° increments. Such devices have been used to describe rip-currents (Smith and Largier, 1995) and Langmuir circulation in the deep ocean (Smith, 1998).

2.2 Surface gravity waves

The action of wind on the UOBL generates many small-scale motions such as ripples, gravity waves and Langmuir cells. Wind transfers momentum to the sea surface via an effective tangential stress, $|\tau|$, given by the bulk formula

$$|\tau| = \rho_a \mathcal{C}_D \mathcal{U}_{10}^2. \tag{2.1}$$

with the air density $\rho_a \sim 1.2$ kgm^{-3} and the wind speed $\mathcal{U}_{10}$ measured at a height of 10 m above the sea level. The drag coefficient $\mathcal{C}_D$ is a momentum exchange coefficient that depends upon the height, $\mathcal{U}_{10}$, the roughness of the sea surface (e.g. $\frac{\mathcal{U}_{10}}{c}$, wave slope, fetch, wind gustiness, currents) and upon the stability of the atmosphere adjoining the sea.

2.2.1 Estimations of the drag coefficient

Since during long field expeditions the atmospheric boundary layer might change from generally stable (with heating and buoyancy reduction of the sea surface) to unstable, estimations of $\mathcal{C}_D$ can result biased from those for neutral stratification. For unstable atmospheric conditions, drag coefficients have larger values than those for neutral stratification, whilst estimations of $\mathcal{C}_D$ in stable conditions fall below the level of neutral $\mathcal{C}_D$ values (Garratt, 1992). Although there is no adequate theory which can explain the dependence of the dimensionless parameter $\mathcal{C}_D$ on all the variables mentioned above, it is customary to correct $\mathcal{C}_D$ for considering neutral atmospheric conditions. This is usually done assuming individual logarithmic profiles of $\mathcal{U}_{10}$, air temperature and specific humidity (denoted all by $\mathcal{F}$) plus a stratification function (f) according to the expression

$$\frac{\partial \mathcal{F}}{\partial z} \frac{\kappa z}{\mathcal{F}_*} = f\left(\frac{z}{\mathcal{L}}\right). \tag{2.2}$$

where $\kappa \sim 0.4$ is the von Kármán constant, $\mathcal{F}_*$ representing characteristic scales of $\mathcal{F}$, and z being the height above the sea surface. The relative height (i.e. the Richardson number) $\frac{z}{\mathcal{L}}$ is used as a thermal stability parameter defined by the Monin-Obukhov scale length ($\mathcal{L}$). This relates the friction velocity in the air (u_*) with surface fluxes of temperature and specific humidity, and characterises the height at which the buoyant destruction of turbulent kinetic energy is of the same order of the shear production of turbulence. Thus in neutral conditions $\frac{z}{\mathcal{L}} = 0$ and the value of $f\left(\frac{z}{\mathcal{L}}\right)$ is a constant to be determined from experiments or equals to one if $\mathcal{F}$, by definition, is the wind speed. For unstable conditions (e.g. cooling the free surface, buoyancy flux promotes free convection and shear production is negligible) $\frac{z}{\mathcal{L}} < 0$ and $f\left(\frac{z}{\mathcal{L}}\right) < 1$. A convenient empirical fit for $\mathcal{C}_D$ in the open ocean, adjusted for neutral stability by applying known functions $f\left(\frac{z}{\mathcal{L}}\right)$ in (2.2), is from Yelland and Taylor (1996)

$$10^3\mathcal{C}_D = 0.60 + 0.070\,\mathcal{U}_{10}, \tag{2.3}$$

valid when $(6 \leq \mathcal{U}_{10} \leq 26)$ ms^{-1}, while for lower wind speeds in the range $(3 \leq \mathcal{U}_{10} < 6)$ ms^{-1}, the fitted relationship is

$$10^3\mathcal{C}_D = 0.29 + \frac{3.1}{\mathcal{U}_{10}} + \frac{7.7}{\mathcal{U}_{10}^2}, \tag{2.4}$$

A typical value of $10^3\mathcal{C}_D = 1.3$ stands at $\mathcal{U}_{10} = 10$ ms^{-1}. Other formulations without considering a correction for neutral $\mathcal{C}_D$ are given by Wu (1994) and errors caused by not using (2.3) and (2.4) can easily be estimated. For example, when $\mathcal{U}_{10} = 3$ ms^{-1}, the value of $\mathcal{C}_D$ without correction for neutral stability represents an underestimation of about 10% with respect to that from (2.4). For strong winds (e.g. $\mathcal{U}_{10} = 15$ ms^{-1}), there is an overestimation of 7% in relation to (2.3). Therefore the correction for neutral stratification is relatively small but important.

Whereas (2.3) predicts a linear decrease of $\mathcal{C}_D$ as wind speed decreases, the expression (2.4) considers an increase of $\mathcal{C}_D$ for low winds. Such increase of $\mathcal{C}_D$ is apparently caused by a transition from a regime where the surface tension is dominant (i.e. capillary waves), at light winds (< 3 ms^{-1}), to a gravity regime at larger winds (> 6 ms^{-1}). Consequently, the formulation proposed by Yelland and Taylor (1996) suggests that $\mathcal{C}_D$ stops decreasing at a $\mathcal{U}_{10}$ of roughly 6 ms^{-1}. An expression for light winds that follows a similar tendency to that proposed by Wu (1994) for describing effects of surface tension is,

$$10^3\mathcal{C}_D = 1.66 + \frac{1.56}{\mathcal{U}_{10}}. \tag{2.5}$$

which is the same of Trenberth *et al.* (1990), except that the constant 1.66 is used instead of 0.62 to match equation (2.4) for $\mathcal{U}_{10} = 3.0$ ms^{-1}.

2.2.2 Breaking waves

It is generally believed that most of the transference of momentum by the wind to the underlying sea surface occurs inside the wave generation zone and that only 5% of the momentum is carried by waves outside this zone. Momentum is delivered through the viscous drag of individual fluid layers sliding over each other and through the local amplification and dissipation of waves. Breaking waves limit the wave height, are a source of vorticity and turbulence, making energy available for mixing surface waters and for generating currents.

In the open ocean, breaking waves are associated with those waves near the peak of the wave-frequency spectrum and with wave groups (Donelan *et al.*, 1972; Thorpe, 1992b). The position of breaking within a group of waves is usually at the centre where successive individual waves are highest, they break with a periodicity of about twice that of the dominant wave period. Signatures of breaking wave groups have been identified by Thorpe and Hall (1983) from the strong acoustic echoes associated with bubbles created by individual breaking waves or, more precisely, by high-frequency breaking waves superimposed on individual waves in the group. The signatures depend upon the view direction of sonar transducers. If the acoustic beam of a sonar is normal to wave crests, the detection of breaking waves is characterised by sets of short-range quasi-vertical staggered lines (see section 7.6) that mark the position of short-duration breaking crests, indicating that breaking occurs almost simultaneously along a portion of the wave crests (Thorpe and Hall, 1983). No patterns of staggered lines are consequently formed when an acoustic beam is parallel to wave crests.

Thorpe and Hall (1983), with a fixed sonar looking into the waves, have found that (in the few cases examined) the ratio of the duration of the wave breaking (i.e. the quasi-vertical line), t_b, to the wave period, T, is a constant that also relates the length of the crest breaking, λ_b, to the wavelength, λ, that is $\frac{t_b}{T} \sim \frac{1}{3} - \frac{1}{2} \sim \frac{\lambda_b}{\lambda}$. This implies that the slope of the breaking crest does determine the phase speed of wind-sea in reasonable agreement with linear theory for short waves (e.g. $\lambda \ll h$, where h is the water depth which indicates the approximation for deep water waves, not the actual depth of the water). The breaking wave may produce a near-surface plume of bubbles as the wave crest advances forward (labels a and b in Fig. 7.10 and label J in Fig. 2.1, see also Deane, 1999) which, in general, is elongated in the wave direction. The initial dimensions of the plume have been estimated by Thorpe and Hall (1983) from its duration (t_p) and phase speed (c), which defines the length (d_p) of the plume in the wave direction as $d_p = ct_p$, and from the length (ℓ) of the crest along which breaking occurs, which defines the plume width. The ratio $\frac{d_p}{\ell}$ is typically about 1.4, but this value may increase (e.g. further elongation) if there is significant vertical shear in the near-surface currents or if turbulence acting to spread the plume is horizontally anisotropic. It is worth noticing that d_p also defines the distance advanced by a wave during breaking (Thorpe, 1995a).

There appears to be poor understanding of the development of near-surface patches of turbulence with some structure created by breaking waves and left behind as deep water waves propagate forward. The shape of patches probably reflects variations in the dynamical processes from which they originate. Some insights have been gained from breaking waves produced in laboratory experiments in the absence of wind, either by changes of the bottom slope (Nadaoka *et al.*, 1989) or by the interference of high lower-frequency waves in a wave channel (Rapp and Melville, 1990; Melville, 1996; Melville

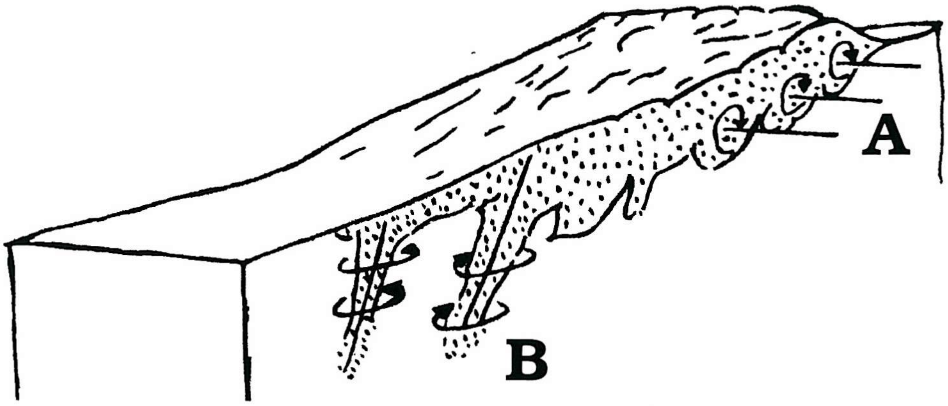

Fig. 2.6: *Sketch showing possible turbulent structures produced by a breaking wave in open ocean. A, a vortex roller with axis parallel to the wave crest. B, slanted vortices with axis tilted downwards. (Adapted from Nadaoka et al. 1989).*

et al., 2002). Breaking drives intermittent air entrainment and transforms the motion of fluid particles from irrotational to rotational, generating vorticity by the relatively strong shear near the surface which develops in organised vortex-like motions or rollers. Bubbles injected by breaking waves, at least initially for a few periods after breaking, may follow the orbital motions of fluid particles (e.g. closed streamlined patterns) beneath the wave crests at speeds close to, or in excess of the speed of the wave itself. That bubbles act like true passive tracers is problematic because of their natural positive buoyancy (see sections 1.1 and 2.1.3). However, small bubbles remaining after breaking and forming an intense turbulent zone are, perhaps, occasionally trapped in slanted rollers (Fig. 2.6). A condition to draw bubbles into a vortex is that of rising speeds negligible in comparison with the speed difference of horizontal orbital speeds across the vortex (e.g. Sene *et al.*, 1994). Near-surface slanted rollers appear effective in extracting energy from the mean flow because they have a principal axis which is not normal to the mean flow direction, but aligned with the mean strain rate. Such rollers might be associated with surface signatures in the form of air-contained spots (e.g. foam) with irregular spatial distribution along the wave crest (Nadaoka *et al.*, 1989). One can speculate that the dissipation of slanted rollers might release large bubbles if temporally trapped. These bubbles, by ascending rapidly upwards (see section 1), could form floating foam in the water surface or the upwelling water on which their drag has been imposed may produce some smooth region after the bursting of large bubbles. The forward motion of horizontal vortices (Fig. 2.6) produced in laboratory experiments has been found to reduce to about 80% of the phase speed of the wave in about 60 periods (Rapp and Melville, 1990) which, for a wave with a period of 3 s,

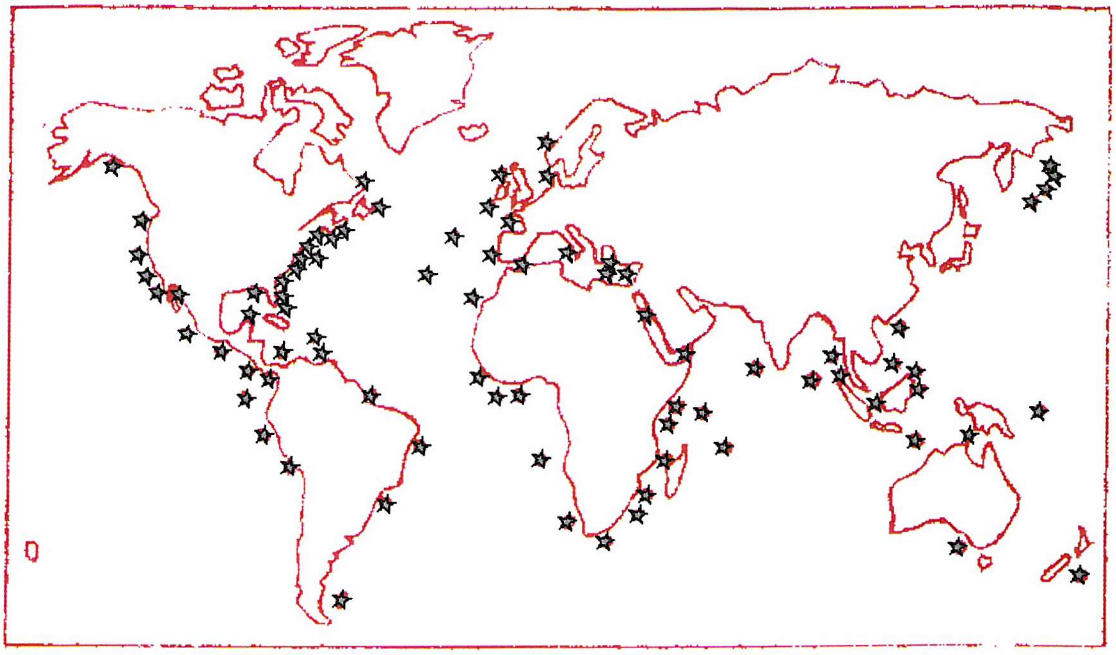

Fig. 2.7: *Map showing sites where trains of internal waves have been reported. The sources are satellite imagery, visual or photographic sightings from aircraft and log books of marine observers in commercial ships. Most of them are thought to be solitons. (Adapted from Fedorov and Ginzburg, 1986 and from Apel et al., 1995).*

will take place in 3 min. It is uncertain, however, if results obtained under laboratory conditions can be extrapolated to the open sea to explain, for example, the pattern of bubbles labelled G and H in Fig. 2.1.

2.3 Internal gravity waves

Internal waves are ubiquitous in the stratified ocean (Garrett and Munk, 1979, see Fig. 2.7). This sort of wave is present on a thermocline as interfacial waves and propagates horizontally along a density interface because of the restoring effect of the buoyancy force. The passage of internal waves is commonly detected by temperature fluctuations ($>$ 1 °C) in the water column for periods of, say, 20 min and by zones of enhanced acoustic scattering, frequently detected in the thermocline (see section 2.1). Internal waves are found to exist on many scales, typically with periods from 5 min to several hours, wavelengths in the range 10 m to 50 km and amplitudes between 0.2 m and 40 m.

The passage of internal waves is also frequently noticed by variations in the patterns of the roughness at the sea surface (e.g. Hughes and Dawson, 1988; Pistek and Violette, 1999) and sometimes by the accompanying bands of breaking waves (e.g. Osborne and

Burch, 1980; Apel *et al.*, 1985) which generate foam and near-surface bubble clouds that can appear as vertical plumes in acoustic images. Few events have been observed in sonographs (see Thorpe and Hall, 1983; Thorpe *et al.*, 1987; Trevorrow, 1998). At the surface, bubbles may form patches or bands of near-surface enhanced scattering in intervals of roughly 7 min. Such regions of dense bubbles were suggested by Thorpe *et al.* (1987) to result from the effects of wind speed and/or horizontal surface straining caused by internal waves inducing groups of surface waves to break. Trevorrow (1998) found short duration (2-5 min) soliton-type internal waves where the position of 'small' surface breaking waves, producing vertical plumes of bubbles that reached a depth of about 3-4 m, was coincident with the region of maximum surface convergence in low wind; the position of the plumes, now attributed to breaking swell, shifted to the centre of the wave trough during presumably strong winds and reached a depth of roughly 10 m. Trevorrow (1998) suggested, probably meaning vertical motion, the association of a circulation of O(30 cms^{-1}) with the latter. Downward displacements caused by the internal waves had amplitudes in the range 5 to 22 m in a 7 m pycnocline (e.g. highly non-linear internal waves). This work, however, needs clarification because it is generally believed that $\mathcal{U}_{10} < 1$ ms^{-1} is too low for breakers and bubbles to occur (see Fig. 1.1). In addition, no information regarding the speed and direction of wind, the direction of surface and internal waves or the frequency of the bubble plume events was reported.

Some background on the relevant sources of information leading to the interpretation of sonographs on these topics is therefore needed. This is done in the next three sections.

2.3.1 Modulation of surface waves

As stated earlier, bubble clouds resulting from breaking waves represent a major source of acoustic scattering observed in sonographs. The occurrence of scattering patches, bands or plumes during periods of internal waves indicate the interaction between surface and internal waves. Factors that determine the position of regions of enhanced scattering over internal wave troughs for instance, and thereby breaking waves, are the angle between the direction of propagation of surface waves and that of internal waves, the wavelength of surface waves, the interaction time and the wind speed.

There is a resonance condition to satisfy for this interaction to occur: regions where the local group speed of surface waves (c_g) is near the phase speed of internal waves are prone to experience the largest interactions or modulations (Phillips, 1973). There, surface waves will be most retarded by the horizontal surface currents of internal waves. Thus, if surface waves propagate in opposite direction to the internal waves, the position of maximum surface modulations (increased amplitudes and decreased wavelengths) will be over the wave troughs (Gargett and Hughes, 1972). The opposite effect results if surface and internal waves are travelling in the same direction of propagation.

Both horizontal currents and phase speeds of internal waves are typically in the range (0.1-1.0) ms^{-1}. For deep-water surface waves, $c_g \sim 0.6\lambda^{\frac{1}{2}}$ with c_g in ms^{-1} and λ in m. Then the resonance condition implies λ from about 0.03 m to 3 m. Gasparovic *et al.* (1988) have found that surface wave modulations are confined typically to wavelengths between 0.10 m and 20 m or periods in the range of 0.25 s to 3.6 s. This is not surprising since the longer the surface waves (e.g. > 100 m), the larger the difference in speeds between surface and internal waves. Further, little time of interaction leads to a very weak modulation, if any.

A different situation occurs when the wind speed is considered because the surface waves most affected are those with an interaction time comparable to the relaxation time (Gasparovic *et al.*, 1989). The functional form of the relaxation time, t_r, is given in terms of a function δ defined as (Hughes, 1978)

$$\delta = k\ u_*\ \cos\phi\ \left(0.01 + 0.016\ |\cos\phi|\ \frac{ku_*}{\omega}\right)\left\{1 - \exp\left[-8.9\ \left(\frac{ku_*}{\omega} - 0.03\right)^{\frac{1}{2}}\right]\right\}. \tag{2.6}$$

where $t_r = \frac{1}{\delta}$ is a measure of how long a perturbed wave spectrum takes to relax back to its state of equilibrium (Apel, 1995), k is the wave number, $u_* = C_D^{\frac{1}{2}}\ \mathcal{U}_{10}$ is the friction speed of air (see section 2.2.1), ω the wave frequency in radians and ϕ is the angle between surface waves and the wind direction. Fig. 2.8 shows that t_r decreases as k increases. Because very short surface waves are tightly coupled with the (restoring force) wind, they are forced rapidly back into equilibrium. It follows that the relaxation time is reduced and hence a weak modulation is also expected. Then for a fixed k, t_r increases as both $\mathcal{U}_{10}$ decreases and ϕ increases. In terms of t_r, Fig. 2.8 also shows that long waves, in comparison with shorter waves, respond more rapidly to changes in the wind speed.

The interaction between surface and internal waves originates a spectral modulation which has been modelled by an action-balance equation for an equilibrium surface wave spectrum (Hughes, 1978; Thompson, 1985; Thompson and Gasparovic, 1986). Such a spectrum represents a sea state composed of many waves of different wave numbers. A varying surface current field induced by internal waves tends to perturb the equilibrium spectrum while a local wind field tends to restore the spectrum back towards equilibrium.

Note that the direction of propagation of internal waves is not explicitly considered in equation (2.6). Provided that surface and internal waves are in opposite (or in the same) direction relative to the wind direction, as normally found by Apel *et al.* (1988),

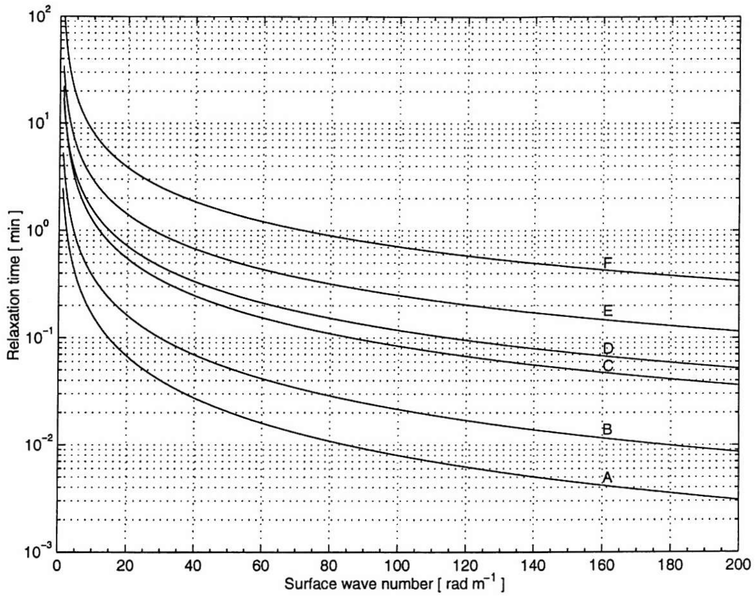

Fig. 2.8: *The dependence of the relaxation time upon the wave number of surface waves for different* ϕ *and* $\mathcal{U}_{10}$. *For* $\phi = 0°$, *the labels A, B C denote* $\mathcal{U}_{10}[\mathrm{ms}^{-1}] = 13, 7$ and 2, *respectively. Labels D, E and F follow the same sequence for* $\mathcal{U}_{10}$, *but for* $\phi = 80°$.

this is not a problem. Fig. 2.9 shows a solution of the action-balance equation for $\mathcal{U}_{10} = 6$ ms^{-1} and $\phi = 35°$. The modulation of surface waves by the current field is described via the horizontal gradient of the current or strain. Maximal modulation or maximal surface roughness for waves of about 1-6 m length occurs near the maximum of the surface current (or nought strain), that is, over the internal wave trough (Fig. 2.9). As the wavelength is reduced, for example to 0.2 m, the maximal modulation becomes weaker for reasons explained already and shifts towards the region of minimum (negative) surface straining, that is, at the region of convergent internal currents (Fig. 2.9c). In the region of divergent currents, the amplitude of the wind waves is reduced. Spectral modulations of surface waves when wind waves are not travelling against the internal wave current field show, according to Apel *et al.* (1988), significant variability depending on the angle between the surface and the internal waves. Such modulations seem to reduce when wind waves propagate normal to internal waves.

Thorpe *et al.* (1987) have found that surface waves break more frequently where internal wave currents tend to oppose the propagation direction of surface waves, for instance, at the internal wave trough. Since the stronger modulations shown in Fig. 2.9c occur over the wave trough, it seems likely that intense breaking events of surface waves are associated with metre-scale waves (e.g. 1-6 m or O(1-2 s)).

Has breaking swell produced the huge plume of bubbles observed by Trevorrow (1998) over the internal wave trough? Despite the lack of a universal criterion stating

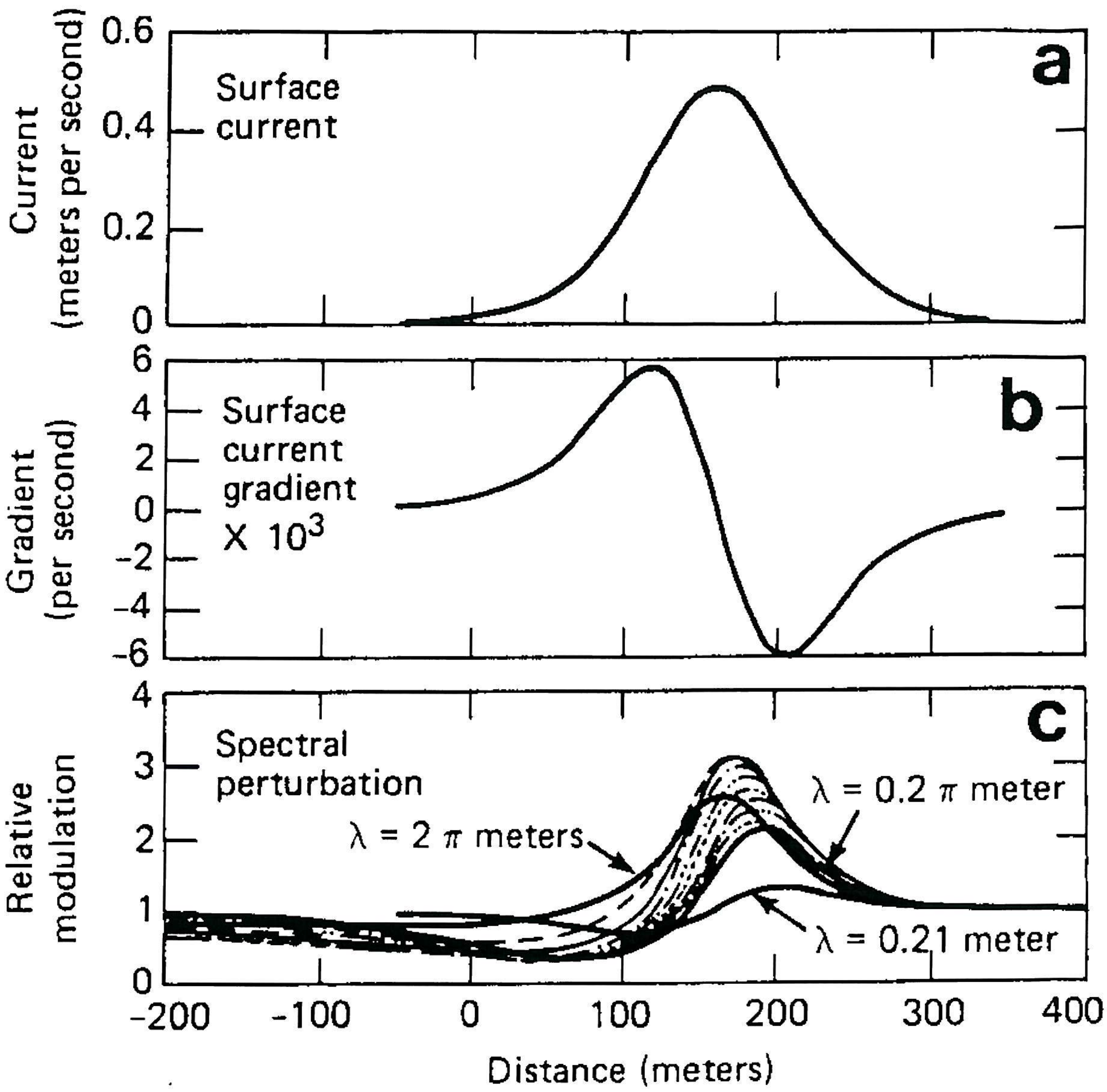

Fig. 2.9: *Spectral modulations of surface waves resulting from the interaction with an internal wave propagating at opposite direction. (a) surface internal-wave current, (b) surface horizontal gradient of the current (straining) and (c) spectral modulation for several different wavelengths where the family of curves between* $\lambda = 2\pi$ *m and* $\lambda = 0.2\pi$ *m corresponds to wave numbers between 1* m^{-1} *and 10* m^{-1} *in increments of 1* m^{-1}*. (Taken from Thompson, 1985).*

how surface waves break (Thorpe, 1995a), there is a dynamical criterion that defines breaking when the acceleration of fluid particles, g_w, exceeds the value of roughly $0.4g$ (Longuet-Higgins and Fox, 1977), where g is the acceleration of gravity. Violent impacts of overturning waves onto the sea surface are perhaps capable of producing huge vertical bubble plumes. Largest accelerations in the overturning jets are typically around $5g$ (Peregrine, 1991). The acceleration of fluid particles at the sea surface with displacement of the form $\eta = \mathbb{A}\cos(kx - \omega t)$ is, for deep-water surface waves, $|g_w| = \omega^2\eta$. Here $\mathbb{A}$, k and ω are, respectively, the wave amplitude, the wave number and the wave frequency in radians. At a breaking crest, $\lambda \sim 16\mathbb{A}$. Therefore, a typical swell with a period of 10 s corresponds to a wave height of about 20 m when breaking. This surface wave, according to the Admiralty Weather Manual Table (Tricker, 1964), would be classified 'Phenomenal' as might be experienced in a hurricane! It is well known, on the other hand, that wind waves with heights larger than 6 m have a frequency of occurrence of 10% and that the highest surface wave ever reliably reported is of 34 m (Kinsman, 1965). Therefore, given the above order of magnitude for breaking wavelengths, it seems more reasonable to think of high-frequency waves breaking on swell than breaking swell, plus some other processes (e.g. a rotor) as responsible for the plumes of bubble clouds reported by Trevorrow (1998).

There are other factors that may affect the modulation of surface gravity waves by internal waves. These are the energy inputs of breaking surface waves which may damp the internal wave currents (Thorpe *et al.*, 1987) and the damping of surface waves by films of varying thickness which might be periodically compacted and expanded within the current field (da Silva *et al.*, 1998). Besides, even though Fig. 2.9c illustrates how the position of the spectral modulations depends on k for fixed $\mathcal{U}_{10}$ and ϕ, there are further dependences on the pycnocline depth and on the speed of the surface current. These effects have recently been addressed by Donato *et al.* (1999). Surface waves travelling in the same direction of propagation of a sinusoidal internal wave current were considered. It was demonstrated that the position of regions of increased surface roughness, that is between the trough and crest of the internal wave, is the same for surface waves with $\lambda = 0.4$ m over a 6 m pycnocline in a 0.04 ms^{-1} surface current as for surface waves with $\lambda \sim 3.7$ m, the pycnocline with 100 m and the surface current of 0.23 ms^{-1}. Notice that, in this latter case, the metre-scale modulations are not occurring over the internal wave trough as in Fig. 2.9c. By decreasing λ and increasing the current speed, the range of steepness of surface waves increases, whereas the position of breaking can be shifted above the internal wave crest. Hence, care should be taken when broadly linking the spectral modulation to a particular position over the internal wave.

2.3.2 Solitary waves

Any solution of a non-linear system representing a wave of permanent shape is defined as a solitary wave (Drazin, 1983). A soliton refers to the non-linear interaction of two different solitary waves which emerge unchanged from such interaction, except for a phase shift in which the interaction retards the slower solitary wave and advances the faster one (Osborne and Burch, 1980). The soliton is either an isolated pulse or a quasi-periodic train of pulses, but a solitary wave is not necessarily a soliton. The wave of permanent shape arises from a balance between linear (dispersive) and non-linear forces, the latter has the tendency to steepen one side of the waveform (e.g. Apel *et al.*, 1995; Lamb, 1997). Laboratory experiments performed by Kao *et al.* (1985) suggest that when internal solitary waves (henceforth ISWs) are propagating up an uniform slope-shelf bottom topography, it is the back side of the waveform that begins to steepen if the wave is of depression and the front side if the wave is of elevation. In order to maintain the balance, a particular relationship between the amplitude and the horizontal length scale of the ISW must be satisfied. For example, a steepening wave crest with increasing amplitude is split up into a train of solitary waves by linear dispersive effects. As a result, each solitary wave retains a constant shape (i.e. length and amplitude) and speed during its propagation.

Isotherm displacements at the thermocline near shelf break regions commonly appear as trains of sech-squared-like waveforms propagating onshore, ideally almost preserving this shape over a distance several times a characteristic spatial length scale before being dissipated by bottom friction and by the breaking of surface waves for example. Such trains are known in the oceanographic literature as ISWs or internal solitons, irrespective whether or not they satisfy the preceding soliton characteristic; consequently, there is a terminology problem. Henyey and Hoering (1997) have pointed out that, for example, the interaction of two ISWs with amplitudes exceeding several times the thermocline depth would permanently change its initial sech-squared-like shapes after the interaction. [The degree of nonlinearity is described as 'weak' if the wave amplitude is small in comparison to the thermocline (pycnocline) depth and as 'high' or 'strong' if the opposite occurs (e.g. Ostrovsky and Stepanyants, 1989; Stanton and Ostrovsky, 1998)]. In addition, a single measurement of a solitary-like waveform might correspond to a wave decaying quickly into a non-solitary wave (Apel *et al.*, 1995), meaning that the wave is not preserving shape. It is not a simple task to determine from field measurements whether internal waves are indeed solitary waves and/or solitons and terms such as solibores, soliton-type internal waves or solitary internal wave-like packets have been coined to describe them. Bearing in mind that the modelling of the propagation of non-linear internal waves is not the aim of the current work, we stick to the usual term 'solitary waves' for the internal waves detected by ARIES II.

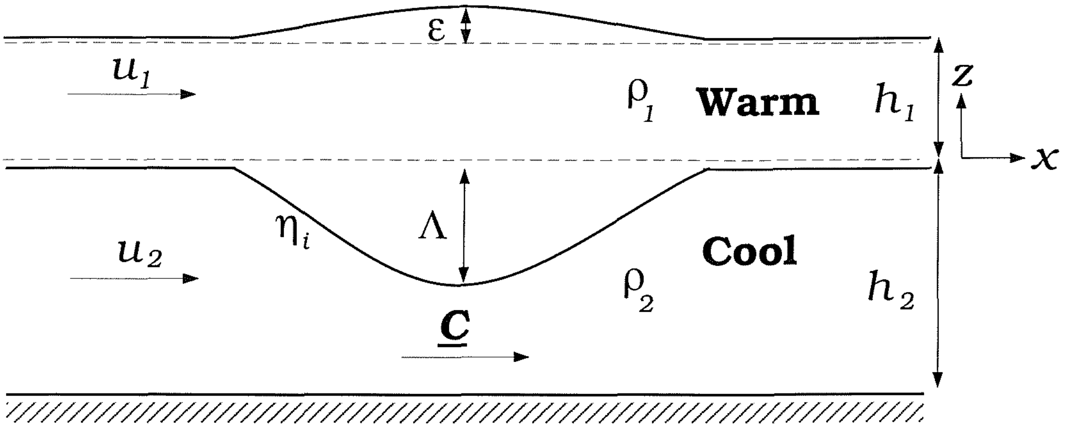

Fig. 2.10: *Non-linear internal wave travelling in a two-layer fluid with* $\rho_1 < \rho_2$ *and* $h_1 < h_2$. *Variables defined in the text.*

In terms of speeds, there are two conditions for the generation and existence of solitary waves prompted by nonlinearity. One is that the speed of the wave-induced horizontal current should be of the same order of magnitude or larger than the phase speed of the internal wave (e.g. Apel, 1995). The other is that the phase speed should exceed some critical linear phase speed (e.g. Peters and Stoker, 1960; Apel *et al.*, 1995). Such critical or limiting speed is $c^2 = gh$ for long surface gravity waves (i.e. $\lambda \gg h$ or $kh \ll 1$, where λ is the wavelength, h the water depth and k the wave number) and represents the limit of waves whose wavelength are allowed to tend to infinity.

We shall focus on long weak-ISWs of small-amplitude (i.e. $\Lambda < L$, where A is the amplitude and L is a characteristic horizontal length scale), but finite (e.g. Λ does not vanish). These waves are moving as depressions at the interface in a two-layer fluid in which a sharp thermocline separates two layers, each of uniform density and velocity over L. The top of the upper layer can be free or rigid (Fig. 2.10). Several perturbation schemes which treat solitary waves have been developed (see Long, 1956; Peters and Stoker, 1960; Clamond, 1999). One scheme considers the distortion of horizontal and time variables by introducing a new variable based upon a 'small parameter'. Then solutions, expanded as power series in the 'small parameter', are sought in the neighbourhood of a flow with constant speed. One characteristic of internal waves is that they move with a phase speed near a critical speed. By using this characteristic, Peters and Stoker (1960) derived an expression for the phase speed (C) in the vicinity of some value ℓ_o, such that $\ell_o - \frac{gh_2}{c^2}$ is a 'small parameter' whose root square defines a new variable. Such expression is given by,

$$C^2 = \frac{gh_2}{\ell_o \pm m}, \tag{2.7}$$

with dimensionless parameters,

$$\ell_\circ = \frac{1 + \gamma + [(1 - \gamma)^2 + 4\gamma\varrho]^{\frac{1}{2}}}{2\gamma(1 - \varrho)}, \tag{2.8}$$

$$m = \frac{\Lambda\ \left[(\ell_\circ\gamma - 1)^2 - \ell_\circ(\ell_\circ - 1)\right]}{h_2\ (\ell_\circ\gamma - 1)\ [2\ell_\circ\gamma(\varrho - 1) + (1 + \gamma)]}. \tag{2.9}$$

where the ratio of depths is $\gamma = \frac{h_1}{h_2}$ with h_1 and h_2 being respectively the depths of the upper and lower layers; the ratio of density of the two layers is $\varrho = \frac{\rho_1}{\rho_2}$ with ρ_1 indicating the fluid density in the upper layer and ρ_2 the density corresponding to the lower layer; g is the acceleration of gravity; and Λ is the amplitude of the interfacial wave. When the positive sign in (2.8) is considered, the displacement of the interface is a depression if $\gamma < 1$, which implies $[(\ell_\circ\gamma - 1)^2 - \ell_\circ(\ell_\circ - 1)] < 0$ because $\varrho < 1$ and $\ell_\circ > 0$, otherwise the non-linear internal wave is a solitary wave of elevation. For $\gamma = 1$ the phase speed approaches the limiting speed $C^2 \sim (1 - \varrho^{\frac{1}{2}})gh$ and this expression, for $\varrho \rightarrow 1$, is near to the limiting linear speed for the phase speed of long surface waves (Peters and Stoker, 1960). Further, the perturbation scheme used by Peters and Stoker (1960) deals with a free upper boundary. The elevation of the sea surface level over the wave trough is,

$$\epsilon = \frac{\Lambda}{1 - \ell_\circ\gamma}. \tag{2.10}$$

The reader will notice that both $C \nrightarrow 0$ in (2.7) and $\epsilon \nrightarrow 0$ in (2.10) when $(1 - \varrho) \rightarrow 0$ because Peters and Stoker's (1960) theory does not use the Boussinesq approximation (i.e. $(1 - \varrho) << 1$, but $g(1 - \varrho)$ finite).

Since the amplitude of the free surface is about two orders of magnitude less than the amplitude at the interface, the motion of the free upper boundary is usually neglected in practical applications. The rigid-lid approximation (e.g. the vertical speed of the fluid is equal to zero at the surface) can then be utilised in a two-layer fluid. Long (1956) treated this case for an ISW with phase speed given by,

$$\frac{C_r^2}{C_{lr}^2} - 1 = \frac{\Lambda(\varrho - \gamma^2)}{h_1(\gamma + \varrho)}, \tag{2.11}$$

$$C_{lr}^2 = \frac{(1 - \varrho)gh_1}{\gamma + \varrho}. \tag{2.12}$$

where C_{lr} is the linear phase speed; it is also assumed that $u_1 = u_2 = C_r$, with u_1 and u_2 being the wave-induced horizontal currents at both layers. The displacement of the interface (η_i) is (Long, 1956),

$$\eta_i = \Lambda\,\mathrm{sech}^2\left(\frac{x - C_r\,t}{L}\right), \tag{2.13}$$

$$L^2 = \frac{4h_1^3(\varrho\,\gamma + 1)}{3\Lambda\gamma(\gamma^2 - \varrho)}. \tag{2.14}$$

Here L is the width at half-amplitude. If the ISW is of depression, $\Lambda < 0$ which satisfies the inequality $\gamma^2 < \varrho$ (Long, 1956). Equivalently, if $(1 - \varrho) \rightarrow 0$, then the interface descends when $h_1 < h_2$ (Benjamin, 1966). Moreover, when $\gamma^2 \sim \varrho$, the rigid-lid approximation is no longer valid, there is no solitary wave solution (i.e. the non-linear term on the right-hand side of (2.11) vanishes) and the inclusion of higher-order non-linear terms in hydrodynamic equations is required (Thorpe, 1968; Ostrovsky and Stepanyants, 1989; Apel *et al.*, 1995). Equation (2.12) is analogous to the limiting speed of long surface waves and specifies the two-layer phase speed of periodic internal waves with wavelength much larger than both h_1 and h_2. This comparison also defines the applicability range of Long's (1956) solution when $2L$ is considered.

If both the phase speed and the horizontal velocity components of the ISW are not equal (e.g. Keulegan, 1953; Segur and Hammack, 1982),

$$\frac{C_{rb}}{C_{lb}} - 1 = \frac{\Lambda(\gamma - 1)}{2h_1}, \tag{2.15}$$

$$u_1 = \frac{\Lambda C_{lb}}{h_1}\,\mathrm{sech}^2\left(\frac{x - C_{rb}\,t}{L_b}\right), \tag{2.16}$$

$$u_2 = -\frac{\Lambda C_{lb}}{h_2}\,\mathrm{sech}^2\left(\frac{x - C_{rb}\,t}{L_b}\right), \tag{2.17}$$

$$C_{lb}^2 = \frac{(1 - \varrho)\,g h_1}{1 + \gamma}, \tag{2.18}$$

$$L_b^2 = \frac{4h_1^3}{3\Lambda\gamma(\gamma - 1)}. \tag{2.19}$$

which show that as Λ increases, the wave speeds also increase but the waveform becomes relatively narrower. Here, both C_{lb} and L_b can be obtained from (2.12) and (2.14) with $\rho_1 \sim \rho_2$, respectively. From (2.16) and (2.17) it is obvious that $\frac{u_2}{u_1} = -\gamma$, where u_1 follows the internal wave direction of propagation and u_2 is 180° opposite to u_1. Both u_1 and u_2 are constant within each layer and, although they are also independent of the total depth $h = h_1 + h_2$ because $L >> h_2 > h_1$, there is shear at the thermocline level. Then a solitary wave of depression (i.e. $\Lambda < 0$ for $h_1 < h_2$) might break when shoaling on a sill or if $\Lambda > h_1$. Equations (2.15-2.19) are valid when $\frac{\Lambda}{h} = \mathrm{O}(\frac{h}{L})^2 << 1$ (Segur and Hammack, 1982). If the motion of the upper boundary is allowed, the elevation of the free surface can be estimated from,

$$\epsilon_b = (1 - \varrho)\Lambda. \tag{2.20}$$

which tends to zero in the Boussinesq limit. Notice that a packet of ISWs can be simulated by expressing, for example, (2.13) into a series of individual waves. In addition, a decaying exponential function probably suffices to simulate the typical decreasing amplitude of an internal wave packet.

2.3.3 Straining

There appears to be a lack of direct measurements of surface straining within a wave trough. The straining produced by non-linear internal waves is the cause of particular scattering signatures often observed in SAR imagery (section 2.3.1). It is generally estimated from the vertical structure of internal waves, described as a sum of vertical displacement modes (e.g. section 4.3.2), and the Korteweg-deVries equation, which describes the evolution of ISWs (Apel, 1995). Another manner is from a compressible Boussinesq equation, that is from pressure variations recorded as ISWs of depression are passing by. The starting point is the equation for conservation of mass,

$$\frac{\partial \rho}{\partial t} + \nabla \cdot (\rho \mathbf{u}) = 0. \tag{2.21}$$

where ρ is the density and $\mathbf{u} = (u, 0, w)$ is the velocity field. Following Apel (1987), a small perturbation approximation for ρ and $\mathbf{u}$ is imposed as $\rho(\mathbf{x}, t) = \rho_\circ + \rho'(\mathbf{x}, t)$ and $\mathbf{u}(\mathbf{x}, t) = \mathbf{u}_\circ + \mathbf{u}'(\mathbf{x}, t)$, where $\rho_\circ$ and $\mathbf{u}_\circ$ are the constant unperturbed density and velocity respectively, ρ' and $\mathbf{u}'$ are variations caused by different sources (e.g. orbital speeds of internal waves, wave groups), $\mathbf{x}$ is a vector of position and $\rho' \ll \rho_\circ$. This approach, however, is different to that followed by Apel (1987) in the sense that $\mathbf{u}$ is not considered to be caused by acoustic pressure pulses. Variations of density with depth are not explicitly considered. Then, the equation for conservation of mass is,

$$\frac{\partial \rho'}{\partial t} + \rho_\circ \nabla \cdot \mathbf{u}' = 0, \tag{2.22}$$

where zero-order variations, products of the velocity, $\mathbf{u}$, with other similar-order variables and products of first-order variables are neglected. Furthermore, the propagation of internal waves produces density and pressure changes that affect the speed of sound, c_s, which is given by $c_s^2 = \frac{\partial p}{\partial \rho}$ and where p is the pressure. A small perturbation for the pressure is, $p = p_\circ(z) + p'(\mathbf{x}, t)$, with $p' \ll p_\circ$; p' is the pressure variation recorded, for example, within the internal wave trough and $p_\circ$ is the unperturbed pressure. It is straightforward to show from the sound speed definition that, $c_s^2 \frac{\partial \rho'}{\partial t} = \frac{\partial p'}{\partial t}$; notice that the integration of this equation enables the estimation of ρ'. Consequently, equation (2.22) can now be expressed as,

$$\frac{\partial p'}{\partial t} + \rho_o c_s^2 \, \nabla \cdot \mathbf{u}' = 0, \tag{2.23}$$

where $\mathbf{u}' < c_s$. Assuming $\frac{\partial w'}{\partial z} \ll \frac{\partial u'}{\partial x}$, a linearised form of equation (2.23) is,

$$\frac{\partial p'}{\partial t} + \rho_o c_s^2 \frac{\partial u'}{\partial x} = 0. \tag{2.24}$$

in which the term $\frac{\partial u'}{\partial x}$ represents horizontal straining. The sound speed, in ms^{-1}, is estimated according to Mackenzie (1981),

$$\begin{aligned} c_s = \; & 1448.96 + 4.591\, T - 5.304 \text{ X } 10^{-2}\, T^2 + 2.374 \text{ X } 10^{-4}\, T^3 \\ & + 1.630 \text{ X } 10^{-2}\, h + 1.675 \text{ X } 10^{-7}\, h^2 - 7.139 \text{ X } 10^{-13}\, T h^3. \end{aligned}$$

where T is the temperature in degrees Celsius and h is the mean depth of ARIES II. Near the surface, the effect of temperature on sound speed dominates over salinity and, therefore, salinity is not considered here. The accuracy of this equation is of about 0.1 ms^{-1}.

There is a parallel relationship in a two-layer fluid (Fig. 2.10). For an ISW of depression (e.g. $\Lambda < 0$ in equation (2.13)), the pressure in the upper-layer is given by $p_1 = \rho_1 g \left[h_1 + \Lambda \, \mathrm{sech}^2 \left(\frac{x - C_{rb}\, t}{L_b} \right) \right]$. It can be shown by using equation (2.16) that $\frac{\partial p_1}{\partial t} + \rho_1 h_1 g \frac{\partial u_1}{\partial x} = 0$. Moreover, the straining produced by surface waves satisfies an equation that is independent of the deep-water or shallow-water approximation; it is similar to equation (2.24), except that the term ρc^2 (see section 2.1.3) is utilised instead of $\rho_o c_s^2$. This suggests that the straining associated with both surface and non-linear internal waves can indeed be estimated from high-resolution pressure measurements through the general equation (2.24).

2.4 Langmuir circulation

Turbulence not only gives the notion of randomness of a flow in time and space, but also the notion of organised motion in a coherent structure. While there is no consensus for coherent structure (Hussain, 1986; Robinson, 1991), a broad definition points to a region of space where vorticity has some sort of organisation (Lesieur, 1997). As mentioned in section (1.1), LC is a coherent structure which is part of turbulence; the degree of organisation is essentially determined by the combined effect of the wind and the Stokes drift (see Leibovich, 1983, and section 2.4.1 below). Nevertheless, the context of LC within turbulence is not totally well-established. Recent laboratory experiments (Melville *et al.*, 1998) and large-eddy simulations (McWilliams *et al.*, 1997) are indicative of pronounced irregularity in time and space of LC in what McWilliams *et al.* (1997) have coined as Langmuir turbulence. Moreover, even the vertical structure of LC may show regions of chaotic behaviour (Bees, 1998; Bees *et al.*, 1998).

Although there were earlier observations (e.g. Leibovich, 1983, cites old descriptions of long elongated streaks or windrows formed by drifting material, such as seaweed, flotsam and foam, lined up in a direction parallel with the wind), the physical significance of windrows was first acknowledged to Langmuir (1938). Langmuir noticed the windrows in *Sargassum sp* on a cruise in 1927 and proved, from experiments carried out in Lake George between 1928 and 1929, that the windrows mark horizontal surface convergences between pairs of counter-rotating roll-vortices (cells) driven by the wind, now known as Langmuir circulation (see Fig. 2.1). From a physical and more general point of view, Langmuir circulation is only an oceanic expression of roll-vortices that occur in nature. Atmospheric roll-vortices are particularly well-known, but they have mechanisms of generation quite different to that of LC (see Etling and Brown, 1993; Smith, 2001).

The historical development of the different physical mechanisms that have been proposed to explain LC can be followed in the works of Faller (1971), Pollard (1977), Leibovich (1983) and Smith (2001). It has advanced in two main trends. In the first trend, notably first elaborated by Stommel (1949), importance is given to assess the effects of LC on the distribution of plankton (e.g. Bees *et al.*, 1998), subsurface bubbles and estimates of vertical diffusion coefficients (e.g. Thorpe, 1984), dispersion of buoyant material (e.g. Thorpe, 1995b; Colbo and Li, 1999), subsurface temperature structure (e.g. Gemmrich and Farmer, 1999), and on the interaction of periodic internal waves with LC (Thorpe, 1997). A second trend, summarised in Leibovich (1983), has concentrated efforts into understanding and modelling of the instability mechanism which gives origin to the circulation.

2.4.1 Models for Langmuir circulation

There are basically two type of models. Regardless of the mechanism of generation, it has been convenient to idealise LC like a plain and simple steady array of successive circular cells moving in opposite senses because this pattern explains some of the observed features of the circulation (e.g. successive lines of divergence and convergence on the sea surface oriented near to the wind direction). Here the main axis of each cell is assumed to lie parallel to the direction of the wind. We designate such pattern of cells as Stommel-type roll vortices in order to differentiate from the Craik-Leibovich instability mechanism.

Stommel-type roll vortices

Stommel (1949) has modelled the trajectories followed by particles in counter-rotating cells. If the density of particles and water is the same, the cellular motion may be specified by

$$\psi = \psi_\circ \sin(\pi x)\, \sin(\pi z) + Vz. \tag{2.25}$$

where ψ is the streamfunction, $\psi_\circ$ a constant vertical speed of the cells, and $u = \frac{\partial \psi}{\partial z}$ and $w = -\frac{\partial \psi}{\partial x}$ are, respectively, the horizontal and vertical velocity components of the flow pattern. This streamfunction describes steady symmetric roll vortices advected at speed V in a x-direction normal to the wind (windrow) direction (see Fig. 2.11). The coordinate z is positive upwards. For the dispersion of buoyant particles in LC, which can produce trajectories out of closed orbits implicit in (2.25), the interested reader is referred to Ledbetter (1979), Thorpe (1984) and Bees (1998). There is, however, interest in the description of the horizontal structure of LC at the sea surface ($z = 0$) where the speed of particles induced by the cells is now defined by Thorpe (1995b) as

$$\begin{aligned} u &= u_\circ \sin\left(\frac{2\pi x}{\mathcal{S}}\right), & (2.26)\\ v &= V_\circ - v_\circ \cos\left(\frac{2\pi x}{\mathcal{S}}\right). & (2.27)\end{aligned}$$

Here particles are initially positioned along divergence lines, midway between neighbouring windrows with spacing $\mathcal{S}$, and directed downwind at speed $V_\circ$. Following Thorpe (1995b), the constants $u_\circ$ and $v_\circ$ are typically in the range 1-20 cms^{-1} and probably depend on the wind speed and its time history, fetch, surface heat flux, and surface waves.

Craik-Leibovich instability mechanism

The accepted explanation for the generation of LC can be traced back to the works of Craik (1977) and Leibovich (1977). The basic physics of their explanation considers the instability of a wind-driven current (uniform in the horizontal but with vertical shear), resulting from the interaction of an infinitesimal perturbation or anomaly of this current with the Stokes drift of the surface waves (Fig. 2.11). The anomaly is in the form of a wind-driven surface shear with a central downwind jet (e.g. a Gaussian distribution). A pair of vertical vortex lines with opposite sense of circulation are formed on both sides of the spanwise anomaly; they interact with the waves through the Stokes drift,

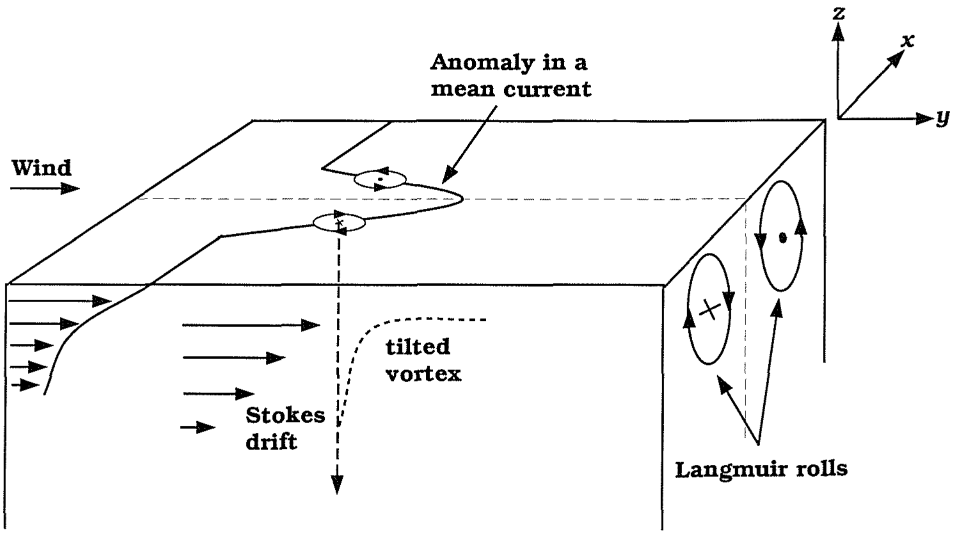

Fig. 2.11: Sketch illustrating the Craik-Leibovich instability mechanism for the generation of Langmuir rolls. The vertical vorticity associated with the spanwise anomaly of an horizontally uniform shear current is tilted and stretched by the Stokes drift to generate streamwise vorticity. (Adapted from Leibovich, 1983).

which tilts and stretches these vertical vortex lines to produce streamwise vorticity (i.e. longitudinal rolls). A surface convergence towards and along the jet maximum is generated as the resultant of a cross product between the Stokes drift and the z-component of vorticity (i.e. the wind-driven surface shear). Hence fluid sinks along the jet maximum and the acceleration of the surface convergence by the wind stress (Leibovich and Paolucci, 1980) reinforces the downwind jet, which also reinforces the vertical vorticity. The growth of the rolls is limited by the available forcing and by the stratification (e.g. pycnocline) or the bottom in the case of both shallow seas and lakes. Whilst stratification limits the penetration depth of cells (Leibovich, 1977), the dominant surface waves control the spacing of windrows via the Stokes drift which distorts the vertical vorticity generated by the wind (Craik, 1977) as described above. A combination of Stokes drift and wind-driven surface shear is, therefore, essential for the rolls to occur. Specifically, the Craik-Leibovich instability mechanism starts to operate when the product between the vertical gradient of the Stokes drift and the vertical gradient of the horizontally uniform wind-driven current is positive (Leibovich, 1983). The relative importance of each other, however, has not been explicitly taken into account and a combination of large waves and weak winds is probably comparable to that of small waves and strong winds (Kantha and Clayson, 2000, see also section 2.4.2 below).

Since the Craik-Leibovich instability mechanism provides a basis to create organised motion, LC or Langmuir rolls (Leibovich and Paolucci, 1980) are considered as a type of coherent structure occurring in the UOBL. It is the Stokes drift of surface waves, which destabilises the vorticity associated with the wind-driven current, that makes Langmuir rolls different from longitudinal rolls in other boundary layers (Garrett, 1996) such as atmospheric roll-vortices (Etling and Brown, 1993) and Kelvin-Helmholtz billows, sometimes associated with temperature ramps (Thorpe, 1995a).

2.4.2 Scales of windrows

LC organise clouds of bubbles, produced by breaking waves and rain, plankton, and surfactants into long bands of convergence near the sea surface whenever winds are larger than 2 ms^{-1} (Thorpe, 1992b, 1995a; Thorpe *et al.*, 1998). Bubble bands can reach widths, which should not be confused with the separation or spacing between consecutive windrows ($\mathcal{S}$), on scales of 3 to 5 m in deep water (Zedel and Farmer, 1991). This is consistent with the widths of O(2-6 m) reported by Langmuir (1938) for continuous bands of marine algae forming windrows in the North Atlantic. In acoustic images, bubble bands are frequently observed as linear features representing zones of enhanced concentration of bubbles. An ad hoc and simple criteria to differentiate bubble clouds from bubble bands (see section 2.1.4) is that the length of linear features should be at least one order of magnitude in excess of their width (Graham and Hall, 1997).

A hierarchy of length, persistence and spacing have been reported in both lakes and ocean (see Leibovich, 1983). Windrows up to about 1-3 km long were observed by Kenney (1977) from the top of a 20 m tower, by Smith *et al.* (1987) from an array of Doppler sonars and by Liu *et al.* (1997) from SAR images. Thorpe *et al.* (1994), however, have found lower lengths (10-500 m) whilst Plueddemann *et al.* (1996) suggested that the strongest windrows (i.e. those where the penetration depth of bubble clouds reached a maximum of about 10 m) can typically extend as far as 2-3 times the spacing; both being estimated through conventional non-Doppler sonographs.

Typical persistence of bubble bands with mean spacings of about 10 m, estimated via side-scan sonars that can achieve ranges of about 250 m, are 2-25 min in wind speeds of less than 10 ms^{-1} (Thorpe, 1992a; Thorpe *et al.*, 1994). By comparison, bands with spacings between 100 m and 160 m in winds of 12-16 ms^{-1} have been observed by Smith *et al.* (1987) to maintain identity over 2 h in deep water. This persistence was estimated from Doppler sonars in ranges from 100 m to 1 km. Maximal persistence for up to a day has been reported by Plueddemann *et al.* (1996) following both an abrupt reduction in wind stress and a slow decay in significant wave height (see Phillips, 2002). Although Plueddemann *et al.* (1996) ascribed such long persistence to surface waves, Kantha and Clayson (2000) have suggested that the wind may not necessarily be the only motive power for the surface shear to generate vertical vorticity (see Fig. 2.8), or the only source of the vertical gradient of the current velocity to trigger instability in the Craik-Leibovich mechanism. Kantha and Clayson (2000), thereby, point to the interaction of any ambient larger-scale shear (e.g. inertial currents) with surface waves as a potential cause of the preceding persistence, but inducing a circulation weaker than that originated solely by the wind stress and, as seems likely, affecting the orientation of linear convergence zones (Skyllingstad *et al.*, 2000, see also section 2.3.2). In addition, Teixeira and Belcher (2002) have recently suggested the possibility of subsurface shear produced by breaking waves (e.g. Melville *et al.*, 2002) as a source mechanism providing vertical vorticity for the initial development of LC. It is worth giving a mention to other sources capable of producing the sideways deflection of windrows. These include, according to Barstow (1983), the interaction of LC with residual currents, tidal currents, ebb tidal plumes, longshore currents and bottom topography.

Maximal observed spacings are probably those of 230 m and 280 m reported, respectively, by Liu *et al.* (1997) and Assaf *et al.* (1971). The spacing and length of windrows changes with time and increases with wind speed (e.g. Plueddemann *et al.*, 1996; Graham and Hall, 1997; Thorpe *et al.*, 1998). Langmuir bands of short spacing (2 m) can subsist for a few minutes in the middle of bands of larger spacing. These small scales can continuously form and die out or slowly be swept up into larger and more permanent scales (Leibovich, 1983). The spacing has also been related to the length of windrows and to the wavelength of surface waves. The ratio between length and spacing is highly variable, from 2 to 100 (e.g. Kenney, 1977; Smith *et al.*, 1987; Plueddemann *et al.*, 1996), whilst that for spacing and wavelength, corresponding to wave periods of 4 s, is of $\frac{2}{3}$ (see Smith, 1992; Phillips, 2001). In analogy with convective motions, it is generally accepted that the spacing is proportional to the vertical extension or penetration depth of Langmuir cells ($\mathcal{D}$). In situ measurements of $\mathcal{D}$ are difficult to obtain, nevertheless $\mathcal{D}$ is associated with the depth of the mixed layer (e.g. thermocline) because the cells appear to stop growing when a significant density gradient is met. Thus field observations of LC show that $\mathcal{S}$ varies in the range 2 or 4 m to maxima from about 1-3 times the depth of the mixed layer (Leibovich, 1983; Smith *et al.*, 1987; Smith, 1992).

An important assumption, and weakness, in the Craik-Leibovich instability mechanism is that the Stokes drift is assumed parallel to the direction of the wind stress (i.e. wind-driven shear flow) which produces rolls aligned to, and invariant in, the mean wind direction. Field observations of windrow orientations, as summarised by Leibovich (1983), are indicative of alignment 'nearly' parallel to the wind direction. Thus, under this assumption, some authors (e.g. Plueddemann *et al.*, 1996) have erroneously attributed recorded wind directions equivalent to windrow orientations. There are, in point of fact, enough field observations suggesting that Langmuir rolls are aligned within some 20° of the direction of the wind (e.g. Leibovich, 1983; Farmer and Li, 1995; Thorpe *et al.*, 1998) and, furthermore, that they do not necessarily form patterns of equally spaced straight windrows (e.g. Smith, 1992; Graham and Hall, 1997, Fig. 1.6).

Tandon and Leibovich (1995a) have identified some causes that may produce the misalignment of Langmuir rolls. These are fluctuations in wind direction, preexisting misaligned currents, Coriolis effects (e.g. Faller, 1964; Thorpe and Hall, 1982) and the instability of the rolls themselves. For unstratified water, the latter yields deviations from the wind direction up to about 5° with windrows drifting laterally roughly at 8 cms^{-1} (Tandon and Leibovich, 1995b) and, for stratified water, deviations are of about $(10 \pm 1)^{\circ}$ as shown by Leibovich and Tandon (1993).

Several approaches for the case when the Stokes drift is not parallel to the direction of the wind have been worked out by Gnanadesikan and Weller (1995), Cox (1997) and Polonichko (1997). These studies suggest that Langmuir rolls form somewhere in between the direction of the Stokes drift and the direction of the mean wind. the latter being the direction of the (Eulerian) wind shear. Field data recently reported by Plueddemann and Weller (1999) show the Stokes drift aligned about 20° to the left of the mean direction of the wind during relatively steady periods of strong winds O(10 ms^{-1}). In addition, when the height of surface waves decayed roughly in accordance with periods where the wind speed dropped rapidly, the Stokes' drift aligned about 30° to the left of the wind and showed a bias towards the direction of swell (Plueddemann and Weller, 1999). More interesting, however, is the evidence that bubble bands may orientate in between the mean wind direction and the direction of high-frequency (e.g. 2.5-3.0 s) surface waves during periods of low (e.g. 4.5 ms^{-1}) and moderate (e.g. 8.8 ms^{-1}) wind conditions. Using a limited data set, Thorpe *et al.* (1998) found cases suggesting bubble bands aligned within $(1-8)^{\circ}$ from the wind direction and within $(60-70)^{\circ}$ from the direction of high-frequency waves, a possible consequence of an Eulerian mean shear larger than the Stokes drift shear according to Polonichko (1997). Here the poor alignment between the wind and the high-frequency waves was probably caused by an unsteady wind field (e.g wind building up or veering) or perhaps by an instrumental problem with the compass (see chapters 3 and 5).

2.5 Interplay between internal waves and bubble bands

Both LC and internal waves are widespread in the UOBL. It is entirely plausible for bubble bands [with spacings of O(10 m) and drifting rates of O(0-6 cms^{-1}) in a direction normal to the wind direction] to be perturbed by internal waves [with wavelengths of

O(400 m) and typical phase speeds and horizontal surface currents of O(10-100 cm^{-1}), that is larger than those for drifting windrows] if the bands are not oriented in a direction parallel to that for the propagation of the waves. Reckoning time scales, the UOBL might include a quasi-steady pattern of LC with a persistence of 1-2 h or longer (e.g. 24 h), and periodic internal waves of 10-40 min. Consequently systematic simultaneous observations using the appropriate instrumentation have hitherto been lacking.

The coexistence of internal waves and LC was probably first documented by Filatov *et al.* (1980) and Ryanzhin (1980) in a deep lake, but without any intent to elucidate their interaction. In particular, Ryanzhin (1980) reports the generation of (2.8-5.6 min) periodic internal waves by the influence of Langmuir cells over the thermocline. The application of novel acoustic technology by Smith *et al.* (1987) has also given evidence of this coexistence. They observed that windrows maintained a spacing of three times the depth of the mixed layer as that depth varied slowly from about 50 to 60 m due to the M_2 internal tide. Further evidence is provided by Smith (1992), during a period of strong winds ($> 8\ \mathrm{ms}^{-1}$), and by Pinkel *et al.* (1996), during periods of both high-frequency internal waves and the semi-diurnal internal tide. The latter, however, appears to be more inclined to filter out Langmuir rolls than to consider their interaction with internal waves. The plausible interaction was hence disregarded.

As for numerical simulations based on the Craik-Leibovich instability mechanism, it seems that Leibovich *et al.* (1989) first mentioned the possibility of including a deformable density interface in a two-layer fluid. This case, however, has recently been tackled by Chini and Leibovich (1998) through long internal waves weakly damped. Their preliminary results indicate that: (i) the waves can in general transfer energy to Langmuir cells which (ii) grow faster than without the presence of the internal waves; (iii) by opposition the cells could also radiate energy to the waves (Chini, 1998; priv. comm.). Thorpe (1997), on the other hand, has independently considered this interaction by representing Langmuir cells as linear-Stommel-type boundary vortices. The first observations regarding the response of bubble bands to perturbations caused by ISWs were provided by Ulloa and Thorpe (1998) using ARIES II.

Consider the vorticity conservation equation

$$\frac{\mathrm{D}\boldsymbol{\Omega}}{\mathrm{D}t} = (\boldsymbol{\Omega} \cdot \nabla)\mathbf{u}. \tag{2.28}$$

where the term $\frac{\mathrm{D}\Omega}{\mathrm{D}t}$ is the rate of change of vorticity $\boldsymbol{\Omega} = (\xi, \vartheta, \zeta)$ following a fluid particle, the term $(\boldsymbol{\Omega} \cdot \nabla)\mathbf{u}$ represents rate of change of vorticity caused by stretching and turning (tilting) of vortex lines and $\mathbf{u} = (u, v, w)$ is the velocity. For simplicity, the effect of viscosity is assumed negligible. The x-component of vorticity along a horizontal array of line vortices, equally spaced at distance r and of same strength Γ

but of opposite sign to its neighbours (Fig. 2.12a) is,

$$\frac{\mathrm{D}\xi}{\mathrm{D}t} = \xi\,\frac{\partial u}{\partial x} + \vartheta\,\frac{\partial u}{\partial y} + \zeta\,\frac{\partial u}{\partial z}, \tag{2.29}$$

where the vortices are assumed to lie parallel to the x-axis and hence parallel to the vorticity vector. Consider now the velocity field generated by a small-amplitude internal wave (i.e. $\frac{\partial u}{\partial z} \equiv 0$) where the streamwise speed does not vary in the spanwise direction (i.e. $\frac{\partial u}{\partial y} \equiv 0$), so the tilting of spanwise (e.g. crosswind) and vertical vortex lines in (2.29) is zero and

$$\frac{\mathrm{D}\xi}{\mathrm{D}t} = \xi\,\frac{\partial u}{\partial x}. \tag{2.30}$$

The strength of the vortices will therefore be modulated by variations of the velocity component u in its own direction and by the vorticity ξ associated with the rotational vortex flow (see Tritton, 1988).

The interaction between line vortices and internal waves has two limiting cases. In the first case, the waves travel parallel to the the vortex lines (Fig. 2.1, 2.10 and 2.12a). If $\frac{\partial u}{\partial x} < 0$ (convergence of horizontal wave-induced currents), the magnitude of ξ decreases with time and fluid particles will be compressed ($\xi = \frac{\Gamma}{\mathrm{A}}$, where A is the cross-sectional area of the vortices). Maximal horizontal compression occurs over the wave troughs where there is minimum vorticity (Thorpe, 1997). Conversely, the horizontal elongation or stretching of line vortices will be greatest over wave crests where maximal vorticity is given by $\Gamma\pi^2 \left(\frac{4}{\mathcal{S}_\circ^2} + \frac{1}{h_1^2}\right)\left(1 + \frac{\Lambda}{h_1}\right)$ with $\mathcal{S}_\circ = 2r$ (Thorpe, 1997). The latter is valid for long internal waves in comparison with h_1, the thickness of the upper layer in a two-layer system. The second case considers line vortices normal to the propagation direction of internal waves (Fig. 2.10 and 2.11 or Fig. 2.12b). Here, $\frac{\partial}{\partial x} \equiv 0$ and straining does not affect ξ but r is altered. The separation of vortices will reduce over the wave trough and increase over a wave crest. Thorpe (1997) has derived the following relationship for the reduction of spacing of line vortices over the wave troughs ($\mathcal{S}_{iw}$), at the depth of the centres ($\frac{h_1}{2}$) of the vortices array

$$\mathcal{S}_{iw} = \mathcal{S}_\circ \left[1 - \frac{\Lambda\varkappa}{2\sinh\left(\frac{\varkappa h_1}{2}\right)}\right], \tag{2.31}$$

where $\mathcal{S}_\circ$ denotes the spacing before the passage of the internal wave and $\Lambda\varkappa$ is the wave slope. For $\varkappa h_1 \ll 1$, equation (2.31) reduces to $\mathcal{S}_{iw} = \mathcal{S}_\circ \left(1 - \frac{\Lambda}{h_1}\right)$. Thus a reduction of about 36% is expected if the amplitude of a periodic internal wave is about 36% of the upper layer thickness. Because disturbances on vortex arrays have growth rates proportional to $\frac{\Gamma}{2\pi r^2}$ (see Thorpe, 1992a) or $\frac{2\Gamma}{\pi\,\mathcal{S}_{iw}^2}$, both the clustering of vortex lines over wave troughs and their stretching over wave crests by internal waves will affect

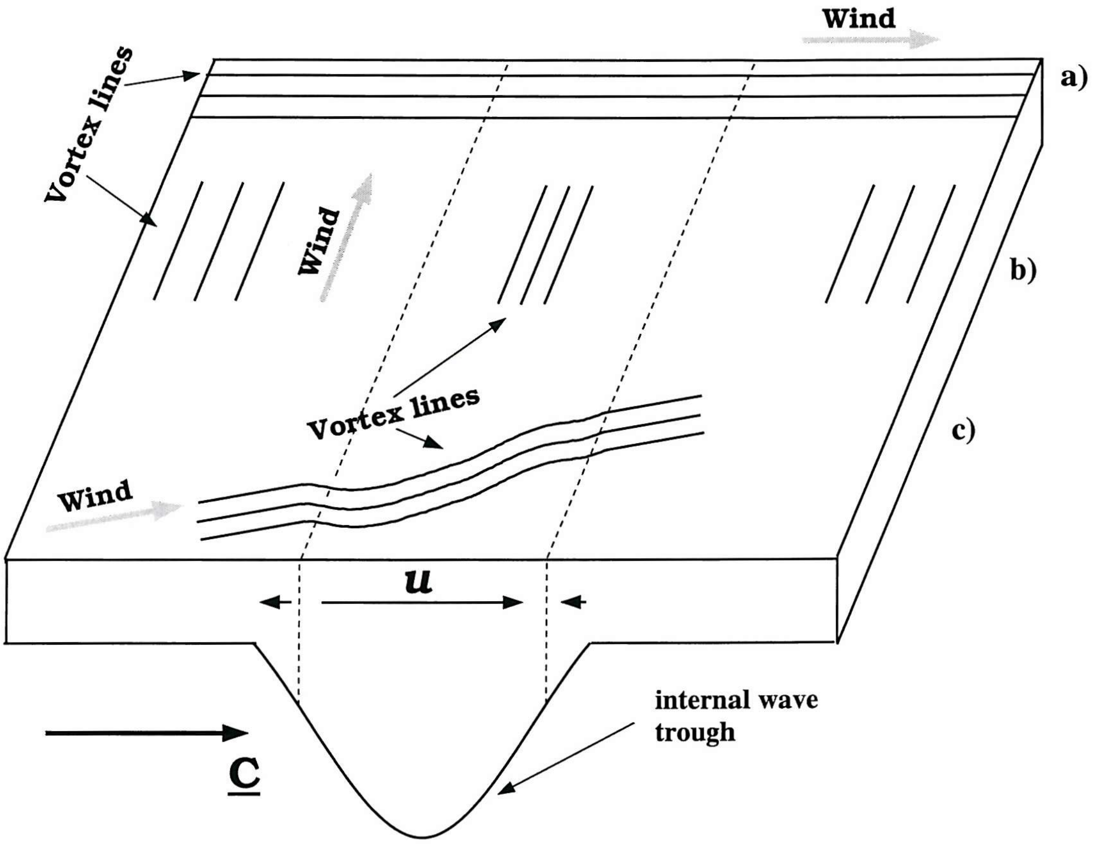

Fig. 2.12: *Schematic diagram showing the passive distortion of boundary layer vortices (e.g. bubble bands) produced solely by an internal wave (e.g. a soliton) with no added wave breaking. (a) The vortex lines are stretched and compressed by the horizontal wave-induced motion if waves and vortices are parallel. The orientation and spacing of vortices will not be altered. (b) The spacing of vortices is altered when the vortex lines have an orientation normal to the direction in which the internal soliton is travelling. As the vortices are advected by the wave-induced motion, the convergent flow brings the vortex lines together over the wave trough. The initial vortex spacing may recover after the internal wave has passed by. (c) If there is some angle between the internal wave propagation and the vortex lines, the vortices become distorted.*

the stability of vortices. The position of breakdown will depend on the growth rate and the period of the internal wave (Thorpe, 1997).

For the general case, the orientations of vortex lines are also affected (Fig. 2.12c). The distortion angle ϑ_{iw}, with respect to the unperturbed vortex line orientation (e.g. parallel to the wind direction), resulting from the interaction between the vortices and the internal wave at the wave troughs and crests is (Thorpe, 1997)

$$\tan \vartheta_{iw} = \frac{\Lambda \varkappa l \, \cosh(Kz)}{K \, \sinh(Kh_1)}, \tag{2.32}$$

in which $K^2 = \varkappa^2 + l^2$ with $\varkappa$ and l the internal wavenumbers in the x- and y-directions respectively. Then for $Kh_1 \ll 1$ and $z = 0$, $\tan \vartheta_{iw} = \frac{\Lambda \varkappa l}{K^2 h_1}$. Long internal waves (with respect to the mixed layer depth) travelling at 45° to the unperturbed vortex orientations (i.e. $\varkappa = l$), with amplitudes of about 36% the mixed layer depth (e.g. $h_1 = 45$ m and $\Lambda = 16$ m), can distort the vortex lines over the wave crests and troughs by 10°. This distortion is comparable to the misalignment of Langmuir rolls mentioned in section 2.4.2.

The line vortices, on the other hand, can disturb the interface. Thorpe (1997) has shown that, if long waves travel in a direction parallel to the vortices, the maximal amplitude of the disturbance occurs when $\mathcal{S}_{\circ} = 2\sqrt{3}h_1$ and ranges from about 2Λ to 13Λ for typical values of currents and length scales of LC and periods of internal waves. In addition, the potential energy of the interface displacements caused by the interplay between vortices and internal waves may contain a significant fraction of the energy in the system (Thorpe, 1997).

The simplification of LC as inviscid line vortices may have only remote bearing on LC because the forcing responsible of LC is not explicitly considered and, in consequence, the vortices could also represent thermal rolls or atmospheric roll vortices for example. Equations (2.31) and (2.32) represent a first order approach to the complex interaction of LC and internal waves. Although these equations are valid for linear internal waves and that the extension of Thorpe's theory towards ISWs is beyond the scope of the current work (see section 1.2), its possible application should not be discouraged unless the influence of other UOBL processes like, for instance, the effect of unsteady wind fields in the stability and lifetimes of LC, the presence of highly non-linear internal waves and the breaking of surface waves caused by the internal wave-induced currents could be dominant (see Fig. 2.1).

Thorpe (1997) has also pursued the interaction in terms of the Craik-Leibovich instability mechanism. Solutions were found for the inviscid case which are probably valid when the cross-cell variation of the downwind jet is not significant, that is at small times after the onset of the circulation. By assuming that a mean flow and a Stokes drift have a linear variation with depth, both aligned with the mean wind direction, Thorpe (1997) showed that the role of the Stokes drift is to reduce the phase speed of internal waves propagating normal the mean flow. Conversely, if interfacial waves travel parallel to the mean shear flow then the phase speed is increased (Thorpe, 1997).

Acoustic images derived from ARIES II have captured distinctive signatures of (i) ISWs (Ulloa, 1998; Thorpe *et al.*, 1998), (ii) bubble bands aligned near to the mean wind direction (Thorpe *et al.*, 1998) and of (iii) their simultaneous occurrence (Ulloa and Thorpe, 1998). Although Smith (1998) has recently suggested that the buoyancy of bubbles could influence the dynamics in the UOBL, bubble bands are generally interpreted as quasi-passive tracers of zones of convergence created in-between adjoining quasi-coherent Langmuir rolls (see Fig. 1.1c and 2.5 for instance). Acoustic images represent a potential tool to estimate the changes in the standard scales of bubble bands (i.e. orientation, lateral drift and spacing) during the passage of ISWs. Since there are no reported quantitative observations of such interaction, either published numerical or theoretical studies accounting for viscosity in the framework provided by the Craik-Leibovich instability mechanism, we can pursue a simple test from comparisons of equations (2.31) and (2.32) with measurements of the mean spacing and distortion angle of bubble bands over a wave trough (see section 7.9).

4. DEPLOYMENT

The current chapter gives a description of the instrumentation deployed around ARIES II and of the deployment site itself. It tells of the need for keeping a complete register of the visual events which occur at the sea surface during scientific cruises, particularly rain, foam alignments or foam structures left behind by breaking waves, and slicks arising from either fronts or internal waves. It also describes some of the temperature signatures of non-linear internal waves recorded by ARIES II during spring and neap tides. Finally, it suggests that although the distance between moorings was relatively short, ARIES II and the current meter at a depth of 55 m sometimes registered different events (e.g. presence and absence of non-linear internal waves).

4.1 The deployed instrumentation

LOIS (section 1) is a substantial UK project aimed to quantify and simulate the fluxes (e.g. water, heat, nutrients) and transformations of materials (e.g. sediments, dissolved and suspended seawater constituents) into and out of the coastal zone. Being a component of LOIS, SES (section 1) focuses on physical processes (e.g. tides, internal waves, mean advective flows) which individually, and through their mutual interactions (e.g. turbulent mixing and dissipation), may contribute to the transfer of water properties and/or energy across the continental slope.

A transference of barotropic tidal energy into non-linear internal waves occurs in particular at sloping topographies. The shelf edge, then, represents a strategic region where novel acoustic instrumentation can potentially detect and monitor the passage of internal waves and its effects on the UOBL. ARIES II is an integral part of LOIS-SES. It has been deployed on a 'U-mooring' (Fig. 4.1) near the shelf break, perhaps in a place where ISWs have still not lost form through, for example, wave interactions and bottom dissipation. ARIES II was deployed at site S140, roughly 200 km from Oban, West coast of Scotland, on 11th August 1995, at 56.4575° N, 8.9682° W into 146 m water depth (Sherwin and Simpson, 1996) and about 4 km East of the 200 m isobath (Fig. 4.2 and 4.3). ARIES II was recovered on 5th September 1995 at 56.4597° N, 8.9670° W (Sherwin and Simpson, 1996), that is about 0.2 km from the deployment position. Since the ARIES II mooring is a subsurface mooring (Fig. 4.1), these positions correspond to the position of the toroidal buoy. The exact position of ARIES II is not

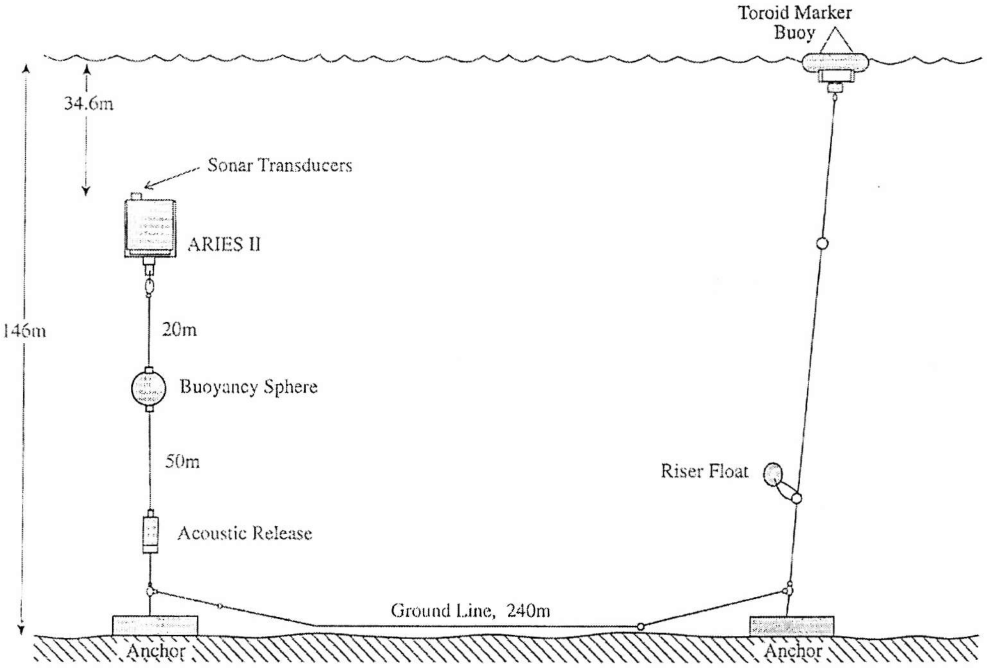

Fig. 4.1: *Diagram of the ARIES II mooring.*

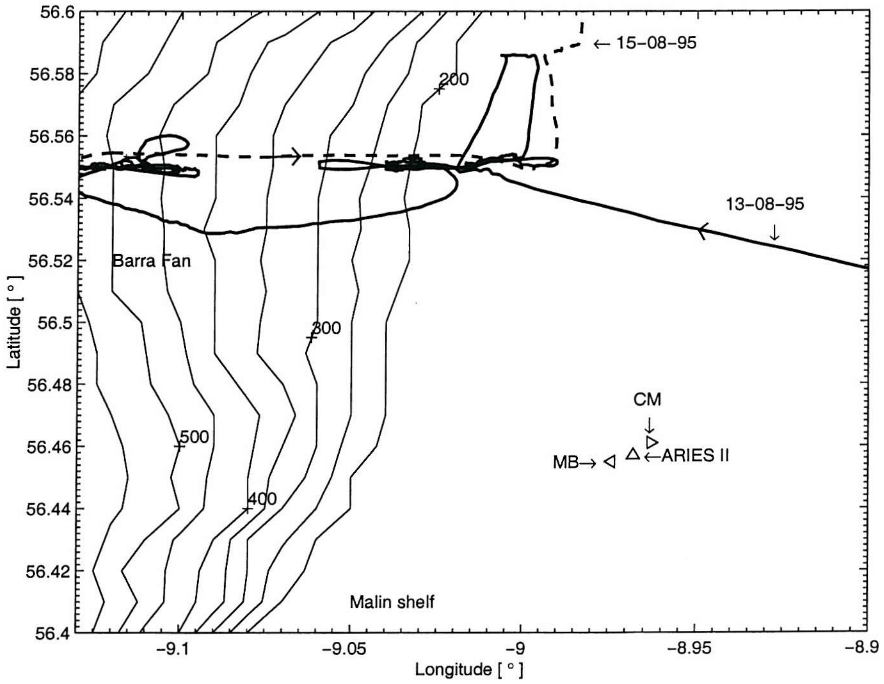

Fig. 4.2: *The Malin Shelf and mooring positions. The current meter mooring (CM) is shown by ▷, the ARIES II site by △ and the meteorological buoy (MB) by ◁. Isobaths, indicated by thin solid lines, are labelled in meters with 50 m intervals. The thick solid line indicates the track followed by the DERA ship on 13th August 1995, whilst the thick dashed line is the corresponding track on 15th August 1995.*

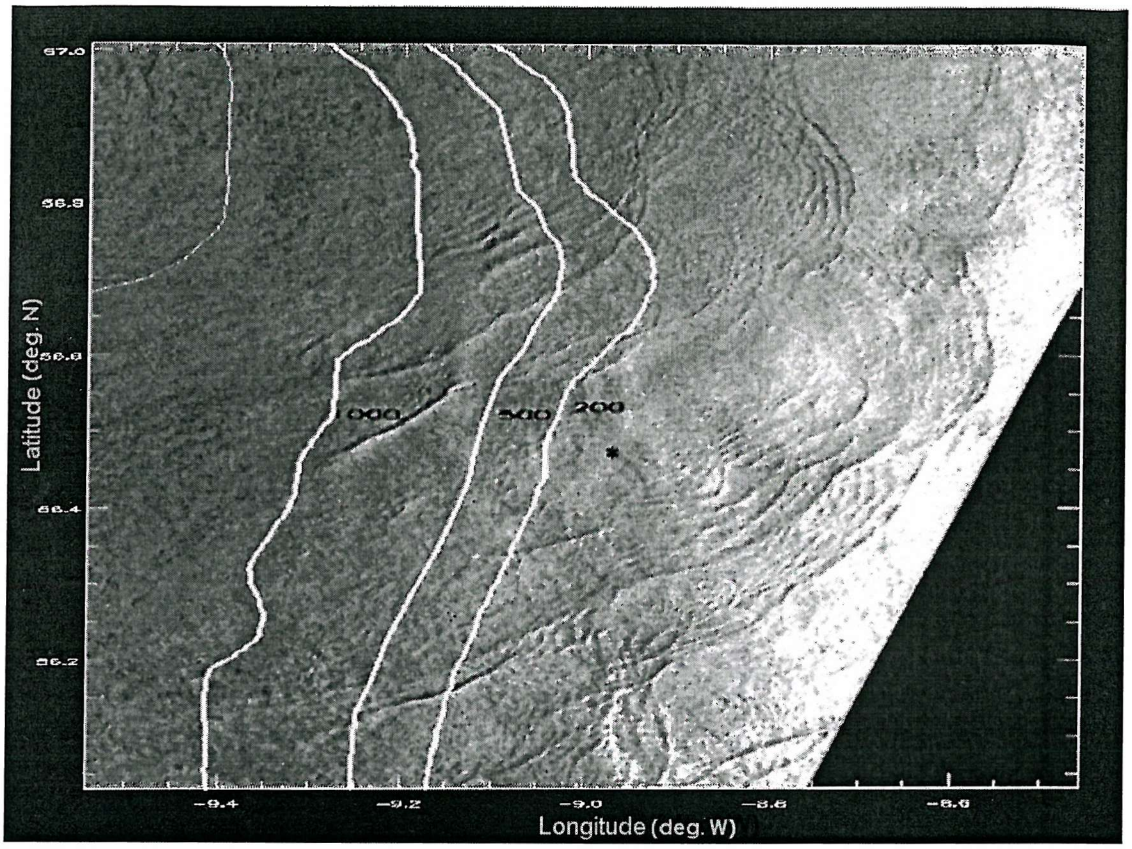

Fig. 4.3: *SAR-image over the Malin-Hebrides shelf area on the 20th August 1995 at 11:36 GMT. The numbers indicate isobaths in meters, whilst the ARIES II mooring is shown by the asterisk. Mean $\mathcal{U}_{10}$ and direction are, respectively,* (4.8 ± 0.1) *ms*$^{-1}$ *from* $(285 \pm 10)°$*T. (Image courtesy of J. Small).*

known, but it is probably around a 0.240 km radius from the toroidal buoy. Moorings are known to be dragged by both semidiurnal tidal and sub-inertial periodic currents in roughly circular paths (Spindel *et al.*, 1978). Hence an error related to the horizontal excursion of moorings, probably of O(100 m), need to be considered in the reported positions on the whole.

The mean depth of ARIES II, measured at the transducers level, was 34.6 m whilst that at the temperature sensor level was 36.11 m. A second mooring with three current meters, an Inter-Ocean S4 at 30 m (without pressure and temperature sensors) and two Aanderaa RCM at 55 m and 140 m, plus a (76 m) chain of ten thermistors, 7.6 m apart, were deployed at 56.4615° N, 8.9628° W into 150 m water depth. The upper current meter was sampling at 10 min intervals and the remainder at a rate of 5 min. The depth of the upper thermistor was set to 56.3 m (i.e. below ARIES II) and the chain was sampling every 1 min. This mooring was deployed on 11th August 1995 and recovered on 31th August 1995, but unfortunately, the thermistor logger stopped (presumably because it was full) after 4 days (Hughes, priv. comm., 1996). A meteorological buoy, sampling wind speed and direction at 10 min intervals, was in operation from 17th August 1995 to 17th November 1995 at 56.4552° N, 8.9740° W. The distance between the ARIES II site and the current meter mooring was about 0.6 km and that between the ARIES II site and the meteorological buoy was roughly 0.5 km. Additional wind data from a ship, obtained on (12-16)th August 1995, were kindly supplied by Dr. J. Scott through the **D**efense **E**valuation **R**esearch **A**gency (DERA) and the SES-Acoustic Measurement Experiment (see Fig. 4.2). In order to estimate the speed and direction of the ship, the distance between consecutive ship's positions and the bearing were calculated using the Plane Sailing Method (Dunne, 1987). Conversion from apparent wind to true wind was done through simple geometry. Wind speed, $\mathcal{U}_{10}$, at 10 m, was calculated assuming a logarithmic boundary layer (see section 2.1.1) with a drag coefficient given by equations (2.3-2.5).

4.2 Ship and scientific log books

A self-contained log book of UOBL observations collected during any deployment of near-surface acoustic instrumentation is a valuable source of information in the interpretation of sonographs. Variations in the intensity of acoustic scattering along a rolled out sonograph record may be hard to discriminate and explain without eyesight confirmation of particular physical events. Rain squalls constitute a typical example (see Fig. 13 of Thorpe *et al.*, 1998, and Smith, 1998). Both the generation of bubbles by rain and the impact of raindrops can contribute to enhance the near-surface acoustic scattering layer (see sections 1.1-1.2 and 2.3), with the possibility of making simultaneous acoustic signatures of bubble bands, surface and internal waves unclear. Thus, temporal variations in the acoustic scattering of bubble bands might be caused by rain only and not by some scattering band associated with fronts or ISWs passing through. Even a research ship may leave an unusual scattering track, a real source of contamination in the acoustic detection of UOBL processes.

Table 4.1 lists the UOBL processes that occurred during the cruise CH121/SES3B according to both the ship's deck log book and to Sherwin and Simpson (1996). Observations are summarised as: (i) the thermocline depth near the shelf break was at about 25 m; (ii) packets of internal waves appeared to be phase locked with the barotropic tide (see also Small *et al.*, 1999; Inall *et al.*, 2000, 2001); (iii) ISWs with vertical excursions of up to 25 m were detected between CTD up-casts and down-casts, and at both spring and neap tides; (iv) surface slicks, probably caused by ISWs, were observed visually and by radar; they had length scales of O(200 m) and travelled onshore (in a south easterly direction) at about 0.5 ms^{-1} (see also Inall *et al.*, 2000, 2001); and (v) the internal wave currents measured at a depth of 5 m appeared weaker during spring tides

Tab. 4.1: *Observations accounted by the Challenger 121 cruise in the Malin-Hebrides region. Notes: (1) IW stands for internal waves; (2) CH121-dlb denotes the Challenger 121 cruise, deck log book; (3) approximated positions; (4) SS96 stands for Sherwin and Simpson (1996); (5) in fact from 19:00-21:00.*

Date	Hour	Position	Event	Source
17-08-95	11:09	56.4494° N, 8.9592° W	S140 crossing IW(1)	CH121-dlb(2)
19-08-95	14:00	56.4359° N, 8.9694° W(3)	IW packets	SS96(4)
	20:00(5)	56.4325° N, 8.9740° W(3)	IW packets	SS96
20-08-95	05:00	56.4340° N, 8.9682° W(3)	IW train	SS96
	08:50	56.4550° N, 9.0648° W(3)	Fishing ship *Izoard*	SS96
21-08-95	20:00	56.4130° N, 9.0196° W(3)	IW train moving on-shelf	SS96
24-08-95	18:24	56.6083° N, 8.9389° W(3)	SW to W wind & heavy swell	CH121-dlb & SS96
	23:59	56.5715° N, 9.0025° W	SW to W wind & heavy swell	CH121-dlb & SS96
25-08-95	02:00	56.5583° N, 8.9967° W	Adverse weather conditions	CH121-dlb
	07:00	56.5250° N, 8.9983° W	Rough sea & heavy swell	CH121-dlb & SS96
	11:27	56.5107° N, 9.1425° W	Swell to east	CH121-dlb & SS96
	20:42	56.4603° N, 9.0687° W	Heavy crossing swell	CH121-dlb & SS96
27-08-95	12:48	55.4183° N, 9.7270° W(3)	Northerly swell	CH121-dlb & SS96

than in neap tides. No particular foam spots or foam patterns left behind by surface breaking waves, rain showers, fronts or windrow events are reported.

4.3 The study site

The West coast of Scotland is an area of intense internal wave activity (e.g. Levine *et al.*, 1983; Bagg and Thomas, 1984; Fedorov and Ginsberg, 1986; Brown and Scott, 1987, and Fig. 4.3). Solitary wave-like packets propagate shoreward from the vicinity of the shelf break and particularly towards the ARIES II site. The predominant direction of propagation lies in the range (60-140)°T which has been estimated by Oikonomou (1997) from SAR images for the period September 1993 to April 1996. The directions of least frequent propagations were also estimated. These are from 140°T to 180°T and from 0°T to about 30°T. In agreement with Oikonomou (1997), SAR images gleaned over the study site on August 1995 and August 1996 (e.g. Fig. 4.3 and those displayed in Small *et al.*, 1999, and Hallock *et al.*, 2000) show many signatures of non-linear internal waves with prominent directions of propagation between 90°T and 135°T; although wave fronts in the NE quadrant are also evident and therefore cannot be totally disregarded. Typical reported phase speeds, wave amplitudes of depression and half width length scales are, respectively, (0.4-0.7) ms^{-1}, (15-50) m and (120-280) m (Thorpe *et al.*, 1998; Guizen *et al.*, 1999; Small *et al.*, 1999; Inall *et al.*, 2000, 2001; Rippeth and Inall, 2002). The preceding amplitude range represents roughly (10-35)% of water depth at the ARIES II mooring.

4.3.1 Internal tide

Since the Malin shelf is a thermally stratified region in summer, it is believed that the internal tide results from the forcing of the stratified flow over the continental slope and shelf edge by the barotropic tide. Thus, broadly speaking, an elevation of the pycnocline is produced during the flood tide and a depression during the ebb tide. This ebbing tidal flow, just when it starts to turn, excites a periodic oscillation with waves propagating both off-shelf and on-shelf; these are the internal tides (e.g. Xing and Davies, 1998; Simpson, 1998b). The internal tide then becomes non-linear and evolves into high-frequency (i.e. in comparison with the inertial frequency) internal waves within a length scale that for a steep topography is of about 20 km (Liu *et al.*, 1998).

Sherwin (1988a) has found evidence that weak M_2 barotropic tidal currents of about 0.13 ms^{-1} can cause a significant linear mode-1 internal tide over a spring-neap cycle; also, there is fresh evidence to support that the internal tide speed near the shelf break is (10 cms^{-1}) in excess of the corresponding tide on the continental slope at depths of some 70 m (Inall *et al.*, 2000). A spur located south of the Rockall Trough, delineated by the 500-1000 m isobaths, has been identified by Sherwin (1988a) as a probable local source for the generation of internal tides. Other possible generation points are both the Anton Dohrn and the Hebrides Terrace seamounts according to Xing and Davies (1998). Recent SAR images and in situ observations analysed by Small *et al.* (1999) suggest that packets of non-linear internal waves are also generated every tidal cycle from a distant deep source, for example in the deep water ($>$ 500 m) of the Rockall Trough (Sherwin, 1988a).

The non-linear internal waves appear to arrive at the ARIES II site during the ebb phase of the barotropic tidal flow in both spring and neap tides (Fig. 5 and 13 in Thorpe *et al.*, 1998, and Fig. 4.4b), however, the waves are also coincident with the barotropic flood tide during each tidal cycle in spring tides (Fig. 5 in Thorpe *et al.*, 1998, and Fig. 4.4a). In addition, the broad area covered in Fig. 4.3 shows that wave fronts

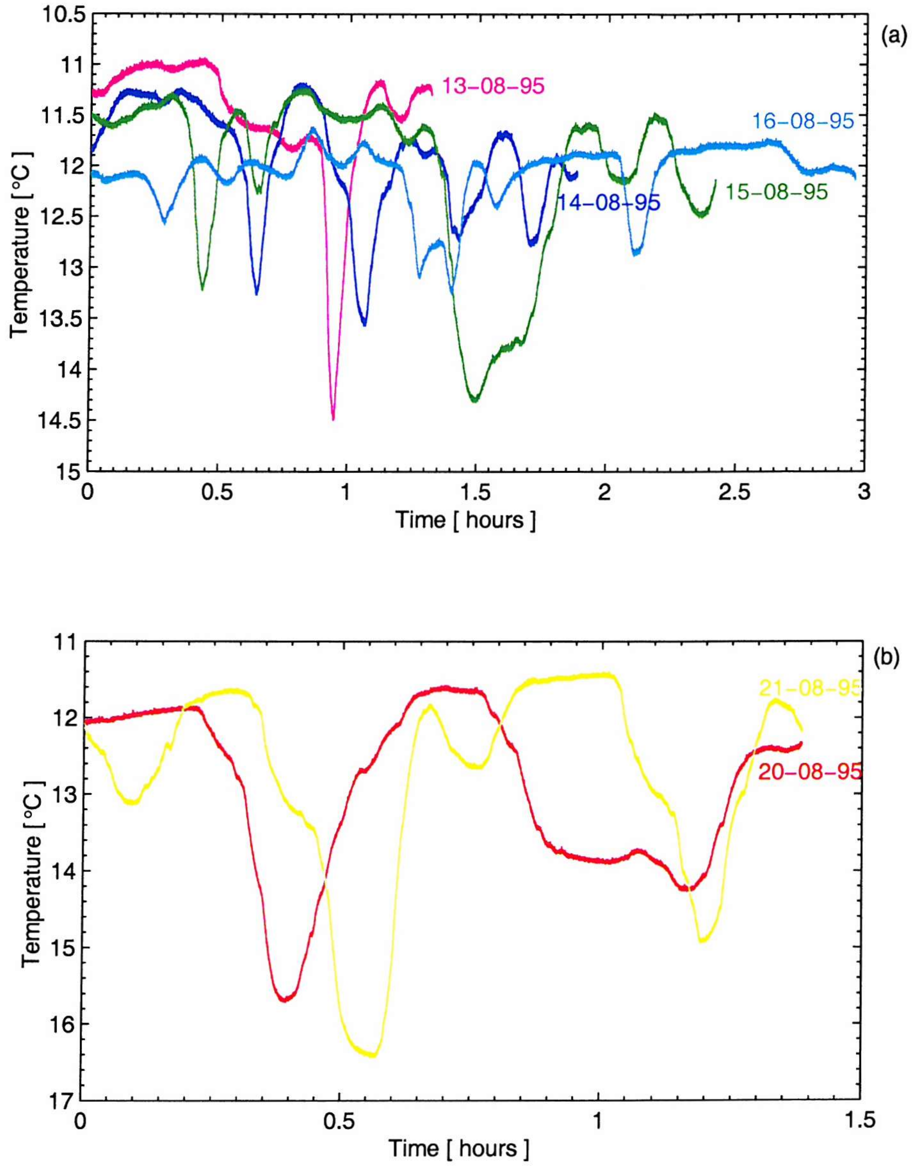

Fig. 4.4: *Non-linear internal waves recorded by ARIES II at similar times. (a) Spring tides. The time series of temperature for each day starts at 18:48 GMT. Estimations of internal wave amplitudes are of the order of (3-24) m, showing a tendency to decrease at the end of the spring tide period on* 16^{th} *August 1995. (b) Neap tides. Each time series starts at 17:00 GMT. Internal wave amplitudes range between 13 m and 37 m, being larger on the* 21^{st} *than on the* 20^{th}*. These estimations suggest that wave amplitudes are larger when the neap tide is on the ebb than during the rising spring tide. Note that temperature fluctuations on both the* 20^{th} *and* 21^{st} *imply rank ordered ISWs, whereas on the* 14^{th} *the second wave appears to have the same amplitude as the leading wave. The latter has been already been observed in the field (e.g. Henyey, 1999) and from satellite imagery (Robinson, priv. comm., 2000). Moreover, a wave with double temperature maxima is clearly seen on the* 16^{th} *suggesting ISWs crossing from different directions.*

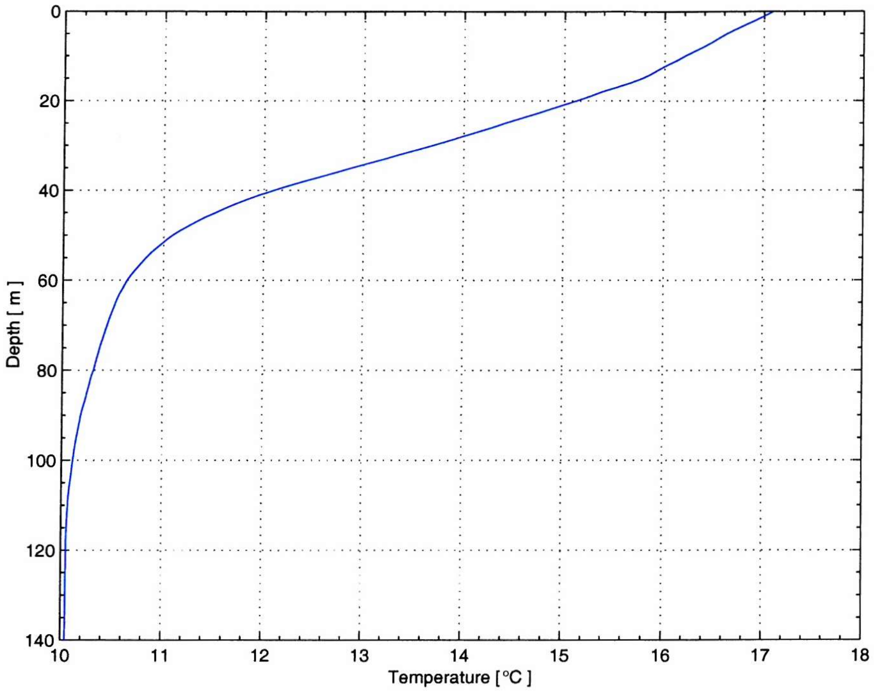

Fig. 4.5: *Mean CTD temperature profile for the period 19-21 August 1995. (By courtesy of J. Small; see Small* et al., *1999).*

can present a pronounced curvature, reflecting perhaps, multiple different generation sources associated with bathymetric variability in the area (e.g. Holt and Thorpe, 1997).

Fig. 4.4 suggests in particular the occurrence of large ($>$ 20 m) ISWs during both spring and neap tides with amplitudes, as registered by ARIES II, larger over the neap tide period. The overall wave amplitudes have been estimated from the temperature fluctuations caused by the passage of ISWs at the sensor depth and the mean temperature profile shown in Fig. 4.5, although the latter is strictly valid for neap tides. Apparently, the largest waves were not recorded by ARIES II but by the 55 m current meter. On 29 August 1995 (spring tides), an internal wave with an amplitude of O(50 m) occurred at about 12:37:30 GMT and on the 20^{th} (neap tides) a wave amplitude of O(45 m) was recorded roughly at 05:37:30 GMT. ARIES II was not operating during these times and, therefore, the streamlined instrument just failed to record the largest internal wave events. Further, the above amplitudes are in opposition to a suggestion made by Inall *et al.* (2001) in the sense of large ISWs encountered only during neap tides and not on spring tides. It should be said, however, that wave amplitudes estimated from a moored ADCP (Inall *et al.*, 2001) are probably better than those presented in the current work.

Sandstrom and Elliot (1984) have estimated that during each tidal cycle, a single soliton is dissipated over distances of O(10-30 km) inshore from the Scotian shelf break,

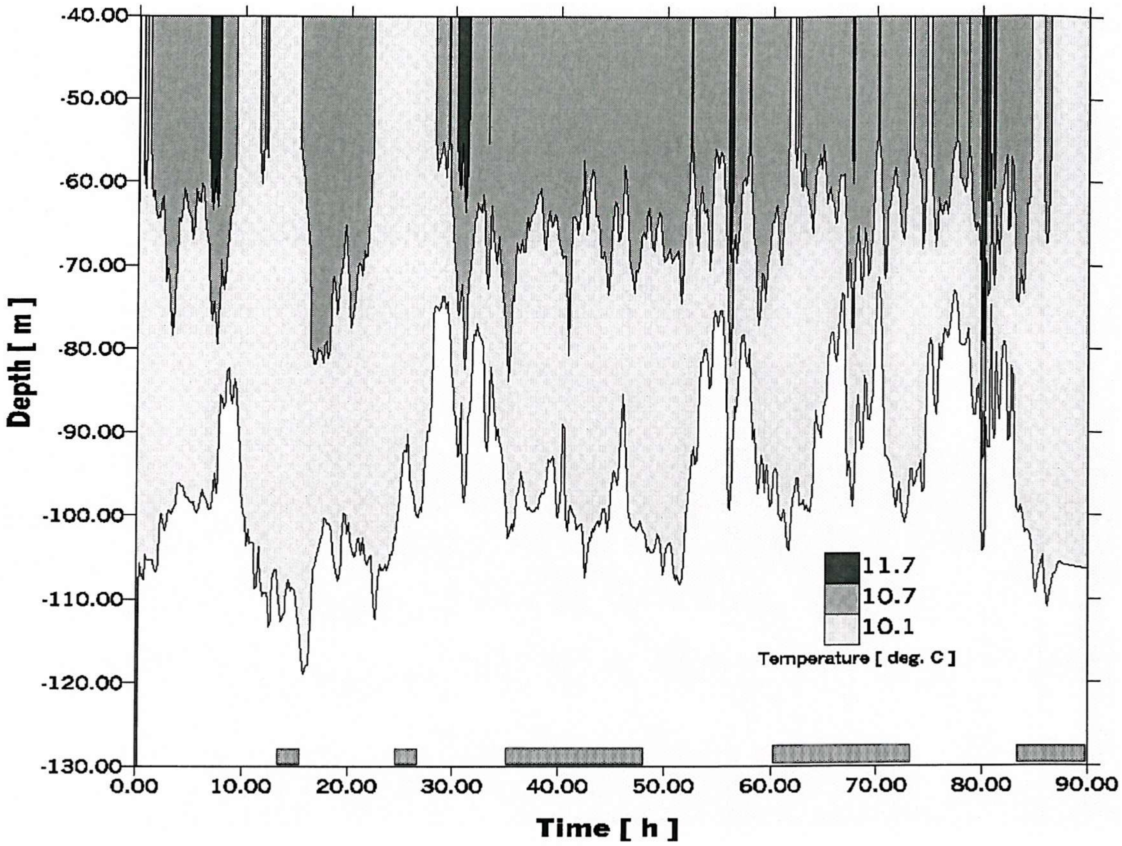

Fig. 4.6: *Isotherms from a nearby thermistor chain mooring located at about 0.6 km from the ARIES II site showing internal wave activity up to a depth of roughly 100 m with depth-dependent amplitudes of O(4-25 m). The record starts on* 11^{th} *August 1995 at 19:18 GMT and stops on* 15^{th} *August 1995 at 10:56 GMT (87.6 h). Contours are based upon a (541,19) grid with time and depth intervals of 10 min and 5 m, respectively (see the beginning of the current chapter for additional details). The shaded rectangles above the time axis indicate periods in which ARIES II was operating.*

whilst for the Celtic Sea shelf the e^{-1} decay length scale for wave packets is typically of 70 km (Pingree *et al.*, 1986). ARIES II, as indicated at the beginning of the current chapter, is deployed about 4 km to the east of the 200 m isobath, a distance in which the effects of shear instability and bottom dissipation are presumably of little importance. Moreover, the slope current (Huthance, 1986; Simpson, 1998a) flows northwards centred roughly over the 500 m isobath (Burrows *et al.*, 1999), some 10 km west of the ARIES II mooring. The mooring is therefore far away enough from its possible influence.

4.3.2 Stratification

Local variations of density which have an effect at the ARIES II site, appear to be dominated by internal waves. Fig. 4.6 shows modulations of isotherms caused by non-linear internal waves of depression. Some modulations can be tracked down from depths of 60 m to 100 m (for example, at roughly 30 h and 68 h into the record), but others lack a definitive temperature signal at a depth of 100 m (for example, at 4 h into the record). There are also periods where no clear internal wave motions are observed, for example, at about 25 h into the record, but in contrast ARIES II has detected temperature signatures of internal waves during this period (not shown).

Inall *et al.* (2000) have estimated that 30% of the total dissipation, integrated over a 145 m water column and over 12.4 h, occurred within the thermocline and the rest within the benthic boundary layer. During a specific neap tide period on 21^{th} August 1995, Inall *et al.* (2000) found dissipation and vertical mixing characterised by ISWs. By contrast, during a spring tide period which occurred on $(30-31)^{th}$ August 1995, the depth-integrated dissipation was more evenly distributed throughout the tidal cycle; vertical mixing enhanced because of an event of weakened stratification (Inall *et al.*, 2000). Although currents at the current meter mooring site are poorly sampled in comparison with both ARIES II and thermistor chain data (see section 4.1 and the beginning of the current chapter), it seems that dissipation during spring tides might be higher than that estimated by Inall *et al.* (2000). Previous figures, such as Fig. 4.4a and 4.6, and Fig. 5 in Thorpe *et al.* (1998), are indicative of more intense variability of internal wave events during M_2 tidal cycles around spring tides (i.e. $(12-16)^{th}$ August 1995) than during the specific spring tide period that Inall *et al.* (2000) have reported. Some events show a complex structure (e.g. waves with double temperature maxima and/or waves with apparent signatures of mixing).

Typical σ_t profiles obtained in the neighbourhood of the ARIES II mooring site are shown in Fig. 4.7a. A water column with uniform σ_t (with a σ_t difference of less than 0.01 in comparison with that from the sea surface), reached roughly 16 m depth on both 15^{th} and 25^{th} August 1995. The times for the casts correspond to the late afternoon, and in terms of the diurnal cycle of heating and cooling, they are probably near the time in which convection starts deepening the mixed layer. Further, since the three profiles show that σ_t tends to increase through the ARIES II measurements period, a cooling of the surface layer is evident in Fig. 4.7a. On the 30^{th}, a mixed layer of only 5 m and the asymmetry in the σ_t profile are perhaps a sign of the competing effects of wind mixing, surface heating, internal wave shear and subsequent mixing (see Price *et al.*, 1986; Pingree and Mardell, 1981; Pingree and New, 1995). Beneath the mixed layer, the pycnocline was of about 30 m thick. Maximal buoyancy frequency of (20 ± 2) cph occurred in the first two casts, but decreased to 15 cph during the last one (Fig. 4.7b). The depth of such maximums remained constant at roughly (27 ± 1) m. These estimations are consistent with the CTD casts described by Inall *et al.* (2000), but inconsistent with the deepening of the maximum buoyancy frequency found by

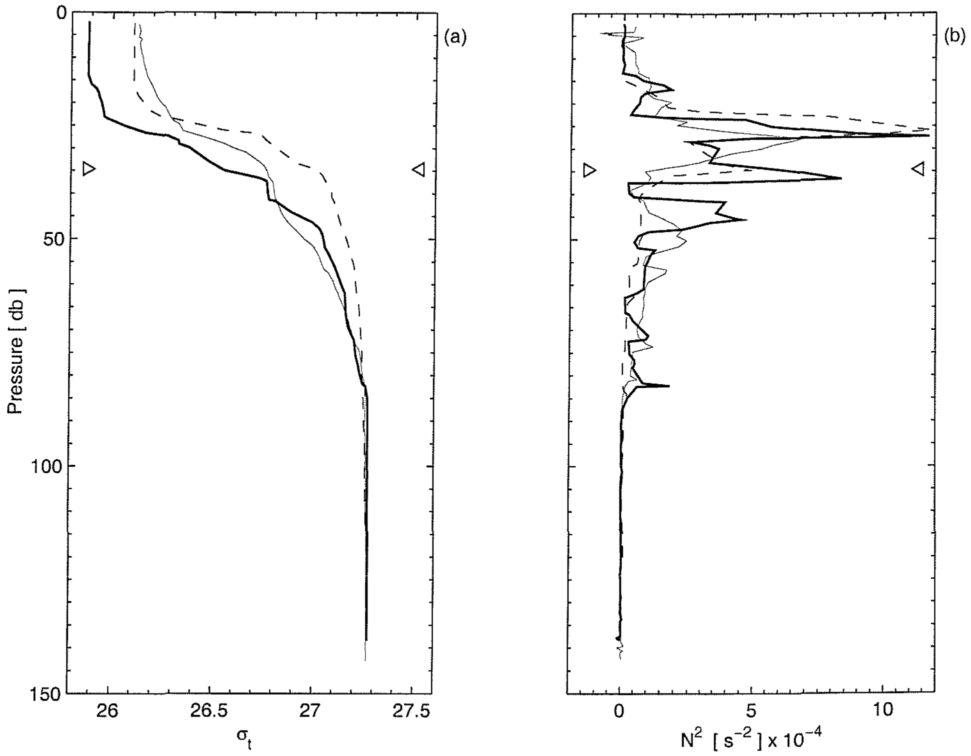

Fig. 4.7: *(a) σ_t and (b) buoyancy frequency squared (N^2) profiles from CTD casts around the ARIES II mooring (its mean depth marked by the ▷ ◁ symbols) during spring tides. The thick solid lines refer to a cast taken on 15th August 1995 (17:18, 1.3, 4.9, 268), thin dashed lines on 25th August 1995 (17:09, 1.1, 6.1, 12) and thin solid lines on 30th August 1995 (17:22, 1.1, 4.3, 12). The numbers between parenthesis indicate the cast time (GMT), the distance from ARIES II (km), the 10 m-wind speed (ms^{-1}) and wind direction (°T). The N^2 profile was calculated using central differences and a reference density of 1026.6 kgm^{-3}.*

Small *et al.* (1999). The cause is probably linked up with the averaging of CTD casts at different depths, to the different cast days chosen (e.g. 4-6 September 1995) and to further cooling of the sea surface yielding a downward migration of the thermocline. ARIES II, therefore, was deployed at a depth below the largest buoyancy frequency and the local stratification can reasonably be represented by a two-layer constant density structure.

As it is generally well-known, a mean density profile from CTD casts is required to obtain the phase speed and modal amplitude for long internal wave modes in a flat-bottomed stably stratified Boussinesq fluid at a particular site. Such calculations were done by Small *et al.* (1999) with no velocity shear or rotation at a depth of 400 m (Table 4.2) and by Inall *et al.* (2000, 2001) near the ARIES II site, also with no current shear but with rotation. Here, one should bear in mind that the current meter at 55 m

Tab. 4.2: *Dynamical normal displacement modes on (19-21)th August 1995 for a 400 m water depth and a wave period of 1 h according to Small* et al. *(1999).*

Displacement Mode	Phase Speed ($\mathrm{ms^{-1}}$)	Wavelength (km)	Displacement Depth (m)
1	0.48	1.7	80
2	0.22	0.8	30, 180
3	0.15	0.6	25, 55, 230

is the only available instrument with a temperature sensor to compare with ARIES II's temperature measurements and, therefore, it is well worth noticing that the depth of the first inflexion point of mode 2 in Table 4.2 is near the mean depth of ARIES II, and that the depth of the second inflexion point of mode 3 (Table 4.2) matches the corresponding depth of this current meter. A possible consequence is that, within a given time, different internal wave modes might well coexist and that both ARIES II and the current meter might have been registering different modes or a combination of them. There is evidence, in particular, that the first and third modes were the vertical mode motions dominant on 19th August 1995 (Small *et al.*, 1999). Furthermore, by means of empirical orthogonal functions (EOF), Small *et al.* (1999) found dominance of the first vertical mode which was confirmed by Inall *et al.* (2000, 2001) using both EOF and a mean density profile on August 1995. However, whilst Small *et al.* (1999) found the node of the first normal mode of the horizontal velocity component to be located at a depth of about 80 m (for the neap tide period and the depth indicated in Table 4.2), Inall *et al.* (2001) found it at the depths of 47 m and 36 m (in 145 m water depth) for individual wave packets on 19 and 22 August 1995 respectively. These results indicate that ARIES II was deployed in the upper layer and the current meter in the lower layer of a two-layered water column. At times it is therefore plausible the presence of definite signatures of internal waves in ARIES II temperature records and the absence of such signatures in the corresponding records of the 55 m current meter.

4.3.3 Currents and tides

Semidiurnal tidal current ellipses on the Malin shelf show clockwise rotation (Simpson, 1998a); also, one point of interest brought out by Burrows *et al.* (1999) is the presence of apparently non-tidal rotatory currents near to the ARIES II site. Drifters drogued at 50 m and released in 200-400 m are notably carried onto the shelf during summer where they appear to follow the circuit of a slow advection recirculating current before their reentry into the slope current (see label H in Fig. 1b of Burrows *et al.*, 1999). The nature of such transient eddies have to be determined yet. It is worth noticing that a sudden change in wind direction, say, from northerly to westerly (e.g. Fig. 5.4), may induce turns of residual surface currents (see Xing and Davies, 1996).

Furthermore, it appears that little is known on the spatial variation of the vertical density structure and, in consequence, on the effects of horizontal gradients of density on currents. Thus for a period of 5 days in August 1996, Hallock *et al.* (2000) found the presence of horizontal gradients of density below 200 m water depth and at a distance of about 200 m seaward from the shelf edge; besides, persistent fronts in the upper 200 m were not seen. Mean currents at 30 m and 55 m are about 2.2 cms^{-1} to 164°T and 1.3 cms^{-1} to 141°T respectively, and tides, predominantly M_2, have current speeds of 0.1-0.2 ms^{-1} and amplitudes of 1 m (Thorpe *et al.*, 1998).

Tidal ellipses obtained from a moored ADCP during August 1995 show a dominant M_2 tidal component oriented in an East-West direction (82°T) with a maximum current speed (semi-major axis) of 26 cms^{-1} and a minimum speed (semi-minor axis) of 7 cms^{-1} (Small *et al.*, 1999). Spring tides occur on 12-13 and 29-30 August 1995 while neap tides occur on 19-21 August 1995. Maximum on-shelf off-shelf speeds during springs are 30-35 cms^{-1} and about 10 cms^{-1} during neaps. The northward tidal current rises up to 25 cms^{-1} at springs and 5 cms^{-1} at neaps, whilst the southward component reaches around 10 cms^{-1} at springs and 4 cms^{-1} at neaps (J. Small, priv. comm.).

5. THE PERFORMANCE OF ARIES II

This chapter brings about a critical assessment of the general response of the streamlined instrument to fluid motions produced by currents, non-linear internal waves and wind-waves. It looks for evidence of a possible lift force resulting from an unevenly streamlined profile of the instrument. Particular attention is paid to the orientation of ARIES II with mean currents and flows induced by internal waves, although a comparison based upon the poor sampling rate of current meters operating in a highly variable environment may result inadequate. It questions whether wind data obtained from the DERA ship are representative for the ARIES II site. It evaluates to what extent temperature variations are caused by the tilting of the mooring line in response to internal wave flows. It estimates the tilting of ARIES II from the attachment point at the base frame according to Packwood (1995), while the corresponding tilting from the mooring line is estimated using a formulation based upon a simple force balance. An expression for the total vertical excursion experienced by the instrument is also given.

5.1 General response to fluid motions

The typical action of fluid motions on the sensors comprising ARIES II is summarised in the mean spectrum shown in Fig. 5.1. Groups of waves, swell and wind-sea induce the acoustic instrument to oscillate with the frequencies defined in Table 5.1. The presence of wave groups at a frequency band of 0.0078 Hz suggests a sea surface containing a narrow energy spectrum formed by a linear combination of different and independent frequency components. There is a frequency shift observed in Fig. 5.1a at the spectral wave group frequency recorded by the forward inclinometer (0.0156 Hz). Since this frequency does not represent an isolated event like the change in the spectrum slope registered at 0.0625 Hz (large swell), it seems that the frequency shift is not caused by some physical effect on wave grouping (e.g. currents or local winds). Speculating on a possible instrumental cause, the positive buoyancy of ARIES II and the weight distribution (see chapter 3) might provide a resistance to a fore-aft oscillation with groups of waves resulting in a higher spectral response (Table 5.1). This might also be the cause of the different spectral response to wind-sea experienced by the forward (i.e 0.3106 Hz) and starboard (i.e. 0.2031 and 0.2656 Hz) inclinometers, clearly seen in Fig. 5.1a. Headings (Fig. 5.1b) show frequency components in the wind-sea range

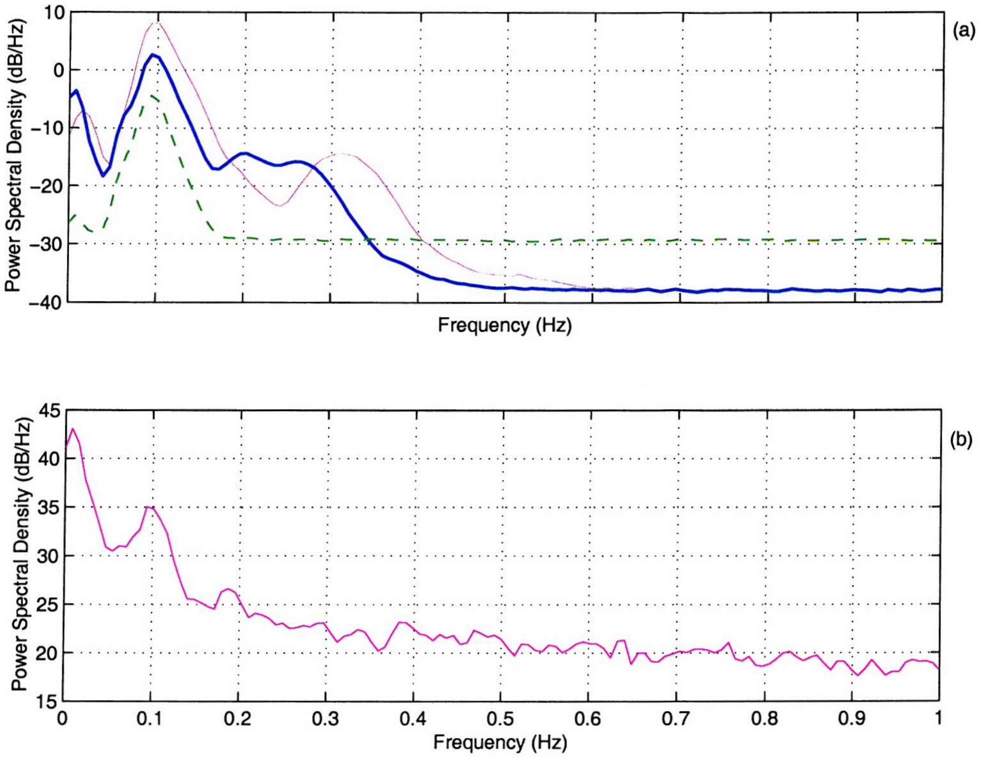

Fig. 5.1: *Mean power spectrum for the instrument sensors, based upon the whole records over periods of 13 h. (a) forward tilt (thin solid line), starboard tilt (thick solid line) and pressure (thick dashed line). (b) headings.*

Tab. 5.1: *Mean maximal frequencies (Hz) corresponding to Fig. 5.1. Superscripts indicate: (1) nil standard deviation; and (2) a single value. Frequencies less than 0.1882 Hz correspond to swell, whilst those with higher values to wind-sea.*

Forward tilt	Starboard tilt	Pressure	Headings
–	0.0078^1	0.0078^1	0.0078^1
0.0156^1	–	–	–
–	0.0625^2	0.0625^2	0.0625 ± 0.0110
0.0997 ± 0.0039	0.0997 ± 0.0039	0.0938 ± 0.0064	0.1016 ± 0.0064
–	0.2031 ± 0.0064	–	0.1882 ± 0.0104
–	0.2656^2	–	–
0.3106 ± 0.0148	–	–	–

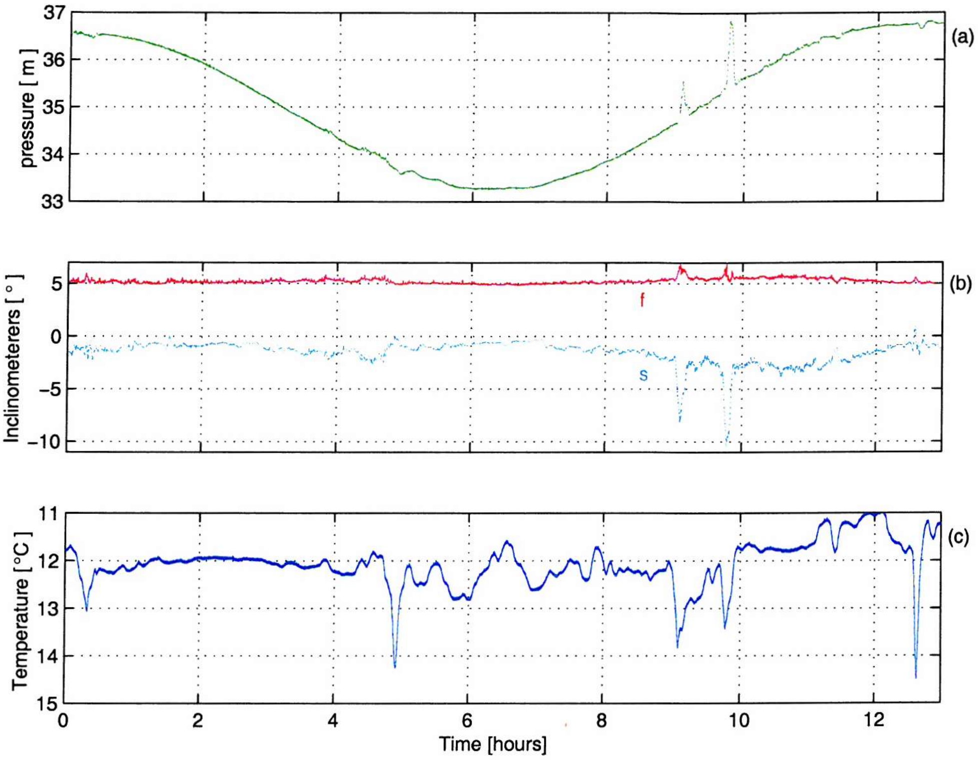

Fig. 5.2: *(a) Pressure obtained from equation (3.1) and corrected to the sonar transducers' level; (b)inclinometers, where fore-aft tilts are labelled 'f' and port-starboard tilts 's' (+ve angles indicate ARIES II tilted up on both the fore and starboard sides); and (c) temperature, increasing downwards. In order to have clear figures, a third order Savitzky-Golay smoothing filter with a frame size of 1 min has been applied to (a) and (b). Record starts at 7:07 GMT on 13th August 1995.*

(0.25 - 0.53) Hz consistent with high-frequency waves measured from acoustic images by Thorpe *et al.* (1998). At frequencies larger than 0.0938 Hz, the pressure spectrum (Fig. 5.1a) does not show evidence of wind-sea because of the exponential decay of wind-waves with depth. Spectral fluctuations observed at high frequencies (> 0.53 Hz) in the headings (Fig. 5.1b) are probably not caused by surface waves. These frequencies have not been identified and may have several different sources, for example magnetic interference or vibrations of the mooring line (see section 5.2).

There are no spectral frequencies associated with internal waves ($< 3.3 \times 10^{-3}$ Hz), suggesting that the solitary-like waveforms recorded by ARIES II are not periodic. Although there is evidence that packets of solitary waves may be generated every tidal cycle (see section 4.3.1), the available records are not long enough (see section 3.4) for a tidal frequency to come out in a spectral analysis. The response of ARIES II to tides, however, is clearly seen in Fig. 5.2a. The amplitude of the tide is of about 1 m. Moreover, the response of ARIES II to non-linear internal waves is also evident in Fig. 5.2, notably at roughly 9 h into the record. A rank ordered wave packet induces the knocking-down of the mooring line, and a maximal vertical excursion of ARIES II of 1.5 m coincident with forward and starboard tilts of 2° and $-8°$ respectively. Thus ARIES II is tilted backwards and laterally down to starboard, suggesting that the instrument does not align fast enough to and/or a misalignment with a changing flow. The maximal vertical excursion caused by internal waves was of 1.7 m on 28 August 1995, inducing $-10°$ port-starboard tilt (see Fig. 5.13 in section 6.3.1 and also section 4.5.2). Periods with large vertical excursions (> 0.5 m) occurred during combinations of strong wind (> 7 ms^{-1}) and spring and neap tides, but represent only 11% of the overall data set. Additionally, it should be said that larger tilts ($> 4°$) are not necessarily coincident with periods of a large knocking-down of the mooring line.

5.2 On the asymmetric sides of ARIES II

Directional flows (e.g. internal waves, tides, drift currents) acting directly on ARIES II or the mooring line and high-frequency motion caused by surface waves are general factors that may contribute to the unsteadiness of this streamlined instrument. In particular, the incapability of the instrument to align with a fluctuating current, the weight distribution of tubes (Fig. 3.1a), the asymmetric streamlined shape of the framework, sideways tilts caused by vortex shedding from the fin, and high-frequency vibrations of the mooring line induced by vortex shedding from subsurface buoyancy spheres during periods of strong currents (e.g. > 25 cms^{-1}, see Loder and Hamilton, 1991) are all important factors. The importance of sway motions of ARIES II resides in the generation of corresponding fluctuations of the relative position of the sensors and of the two sonar beam axes; targets might be missed or ensonified several times. A failure of ARIES II to align properly into the local flow is indicative of increased drag with the possible formation of eddies on both sides of the instrument (characterising separated boundary layers) and undesirable instrument rolling. Either imperfections in the streamlined profile or an uneven weight distribution are also liable to alter the time response of the fin when aligning towards some incoming flow. If during low current speeds, for example, the time scale of this alteration is comparable to the period of swell (e.g. 8-12 s), the recorded headings might become contaminated since they are sampled at a rate of 0.5 s. As a consequence, it might not be possible to distinguish high-frequency angular motions arising from instrumental imperfections from those associated with surface waves (see for instance Sherwin, 1988b).

ARIES II represents a streamlined obstacle that induces the deflection of an incoming flow with the consequent formation of an adverse pressure gradient. It has been recognised (see Tritton, 1988) that a streamlined object with a convex surface under a steady flow can induce the distance between consecutive streamlines to be reduced there and, as result, the flow increases speed. Then, according to Bernoulli's equation, the pressure alongside the convex surface will be reduced. Similarly, the speed of the flow is reduced and the pressure increased along a streamlined object with a concave surface. The thickness of the boundary layer will be relatively thin and thick on the convex and concave surfaces, respectively. Therefore the boundary layer will be forced to separate from the above surfaces, in an undesirable position perhaps, if the flow of momentum is not strong enough to overcome the increasing pressure gradient along the concave surface. A point of separation in the middle of the surface, for example, could induce the formation of eddies in a wide turbulent wake.

Following Packwood (1995), the fin aligns ARIES II with the flow and suppresses vortex shedding from sway motions of the body of the instrument. To fix the boundary layer separation point at some position on the rear end of the instrument and to eliminate side forces caused by vortex shedding, the tubes have been designed to be in a square section frame. There, a buoyant fairing is at the front with the fin at the rear, as outlined in Fig. 3.1. Flexible sheets of plastic are attached on both sides of the instrument. These sheets, however, are not perfectly uniform after being screwed on and one side remained slightly convex and the other concave so leading to small, but perhaps significant, lift forces driving instrument vibrations (e.g. tilts transverse to the flow direction).

If the asymmetry in the streamlined instrument is giving a pressure increase on the concave side, and assuming that ARIES II is aligned with an incoming flow, a resultant lift force will induce a horizontal pull normal to the flow direction. As ARIES II is tethered from a buoyancy sphere (Fig. 4.1), the tension in the cable may provide a balance to the horizontal pull, otherwise the instrument will experience a transverse tilt. Ignoring for a moment the asymmetry, and in order to orientate into the flow, there will be another lift force when a current changes direction and a component of this horizontal pull should induce a centripetal force, which implies a transverse tilt allowing the instrument to turn into the flow via the rotation unit (Fig. 3.1). It is therefore expected some correlation between the headings and sideways tilts (see Fig. 5.5). Since a lift force tends to increase with the angle of attack, that is the angle of ARIES II to the direction of relative motion, then the horizontal pull caused by an streamlined profile which is roughly uneven might compete with the lift force inherent in the streamlined instrument; the latter directed perhaps in the opposite direction and therefore leading to transverse tilts. Thus, in addition, there might be some correlation between angles of attack and transverse tilts.

A correlation between headings and sideways tilts is looked during periods without internal waves in Fig. 5.3 and 5.4. Although high-frequency fluctuations observed in

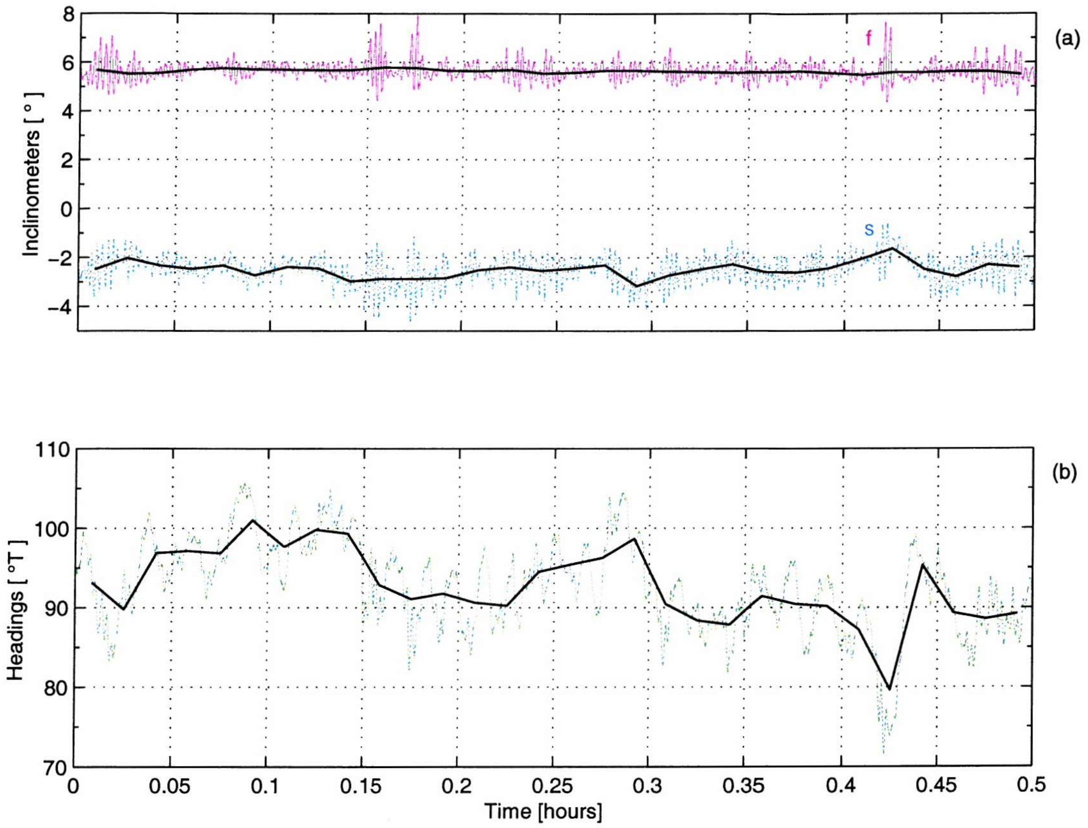

Fig. 5.3: *(a) Inclinometers: fore-aft (labelled f) and port-starboard (labelled s) tilts; (b) headings. Bold-thick solid lines indicate 1 min averages. Mean wind speed is* (8.1 ± 1.0) *ms*$^{-1}$ *from* $(280 \pm 7)°T$*. Mean current speeds at 30 m and 55 m water depth from a nearby current meter mooring (see Fig. 4.2 for its position) are, respectively,* (31.2 ± 3.1) *cms*$^{-1}$ *towards* $(321 \pm 4)°T$ *and* (16.9 ± 1.2) *cms*$^{-1}$ *towards* $(218 \pm 4)°T$*. Mean ARIES II orientation is* $(93 \pm 5)°T$*. Records start at 11:41 GMT on 14*th *August 1995.*

Fig. 5.3 are attributed to groups of surface waves, there might be a contribution from the mooring line as well. Under unsteady flow conditions, a spherical buoy may oscillate, with a frequency controlled by an oscillating flow developed from vortex shedding, perhaps irregularly or at relatively short periods of time with some amplitude transmitted to ARIES II through the vibration of the mooring line. The buoyancy sphere in the mooring line (see Fig. 4.1) has a diameter of 0.8 m and in a typical 0.3 ms^{-1} mean flow is potentially able to produce a Strouhal cross-flow oscillation of the mooring line with a frequency (≈ 0.2xspeed/diameter; see Wiseman *et al.*, 1983; Loder and Hamilton, 1991) of 0.075 Hz or period of 13.3 s. Larger currents would induce frequencies difficult to discriminate from swell. A simple 1 min average to the headings shows other fluctuations more clearly (Fig. 5.3b). Although currents are under-sampled (details in chapter 4), a first mean fluctuation, for example, from roughly the beginning of the record until it reaches 0.2 h, is perhaps caused by currents (with unidentified origin, but not produced by wind or internal waves; it is possibly a variation on the ebb tide). There are also fluctuations that overlap the first one suggesting a correlation with the starboard inclinometer (Fig. 5.3a). Thus, it appears that when ARIES II is rotating anticlockwise a transverse tilting up to starboard (or down to port) also occurs and vice versa.

A 2 h period where mean fluctuations of the external temperature are of O(0.3°C) waves is shown in Fig. 5.4c. There is some correlation between currents not driven by internal waves (Fig. 5.4b) and the lateral swinging of ARIES II (Fig. 5.4c, label s). As is shown in Fig. 5.4e, the tide is on the ebb which is consistent with the currents rotating roughly anticlockwise (see Fig. 5.4b); besides, the second half of Fig. 5.4a and 5.4b suggest currents and winds relatively aligned. Under these circumstances, the instrument is swinging irregularly from side to side, but the mean is $(-0.6 \pm 0.4)^\circ$; by contrast, the fore-aft movements are more steady with a mean of $(5.0 \pm 0.3)^\circ$. Pulses associated with groups of surface waves are evident in the inclinometers and pressure records (Fig. 5.4c and 5.4e). Mean heading fluctuations are of O(25°) in Fig. 5.4d, and show an unsatisfactory alignment of ARIES II with either currents at 30 m depth or the wind direction. A much better comparison cannot be done because of the poor (10 min) sampling rate of the current meter (assuming a reliable alignment of this meter with the relative flow direction) and the source of wind data. The latter refers to the remote position of the DERA ship relative to the ARIES II site, shown in Fig. 4.2. If there is a weight imbalance in the instrument, then during low flow conditions (e.g. < 15 cms^{-1}) the time response of the vane might be larger than during relatively high current speeds. This, therefore, might also lead to ARIES II and currents out of alignment. In comparison to the observations on Fig. 5.3, the observed irregularity in the transverse tilts (Fig. 5.4c) indicates that ARIES II can also lean over up to starboard with a clockwise rotation. This occurs, for example, between 0.40 h and 0.45 h (marked X) into Fig. 5.4d, suggesting an unsteady condition. The alignment of ARIES II with currents is discussed further in section 5.3.

To explore the possible dependence between headings and transverse tilts further, scatter diagrams for the few periods without internal waves found in all the 13 h records are displayed in Fig. 5.5. It is clear that (i) there is no linear correlation between headings and transverse tilts; (ii) ARIES II sways gently roughly -0.5°, from a reference transverse tilt of about -1.0°, as slowly rotating clockwise or anticlockwise; (iii) the relatively large fluctuations in the headings rate are probably associated with wind speed and groups of waves (see also Fig. 5.11 and 5.12), and (iv) maximal transverse tilts $[(-2.5 \pm 0.3)^\circ$ down to starboard] occur when the instrument is oriented eastwards, probably in response to the ebb tide. Fig. 5.5c, on the other hand, suggests

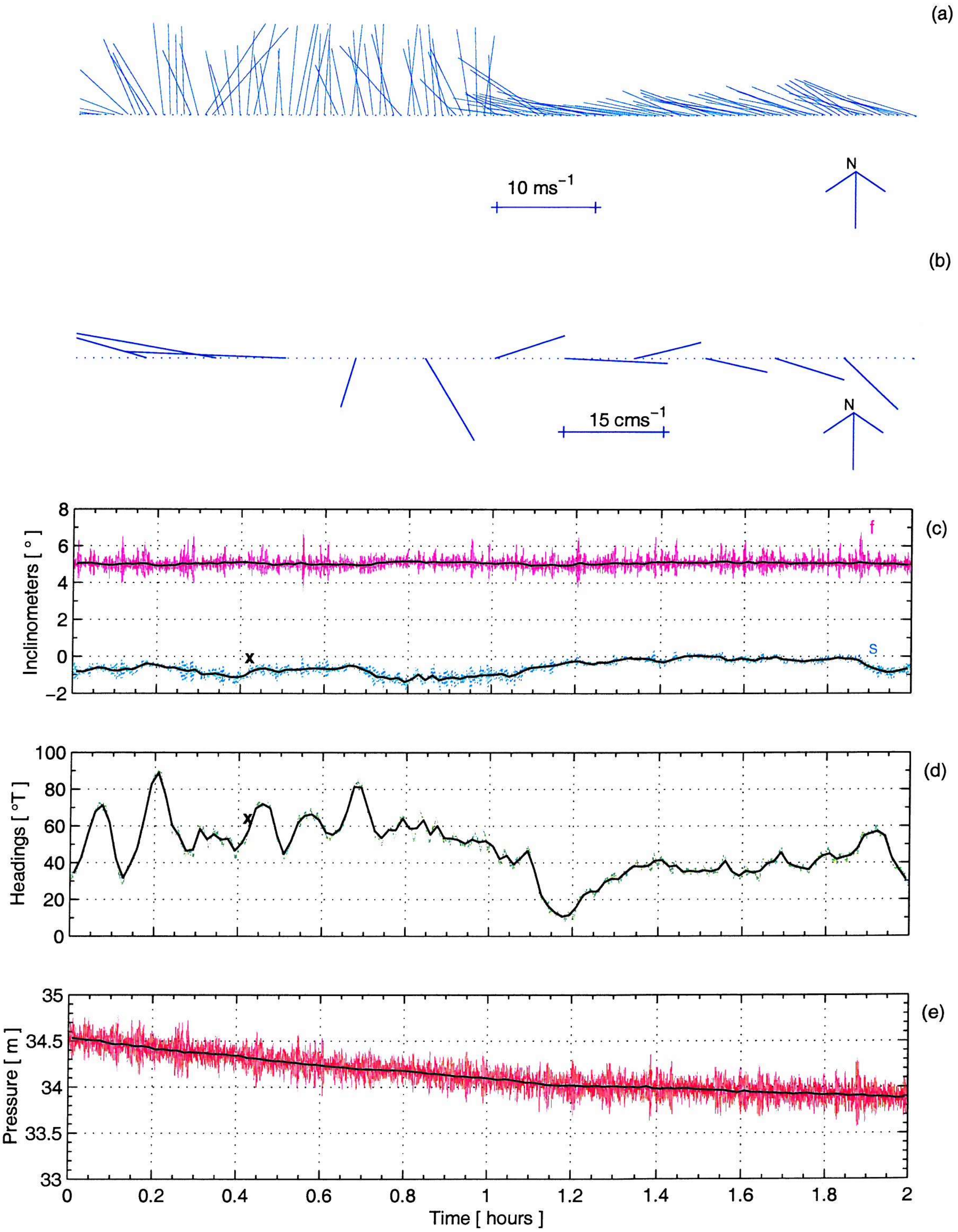

Fig. 5.4: *(a) Wind speed at 10 m above the sea surface from ship measurements. The maximal magnitude is 12.6 ms^{-1} from 31°T, at about 0.3 h into the record. (b) Currents measured at 30 m water depth. Maximal speed, also at about 0.3 h into the record, is 25.2 cms^{-1} towards 280°T. (c) Inclinometers; (d) headings; and (e) pressure at transducers level (see section 4.1 for details). Thick solid lines in (c)-(e) indicate 1 min averages. The sample rate for wind is 1 min, whilst that for currents is 10 min, both with time scale referred to that of ARIES II. Records start at 13:16 GMT on 16th August 1995.*

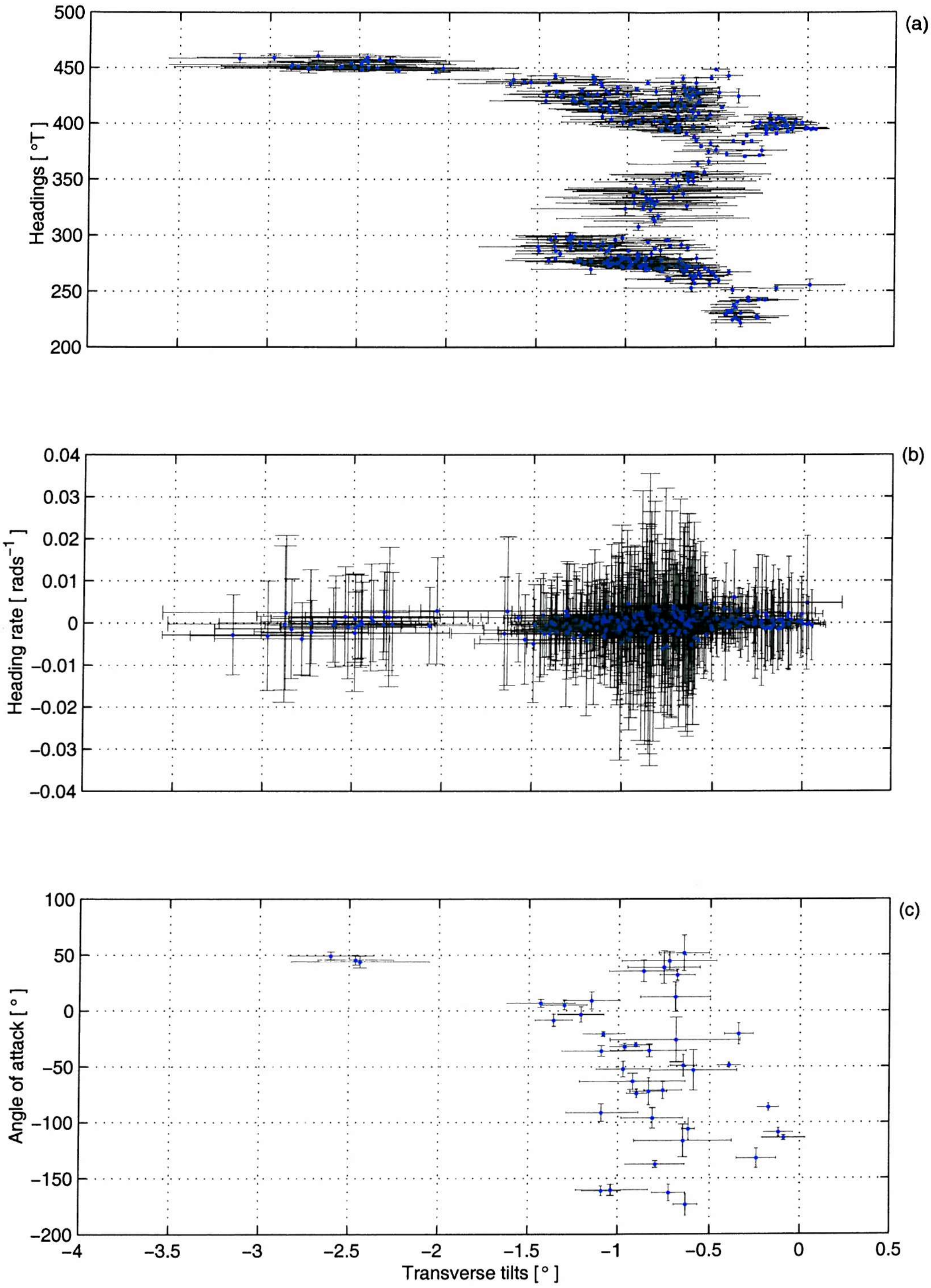

Fig. 5.5: *(a) Scatter diagram for headings vs transverse tilts. The vertical scale is rolled over beyond 360°T for convenience. (b) The rotation rate vs transverse tilts, which is calculated using centred finite-differences. Positive rates indicate clockwise rotations. Means are taken over periods of 1 min for both (a) and (b). (c) The angle of attack, with reference to the current meter at 30 m depth, vs transverse tilts. Here means are taken over 10 min periods. Positive angles indicate currents to the right of (e.g. starboard) ARIES II. Similar patterns to those shown in (a)-(c) are found using low-pass filtered data with a cutoff at 0.25 cph instead of 1 min averages.*

no correlation between angles of attack and sideways tilts. It does show, however, a mismatched alignment between currents and ARIES II which is inconsistent with a ±2° alignment reported briskly by Thorpe and Baldwin (1995), but in very different oceanic conditions.

It is uncertain whether the swaying of ARIES II is indeed caused by a lift force arising from the asymmetry of the flexible plastic sheets covering the streamlined instrument. The power spectrum in Fig. 5.1a does not show significant fluctuations at high-frequencies, which may indicate that sideways tilts caused by instrument imperfections, if any, are at least not periodic. It is also uncertain to what extent the time response of the fin and the instrument alignment into a current might be affected. In order to prove these points, laboratory tests and numerical modelling are needed. But such engineering work is not treated here. Apart from instrument imperfections, one can speculate about physical processes and mooring stability. Looking for other possible causes of the ARIES II transverse tilt we have: vertical shear either (i) not driven by the wind, for example, that produced by tidal flows or by the sub-inertial variability (the inertial period in the ARIES II site is $\frac{12\,\mathrm{h}}{\sin\varphi} \approx 14$ h with $\varphi = 56.4575°$) of the vertical structure of density and velocity deriving from fronts or, internal waves; or (ii) driven by the wind, such as local wind forcing producing transient shear linked up with drifting Langmuir roll vortices or that with near-inertial and sub-inertial frequencies at the base of the UOBL and related to wind-driven deepening of the mixed layer (Weller and Plueddemann, 1996; Plueddemann and Weller, 1999); and finally, tilting of the mooring line yielding instrumental motions in response to drag associated with mean flows. However, the low resolution of the current meter in comparison with the ARIES II sample rate should be borne in mind, and also that both the pressure and the shear stress distribution around the entire instrument are unknown.

Aside from Packwood's (1995) report, it is to the author's knowledge that there are no other detailed technical documentation concerning numerical or dynamical tests performed for ARIES II in either laboratory or fieldwork. In consequence, both the critical Reynolds number at which eddies might form behind the instrument and, since Fig. 5.5c shows inconclusive evidence, the possible effects of convex-concave plastic sides on the boundary layer point of separation are unknown. Based upon Fig. 5.5c, therefore, one has to assume at this point that the variation of pressure induced by this geometric irregularity on both sides of ARIES II is not significant and, in consequence, the pressure at the front and at the rear of the instrument are perhaps almost in balance. Therefore it seems probable that the separation is occurring near the rear end of ARIES II.

These results provide baseline data to conduct numerical modelling for examining the effects of asymmetric walls on lift forces and transverse tilts of ARIES II. Further, by measuring in the lab or in a tidal channel the velocity field along the instrument wake, at different points separated by a known distance, it would be possible to derive evidence of organised motion behind this streamlined instrument. Such issues require further observations to be verified. They are left over, in spite of their relative significance, for future research and therefore not pursued in the current work.

As mentioned at the beginning of section 5.2, another source of instrument unsteadiness is the distribution of the instrument tubes in relation to their weight. In order to help the fin to rotate ARIES II into the flow when a current increases the instrument tilt from the vertical, the heaviest tube has been fitted aft. It is unclear, however, whether the pivot point is the tail of the fin, the aft tube itself or the axis of the centre tube, which is in line with the mooring attachment point (see Fig. 3.1a). That ARIES II is indeed pivoting about the axis of the centre tube, as Packwood (1995) approximates, has not been unequivocally determined. The disadvantage that arises from this asymmetric weight distribution during no-flow conditions is an instrument tilt of 2.6° to the vertical (Packwood, 1995), probably in the fore-aft direction. Such conditions (e.g. ≤ 2 cms^{-1}), however, were very rare during the period of measurements and lasted for 10 min at most. Mean pitch and roll in these conditions, from non-averaged data, was $(5.2 \pm 0.2)°$ and $(-0.7 \pm 0.3)°$, respectively.

5.3 Orientation and tilt

In the preceding section, concern was expressed about the capability of ARIES II to orientate into an incoming flow, particularly with flows not produced by internal waves (Fig. 5.5b). It started by considering several causes capable of inducing transverse tilts of the streamlined instrument. These are: (a) high-frequency vibrations of the ARIES II mooring line produced by vortex shedding from the buoyancy sphere, which may induce transverse tilts with frequencies of the same order of magnitude than the frequencies of swell; (b) vortex shedding from the fin caused by the asymmetric sides of the streamlined instrument; and (c) physical events producing significant vertical shear. The evidence shown points towards uncertainty about whether the above factors are indeed responsible for the continuous swaying of ARIES II. What has emerged, however, is: (a) a notorious misalignment of ARIES II with currents; (b) a claim for the undersampling of currents which prevents a better comparison between ARIES II and current meter headings; and (c) the need of theoretical, numerical and/or lab tests regarding the time response of the fin and the role of the tube-bearing weights in relation to the misalignment of ARIES II into currents. Here, other causes affecting the alignment of ARIES II with currents are identified.

5.3.1 The alignment of ARIES II into the mean flow

The mean orientation of ARIES II into the mean current direction, estimated from current meters at 30 m and 55 m (see section 4.1) and weighted to the depth of sonar transducers (34.6 m), is tested in Fig. 5.6. We are interested in discriminating whether the scatter of points is produced by physical events occurring in the deployment site or by instrument failure.

There are two groups of points associated with periods in which ISWs were passing the ARIES II and the current meter moorings. One group is located relatively far from the ideal straight line with mean current direction in the range (400 – 500)°T (labelled Y in Fig. 5.6), whilst the other group is located below the ideal straight line with mean true headings near 330°T and (400 – 500)°T (labelled X in Fig. 5.6). These groups are not aligned with the ideal straight line because the estimation of internal wave currents using a poor sampling rate is, obviously, not good enough and also because Fig. 5.6 shows a comparison with a mean flow direction and not directly with the direction of the internal wave. The rms scatter of points is about 45°. This scatter is accounted for by the separation of both current meters from the streamlined instrument (0.6 km), the rms scatter of the measurements within the 30 min periods and by the vertical and horizontal variability caused by internal waves passing through the moorings. Also, no new information is gleaned from Fig. 5.6 when the mean orientation of ARIES II is tested using only the mean direction from the 30 m current meter (not shown), where the rms scatter of points is of roughly 46°. This is attributed to the internal wave activity at the deployment site. A similar comparison with the mean current direction at 55 m gave a rms scatter of about 52°.

A better alignment is found when looking for particular wind conditions after selecting periods which are not affected by internal waves (Fig. 5.7). The rms scatter of the measurements for low wind ($\mathcal{U}_{10} \leq 7 \text{ ms}^{-1}$) is 34°, whereas that for high wind decreases to 23°. Currents have not been interpolated to the depth of ARIES II in this case and the comparison between headings and current directions has been done without particularly examining the temperature record at the depth of 55 m. The main causes inducing the misalignment of ARIES II with currents have been identified from Fig. 5.7 as follows: (1) motions of the water column associated with temperature fluctuations of O(0.5°C) at mean ARIES II depth occurring just before the arrival of packets of non-linear internal waves to the study site. This is the case of the group of points with headings from 100°T to 160°T and current directions ≤ 100°T (labelled X) and also for the group with headings and current directions about 300°T and 350°T respectively (labelled Y), all shown in Fig. 5.7a. As for Fig. 5.7b, the same explanation is valid for the group of points with headings in the range (150 – 200)°T and current directions roughly 100°T (label U), and for points with headings about 300°T

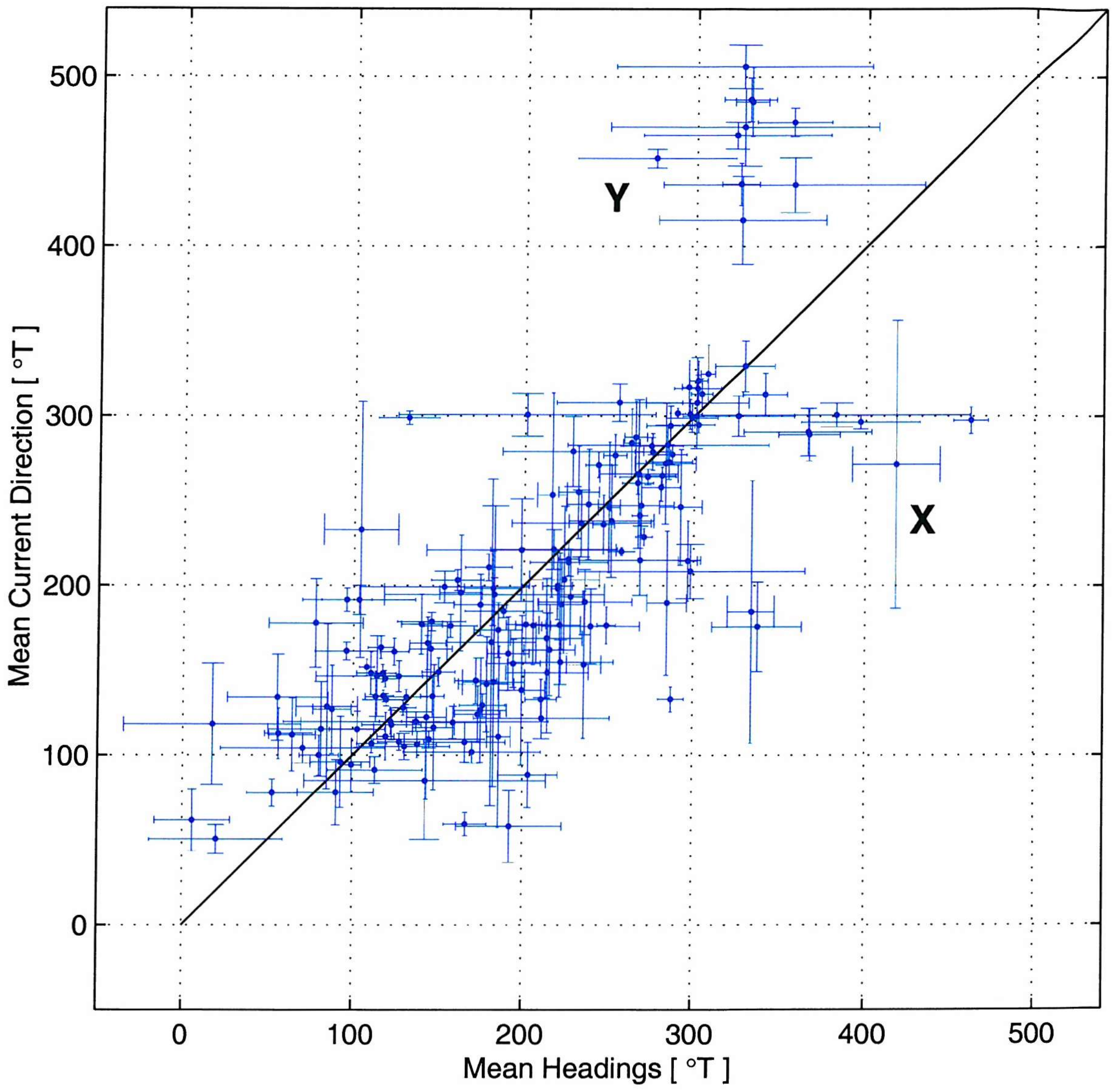

Fig. 5.6: *The alignment of ARIES II at 34.6 m compared with the depth weighted mean current direction from current meters at 30 m and 55 m water depth. The scale has been rolled over beyond 360° T and means are taken over periods of 30 min with standard deviation indicated by the error bars.*

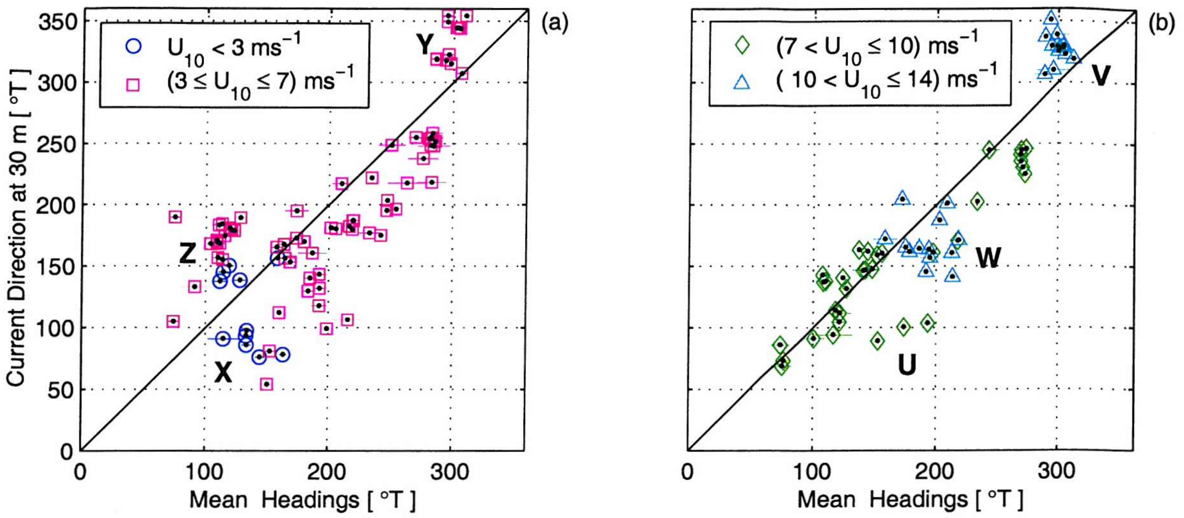

Fig. 5.7: *The mean alignment of ARIES II against the current direction measured at a depth of 30 m for several different wind conditions. (a) low wind; (b) high wind. The direction of ARIES II has been corrected to follow that corresponding to the convention for the current direction (the bearing that the current is moving towards; see also section 4.1). Headings based on means taken over periods of 5 min, selected from brief recording periods in the absence of internal waves. These data include all the 2 h and 4 h records spreading over* $(17-30)^{th}$ *August 1995.*

and current directions about 325°T (label V). (2) The possibility of different events registered by ARIES II and the 30 m current meter, suggested from the comparison of measurements of the temperature sensor of ARIES II with those corresponding to the 55 m current meter. We have identified, for example, periods where the temperature remained constant at about 15°C at the ARIES II depth, while the temperature at 55 m shown evidence of internal waves. Illustrative group of points have (170 – 230)°T headings and current directions about 150°T in Fig. 5.7b (label W), and the group of points with $(3 \leq \mathcal{U}_{10} \leq 7)$ ms^{-1} wind speed shown in Fig. 5.7a (label Z) with headings in the range (75 – 120)°T and current directions about 180°T.

The cause of the scatter of other points is not quite apparent and might depend upon the capability of ARIES II for aligning under currents with different speeds. One would expect, therefore, a much better alignment with relatively large currents (see section 5.2). For this reason, the scatter between ARIES IIs' headings and current meter directions was reordered for current speeds ranging from 40 cms^{-1} to the maximum speed found in the particular data set (75 cms^{-1}). A slight improvement was achieved, however, giving a rms of 19°.

An additional comparison has been pursued by selecting headings where the temperature remained roughly constant during periods of 30 min occurring just before the

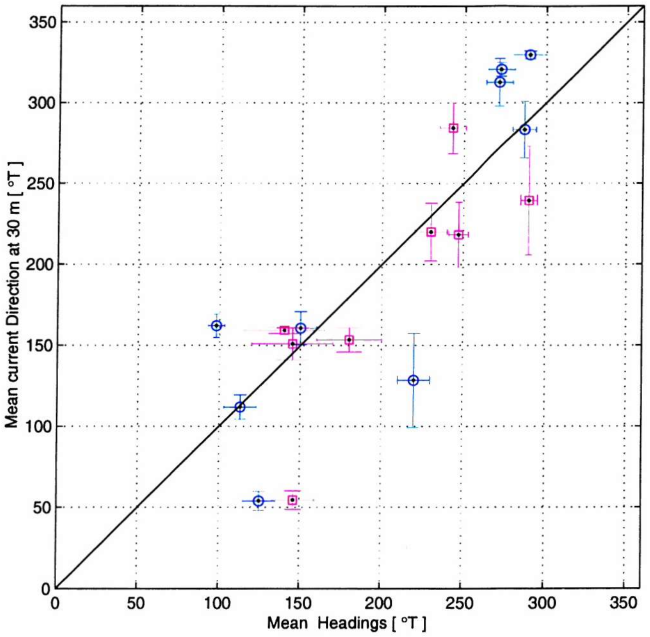

Fig. 5.8: *The alignment of ARIES II with 30 m currents on the eve of non-linear internal waves. Points marked with a ○-symbol indicate spring tides (rms is 36°), whilst those showing a □-symbol correspond to neap tides (rms is 30°). The direction of ARIES II is as for Fig. 5.7. Mean headings and current directions were taken over periods of 30 min, whilst vertical excursions of ARIES II during these periods were less than* ±0.4 m.

arrival of the leading wave of packets of ISWs or before the presence of temperature fluctuations of O(0.5°C) that may precede the passage of the waves. The few points almost matching the ideal straight line in Fig. 5.8 are coincident with current speeds less than 36 cms^{-1} and a combination of calm or strong (> 7 ms^{-1}) winds. The alignment of ARIES II during this short-time periods is within (6 ± 4)°T from the current direction. It appears, therefore, that the scatter of points is not necessarily caused by the action of weak currents and/or low wind speeds or by tidal effects when currents change direction from the ebbing to flood tide and vice versa. Most of the large variability observed in the error bars of current directions is linked to clockwise or anticlockwise rotations of the order of 40° in 30 min. Even though a plausible explanation is that the presence of residual rotary currents (see section 4.3.3) cause ARIES II and the 30 m current meter to register different events, such currents may also bring ARIES II into or out of alignment with mean currents.

The fact that Fig. 5.8 shows a few points aligned with mean currents appears to imply that the dynamics taking place in the ARIES II site is causing the scatter of points. Nevertheless, the rms of the best alignment obtained was of only 19° and the lack of better alignment might well be an indication of imperfections in the construction or assemblage of the streamlined instrument. It follows that if the dynamics are insufficient to explain the misalignment between ARIES II and mean currents, then attention must be directed towards instrument failure (e.g. an increasing drag). Therefore it is suggested that vortices or eddies shedding from the fin are the most likely source of both lateral forces and the continuous lateral swinging of the streamlined instrument. For example, the source of vortex shedding on both sides of ARIES II might occur in different positions leading to transverse motions, perhaps oscillatory. In the course of time the transverse motions might potentially evolve in a whole shaking motion, namely port-starboard and fore-aft tilts and variations in headings.

Mean fore-aft and port-starboard tilts are of about 5° and 1° respectively, with variations not induced by internal waves of less than 1° for both tilts. This is consistent with the typical position of ARIES II which can be observed in Fig. 5.3a and 5.4c. Mean fore-aft and sideways tilts for all the 13-hour records (averaged over 1 min and coincident with spring tides) are, respectively, $(5.1 \pm 0.2)^\circ$ and $(1.0 \pm 0.7)^\circ$. Larger tilts ($> 4^\circ$) are produced by non-linear internal waves and show a significant effect in the port-starboard inclinometer $(-7.0 \pm 1.5)^\circ$. As a matter of comparison, Thorpe and Baldwin (1995) have reported a fore-aft angle of $(7.0 \pm 0.5)^\circ$ and a corresponding port-starboard tilt of $(-9.0 \pm 3.0)^\circ$ apparently caused by a mooring rope during a trial in 4 m water depth (see also section 5.1). The ARIES II steadiness to fore-aft motions probably reflects its positive buoyancy and weight distribution, and weak vertical currents. But the continuous lateral swinging may in turn be affecting the capability of ARIES II to a better alignment with currents by retarding the time response of the fin to a changing flow (section 5.2). If the sideways tilts are avoiding the instrument to orientate properly into the flow, then its cross-sectional area might increase which reinforces the significance of the drag force since a lift force is independent of the instrument cross-section. Maximal fluctuations linked to the knocking down of the mooring line are further analysed in sections 5.5 and 5.6.

Apart from the above, one must bear in mind that under-sampled (30 m) current meter directions are not the best source of comparison with high-resolution headings. More importantly, however, is that suggestions based only upon descriptive data analyses are speculative. Further future theoretical-based or numerical-based analytical research and additional field or laboratory tests are therefore needed to demonstrate or invalidate all the suggestions made so far.

5.3.2 The alignment of ARIES II into internal wave flows

Since the ARIES II deployment site is a zone of intense internal wave activity (see section 4.3), it is important to assess the instrument's ability to respond to flows induced by non-linear internal waves. The speed and direction of propagation of internal waves can be estimated from the wave-induced fluctuations about a mean current (i.e. the relative current) recorded by the current meters at 30 m and 55 m water depth. This is possible because if the Earth's rotation can be ignored, then the horizontal wave-induced flows are generally aligned in the direction of wave propagation. Therefore, at the time of the passage of soliton-type waves, it is likely that the relative current is induced by the internal wave flows in a direction consistent with the wave propagation. To this end, the internal wave direction is estimated from the current meter mooring following a simple method. First mean velocities at 30 m water depth are obtained from 3 h current recordings just before the ISWs arrive at the current meter mooring and then internal wave-induced fluctuations are localised using the 55 m temperature record to register the corresponding velocity at the wave trough at a depth of 30 m. The speed and direction of the relative current is therefore estimated from the mean current and the internal wave-induced velocity fluctuation at the wave trough. Two sources of error are present under this approach, namely the poor sample rate of currents and the estimation of the mean current. The first source refers to the position within the wave trough where a current meter sampling at a 10 min rate records the wave-induced fluctuation. For example, speed fluctuations less than 10 cms^{-1} may result in unusual directions (NW or WSW) of the relative current. The second source bears upon how to specify the mean current. For simplicity, currents measurements have not been smoothed, however we have selected periods of the 3 h recordings in which the current speed and direction varied within 10 cms^{-1} and 35°T respectively. The selection of these values is arbitrary and means have been taken over periods typically in the range $(0.7-2.0)$ h. A much better method to estimate the propagation of single internal wave packets is accessible from Hallock *et al.* (2000), however the method is more appropriate for current meter data with additional resolution (e.g. 1-2 min) and therefore was not pursued.

Time periods where both ARIES II and the 55 m current meter recorded the same internal wave events have been selected to estimate the relative current, and moreover, temperature fluctuations associated with pressure fluctuations larger than 0.4 m have not been considered at all. These periods correspond to spring tides ($(12-16)^{th}$ August 1995) and neap tides ($(19-22)^{nd}$ August 1995). No clear signatures of internal waves were registered by ARIES II during the spring tide period at the end of August 1995. The directions of the relative current are shown in Fig. 5.9 and represent the best estimations one can do with under-sampled current meter data. Most of the unusual directions (those in the range $(90-270)°$ in Fig. 5.9) occurred during spring tides. In principle, this is attributed to the method utilised rather than physical reasons. It is valid, however, to question whether the directions of the relative current are associated

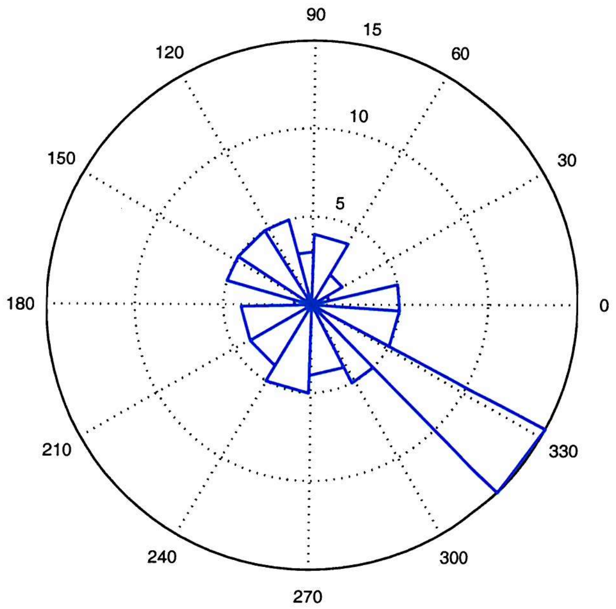

Fig. 5.9: *Histogram in polar coordinates indicating the direction of the relative current inferred from the current meter mooring during spring and neap tides. True North directions have been converted into angles relative to the origin starting from* 0° *along the x-axis. The numbers over consecutive concentric circles show the number of values falling within groups of* 22.5°.

with internal wave flows, show the influence of shear, tidal or non-tidal residual flows (e.g. Burrows *et al.*, 1999) or indicate the presence of strong curving internal wave fronts (e.g. Small, 2001).

The histogram does not follow a normal distribution and therefore it is not possible to estimate means with confidence intervals. During the neap tide, however, the mean direction is $(146 \pm 45)^\circ$T which matches the range of internal wave directions reported by Small *et al.* (1999) for this tidal period (see section 4.3).

The orientation of ARIES II in relation to the direction of the relative current is now assessed. We have examined directions in the general range (i.e. $(0 - 180)^\circ$T) estimated by Oikonomou (1997) and unusual directions showing some consistency with the orientation of ARIES II. The scatter of points obtained has a rms of 45° for spring tides and a rms of 84° for neap tides. It is probably better to observe the scatter of points in terms of differences between the direction of the relative current and the orientation of ARIES II (Fig. 5.10a). It is interesting that ARIES II shows alignment with unusual directions of the relative current, represented by the group of points between 300°T and 350°T and differences less than 20°T (marked X in Fig. 5.10a). Points with relatively large error bars are associated with directions of mean currents gradually increasing with time and relatively fluctuating speeds. This is probably caused by the influence of the tidal ellipse, rotary currents or shear on mean currents. It is also possible, therefore,

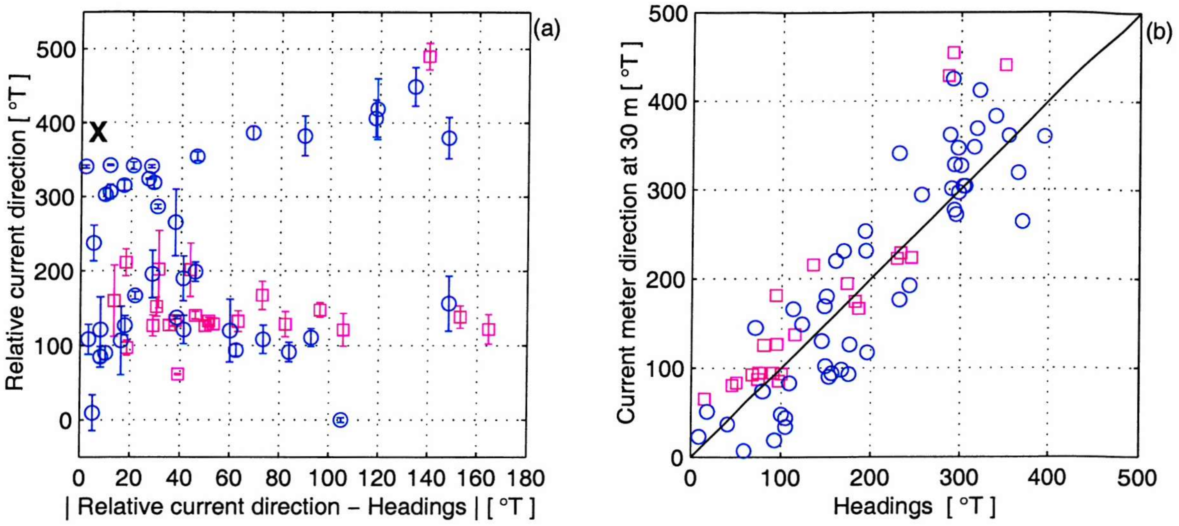

Fig. 5.10: *(a) The direction of the relative current at a depth of 30 m against the difference between this direction and the orientation (headings) of ARIES II at the trough of non-linear internal waves. (b) The direction of the 30 m current meter against the headings at about 35 m, both measured at the internal wave trough, for all data included in Fig. 5.9. The rms scatter of points is of about 40° for spring tides and about 42° for neap tides. Symbols for spring and neap tides are defined in Fig. 5.8. Headings have been converted to follow the current direction as in Fig. 5.7 and the scale is rolled over beyond 360°.*

that the estimation of the relative current shows these effects.

Since the scatter of points for the orientation of ARIES II with the relative current is large, we have also examined the orientation of ARIES II and the current meter direction at the time of the passage of non-linear internal waves (Fig. 5.10b). There is no substantial decrease in the scatter of points. Such a scatter may only show the effect of an un-calibrated compass or electromagnetic interference, meaning that ARIES II indeed aligns within a few degrees to internal wave flows but with this response not registered properly by the compass. However, the large scatter may also indicate that the general alignment of the streamlined instrument was not good.

There are two options to pursue concerning the quantification of organised motions from acoustic images. The first option consists of the assessment of the capability of ARIES II to align into mean and internal wave flows, in which one has to demonstrate that the alignment of the streamlined instrument is consistent with known directions of currents and waves. Although the general rms scatter of points is relatively large ($\approx$ 30°), figures 5.7-5.8 and 5.10 show individual points where ARIES II indeed aligns with flows caused by mean currents and internal waves during both spring and neap tides. It is possible, therefore, to select particular periods for acoustic images to analyse. A

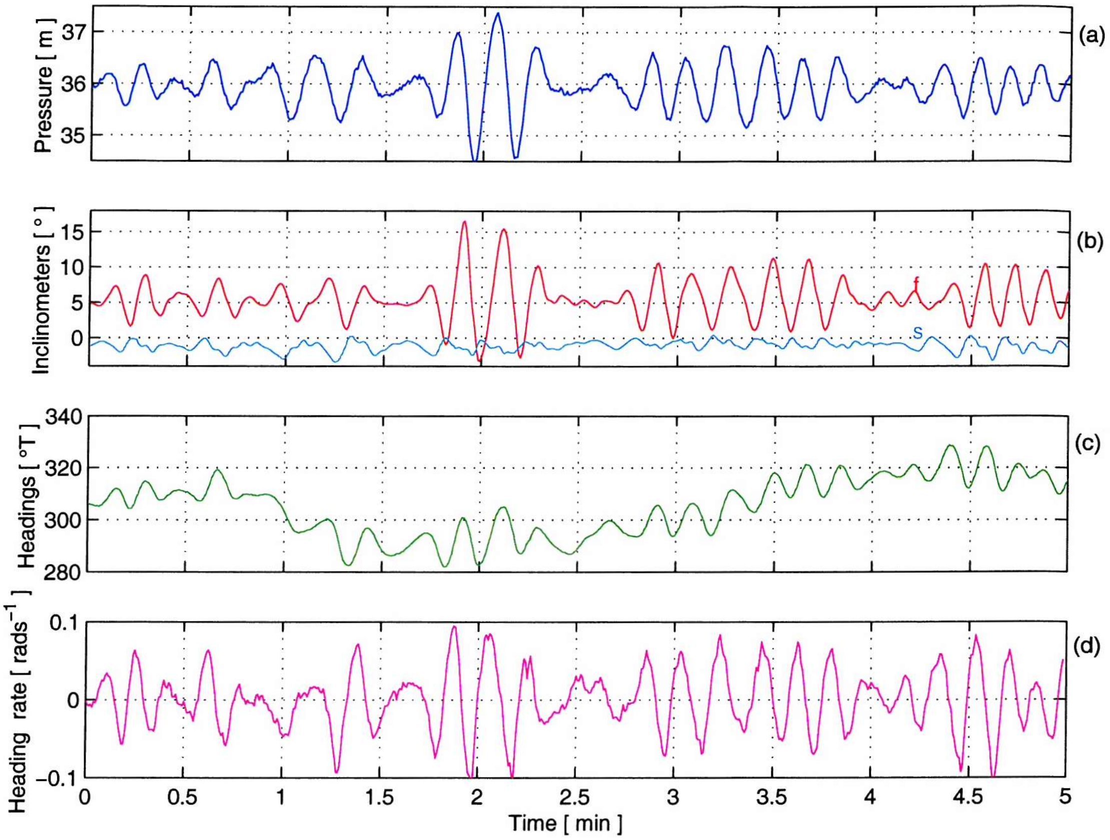

Fig. 5.11: *The effects of surface waves on ARIES II sensors. (a) Pressure at the level of the sonar transducers; (b) Inclinometers. Labels defined in Fig. 5.2; (c) Headings, indicating the direction in which the streamlined instrument is pointing (i.e. contrary to the direction of currents); and (d) The rate at which ARIES II is rotating (see caption in Fig. 5.5). Values of* $\mathcal{U}_{10}$ *and wind direction are, in respective order,* (15.3 ± 0.1) ms^{-1} *and* $(51 \pm 13)°T$. *Currents at 30 m have a speed of* (41.4 ± 1.2) cms^{-1} *towards* $(205 \pm 5)°T$. *The records start at 6:42 GMT on 25th August 1995 (see Table 4.1).*

second option is to reject these results and give confidence to the streamlined instrument because of the poor sampling rate of currents, which affects in particular the estimation of the relative current. The reliability of quantitatives obtained from acoustic images and of ARIES II itself, therefore, will depend upon their consistency with the known physics of processes occurring in the UOBL. A consequent extension would be the utilisation of ARIES II for inferring interactions among different organised motions. Both options, however, are disadvantageous in the sense of an un-calibrated compass and magnetic interference. What arises here is uncertainty about the capability of ARIES II to provide reliable information, which points to the need for additional future research in the field and under controlled conditions.

5.3.3 The effect of surface waves

The effects of surface waves on ARIES II during high-wind conditions are illustrated in Fig. 5.11 and 5.12 which correspond to, respectively, the maximal wind speeds recorded by the meteorological buoy and the DERA ship when ARIES II was operating.

Fig. 5.11a shows clearly oscillations at swell and wave group frequencies. The period of swell is roughly 12.0 s, which has been estimated by following the zero-up crossing method (e.g. Bowden, 1983). The dispersion relationship for surface waves is, according to linear theory (e.g. Kinsman, 1965), $\omega^2 = gk\tanh(kh)$. For deep-water waves ($kh \gg 1$), $\tan(kh) \approx 1$ and the wavelength derived from the dispersion relationship is $\lambda = \frac{g}{2\pi}T^2$. The corresponding wavelength for a zero-up crossing period of 12.0 s is therefore 224.6 m and $\frac{h}{\lambda} = \frac{146.0\ \mathrm{m}}{224.5\ \mathrm{m}} = 0.650$. For $\frac{h}{\lambda} > 0.250$, the deep-water approximation gives a 5% error and the differences between the zero-up crossing and zero-down crossing methods are not significant (Horikawa, 1988). The wave amplitude of surface waves is estimated from the amplitude of the oscillation recorded by the pressure sensor (Δp) assuming, first, that the vertical excursions of ARIES II caused by individual waves can be neglected in comparison with the wave amplitude and, second, that waves are of small amplitude (i.e. $\mathbb{A} < \lambda$). To a first approximation, the pressure fluctuations caused by deep-water waves are $\Delta p_1 = \rho g \mathbb{A} \exp(-kh)$ where $\rho = 1026.6\ \mathrm{kgm}^{-3}$ (see Fig. 4.7) and the depth of ARIES II at the transducers level, h, is 34.60 m (see section 4.1). Pressure fluctuations are expressed in m (see equation (3.1)) and a conversion to Pa is done assuming 1 m $\approx$ 0.1bar, that is, 10^4 Pa. The maximal pressure fluctuation shown in Fig. 5.11a, which is of about 1.4 m, is caused by wave groups and corresponds to a surface wave amplitude of 3.7 m, which is consistent with waves of small amplitude. Fluctuations caused by swell and wave groups are also visible in the inclinometer, heading and heading rate records (Fig. 5.11b-d), although with a slight phase change among them and with respect to the pressure record. This change of phase may reflect the effect of horizontal currents induced by surface waves on the sensors, rather than any instability of the streamlined instrument (Thorpe *et al.*, 1998) or forcing from the mooring line from which it is tethered, however, magnetic interference might also be a valid cause (see section 3.2). The largest tilt amplitude of about 10° is produced by the passage of a wave group (see also sections 5.1 and 5.3.1 for comparison); lateral tilts down to starboard are coincident with forward-up tilts. Further, the heading variation observed between 1 min and 3 min into Fig. 5.11c is coincident with a 0.3°C temperature fluctuation (not shown) producing a 0.04 m vertical excursion of ARIES II. Since the record starts 7 min before the arrival of a non-linear internal wave with an amplitude of about 24 m, the temperature fluctuation is perhaps induced by the presence of this non-linear wave. Notice that wind and currents are aligned within 26°, roughly towards southwest, whilst the instrument headings imply currents spread to

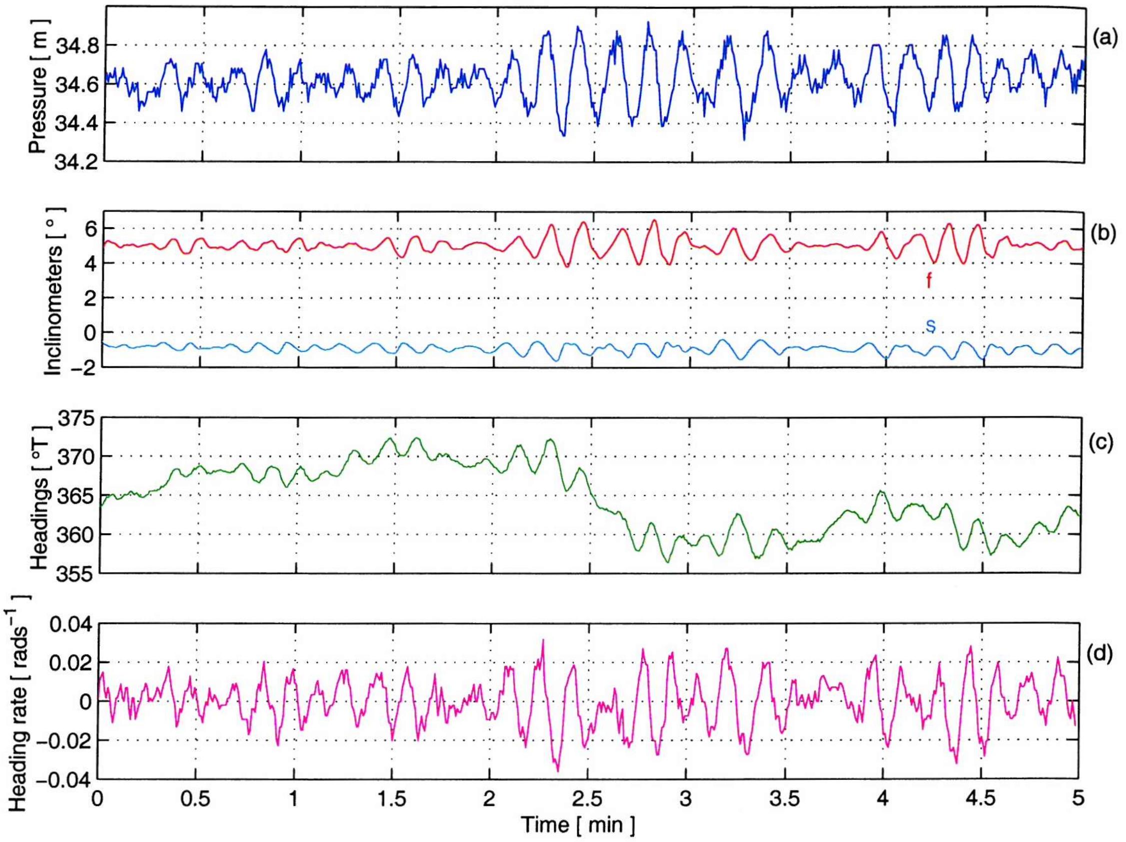

Fig. 5.12: *As Fig. 5.11, except that records start at 17:55 GMT on 16th August 1995,* $\mathcal{U}_{10} = 22.4 \pm 1.4$ *ms*$^{-1}$*, wind direction is from* $(278 \pm 3)°T$ *and currents at 30 m have a speed of* (14.9 ± 2.4) *cms*$^{-1}$ *towards* $(145 \pm 2)°T$*. The heading scale is rolled over beyond* $360°T$ *for convenience. A mean position for the DERA ship at this time is* $56°47'12''$ *N,* $8°40'20''$ *W, that is about 41 km from the ARIES II site.*

southeasterly regions.

Although Fig. 5.12a is coincident with a wind speed of 22.4 ms^{-1}, the maximal pressure fluctuation is of only about 0.3 m. A surface wave amplitude of 1.7 m results from a swell zero-up crossing period of roughly 9.0 s (λ = 126.3 m). This suggests that horizontal gradients of the wind stress are probably important in the study site and therefore wind data obtained from the DERA ship should be taken with caution. Fig. 5.12a shows, in addition, small fluctuations in the range $(0.02 - 0.17)$ m occurring over periods of 0.5 s. Particle displacements caused by the wave-induced pressures can also be estimated by integrating the vertical velocity. For deep-water waves the maximal vertical displacements are $\Delta z = \mathbb{A}\exp(-kh)$, that is 0.3 m or 18% of the surface value. Therefore, it is unlikely that these fluctuations might indicate effects of surface waves because of their exponential attenuation with depth, but the waves are not exactly linear and second-order effects are possible. To a second order approximation, pressure fluctuations for deep-water waves are given by (e.g. Bowden, 1983), $\Delta p_2 = \frac{1}{2}\rho g k \mathbb{A}^2 \exp(-2kh)$. Thus for the wave amplitude, zero-up crossing period and wavelength referred to above, $\Delta p_2 \approx 0.002$ m, a negligible contribution lying outside the preceding range. Port-starboard and fore-aft tilts represent another possibility for the origin of these pressure fluctuations, however, a correlation between Fig. 5.12a and 5.12b is not observed. There is also the possibility that background shear acting upon the tension of the mooring line connecting the buoyancy sphere with the ARIES II attachment point (see Fig. 4.1) operates against the positive buoyancy of the instrument to induce vertical motions. Perhaps vibrations of the mooring line, like those resulting by vortices shedding from the cable or from the body of the streamlined instrument itself, or vertical excursions associated with the barotropic tide (see section 5.5) may account for the pressure fluctuations. However, since the fluctuations themselves are consecutive values recorded at the sample rate, it is most likely that they represent noise only (see also section 3.2). Fig. 5.12a-c also show a slight phase change (about 1 s), and minor fluctuations in Fig. 5.12d result from the centred finite-differences discretisation. This 1 s phase change might represent the time response of fore-aft tilts to pressure fluctuations caused by surface waves. The orientation of ARIES II is also misaligned with both wind and currents.

5.4 Temperature variations caused by the tilting of the mooring line

Apart from Fig. 5.2c, the temperature records associated with ISWs shown up until now have been limited to records in which the vertical excursions of ARIES II (estimated directly from the pressure records) are less than 0.5 m. Fig. 5.13 displays in particular the registered maximal vertical excursion (see also section 5.1). This is an important piece of evidence showing that some of the temperature variation is affected by the tilting of the mooring line from a position of equilibrium owing to relatively strong orbital speeds. Consequently, the aim of this section is to test whether a correction for the temperature can be provided at all. To this purpose, it is assumed that ARIES II does not exchange heat with the surrounding water and retains a fixed temperature when it experiences a change of depth by the passage of ISWs. The instantaneous temperature measured, T, is therefore $T = T(p)$ with changes given by,

$$dT = \frac{\partial T}{\partial p} dp, \tag{5.1}$$

where $\frac{\partial T}{\partial p}$, in °C m^{-1}, represents a temporal median of the local change in temperature per unit change in pressure occurring during the vertical displacement (e.g. Apel,

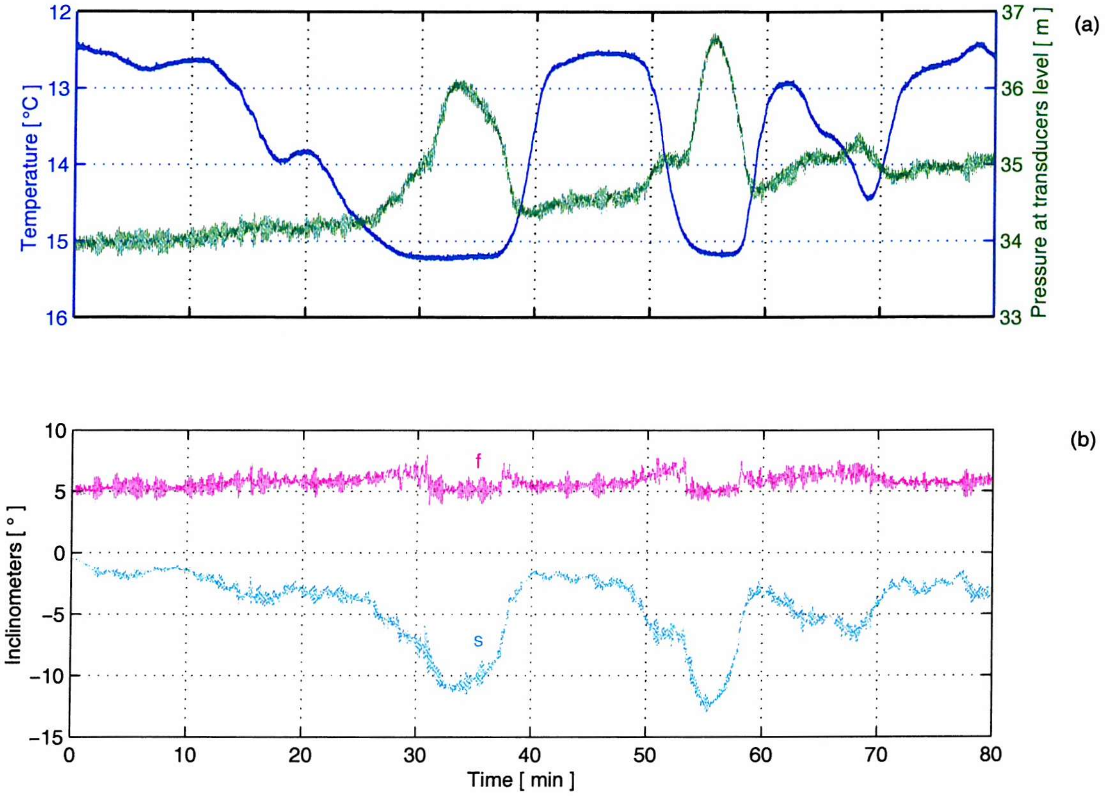

Fig. 5.13: *The vertical excursion of the streamlined instrument caused by the knocking-down of the mooring line in response to a non-linear internal wave packet. (a) Temperature (thick solid line) with the scale inverted, and pressure (thin solid line); (b) Inclinometers (labels defined in Fig. 5.2). The amplitudes of the rank ordered wave packet of depression are 17.5 m, 16.0 m and 10.0 m, respectively. Mean wind speed and direction are* $\mathcal{U}_{10} = 7.9 \pm 0.8$ *ms*$^{-1}$ *and* $(328 \pm 31)^\circ T$, *while currents at 30 m have a speed of* (47.0 ± 6.0) *cms*$^{-1}$ *towards* $(94 \pm 17)^\circ T$. *The record starts at 14:32 GMT on 28th August 1995.*

1987). This is easily estimated from ARIES II sensors using, for example, centred finite-differences. In the absence of internal waves $\frac{\partial T}{\partial p}$ is generally negative. Here, temperature and pressure are defined as $T = T_c + \Delta T$ and $p = \overline{p} + \Delta p$, where T_c stands for a non-spurious or mean temperature signal, $\overline{p}$ is a mean pressure and both ΔT and Δp describe temperature and pressure variations during the presence of internal waves. Following equation (5.1), a corrected temperature (T_c) is estimated as,

$$T_c = T - (p - \overline{p}) \frac{\partial T}{\partial p}. \tag{5.2}$$

When the mooring line maintains a vertical position as internal waves are passing by, then $\Delta p = 0$. When the mooring line is being knocked-down, $\Delta p > 0$ and $\frac{\partial T}{\partial p} > 0$; if on the other hand the mooring line is being knocked-up, $\Delta p < 0$ but $\frac{\partial T}{\partial p} > 0$. However,

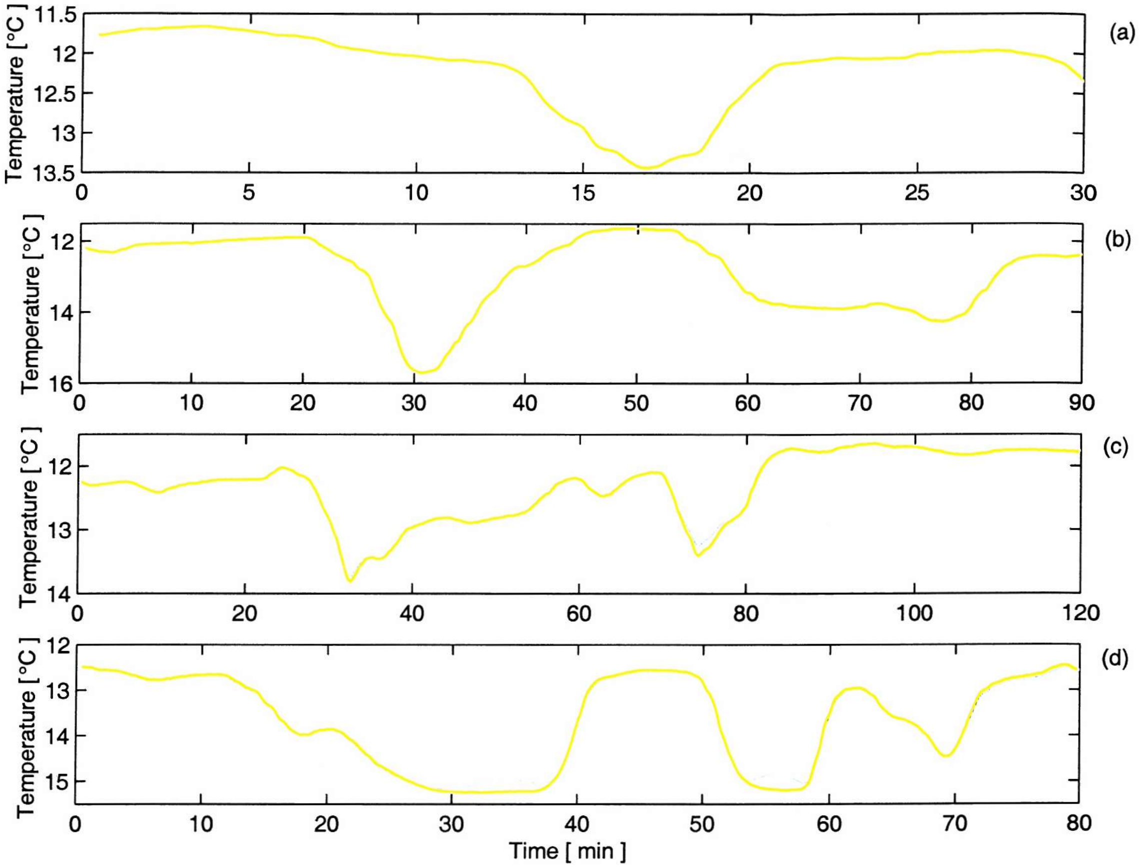

Fig. 5.14: *Non-corrected temperature (thick solid line) and corrected temperature (thin solid line) for single and packets of non-linear internal waves. Dates and starting hours for each record, in respective order, are as follows: (a) 16th August 1995, 09:10 GMT; (b) 20th August 1995, 16:53 GMT (see also Fig. 4.4b and 7.15); (c) 13th August 1995, 15:40 GMT (see also Fig. 5.2c); and (d) 28th August 1995, 14:32 GMT (see also Fig. 5.13). Notice that the abscissa represents a different time scale for each day and the vertical scale increases downwards.*

if the mooring line is slightly knocked-down before the internal waves arrive (e.g. tidal effects), then $\frac{\partial T}{\partial p}$ may become negative during the passage of the waves.

Temperature and pressure have been low-pass filtered, with a cut-off frequency of 60^{-1} Hz, in order to attenuate variations owing to surface waves and possible instrumental noise (see section 5.2). Fig. 5.14 shows the corrected temperature for several different days in both neap and spring tides. Values for $\frac{\partial T}{\partial p}$ (°C m^{-1}) utilised for Fig. 5.14a and 5.14b in respective order are -0.19 and -0.11, whilst for Fig. 5.14c and 5.14d are 0.11 and 0.21 respectively. What Fig. 5.14 suggests is that the estimations of the wave amplitudes are not significantly affected by the tilting of the mooring line.

Deep internal tide troughs composed of apparently two different waves (i.e double temperature maxima) have been observed at spring tides by Pingree (1984) and Pingree and New (1995). The troughs formed when the tide was streaming off-shelf and propagated on-shelf against a component of the tidal current opposite to the internal tide propagation. This effect, known as barotropic tidal distortion (Pingree and New, 1995), produces a notorious steepening of the internal tide. When the tidal currents exceed the maximal shoreward propagation speed of the internal tidal waves, a wave trough measured in a mooring position may be advected back to be measured for second time during a single tidal cycle, thereby becoming a trough with double temperature maxima. A correction for the shape of the wave was developed by Pingree and New (1995) assuming linear internal tides without rotation. These temperature variations, on the other hand, may also reflect the influence of rotation on non-linear internal tides (Gerkema and Zimmerman, 1995).

As already mentioned in section 4.3.2, ARIES II has measured temperature variations with double and triple maxima associated with ISWs. Possible physical reasons which may explain these maxima are: wave packets crossing from different directions (e.g. Fig. 4.3), shear instability limiting the wave amplitude and subsequent breaking, barotropic tidal distortion and near inertial oscillations increasing the variability in measurements of temperature (Pingree and New, 1995), and effects of Earth's rotation on the wave amplitude distribution (Gerkema and Zimmerman, 1995). Utilising equation (5.2), tests were performed to assess to what extent such kind of temperature variations are spurious in the sense of reflecting the tilting of the mooring line. Although not shown, results are similar to those illustrated in Fig. 5.14 indicating that the variations are probably not caused by the motions of the instrument's mooring.

5.5 The tilting of ARIES II from the mooring attachment point

Packwood (1995) estimated the tilt of the instrument from a vertical attitude using a moment equation about the ARIES II mooring attachment point with drag forces centred at the middle of the upper buoyancy unit, D_1, and at the centre of the frame, D_2 (see Fig. 3.1 for reference). It is given by,

$$\theta = \arctan\left(\frac{8.58 + 1.56D_1 + 0.65D_2}{189.3}\right). \tag{5.3}$$

where θ is the tilt angle from vertical. For a vertically uniform design current with a magnitude of 0.575 ms^{-1} the tilt angle is 7.8° (with $D_1 = 5.6$ Kgf and $D_2 = 13.5$ Kgf); during no-flow conditions the tilt angle is 2.6° (Packwood, 1995). Further, when the shape of the mooring and tensions in the line are taking into account, Packwood (1995) has also estimated a tilt angle of 16° using a mooring/towed body analysis programme (Fig. 5.15).

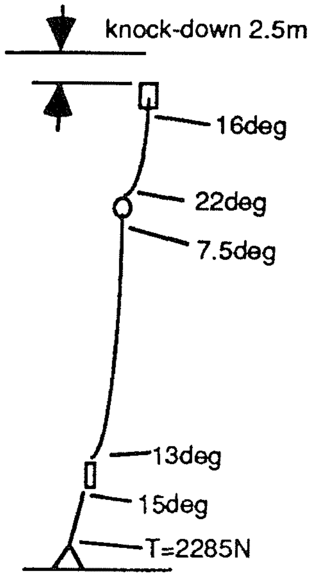

Fig. 5.15: *Deviations of the mooring line from the vertical for design conditions of a uniform current at 0.575 ms^{-1}. The corresponding vertical excursion of the instrument has been labelled 'knock-down', whilst the tension at the anchor is labelled 'T'. (Taken from Packwood, 1995).*

In order to apply equation (5.3) to ARIES II using the available data, a uniform velocity is obtained from a depth-weighted mean barotropic current, $\overline{U}$, as follows:

$$\overline{U} = \frac{36.5U_1 \ + 21U_2 \ + 92.5U_3}{150}. \tag{5.4}$$

where U_1, U_2 and U_3 indicate the current meters as described in section 4.1. Effects of viscosity on the current (e.g. in the bottom boundary layer) are ignored in equation (5.4). The drag force, in Kgf, is defined as $\frac{\rho_o A_s C_d}{2g}\ \overline{U}^2$ where A_s is the cross-sectional area of the instrument and C_d is the dimensionless drag coefficient. Following Packwood (1995), we use $A_s C_d = 0.35$ m^2 for D_1 (where $C_d = 1$ for the buoyancy component), and $A_s C_d = 0.78$ m^2 for D_2 (where $C_d = 1.2$, 1.55 and 1.2 for the instrument tubes, square section and round section, respectively), but with $\rho_o = 1026.6$ Kgm^{-3}.

When the mooring line is pulled from the vertical by currents, the streamlined instrument will experience both horizontal and vertical excursions. The horizontal excursion is $C_a \sin\theta$, where C_a is the 21.9 m line connecting the buoyancy sphere with the instrument at the level of sonar transducers (Fig. 4.1), whilst the vertical excursion, V_e, is

$$V_e = C_a \sin\theta \tan\theta. \tag{5.5}$$

The variation of the tilt angle during the measurements period follows the pattern of currents (e.g. Fig. 5.18) with a maximum of 6.68° in spring tides corresponding to 0.30 m of vertical excursion. For a mean tilt angle of 3.4° the vertical excursion is 0.08 m, which is within the range of the small pressure variations observed in Fig. 5.12a.

We now proceed to test whether equation (5.3) can be utilised to explain particular measurements during the propagation of ISWs. Consider a situation in which ARIES II has been severely knocked-down; it is illustrated from 8 to 10 hours into Fig. 5.2, but since ARIES II remained aligned within $(-3.6 \pm 27)^\circ$T of the 30 m current direction for about 4 hours, a period from 8 to 12 hours is selected. This alignment is however affected by the poor sampling rate of the current meter. ARIES II headings were low-pass filtered with a cut-off frequency of $5.55 \text{ X } 10^{-3}$ Hz, averaged over 10 min periods and corrected to follow the convention for current directions. The component of the (30 m) current parallel to the streamlined instrument was utilised for calculating the drag force. Fig. 5.16 shows that the maximal tilt angle and vertical excursion during this period are 8.28° and 0.46 m, respectively. The estimated value for the tilt angle is consistent with the observed starboard tilt (section 5.1), whilst the underestimation of the vertical excursion suggests that a contribution from the tilting of the whole mooring line is lacking in the above estimation.

The inclinometers measure tilt of the instrument, which causes pressure variations and one can ask here, what is the mean value of these variations?. This is embarrassing to answer since the distance from the ARIES II attachment point to the pressure sensor is not known. In addition, the orientation of both pressure and temperature sensors with regard to the fore-aft axis of the frame is unknown (Hall, priv. comm., 1996). Nevertheless, the horizontal distance between pressure and temperature sensors is known for certain to be of 0.07 m. Following Packwood (1995), the attachment point of the instrument at the base frame is the rotation axis about which the frame pivots in azimuth. It is assumed that this point is on the same line as the central recording tube (see Fig. 3.1 for reference). Now the distance from the attachment point to the acoustics electronics tube is determined by the instrument chord divided by 4 (Packwood, 1995), which for ARIES II is of about 0.45 m. Assuming that the pressure sensor is aligned with the long axis of the frame and fitted farther forward, the distance of the attachment point to the sensor is of say 0.40 m. With reference to section 5.1, the maximal pressure variation caused by the fore-aft tilting of the instrument is therefore $0.40 \tan(2^\circ) = 0.01$ m, whilst that corresponding to the port-starboard tilting of ARIES H is $0.40 \tan(-8^\circ) = -0.06$ m. Consequently the 1.5 m pressure variation shown in Fig. 5.2 is not caused by the tilting of the streamlined instrument.

Another possibility is that of increasing drag because of the misalignment of ARIES II with currents (section 5.3.1). Variations in the normal pressure and tangential stress

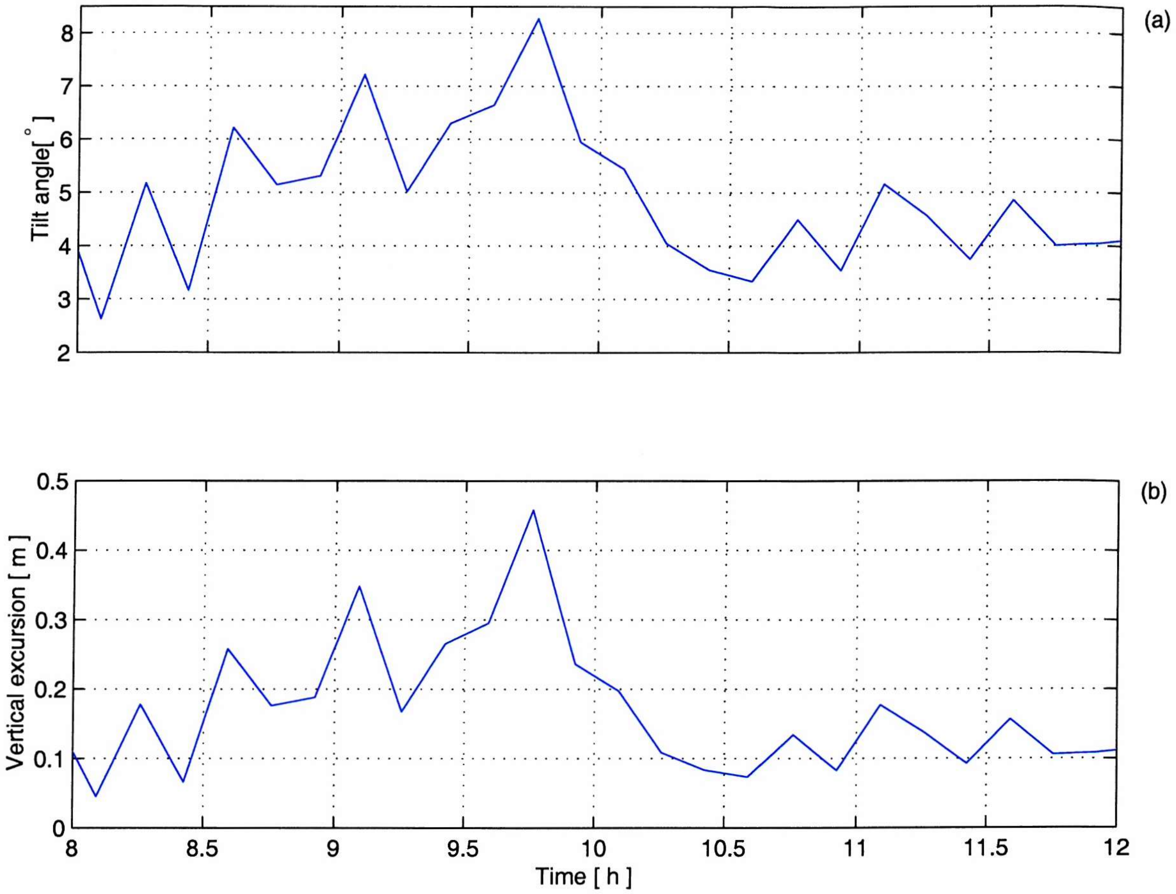

Fig. 5.16: *The migration of ARIES II from a vertical attitude where the time scale is consistent with Fig. 5.2. (a) The tilt angle ; (b) the vertical excursion of the instrument. Mean wind speed and direction are, in respective order,* $\mathcal{U}_{10} = 6.8 \pm 1.4\ ms^{-1}$ *and* $(286 \pm 11)°T$.

distributions on the surface, for example, or variations in the cross-sectional area of the instrument exposed to the flow may increase the instrument's drag. It is therefore pertinent to modify the drag coefficient in equation (5.3) to reproduce the observations. A vertical excursion of 1.5 m is obtained using $A_s C_d = 0.80\ \mathrm{m}^2$ for D_1 (where $C_d = 2.3$ for the buoyancy component) and $A_s C_d = 1.68\ \mathrm{m}^2$ for D_2 (where $C_d = 2.9$, for all the instrument tubes, square section and round section). However, this implies an overestimation of 81% of the tilt angle and a total C_d of 5.20 instead of 4.95 as utilised by Packwood (1995).

5.6 Vertical excursions caused by the tilting of the mooring line

Drag forces do not only act over ARIES II, but also on the buoyancy sphere and the whole mooring line (Fig. 4.1 and 5.17) preventing measurements from being obtained at a fixed vertical position or desired depth. ARIES II has been designed to experi-

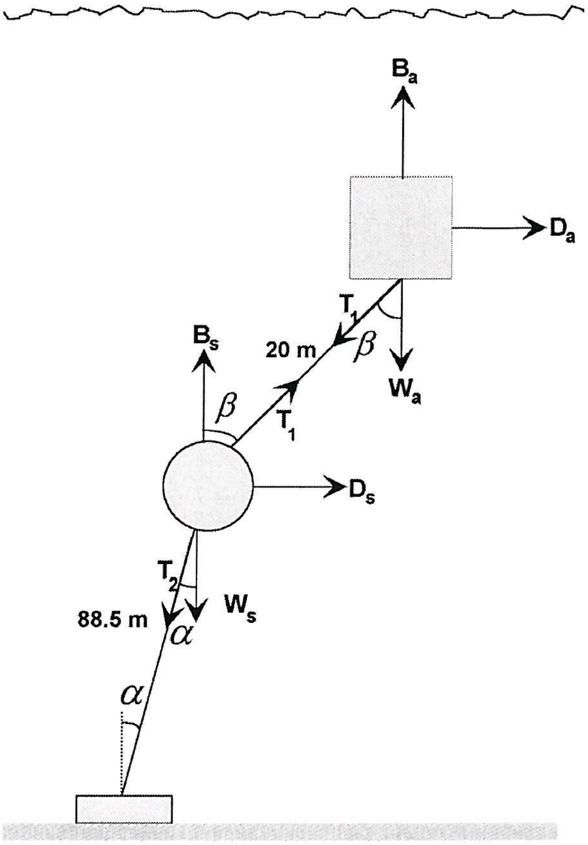

Fig. 5.17: Simplified diagram for the forces acting on the mooring system. Symbols defined in the text.

ence vertical excursions less than 5 m and vertical deviations less than 10°. Utilising a numerical programme, Packwood (1995) has derived the deviation of the mooring line from the vertical at various points and a vertical excursion of 2.5 m from design conditions as shown in Fig. 5.15.

An approximation to the knocking-down of the mooring line has been derived from simple force balance equations for the mooring system (Fig. 5.17). The tilt angles of the mooring are given by,

$$\alpha = \arctan\left(\frac{D_a + D_s}{U_a + U_s}\right), \tag{5.6}$$

$$\beta = \arctan\left(\frac{D_a}{U_a}\right). \tag{5.7}$$

where α and β denote the tilts at the anchor and buoyancy sphere attachment points respectively, D is the drag force, $U = B - W$ is the net upthrust, with B indicating the buoyancy and W the weight in water. The subscripts a and b denote, in the respective order, ARIES II and the sphere. Thus, in particular for ARIES II, $A_s C_d = 1.13$ m^2.

It is assumed that the cables in the mooring line are straight lines, that is without any catenary effects. Tension in cables and the effect of cable drag on the system are ignored. By fairing the cable with an extruded plastic cover, for example, would decrease the cable drag to produce a more streamlined profile. The effect of the surface (e.g. wave drag) is also disregarded. It is also assumed that ARIES II is rigidly joined to the mooring line, meaning that the tilt from vertical at the base frame (θ) is ignored.

The vertical excursion of ARIES II is,

$$\mathcal{V}_e = C_s \sin\alpha \tan\alpha \ + \ C_a \sin\beta \tan\beta. \tag{5.8}$$

where $C_a = 21.9$ m and $C_s = 89.5$ m relate, respectively, the length of lines connecting the buoyancy sphere with both ARIES II and the anchor; these values are including the height of ARIES II as well as the diameter of the steel sphere plus upper and lower attachment points, that is 1.0 m (Thorpe and Baldwin, 1995). The Reynolds number, for the design current and the deployed sphere, is $\frac{(0.575 \text{ ms}^{-1})(0.86 \text{ m})}{10^{-6} \text{ m}^2\text{s}^{-1}} \approx 5 \text{ x } 10^5$, corresponding to a drag coefficient of roughly 0.2. This coefficient is within the range of an abrupt fall in the experimental drag coefficient for spheres as the Reynolds number increases where the drag resulting from pressure forces is decreased and the corresponding drag exerted by shear stresses at the sphere's surface is increased. It is therefore expected that the transition of the laminar boundary layer into a turbulent one at the sphere is sensitive to irregularities in both the roughness of the surface itself and fluid motion. The maximum cross-sectional area in a plane normal to $\overline{U}$ is, for the buoyancy sphere, $(\pi)(0.43 \text{ m})^2 = 0.58$ m^2 and therefore $(A_s C_d)_s = 0.12$ m^2. In addition, $B_s = 186.0$ Kgf, $W_s = 86.0$ Kgf, $B_a = 142.8$ Kgf and $W_a = 58.8$ Kgf.

Fig. 5.18 shows the knocking-down of the mooring line during the period in which ARIES II remained operating at sea. It is estimated that maximal tilts and migration from vertical position occurred at 04:12 GMT on 12^{th} August 1995 with the following values: $\alpha = 5.0°$, $\beta = 9.9°$ and $\mathcal{V}_e = 1.3$ m; these values represent underestimations of those shown in Fig. 5.15. Also, no comparison is possible with ARIES II data because it started to operate at 08:32 GMT on 12^{th} August 1995. The maximal pressure variation recorded by the streamlined instrument during this day is associated with internal waves and was of 1.2 m at about 22:29 GMT, but in contrast Fig. 5.18c shows an estimated vertical excursion of 0.7 m. Again, these results suggest that the vertical excursion of ARIES II has contributions from the instrument's tilting from both the mooring line and the attachment point at the base frame.

In order to test whether equations (5.6-5.8) are able to explain the observation

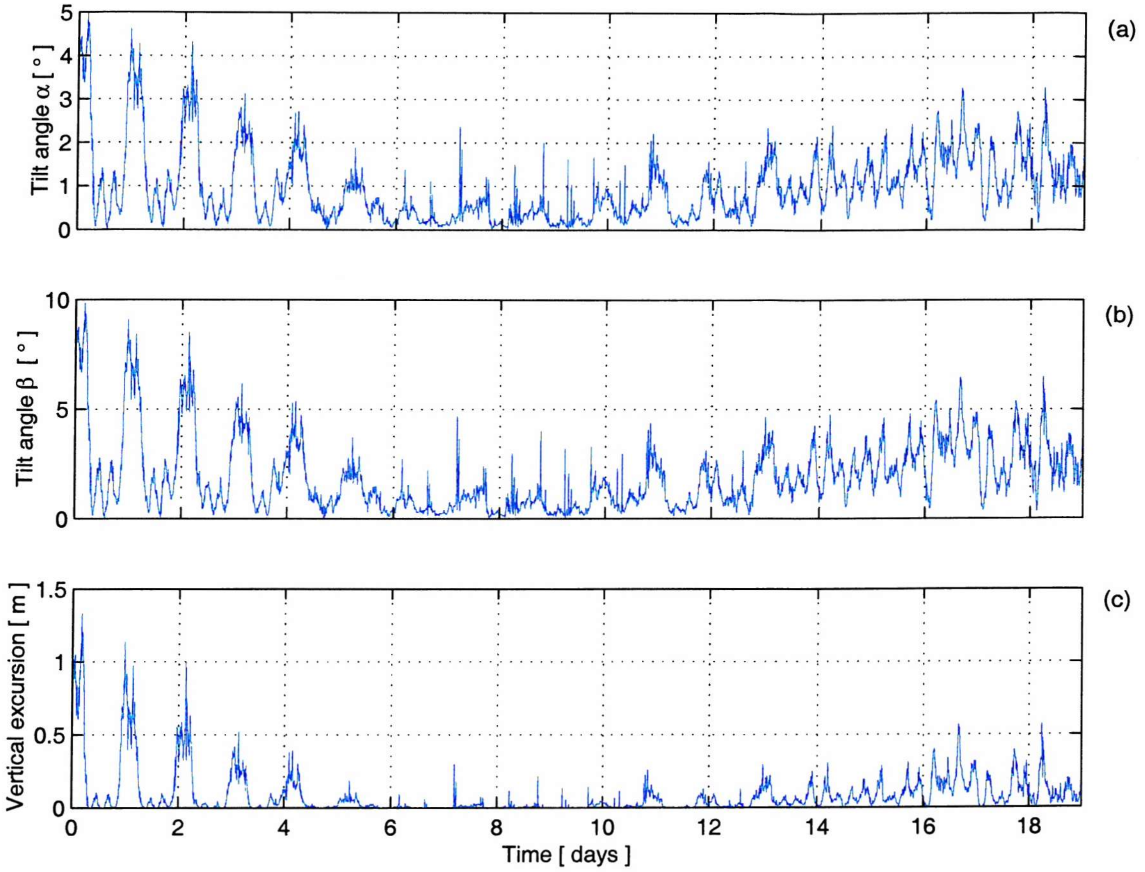

Fig. 5.18: The tilting of the mooring line caused by variations in the intensity of a vertically uniform depth-weighted mean current according to the force diagram shown in Fig. 5.17. (a) The tilting from the anchor attachment point; (b) the tilting from the buoyancy sphere's upper attachment point; and (c) the total vertical excursion experienced by ARIES II. The record starts at 00:02 GMT on 12th August 1995.

period considered in section 5.5 for Fig. 5.2, the component of the (30 m) current parallel to the streamlined instrument is utilised again for calculating the drag force on ARIES II. However, for the drag on the buoyance sphere, the following depth-weighted current is used: $\frac{21U_2 + 92.5U_3}{113.5}$. It is seen in Fig. 5.19 that maximal tilt angles are, $\alpha = 6.3°$ (corresponding to a vertical excursion of 1.1 m) and $\beta = 13.6°$ (corresponding to a vertical excursion of 1.2 m). The 2.3 m maximal excursion experienced by ARIES II clearly overestimates the 1.5 m excursion recorded by the pressure sensor, which is attributed to the assumptions implicit in equations (5.6-5.8). Interestingly enough the vertical excursion associated with the instrument's tilting at the base frame (0.46 m) added to the tilt from the buoyancy sphere attachment point (1.2 m) gives roughly the recorded pressure variation. If the tilt angle α is less than the estimated value, then it is possible that both the positive buoyancy and the low drag coefficient of the buoyancy

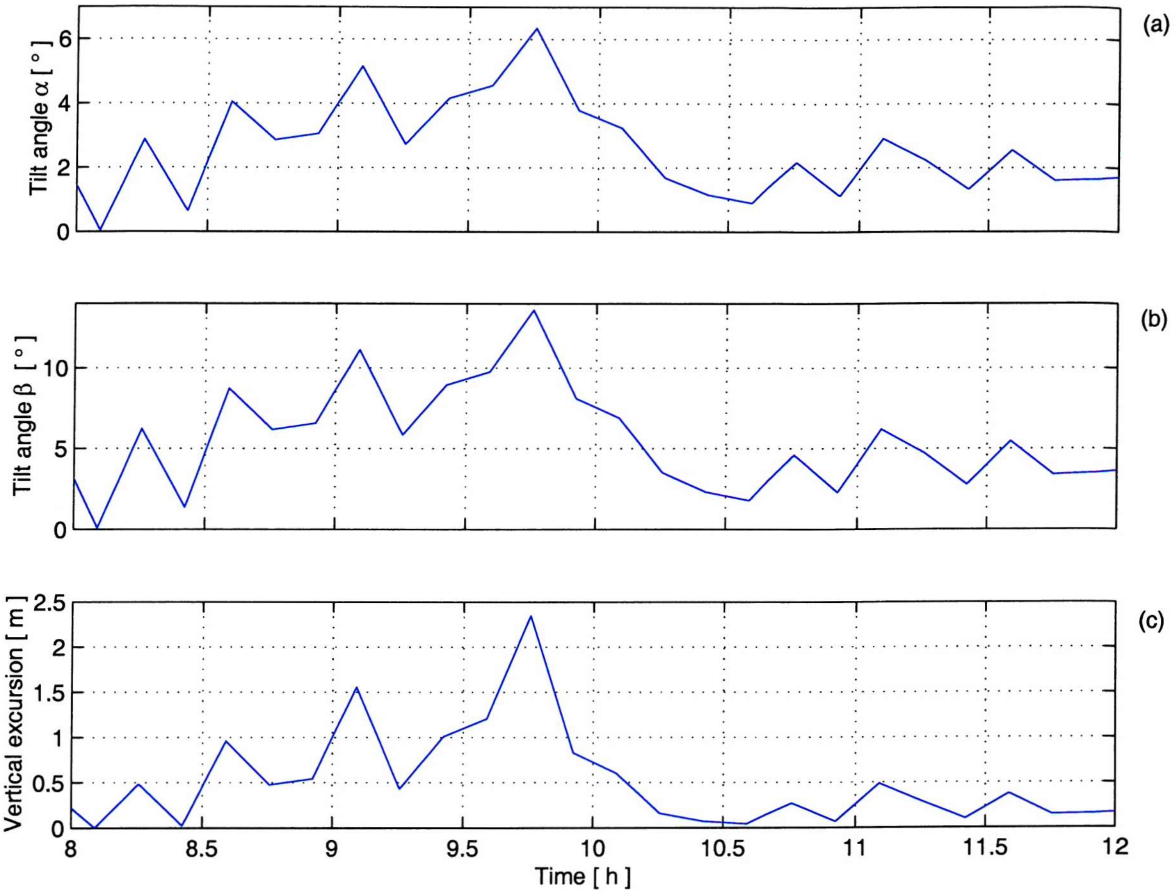

Fig. 5.19: *Idem to Fig. 5.18, but with a time scale consistent with Fig. 5.2 (see also Fig. 5.16 for comparison).*

sphere may reduce the effect of drag on the cable (i.e. the transmission of undesirable motions through the cable itself towards the sphere and ARIES II) to maintain tension in the mooring line, providing resistance to currents in the form of a stable taut mooring. However, there is no evidence to support this point because the ARIES II rig did not have any pressure sensor near the anchor. Furthermore, the pressure sensors on the Aanderaa current meters do not accurately reflect the position of these instruments in the water column, but do give an idea of rig stability (Hughes, priv. comm., 1996). This means that current meters maintain a vertical position when the cable above them deviates from vertical. Thus the 1.0 m and 2.0 m pressure variations recorded respectively by the 55 m and 140 m current meters during the period ranging from 9 to 10 h into Fig. 5.19, do not indicate vertical excursions. Therefore it might have been useless to install an additional pressure sensor on the ARIES II rig. Another point to consider is the drag coefficient for the buoyancy sphere whose selection is based upon a magnitude order for viscosity of 10^{-6} m^2s^{-1} since a local value is unknown. If the effect of the fluid viscosity is decreased by increasing the drag coefficient from 0.2 to

0.5, implying a Reynolds number of about 10^4, the maximal tilt angle α and associated vertical excursion will increase a factor of only 0.1° and 0.02 m respectively.

5.7 Summary

A summary of the main results is listed below.

- ARIES II has shown ability to respond to the motions produced by wind-sea [(0.1882-0.3106) Hz], swell [(0.0938-0.1016) Hz], and wave groups (0.0078 Hz). The spectral response of the starboard inclinometer to wind-sea seems to be bimodal. In addition, the response of ARIES II to the tide and non-linear internal waves is better observed in the pressure sensor because of the limited length of records.

- The rms scatter of the mean alignment of ARIES H with currents are 34°T for $\mathcal{U}_{10} \leq 7$ ms^{-1} and 23°T for larger wind speeds. In terms of current speeds, the rms scatter of points is 19°T for speeds in the range (40-75) cms^{-1}, whilst a few points align within 6°T for lower speeds.

- The direction of propagation of solitary-type internal waves, estimated from low-resolution current meter records, is (146 ± 45)°T during neap tides and range of about $(180 - 360)$°T during spring tides.

- The rms scatter of points for the alignment of ARIES II with internal-wave induced flows are 45°T during spring tides and 84°T during neap tides. The corresponding rms when the orientation of ARIES II is compared with the current meter direction at the time of the internal wave trough are 40°T and 42°T for spring and neap tides respectively.

- The maximal vertical excursion experienced by the streamlined instrument was of 1.7 m; it is attributed to non-linear internal waves which caused a 10° tilt down to starboard.

- Although mean fore-aft (pitching) and port-starboard (rolling) tilts are respectively of about 5° and 1°, wave groups may induce fluctuations roughly ±10° in the forward beam during high wind conditions. By contrast, maximal sideways tilts atributed to tidal flows are $-2.5°$.

- Following Packwood (1995), it is estimated that vertical excursions caused by the tilting of ARIES H from the mooring attachment point are typically of 0.08 m and show a maximum of 0.30 m. By using simple equations for the ARIES II mooring system, it is estimated that the maximal vertical excursion associated with the tilting of the mooring line is 1.3 m. Neither of the methods reproduce the measurements obtained from ARIES II.

6. THE EFFECT OF ARIES II MOVEMENT ON SONAR BEAMS AND SONOGRAPHS

This chapter aims to analyse several different factors that affect the acoustic images. First, it describes how acoustic images are interpreted, second it quantifies the effect of variations of temperature and motion of the streamlined instrument on the sonar beams, and third it explains the distortion of acoustic features captured in sonographs with specific formulations. It builds on the discussion of Thorpe *et al.* (1998), but explores in greater detail the assumptions in the formulations developed from simple but effective geometric considerations. In addition, it contributes with new material regarding the refraction of sound rays through the thermocline, the coherence of bubble bands reckoned to be plane waves, the hyperbolic distortion of targets crossing the range of the sea surface, the shadowing of surface waves, the effect of headings on non-stationary bubble bands, the errors in the estimation of the orientation and lateral advection speed of bubble bands when ARIES II rotates to minimise drag, and the passive distortion of bubble bands caused by internal waves.

6.1 The interpretation of acoustic images

Two orthogonal side-scan sonars transmit alternately pulses of sound with a repetition rate of 2 Hz on both beams and receive return echoes or scattered sound from targets (e.g. bubbles) situated in the ensonified regions (see sections 1.1, 2.1 and 3.3 for additional details). An acoustic image or sonograph displays the relative scattering strength as a function of slant range and time, thus allowing a detailed visualisation of acoustic structures from variations in the scattering intensity of targets. Acoustic structures do usually form patterns (i.e. acoustic signatures) of physical processes progressing through the UOBL (Fig. 2.1). Recall that for ARIES II in particular, the strength of targets cannot be established since sonars are un-calibrated and acoustic signatures are presented as raw voltages or dimensionless in the case of normalised sonographs. An idealisation of the beam pattern formed by the sonars is shown in Fig. 6.1, while examples of digitised acoustic images are illustrated in Fig. 6.2 and chapter 8 (e.g. Fig. 7.8) which in particular have been normalised to correct for attenuation. The vertical axis

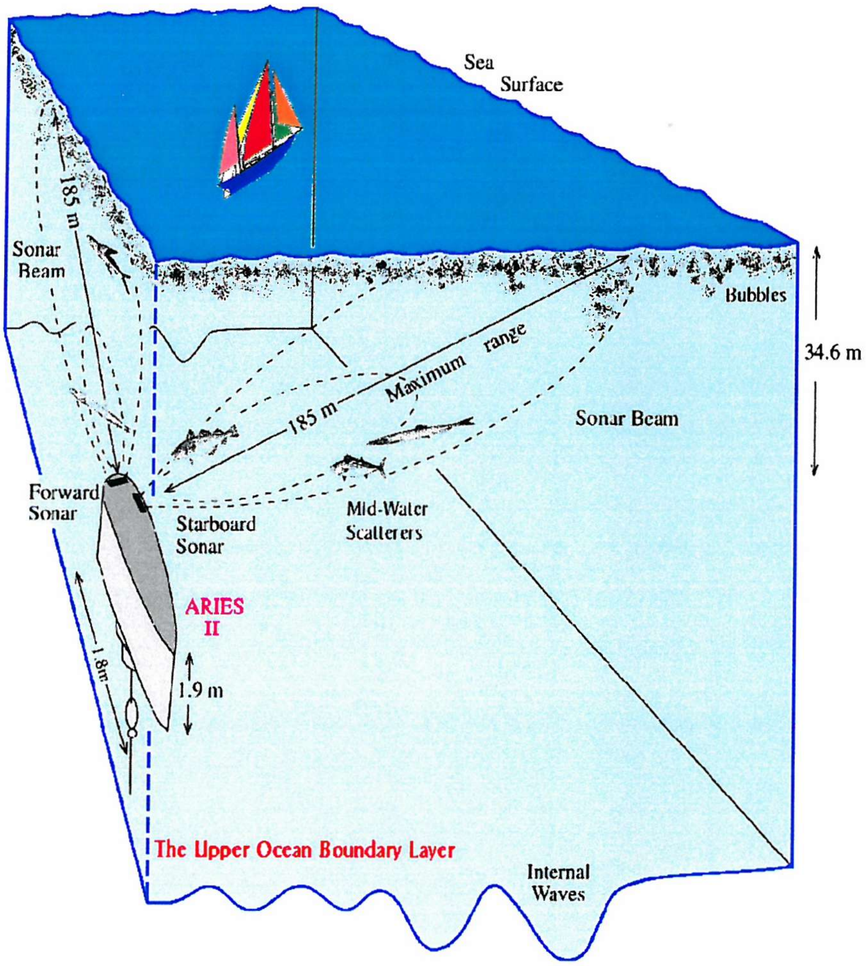

Fig. 6.1: *Schematic showing ARIES II and the fan-like beam pattern generated by the two-component side-scan sonar operating in a zone of active fishing. See also Fig. 2.1 for reference.*

in a sonograph is the slant range of targets (hereafter referred to as range) representing the time delay between transmission of sound and reflected echo converted into distance using a constant sound speed of 1500 ms^{-1} (e.g. variations in the speed of sound resulting from bubble distributions are not implicitly considered). The horizontal axis is the time at which the pulses of sound were emitted.

The first return or echo received is a reflexion from the sea surface directly above the sonars, for example, the wavy line at a range of about 35 m in Fig. 7.8, which is being modulated by swell and wave groups. Although with insufficient power to detect bubbles, this return is presumably from a side-lobe directed vertically upwards, towards the sea surface (Thorpe and Hall, 1983; Thorpe, 1986a). At ranges less than that of the sea surface, the echoes come from mid-water scatterers located in the water column (e.g. the gas bladders of small fish, sometimes transient, and/or zoo-plankton moving or carried near the sonars at short range as described in section 2.1.1). At ranges beyond that of the sea surface (i.e. along the surface), the scattered sound is reflected from bubble clouds advected by mean flows towards or away from the sonars (e.g. the inclined streaks shown in 7.10). Sonographs commonly contain plenty of acoustic signatures in wind speeds greater than $(2-3)$ ms^{-1} as surface waves break to produce bubbles, but reflections from the sea bed or the toroidal buoy and sometimes scattering of biological origin are present when the sea is calm.

Fig. 6.2 illustrates in particular several acoustic features detected during the propagation of an internal wave packet; they are offered without explanation and the reader is referred to Fig. 13a in Thorpe *et al.* (1998) for details. At ranges beneath the sea surface, there are echoes marking a gradual rotation of the streamlined instrument (A) and biological scatterers (B); high local scattering over the forward flank of an internal wave trough (C) and inclined linear features indicating local flow at depth towards the sonars (D); and stationary targets (E). At greater ranges there are acoustic signatures of breaking surface waves (F), a vertical scattering band coinciding with a rapid change in orientation of ARIES II (G) and an intensification of surface scattering over the wave trough in the form of a scattering band approaching the sonar and associated with a large concentration of bubbles per unit area, probably caused by surface breaking waves (H). At the range of the sea surface the presence of wave groups is enhanced by scattering caused perhaps by the superposition of high-frequency waves to mark a region relatively rough over the wave trough (I).

6.2 The influence of temperature variations on the sonar beam

Sound speed depends primarily upon temperature and to a lesser degree on pressure and salinity. Thus the scales ascribed to sonographs, the relative position of acoustic scatterers and the scheme adopted to obtain quantitative information depend in consequence upon the conversion of the time delay into distance and the assumptions regarding the sound speed in the water column. Errors in the range estimation of reflecting targets on the depth of the transducers are produced by neglecting the variations of temperature in the water column as sound propagates through the thermocline. Moreover, rain also induces changes of temperature and salinity in a layer immediately beneath the sea surface (Green and Houk, 1979). Internal waves may additionally induce a redistribution of temperature causing variations in the sound speed and errors in the range ascribed to acoustic scatterers during the generation of sonographs. In order to visualise the acoustic situations involved in these errors, a geometric approach

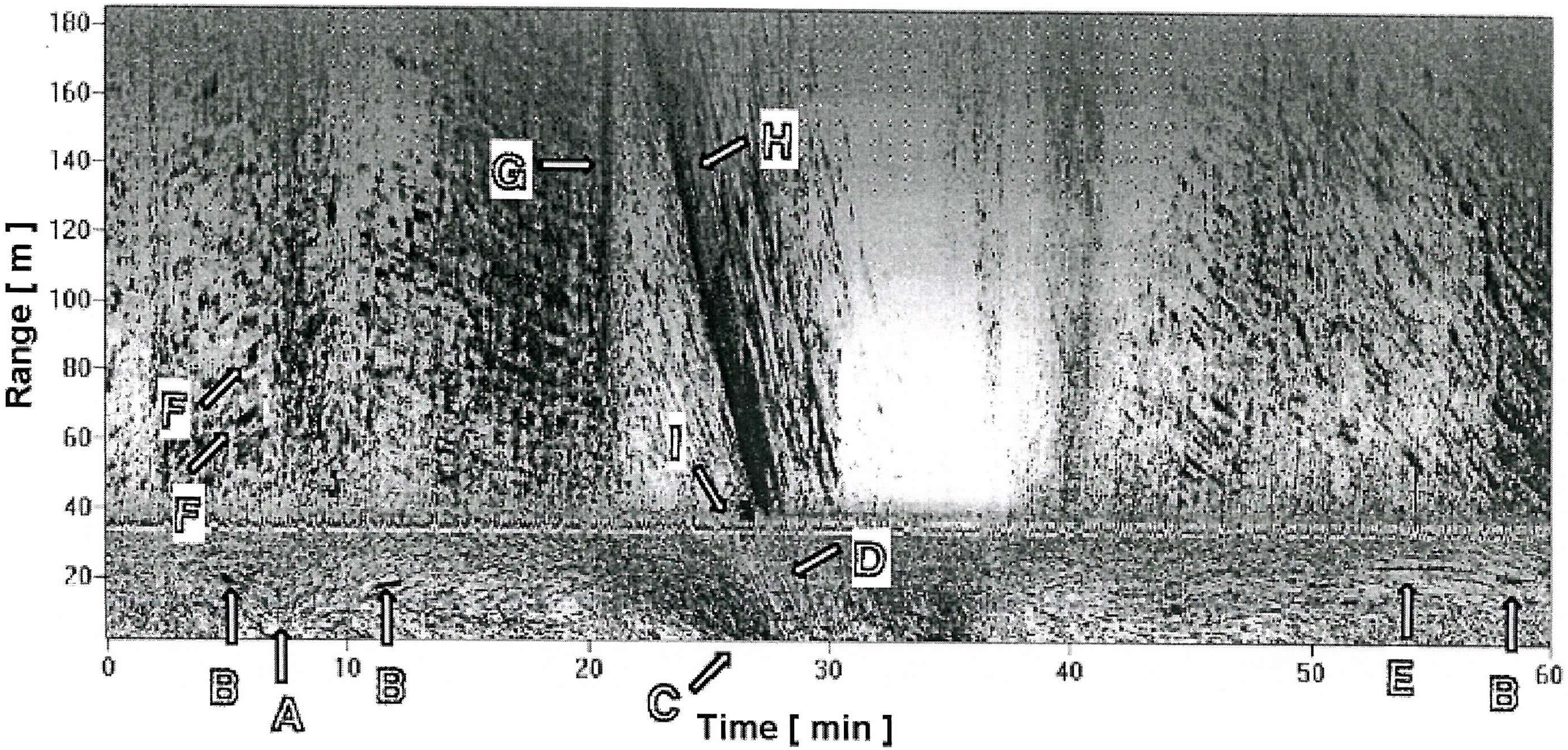

Fig. 6.2: *Normalised sonograph starting at 17:00 GMT on* 21^{st} *August 1995. The strongest acoustic reflections are shown in black. Labels explained in the text.*

is adopted for their estimation.

6.2.1 Variations of range in the water column

The level of the sea surface is the range of the surface directly over the transducers. It is modulated by the tide, surface waves, wave groups and by the tilting of the mooring line induced by internal wave flows (e.g. Fig. 6.2). This range, however, is an apparent range because the effect of temperature on the speed of sound is ignored. Changes in apparent range indicate how much the apparent depth of the movement of ARIES II seen in sonographs appears to change as a consequence of the temperature variations in the whole column water if there is no refraction. Internal waves give rise to changes in apparent range through a redistribution of temperature in the water column and hence in sound speed. Maximal apparent range is expected to be produced by the leading wave of a rank ordered internal wave packet.

The change in apparent range ($\Delta\mathcal{R}$) is calculated from the time interval (Δt) for the sound to pass from the sonar to the surface and back, that is,

$$\Delta\mathcal{R} = \frac{c_{s1}}{2}\Delta t. \tag{6.1}$$

where c_{s1} is the sound speed for the vertical path of a sound ray in a warm upper layer. Variations in the sea surface roughness generated by surface waves are neglected. Currents have no effect on $\Delta\mathcal{R}$ because the sound speed is much greater than the speed of currents. The time needed by a sound ray to pass through an internal wave trough, t_1, is (Fig. 6.3)

$$t_1 = 2\left[\frac{h - (h_1 + \Lambda)}{c_{s2}} + \frac{h_1 + \Lambda}{c_{s1}}\right], \tag{6.2}$$

where c_{s2} is the sound speed when the ray passes a cool lower layer, and the time needed to pass through the wave crest, t_2, is

$$t_2 = 2\left[\frac{h - h_1}{c_{s2}} + \frac{h_1}{c_{s1}}\right], \tag{6.3}$$

in which the elevation of the sea surface caused by the leading internal wave and the corresponding wave amplitude above the upper layer are both neglected. By applying equation (6.1) to the water column and defining $\Delta t = t_1 - t_2$ and $\Delta c_s = c_{s1} - c_{s2}$, the change in apparent range is

$$\Delta\mathcal{R} = -\frac{\Lambda\Delta c_s}{c_{s2}}. \tag{6.4}$$

Since sound speed increases with temperature, $c_{s1} > c_{s2}$ and so the internal wave brings about an apparent decrease in the range to the sea surface (i.e. a trough). This

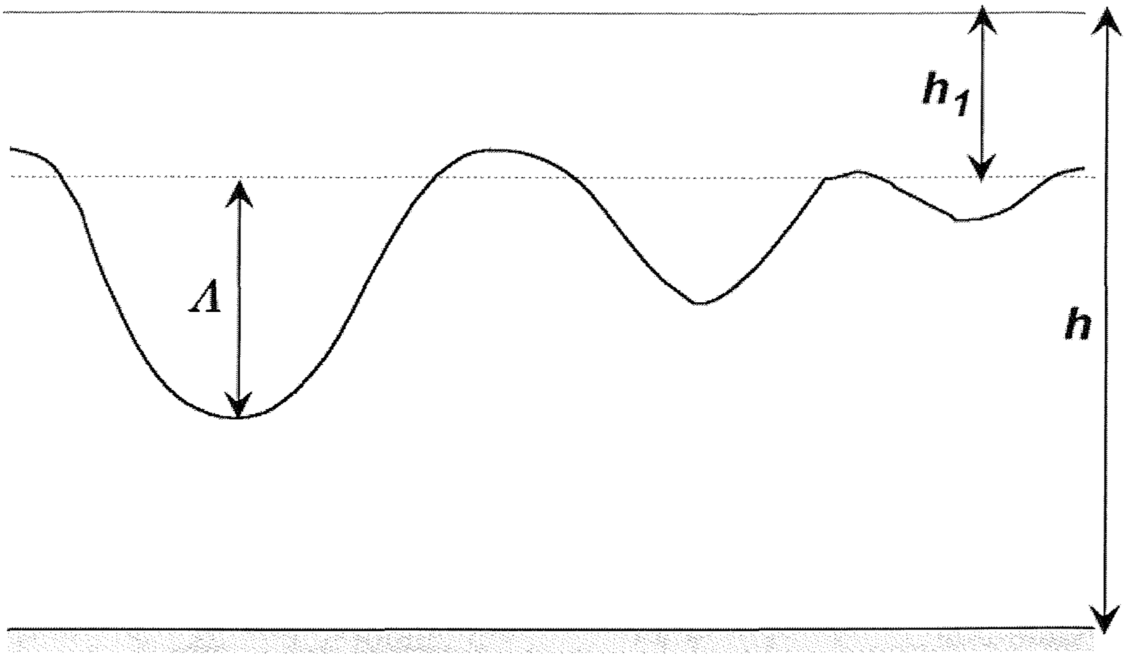

Fig. 6.3: *Schematic showing a rank ordered non-linear internal wave propagating in a two-layer fluid and utilised in deriving a relation for the change in apparent range of the sea surface. Variables defined in section 2.3.2.*

is explained from the equations (6.2-6.3) where $t_2 > t_1$ by the addend $\frac{2\Lambda\Delta c_s}{c_{s1}c_{s2}}$ and in consequence the acoustic signal from the wave trough arrives first to the sonars.

In order to evaluate equation (6.4), a temperature of 16°C for the upper layer and 10°C for the lower layer are selected according to Thorpe *et al.* (1998). The sound speed for this two-layer temperature structure is, respectively, 1510.4 $\mathrm{ms^{-1}}$ and 1490.4 $\mathrm{ms^{-1}}$; hence $\Delta c_s = 20$ $\mathrm{ms^{-1}}$. The latter representing about 1% of the nominal value of 1500 $\mathrm{ms^{-1}}$. Consequently the apparent reduction in the range of the sea surface for a typical internal wave amplitude of 15 m is roughly 0.2 m. Moreover the largest wave amplitude detected by ARIES II occurred during neap tides and was of 37 m, corresponding to a range reduction of about 0.5 m. These reductions are now compared with the elevation of the sea surface over the leading wave trough by means of equation (2.20). From a mean density profile kindly supplied by Dr. J. Small, $\rho_1 = 1025.9$ $\mathrm{Kgm^{-3}}$, $\rho_2 = 1027.2$ $\mathrm{Kgm^{-3}}$ and therefore $\varrho = 0.9987$. The elevation of the sea surface for the above internal wave amplitudes are 0.02 m and 0.05 m respectively.

An obvious question is whether the estimated reductions in the apparent range of the sea surface are detectable in the sonographs. Several attempts were carried out by averaging in range the strongest colours from a black and white palette utilised to display the sonographs. A number of range intervals were selected and the time series plotted. Unfortunately, the resulting graphs were very noisy and this method was discarded. This is not surprising because the sonar resolution is 0.23 m and since

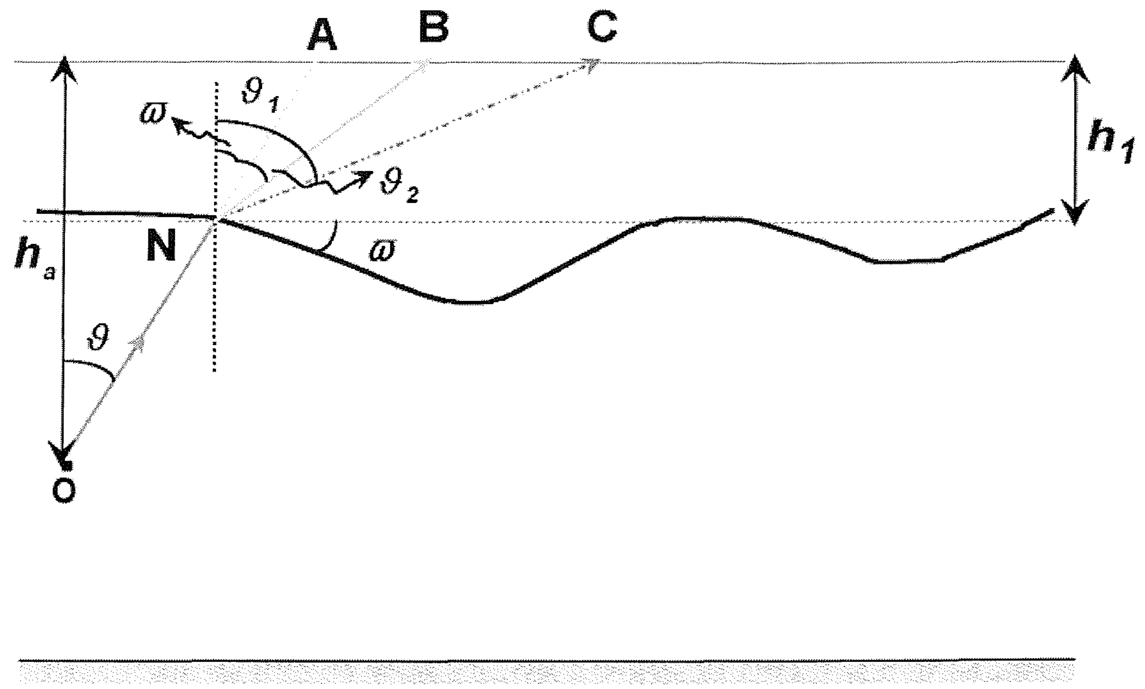

Fig. 6.4: *Diagram showing an acoustic source and the refraction of sound rays after passing through the thermocline. The ray ONA indicates the path followed by the sound when there is no refraction; the ray ONC is the refracted sound path in the absence of internal waves; and the ray ONB represents the effect of internal waves on the path of a sound ray.*

the maximum signal that one is looking for is of 0.50 m (about two pixels), the graphs contained a large surface wave/bubble cloud contamination.

The effect of wave slope on the apparent range is easy to infer from Fig. 6.4. By expressing equation (6.4) like $\Delta\mathcal{R} = -\frac{L\Delta c_s}{c_{s2}} \tan\varpi$, after using $\tan\varpi = \frac{A}{L}$ in which ϖ is the internal wave slope and L an horizontal length scale at half-amplitude, it is deduced that, the steeper the internal wave, the larger the reduction in apparent range.

6.2.2 Refraction through the thermocline

Non-vertical sound rays emitted by the sonar transducers are distorted when refracted through the thermocline as shown in Fig. 6.4. If there are no internal waves, a path of sound ON at oblique incidence ϑ from the normal is refracted an angle ϑ_1 away from the normal towards point C because $c_{s1} > c_{s2}$. By assuming a plane sea surface, an estimate of the error in detecting the reflecting target A is given by the length of the segment $\overline{\mathrm{AC}}$, that is, $h_1(\tan\vartheta_1 - \tan\vartheta)$. For $h_1 = 30$ m (e.g. the depth of the upper current meter) and $\vartheta = 70°$ (e.g. the inclination of sonar transducers), this length is 11 m or about 6% of the maximal effective range of targets observed in sonographs (e.g.

Fig. 6.1). Here, Snell's law is used for estimating the distortion angle of the acoustic path, $\vartheta_1 = \arcsin\left(\frac{c_{s1}}{c_{s2}} \sin\vartheta\right)$. Alternatively the range of target A is,

$$\mathcal{R} = \left\{ \mathcal{R}_r^2 - \frac{h_1^2}{\tan^2\vartheta} \left(\left[\frac{\tan\vartheta_1 - \tan\vartheta}{\tan(\vartheta_1 - \vartheta)} \right]^2 - \sec^4\vartheta \right) \right\}^{\frac{1}{2}}. \tag{6.5}$$

where $\mathcal{R}$ is the distance from O to A and $\mathcal{R}_r$ is the range of target C, the distance from O to C measured in sonographs. Thus for incidence angles of 45° and measured ranges of 180 m, an error of about 0.2% is deduced from equation (6.5). Further if refraction effects are not taken into account, a reflecting target ensonified by an acoustic ray 80° from the normal at a range of 180 m (e.g. when the instrument is tilted down to port), would be detected at a range of about 480 m; a range too large for targets to be observed in sonographs.

There are however several important factors to consider under this simple geometrical approach. ARIES II is not really beneath the thermocline, but in the region of maximal temperature gradients where the changes of sound speed with depth are not known. Effects such as the positive buoyancy and lurching movements of ARIES II on incident sound rays, or the presence of acoustic scatterers in the medium are all neglected. It should be said finally that the exact directionality of the beam patterns, that is the angles of incidence at which the pulses of sound are transmitted, are not known since sonars are un-calibrated.

With the presence of internal waves in the thermocline the position of point N does change, however we keep it fixed for convenience since there is a poor understanding about which part of the wave hits the the sonar beams. The propagation of internal waves changes the normal to be aligned with the wave slope and in consequence the refracted path of sound hits point B rather than C (Fig. 6.4), introducing an additional error in the estimation of the range of the reflecting target A. This error is estimated by comparing the difference in range of the acoustic paths ONC and ONB. A simple formulation for the range ONC is,

$$\mathrm{ONC} = (h_a - h_1)\sec\vartheta + h_1 \sec\vartheta_1,$$

whilst for the range ONB,

$$\mathrm{ONB} = (h_a - h_1)\sec\vartheta + h_1 \sec(\varpi + \vartheta_2),$$

where $\vartheta_2 = \arcsin\left[\frac{c_{s1}}{c_{s2}} \sin(\vartheta - \varpi)\right]$ and ϖ is the inclination angle of the leading wave profile. The change in range ($\Delta\mathcal{R}_{iw}$) for non-vertical sound rays because of the refraction of acoustic paths by internal waves is therefore,

$$\Delta\mathcal{R}_{iw} = h_1 \left[\sec\vartheta_1 \; - \; \sec(\varpi \; + \; \vartheta_2)\right] . \tag{6.6}$$

which is now evaluated for an internal wave amplitude of $\Lambda = 37$ m. This internal wave is associated with a variation of temperature at the instrument's depth from 12°C to 16.7°C, the latter implying for example $c_{s1} = 1512.5$ ms^{-1}. Using equation (2.14) with $h_1 = 30$ m and $h_2 = 116$ m, the wave slope is 27.5° for $L = 71.2$ m. Furthermore by applying Snell's law for $\vartheta = 70°$, the following values are obtained: $\vartheta_1 = 72.2°$ and $\vartheta_2 = 43.2°$; thus $\Delta\mathcal{R}_{iw}$ is of about 7 m or roughly 4% of the maximal range of sonographs. Although the distance defined by the segment $\overline{\text{AB}}$, given by $h_1 \left[\tan(\varpi \; + \; \vartheta_2) \; - \; \tan\varpi\right]$, is for the preceding values of about 3 m, the obvious implication is that ARIES II seems unable to detecting refracted targets along the surface during the propagation of steep internal waves. A scattering contribution from ranges beneath the sea surface for acoustic returns over internal wave troughs is therefore expected.

6.2.3 Reflection from the thermocline

The acoustic paths of interest are those that propagate parallel to the thermocline, and accordingly there is a critical incident angle below which the transmission of sound is nil. It is given by: $\arcsin\left(\frac{c_{s2}}{c_{s1}}\right)$, being of about 81° if internal waves are ignored. Sound rays will then be reflected downward, to the level of decreasing sound speed, at incidence angles larger than this critical angle. The range of the corresponding acoustic path is, $(h_a \; - \; h_1)\sec\vartheta$ or 29 m. When internal waves are passing through the sonar beams, the sound ray of interest is that parallel to the wave trough, that is $\vartheta_2 = 90°$. By considering the normal to the thermocline, the critical angle is: $\arcsin\left(\frac{c_{s2}}{c_{s1}} \; \cos\varpi\right)$, or 61° for $\varpi = 27.5°$, corresponding to a range of 10 m. Therefore, if reflection from the thermocline is important, then no scattering should be observed in sonographs at short ranges from the sonars, unless mid-water scatterers are moving within the fan-like pattern of acoustic beams.

6.3 The effect of the instrument motion on the sonar beam

When the inclination of ARIES II changes along the fore-aft axis of reference (section 4.1), there is a variation in the vertical inclination of the starboard sonar beam (Fig. 6.5). Assuming that the sonars are like point sources transmitting sound mainly along the axis of the beam pattern central lobe, the intersection of the starboard beam

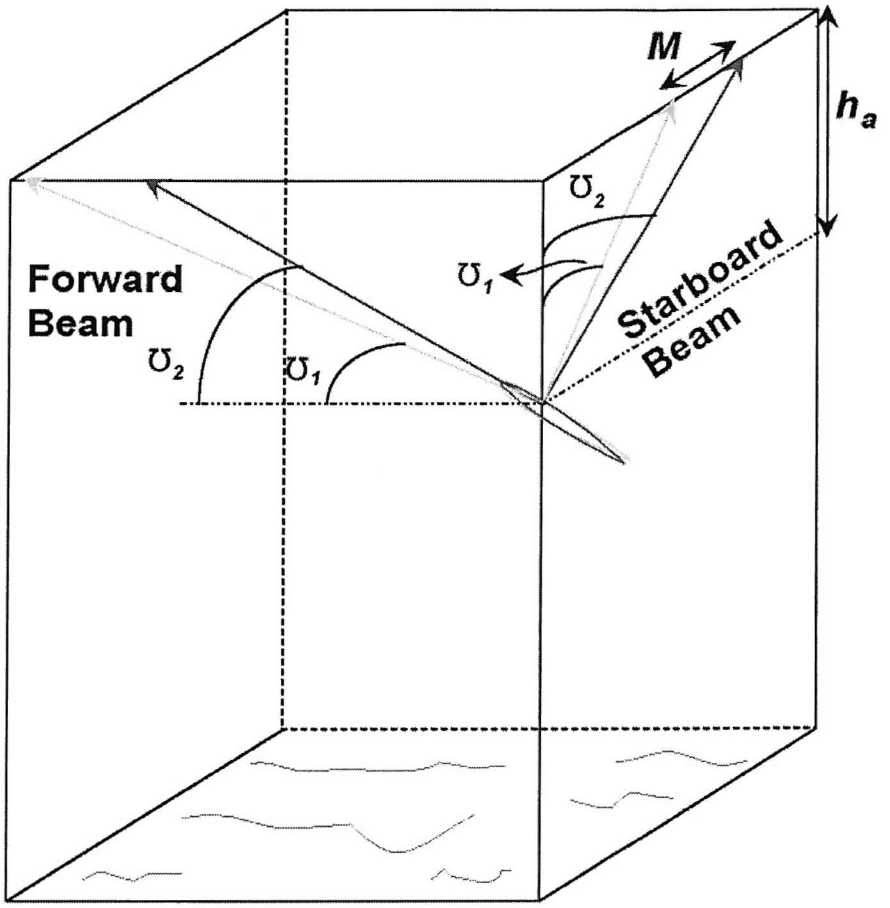

Fig. 6.5: *The variation of the vertical inclination of the starboard sonar beam induced by the fore-aft movements of the streamlined instrument. Variables defined in the text.*

along the sea surface migrates a distance, M, given by,

$$M = h_a\,(1\,+\,\tan\mho_2\,\tan\mho_1)\tan\Delta\mho,$$

where $\Delta\mho = \mho_2\,-\,\mho_1$, and both $\mho_2$ and $\mho_1$ are measurements of the instrument's fore-aft tilts or pitch angles. Refraction effects on sonar beams are not explicitly considered. Further neglecting products of these tilts, the migration of the starboard beam is,

$$M = h_a\,\tan\Delta\mho. \qquad (6.7)$$

Typical fluctuations of ±1° (e.g. Fig. 5.12b) in the pitch angle lead to a migration in the starboard beam of about 0.6 m. Maximal migrations of 6.1 m at the surface correspond to fluctuations of ±10° caused by wave groups during high wind conditions (e.g. Fig. 5.11b).

Moreover both fore-aft and port-starboard tilts of ARIES II may induce geometric distortions affecting the relative location of acoustic targets in sonographs. Targets advected slowly towards the forward beam and captured when ARIES II is tilted down to fore, for example, could be missed or replicated later when the instrument recovers its normal position. Conversely, the forward beam will capture targets previously ensonified if ARIES II is tilted up to fore. Therefore acoustic targets appearing either triplicated or suddenly interrupted are indicative of pitching effects (e.g. Flemming, 1982). Many short-period sonographs have been qualitatively scrutinised, with the result that they do not look severely affected by pitching.

The effects of port-starboard movements of ARIES II on the vertical inclination of the forward sonar beam are also given by equation (6.7), except that $\Delta\mho$ relates to fluctuations in lateral tilts. Fluctuations are typically of $\pm 0.5^\circ$ with corresponding migrations of the forward beam of 0.3 m. Internal waves produce greater migrations of the forward beam whilst the instrument is tilted down to starboard (e.g. section 6.1 and Fig. 5.13b). Thus the maximal migration estimated for a variation of -10° is of about 6 m.

In addition, the rolling of ARIES II induces the rotation of the forward beam, leading to variations in the scattering intensity and misposition of targets because of the sideways migration of vertical side-lobes (equation (6.7)). As in the previous paragraph, a maximal misposition of about 6 m is estimated to occur during the propagation of ISWs.

6.4 The movement of ARIES II and the range of acoustic targets

The most common targets visible in sonographs are regions of strong acoustic scattering forming inclined features or lines of scatterers. Features appearing almost vertical, that is with range variations occurring for periods of few seconds, propagate at speeds consistent with the phase speed of surface waves (e.g. labels C and D in Fig. 7.10). These features constitute the acoustic signatures of surface waves and represent the visual manifestation of sound scattered from bubbles created by breaking waves (see also sections 2.1.4 and 2.2.2). Acoustic signatures of surface waves are typically present as linear and curvilinear features in long-period (e.g. $>$ 2 h) and short-period (e.g. 2 min) sonographs respectively. When acoustic linear features appear as more persistent patterns slightly tilted, with lengths at least one order of magnitude in excess of their width, they constitute the acoustic signatures of bubble bands, depicting regions of enhanced concentration of bubbles being carried and clustered by surface convergent flows (section 2.4.2). Bubble bands are attributed to lie along the convergence zones of Langmuir circulation if they are aligned with the wind direction whilst being slowly advected by mean currents.

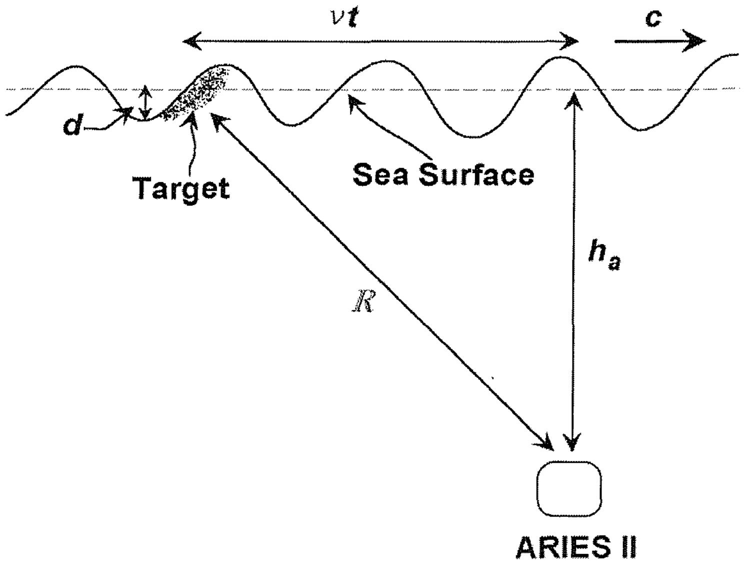

Fig. 6.6: *Schematic diagram of a target, a near-surface bubble cloud, propagating along the sea surface and approaching ARIES II. Only the configuration of a single beam is sketched with variables defined in the text.*

The range of targets and the whole appearance of acoustic features captured in sonographs are affected by the motions of the streamlined instrument (sections 5.2 and 5.3). In order to separate particular instrument motions, it is necessary to establish a geometrical framework for developing specific formulations. This framework is based upon the concept of plane wave. In the case of surface waves, the wave plane concept is traditionally applied to represent wave trains as lines of constant phase on any plane normal to the direction of wave propagation. Langmuir circulation, on the other hand, may also be represented as a train of wave planes by denoting wave crests as bubble bands or lines of maximal concentration of bubbles. Wave troughs therefore indicate minimal concentration of bubbles, that is in the divergence zones of Langmuir circulation. Thus the Langmuir circulation will remain coherent if bubble bands can always be described in terms of a wave number, $\mathbf{k}$, such that the band spacing, $\mathcal{S}$, is defined as $\frac{2\pi}{|\mathbf{k}|}$.

6.4.1 The hyperbolic distortion of linear features

Consider the sketch in Fig. 6.6 showing the range ($\mathcal{R}$) of a target from a single sonar beam. The target travels along the surface a distance $x_\circ + vt$, measured from a position immediately above ARIES II, at constant speed (v). If $x_\circ = 0$ when $t = 0$, then the target range in a fixed beam is,

$$\mathcal{R}^2 = (h_a - d)^2 + (vt)^2. \tag{6.8}$$

which traces an hyperbola with asymptotes $\mathcal{R} = \pm vt$ in the $(t\text{–}\mathcal{R})$ frame of reference of the sonographs and where d indicates the target depth from the still water surface. The range variation of the target is therefore hyperbolic and the slope of the hyperbola asymptotes, measured in sonographs, is what determines the target speed in the direction of the sonar beam. Hence the target slope, $\frac{d\mathcal{R}}{dt}$, asymptotes to v at large values of $\mathcal{R}$ (e.g. > 80 m). As stated earlier, the hyperbola will form the acoustic signature of a surface wave as long as the target is passively advected by the near-surface orbital wave motion, when $v \approx c$, in which c stands for the phase speed of surface waves. When the hyperbola is observed in sonographs to traverse the range of the sea surface, the relative depth $(h_a \; - \; d)$, with $d < h_a$, is utilised to fix the position of the hyperbola beneath the sea surface. The former is attributed to the presence of near-surface shear during high wind conditions. When $d = 0$, the hyperbola is tangential to the surface at the apex $r = h_a$.

There are several assumptions intrinsic to Fig. 6.6 that deserve to be mentioned. Sound is assumed to be transmitted along the main axis of the beam pattern with uniform strength. Furthermore, a severe assumption in equation (6.8) is that the estimation of $\mathcal{R}$ does not account for variations of temperature on the sonar beam (e.g. those produced by rain), nor the refraction of sound rays at the base of near-surface bubble concentrations undulating beneath the surface waves or the generation of additional bubble clouds by rain-drops. Since the surface wave profile receives and reflects sound from the sonar's beams, it is most probable that the sonars receive backscattering from the flanks of the wave rather than from the crest itself (Thorpe, 1982). Backscattering sources from the wave profile are therefore the flanks of low-frequency surface waves and high-frequency waves riding on the tilted surfaces of swell. However when the transmitted sound hits a wave trough, that is the portion of the wave profile nearer to the sonar, there will be no reflected sound from the part of the wave more distant from the sonar. A portion of the wave crest is therefore hidden or shadowed by the wave trough because it is not directly exposed to incident sound rays. Although this effect is not considered in equation (6.8), a simple condition for shadowing is derived. Assuming that the wave displacement is of the form $\eta = \mathbb{A}\sin(kx - \omega t)$, the largest inclination of the wave profile to the horizontal is $\tan^{-1} s$ where $s = \mathbb{A}k$ is the wave slope. By expressing the inclination of an incident sound ray as $\sin^{-1}\left(\frac{h_a + \mathbb{A}}{\mathcal{R}}\right)$ (or with $(h_a \; - \; \mathbb{A})$ if the wave trough is taken as reference), shadowing will occur when,

$$\sin^{-1}\left(\frac{h_a + \mathbb{A}}{\mathcal{R}}\right) \leq \tan^{-1} s,$$

or equivalently,

$$\mathcal{R} \geq \frac{h_a + \mathbb{A}}{\sin(\tan^{-1} s)}. \tag{6.9}$$

which increases to infinite as s tends to $\frac{\pi}{2}$. When the incident ray intersects the wave profile node, $\mathbb{A} = 0$. For the waves in Fig. 5.11 and 5.12, s is about 0.104 and 0.084 respectively, corresponding to approximated ranges of 372.0 m and 431.1 m. High-frequency waves with mean periods of about 2.8 s have also been captured in sonographs (e.g. Thorpe *et al.*, 1998). Assuming a wave amplitude of, say, 0.1 m the corresponding range for $s = 0.051$ is 676.2 m. All these ranges are more than two times the maximal effective range of sonographs.

6.4.2 The estimation of surface wave dimensions from sonographs

The phase speed

Consider the situation depicted in Fig. 6.7 where a train of wave planes are travelling in the direction of the wave number $\mathbf{k} = (k,l)$ and crossing the acoustic field emitted by orthogonal side-scan sonars. Here k and l define in respective order the wave numbers in the direction of the starboard and forward beams. The wave crest at QP has constant phase, $\mathbf{k} \cdot \mathbf{x} - \omega t = 0$, with $\mathbf{x} = (x,y)$. Assuming that, at ranges $>> h_a$, the position of both targets Q and P on the wave surface are fixed and in phase relative to the wave crest, the asymptotic speed of Q along the forward beam is, $C_f = \frac{\mathrm{OQ}}{\Delta t} = \frac{\omega}{l}$, whilst that corresponding to target P for the starboard beam is, $C_s = \frac{\mathrm{OP}}{\Delta t} = \frac{\omega}{k}$. The phase speed of the receding surface waves is in consequence, $c = \frac{\mathrm{OR}}{\Delta t} = \frac{\omega}{l} \cos \psi = \frac{\omega}{|\mathbf{k}|}$. In terms of C_f and C_s, the phase speed is easily derived from $|\mathbf{k}| = \omega \left(\frac{1}{C_f^2} + \frac{1}{C_s^2} \right)^{\frac{1}{2}}$, and then expressed as

$$c = \frac{C_f C_s}{\left(C_f^2 + C_s^2\right)^{\frac{1}{2}}}, \tag{6.10}$$

where $c^2 \neq C_f^2 + C_s^2$ because OP and OQ are both larger than OR. The asymptotic speeds of wave targets, C_f and C_s, are directly measured in sonographs at far ranges (e.g. > 80 m). A test of consistency of c is through the comparison with that obtained from linear wave theory (i.e. $c = \frac{g}{\omega}$ for deep water) using the measured frequencies from the upward pointing side-lobes, provided that the same frequencies are detected by the two sonars. The rotation rate of sonar beams is generally $<< c$ and therefore disregarded (section 6.4.5).

The direction of wave propagation

The local wave direction or the direction of wave propagation with respect to that of the forward beam is,

$$\psi = \arctan \left(\frac{C_f}{C_s} \right), \tag{6.11}$$

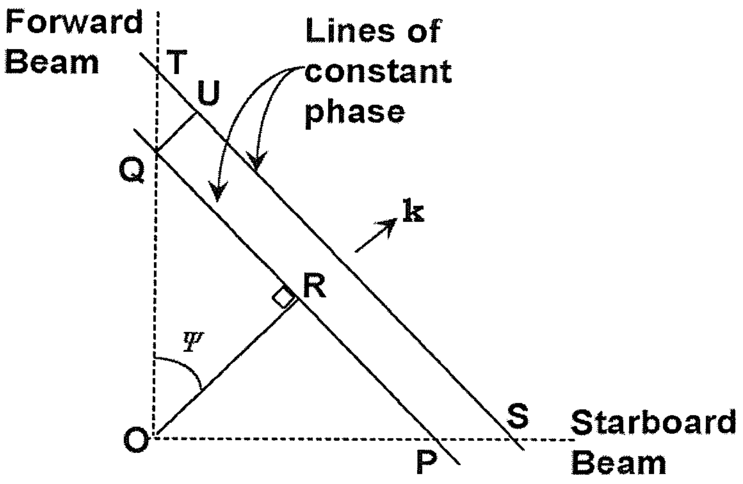

Fig. 6.7: *Plan view of a train of surface waves moving away from the sonars. Targets Q and P are located in the intersection of the sonar beams with the sea surface directly above ARIES II.*

which is dependent upon the signs of both C_f and C_s, being positive for surface waves receding from the sonars. Equation (6.10) cannot be utilised when either C_f or $C_s = 0$, or if either speed cannot be determined from acoustic images since ψ is not known beforehand. A rough approximation of c is then $c \approx C_f$ when $\psi = 0$ and $c \approx C_s$ when $\psi = \frac{\pi}{2}$.

The wavelength

When the acoustic signatures of surface waves are visible simultaneously in the sonographs, the wavelength may also be estimated. By denoting the distances TQ, SP and UQ in Fig. 6.7 as λ_f, λ_s and λ respectively, it is easy to show that, $\sin^2\psi + \cos^2\psi = \frac{\lambda^2(\lambda_f^2 + \lambda_s^2)}{\lambda_f^2\lambda_s^2}$, or

$$\lambda = \frac{\lambda_f \lambda_s}{(\lambda_f^2 + \lambda_s^2)}. \tag{6.12}$$

where λ_f and λ_s represent the distances between wave crests along each beam direction, being both less than the range. A check of consistency for equation (6.11) results from the comparison with $\psi = \arctan\left(\frac{\lambda_f}{\lambda_s}\right)$.

6.4.3 The effect of surface waves on bubble bands

The position of bubble clouds either isolated or those passively collected by convergent near-surface currents to delineate bands, is perturbed by the near-surface orbital motions of surface waves. At the time a surface wave intersects a band, the bubble clouds are displaced horizontally following the trajectory of water particles. According to lin-

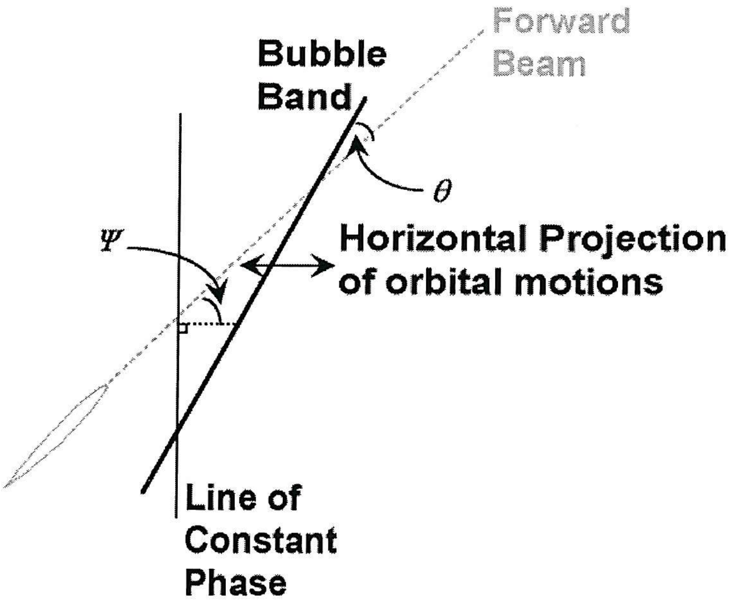

Fig. 6.8: *Geometry of the movement of bubble clouds within a band caused by the orbital motions of a passing surface wave in the forward sonar beam. The bubble band is moved and then bent by the wave, changing its range in the beam.*

ear theory, the horizontal velocity component at a fixed point (x,z) is, $\omega\eta\ \frac{\cosh[k(z+h)]}{\sinh(kh)}$, for a surface wave, $\eta = \mathbb{A}\cos(kx - \omega t)$. The horizontal motion is in phase with the water surface displacement and the motion of water particles follows an elliptical path with center in the mean particle position (x_1,z_1). Hence the horizontal position of a water particle is determined by, $\mathbb{A}\frac{\cosh[k(z_1+h)]}{\sinh(kh)}\ \sin(kx_1 - \omega t)$. At the surface, the horizontal orbital motions being of length equal to, $2\mathbb{A}\coth(kh)$, will induce changes in the range of bubble bands detected by both sonar transducers. This is particularly evident at large range, where the sonar beams intersect the surface at a small glancing angle. Assuming that bubble bands are only moved and bend by wave-induced orbital motions, the amplitude of the change in range in the forward sonar beam (Fig. 6.8) of the bands is $\frac{2\mathbb{A}\ \coth(kh)\ \sin(\psi+\theta)}{\sin\theta}$. Here θ and ψ are the angles formed by the bubble band and the direction of wave propagation with the forward beam respectively. The corresponding amplitude in the starboard beam is, $\frac{2\mathbb{A}\ \coth(kh)\ \sin(\psi+\theta)}{\cos\theta}$. These oscillations of bubble clouds, which are in phase with range, advance at the phase speed of the waves with amplitudes not increasing with range.

6.4.4 The effect of heading on bubble bands

Changes in the instrument heading lead to variations in the direction in which the two sonar beams point, and in consequence the position of targets in sonographs is distorted. There are two possible cases depending upon whether the targets are stationary or

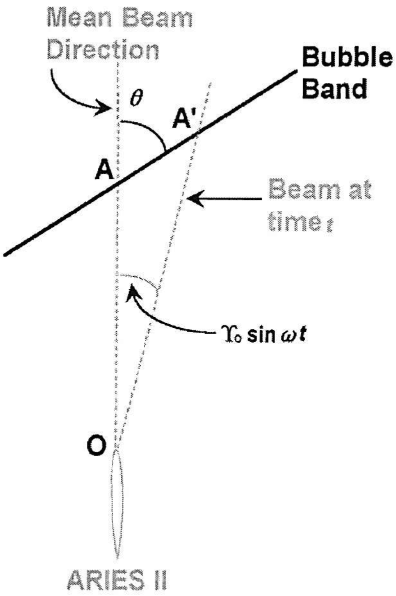

Fig. 6.9: *Plan view geometry of a sonar beam intersecting a band of scatterers, the line AA', from the position of ARIES II, O. The beam is initially oriented in the mean direction OA. At time t the beam, OA', is oscillating an angle,* $\Upsilon_\circ \sin(\omega t)$*, to the mean direction.*

slowly advected by, for example, a component of the wind speed or tidal current normal to the band.

Stationary case

Fig. 6.9 displays a plan view of the intersection between a stationary band of bubbles and the mean orientation of a sonar beam, where at the initial time, $t = 0$, the distance from O to A is of length $x_\circ$ (i.e. the target position from a point directly above the sonar). At time t, when the beam heading oscillates at an angle, $\Upsilon = \Upsilon_\circ \sin(\omega t)$, relative to the mean direction OA', it may be shown by simple geometry that, $x \sin(\theta - \Upsilon) = x_\circ \sin\theta$, where x denotes the distance from O to A'. A correction for depth is easily obtained since at range, $\mathcal{R}_\circ$, the beam points in the direction OA and thus $x_\circ^2 = \mathcal{R}_\circ^2 - h_a^2$. The variations in range leading to the apparent distortion of a bubble band by oscillations in the heading of sonars are then given by,

$$\mathcal{R}^2 - h_a^2 = \frac{(\mathcal{R}_\circ^2 - h_a^2)\sin^2\theta}{\sin^2[\theta - \Upsilon_\circ \sin(\omega t)]}. \tag{6.13}$$

Variations are in phase at all ranges. Unlike the range variations produced by orbital motions (section 6.4.3), these do increase in amplitude as $\mathcal{R}_\circ$ increases and also as θ decreases (i.e. when the bands become closely aligned to the beam direction).

Non-stationary case

When a bubble band is no longer stationary, but drifts at speed v towards the sonar (Fig. 6.10) as the sound beam intersecting the band at different times (i.e. the points A and A') oscillates according to, Υ, the following relationship can be obtained, $x_\circ \sin\theta = x \sin[\theta - \Upsilon_\circ \sin(\omega t)] + vt$. It is assumed that θ remains constant during the band advection. Hence the range of the band is,

$$\mathcal{R}^2 - h_a^2 = \frac{[(\mathcal{R}_\circ^2 - h_a^2)^{\frac{1}{2}} \sin\theta - vt]^2}{\sin^2[\theta - \Upsilon_\circ \sin(\omega t)]}. \qquad (6.14)$$

For $v = 0$, equation (6.13) is recovered. If the beam headings are not oscillating, then the range at $t = 0$ is,

$$\mathcal{R}_1^2 = \frac{v^2 t^2}{\sin^2\theta} + h_a^2,$$

which represents an hyperbola distorted by the hyperbola,

$$\mathcal{R}_2^2 = \frac{v^2 t^2}{\sin^2[\theta - \Upsilon_\circ \sin(\omega t)]} + h_a^2,$$

with variations $\mathcal{R}_2 - \mathcal{R}_1$ given by,

$$\mathcal{R}_2 - \mathcal{R}_1 = vt \left\{ \csc[\theta - \Upsilon_\circ \sin(\omega t)] - \csc\theta \right\}. \qquad (6.15)$$

These range variations increase linearly with t as, $2vt \left[\frac{\cot\theta \tan\Upsilon_\circ}{\sin\theta \cos\Upsilon_\circ}\right]$, for a sufficiently large t and $\Upsilon_\circ << 1$.

6.4.5 The estimation of bubble band dimensions from sonographs

Simple geometry is also frequently utilised to provide estimations of the advection, orientation, spacing and thickness of bubble bands. Specific formulations depend upon whether sonar beams are fixed or rotating as the streamlined instrument changes orientation in order to minimise drag.

Fixed Sonar Beams

A set of bubble bands traversing fixed sonar beams are sketched in Fig. 6.11. These bands intersect the forward beam at angle θ and drift laterally at speed V. Assuming that the orientation of bands does not change during their advection through both the forward and starboard sonar beams, the speeds measured in each beam direction are, in respective order, $V_f = \frac{V}{\sin\theta}$ and $V_s = \frac{V}{\cos\theta}$. Each can be measured from the slope of the bands seen in sonographs without targets beneath the range of the sea surface, that

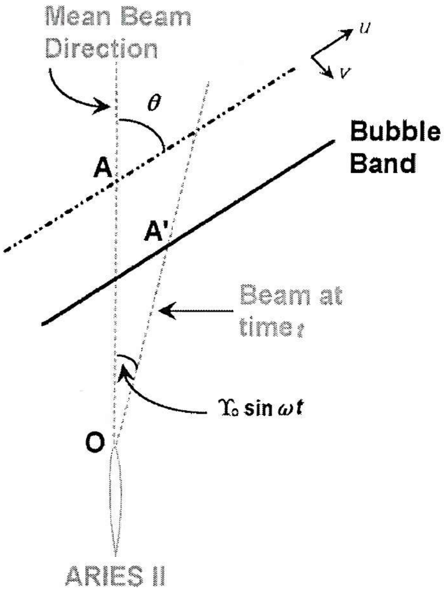

Fig. 6.10: Plan view geometry of a band of scatterers being advected by, say, the normal component of a tidal flow approaching a sonar at speed v. The sonar beam is initially intersecting the band at A, but at time t the band moves, the beam oscillates an angle, $\Upsilon_\circ \sin(\omega t)$, and the intersection point is now A'.

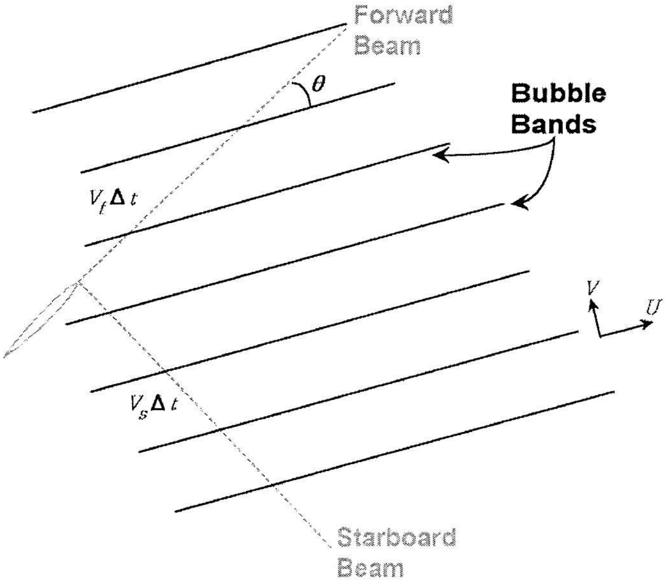

Fig. 6.11: Plan view geometry of a pattern of bubble bands advected laterally within fixed sonar beams. Notice that the number of bands along each beam depends upon the sonar's view direction.

is by determining the changes in position along the surface ($x = vt$ in Fig. 6.6), rather than range. Consequently the lateral drift speed of bubble bands or the near-surface advection of bands normal to their orientation is,

$$V = \frac{V_f V_s}{\left(V_f^2 + V_s^2\right)^{\frac{1}{2}}}, \tag{6.16}$$

which not surprisingly has the same form of equations (6.10) and (6.12) since bubble bands are considered as a set of plane waves. There are no constraints about the length or continuity of bubble bands. They may be of insufficient length to appear simultaneously in the two sonar beams or fragmented, meaning that the distribution of bubbles along the bands is not constant. The bands must have, however, the same orientation and lateral drift speed in both beams. Equation (6.16) fails when either V_f or V_s equals to zero. This does not necessarily imply the absence of bands since, for example, they may be obscured during periods of rain squalls or remain as stationary targets. When the instrument's tilts are significant, measurements of bubble bands are unreliable because its acoustic signal is difficult to recognise.

The orientation of bubble bands relative to the forward sonar beam is,

$$\theta = \arctan\frac{V_s}{V_f}, \tag{6.17}$$

where the angle in the direction of True North is obtained by adding or subtracting to θ the corresponding instrument's headings. The band direction is thus ambiguous to a factor of 180°T, and it is generally chosen to be the direction closest to the wind direction.

The spacing of bubble bands, $\mathcal{S}$, is estimated from the average between neighbouring bands, $\mathcal{S}_f$ and $\mathcal{S}_s$, measured in the directions of the forward and starboard sonar beams respectively. It may be obtained from Fig. 6.7 by denoting the distances QT and PS, as $\mathcal{S}_f$ and $\mathcal{S}_s$ respectively, for example, $\mathcal{S} = \mathcal{S}_s \cos\theta$, or

$$\mathcal{S} = \frac{\mathcal{S}_f \mathcal{S}_s}{\left(\mathcal{S}_f^2 + \mathcal{S}_s^2\right)^{\frac{1}{2}}}. \tag{6.18}$$

Equation (6.18) is also used to estimate the thickness of bubble bands, and a check of consistency on equation (6.17) is the ratio $\frac{\mathcal{S}_s}{\mathcal{S}_f}$. Further if there is a poor estimation to $\mathcal{S}_s$ (i.e. when the acoustic signature of bubble bands in the starboard sonograph becomes faint or absent), then a valid approximation is $\mathcal{S} \approx \mathcal{S}_f \sin\theta$, provided that the band orientation is first calculated (e.g. from equation (6.17)). The opposite applies also to $\mathcal{S}_f$.

Unfixed sonar beams

ARIES II performs its gyrations alternately from clockwise to anticlockwise and vice versa, thereby driving the rotation of the two orthogonal side-scan sonars and affecting the range of the bands detected by both sonar beams.

Consider Fig. 6.12 where the intersection of a bubble band or line of scatterers with the forward and starboard beams is indicated at time t by the points A and B, respectively. At time $t + \delta t$, the beams rotate clockwise at a speed $\frac{\mathrm{d}\Game}{\mathrm{d}t} = \dot{\Game}$, leading to a change in the view direction of the intersection points to A' and B'. Thus when the forward beam has rotated an angular distance R $= \dot{\Game}\delta t$, the line has moved a linear distance $V\delta t$, but the latter maintains a constant orientation θ and lateral drift speed V. To derive a parallel with equations (6.16-6.17) accounting for the effects of beam rotation on the lateral motion of bubble bands, expressions for the apparent speed of the band along each beam are first obtained. By denoting in respective order the distances OA, at time t, and OA', at time $t + \delta t$, as $x_f(t)$ and $x_f(t + \delta t)$, the change in range of the forward beam in the sea surface, $\delta x_f = x_f(t) - x_f(t + \delta t)$, is

$$\delta x_f = \frac{x_f \left[\sin\theta \; - \; \sin(\theta \; + \; \dot{\Game}\delta t)\right] \; + \; V\delta t}{\sin(\theta \; + \; \dot{\Game}\delta t)},$$

after using $\mathrm{OA}' = \mathrm{OC} + \mathrm{CA}'$. The equivalent expression for the starboard beam is,

$$\delta x_s = \frac{x_s \left[\cos\theta \; - \; \cos(\theta \; + \; \dot{\Game}\delta t)\right] \; + \; V\delta t}{\cos(\theta \; + \; \dot{\Game}\delta t)},$$

These expressions simplify to

$$\begin{aligned} \frac{\delta x_f}{\delta t} &= -x_f\dot{\Game} \, \cot\theta \, + \, V \, \csc\theta, \qquad (6.19) \\ \frac{\delta x_s}{\delta t} &= x_s\dot{\Game} \, \tan\theta \, + \, V \, \sec\theta, \qquad (6.20) \end{aligned}$$

for angular distances $\dot{\Game}\delta t << 1$ where terms of the order of $(\delta t)^2$ have been neglected. Equation (6.16) is recovered when $\dot{\Game} = 0$. Assuming that the range of targets along each beam direction, $r_f = r_s = r$ and $x_f = x_s = x$, equations (6.19-6.20) at the depth of sonar transducers are given by,

$$\begin{aligned} V_f &= \left(\frac{R}{r}\right)^{\frac{1}{2}} \left[V\csc\theta \; - \; \dot{\Game}(Rr)^{\frac{1}{2}} \, \cot\theta\right], \qquad (6.21) \\ V_s &= \left(\frac{R}{r}\right)^{\frac{1}{2}} \left[V\sec\theta \; - \; \dot{\Game}(Rr)^{\frac{1}{2}} \, \tan\theta\right], \qquad (6.22) \end{aligned}$$

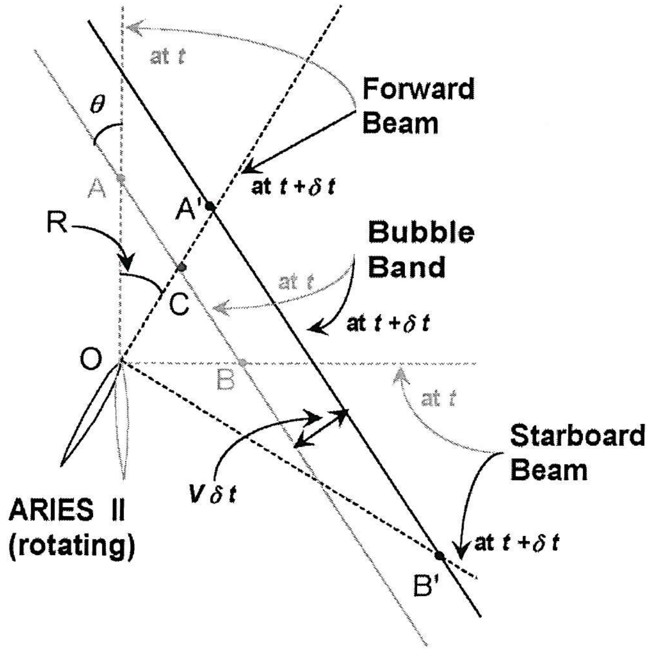

Fig. 6.12: *Plan view geometry illustrating the effect of the instrument's rotation, R, in the estimation of the orientation (θ) and lateral drift speed (V) of bubble bands. The apparent range OA' is measured in sonographs rather than the range OA. Other labels are defined in the text.*

with $R = \frac{r^2 - h_a^2}{r}$, $x^2 = Rr$, $V_f = \frac{\mathrm{d}r_f}{\mathrm{d}t}$, and $V_s = \frac{\mathrm{d}r_s}{\mathrm{d}t}$, the latter two representing the rate of change in time of the position of the bands along the line of intersection of the forward and starboard beams with the surface, respectively. The subtraction of equation (6.22) from (6.21) gives,

$$\theta = \arctan\left(\frac{V_s \; - \; R\dot{\Game}}{V_f \; + \; R\dot{\Game}}\right), \tag{6.23}$$

which reduces to equation (6.17) for $\dot{\Game} = 0$. The rotation of ARIES II is clockwise for $\dot{\Game} > 0$ and the orientation of the band depends upon the sign of both V_f and V_s. A bubble band locally oriented to the right of the forward beam implies $\theta < 0$, whilst for a band to the left of the forward beam, $\theta > 0$. The lateral advection speed is here expressed as,

$$V = \frac{r(V_f \; \tan\theta \; + \; R\dot{\Game})}{[Rr \; (\tan^2\theta \; + \; 1)]^{\frac{1}{2}}}. \tag{6.24}$$

where it is remarked that the speeds V_f and V_s are measured at the same range r in each sonar beam. The sign of V cannot be determined from equation (6.24) because of the root square. It is ascribed to be positive for bands migrating to the right of the estimated true orientation, negative to the left.

The spacing of bubble bands is generally insensitive to changes in the instrument's headings or forward beam orientation, unless there is a change in the wind speed or direction. Equation (6.18) is, in consequence, valid for unfixed sonar beams.

Errors in calculations

Estimations of bubble band dimensions are based upon the visual interpretation of acoustic features, with measurements obtained by overlapping tracing paper onto sonographs in a pseudo-random manner, to avoid tendencies. This simple measurement scheme gives a physical feeling of the evolution of upper ocean processes under different wind conditions and provides a source of comparison for future more robust numerical methods, but introduces errors that are quantified below.

Errors in the estimations of θ and V from sonographs are associated with the uncertainty in estimates of V_f, V_s and $\dot{\eth}$, denoted respectively as σ_F, σ_S and σ_R. The total variance (σ_T^2) for a linear combination of these estimates, $\mathcal{A}V_f + \mathcal{B}V_s + \mathcal{C}\dot{\eth}$, is easily obtained from simple statistics for independent random variables. Thus,

$$\sigma_T^2 = \mathcal{A}^2\sigma_F^2 + \mathcal{B}^2\sigma_S^2 + \mathcal{C}^2\sigma_R^2, \tag{6.25}$$

where equations (6.21) and (6.22) are utilised to derive the following coefficients: $\mathcal{A}^2 = \sin^2\theta$, $\mathcal{B}^2 = \cos^2\theta$, and $\mathcal{C}^2 = R^2\ \sin(2\theta)$. When the orientation of bubble bands is given relative to the True North, the variance of headings and the uncertainty in its alignment with incoming flows (being in general of about ±27°T for mean currents and ±45°T for internal wave flows in spring tides) are added to σ_R^2.

6.5 The passive advection of bubble bands by internal waves

Consider the passage of an internal wave through the pattern of bubble bands sketched in Fig. 6.13. 'Individual' bubbles are initially separated at distance $\mathcal{S}$ apart. If these are neutrally buoyant 'free' bubbles (e.g. there is no mean flow), then they will each experience an advective velocity caused by the internal wave on different times and acting in a direction normal to the orientation of bands. The band will thus be distorted in this direction, and accordingly the spacing $\mathcal{S}$ is altered by the wave. A practical formulation for linking up estimates of the spacing of bubble bands with the distortion produced by the internal wave is devised as follows. Consider now the position of individual bubbles along the internal wave front (Fig. 6.13). Since they are being advected at the same time by an horizontal current with speed U, the distortion of bubble bands (see Fig. 2.7c, for example) will be passive if it is caused solely by the internal wave in a simple advective process with no added surface wave breaking. This

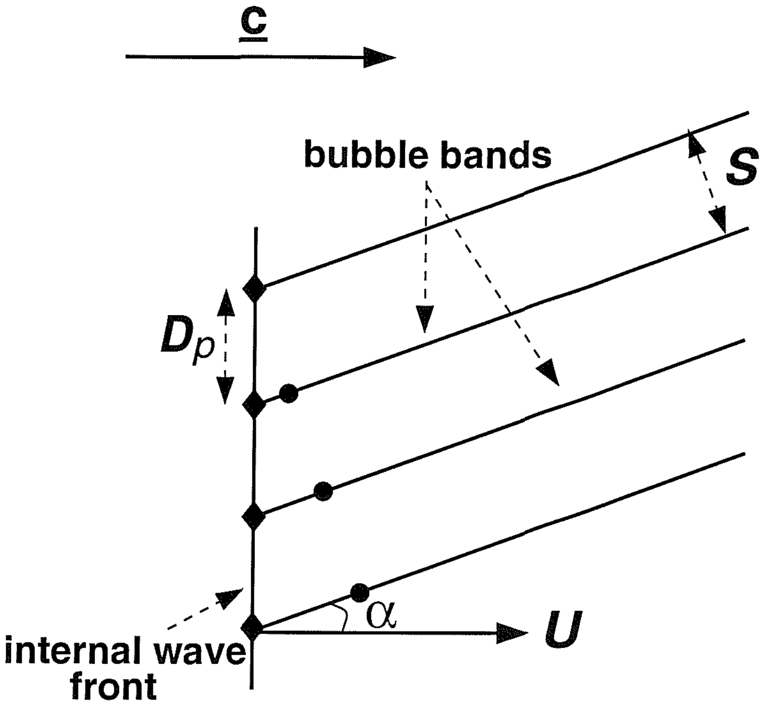

Fig. 6.13: *A diagram for the interaction between a steady and stable pattern of bubble bands and an internal wave. Positions of 'individual' bubbles in the direction normal to the band orientation are indicated by the symbol • and those along the internal wave front by ♦. The wave front represents the line of interaction between bubbles and particles of fluid advected by the wave where $\mathcal{D}_p$ is the distance of passive advection. The spacing of bubble bands is denoted by $\mathcal{S}$, the speed of the horizontal current induced by the wave travelling to the right with phase speed C, is denoted by U and the angle between bubble bands and the direction of propagation of the internal waves by α.*

can be defined using a parameter ($\mathcal{P}$) given by,

$$\mathcal{P} \doteq \frac{\mathcal{S}}{\mathcal{D}_p \cos(\alpha)} = 1, \tag{6.26}$$

where the distance $\mathcal{D}_p$ will remain constant during the wave propagation, more accurately, within some percentage determined by error bars associated with measurements of both $\mathcal{S}$ and α. Therefore the distortion of bubble bands will be active when equation (6.26) is not satisfied. We can further assess the variation of $\mathcal{S}$ from its projection along the propagation of the wave, that is

$$\mathcal{X} = \mathcal{S} \sin(\alpha), \tag{6.27}$$

which, assuming that the band orientation remains constant during the propagation of the internal wave, is independent from the view direction of sonar beams and, if the distortion is passive, then

$$\mathcal{X}_p = \frac{1}{2}\,\mathcal{D}_p\,\sin(2\alpha). \qquad (6.28)$$

Whilst equation (6.26) provides a test of consistency for passive advection, both (6.27) and (6.28) are convenient for estimating whether the spacing of bubble bands might be closer over the wave trough than over the convergence zone of the internal wave. Thus, for example, the number of bubble bands (N) in the direction of wave propagation is, $N = \frac{2L\mathcal{X}}{\mathcal{S}^2} + 1$, where L may be estimated from equations (2.14) or (2.19) and $2L >> \mathcal{S}$.

6.6 Summary

A summary of the main quantitative results obtained in the current chapter are given in the following bulleted list.

- Non-linear internal waves of depression registered by ARIES II produce a maximal apparent reduction in the range of the sea surface of 0.5 m, a result of ignoring the effect of temperature on the speed of sound.
- It is estimated that the errors in detecting near-surface targets when the refraction of sound rays through the thermocline is neglected are roughly, in the absence and during the passage of internal waves, 6% and 2% the maximal effective range of targets (i.e. 188 m) respectively. The latter is probably larger for steep waves.
- Sound rays appear to be reflected downward from the thermocline at a critical angle of about $(70 \pm 10)^\circ$, implying ranges less than 30 m.
- Maximal variations in the vertical inclination of the starboard beam caused by fore-aft tilts of the instrument, together with the reverse effect, are both of the same order of magnitude leading to beam migration of 6 m at the surface.
- The effect of shadowing of a portion of a surface wave crest by a wave trough is only important at ranges beyond the maximal effective range of sonar beams (i.e. 188 m).

Part III

OBSERVATIONS AND CONCLUSIONS

7. NOVEL FEATURES CAPTURED IN SONOGRAPHS

The purpose of the current chapter is to give a description of the main characteristics of acoustic images captured by ARIES II. Although part of the material has already been presented by Thorpe *et al.* (1998), this description places greater emphasis on the inspection of particular novel acoustic features not detected, or at least not reported, by any other sonar technology. In addition, some applications that demonstrate the potential use of ARIES II to examine and quantify turbulent phenomena in the upper ocean are briefly described.

7.1 Tides and internal waves

The surface tide in the Malin-Hebrides Shelf is evident in the pressure record (Fig. 5.2a) and at the range of the sea surface in long-period sonographs (Fig. 7.1a,b; label A), both showing sinusoidal variations which are in phase and have equal amplitude. Therefore, Fig. 7.1 complements Fig. 5.2. There are also acoustic targets that contribute to the zones of high local scattering observed beneath the range of the sea surface (e.g. Fig. 7.1b, label C; see also Fig. 6.2), but attenuate the signal from larger ranges (e.g at label D). These targets are coincident with the troughs of ISWs shown in Fig. 7.1e, thereby forming themselves the acoustic signatures of non-linear internal waves. The origin of targets is attributed to be biological, probably zoo-plankton and small fish, but many marine organisms (e.g. shrimp) will scatter sound. Biological scatterers are therefore carried down near the beams, at sonar depth, in the internal wave flows which may induce a downwards migration of the streamlined instrument and an apparent elevation of the sea surface (e.g. Fig. 7.1a,b; label B). At this time (i.e. 9.8 h into the record), ARIES II displays a rapid change in direction from about 300°T to 340°T, implying a 160°T flow associated with internal waves (Fig. 7.1e,f). Although the presence of internal waves is elusive at 55 m (Fig. 7.1e), the current meters at both levels also change direction towards NE as the waves pass. At a depth of 30 m in particular, the current meter is oriented to 133°T by a (151 ± 12)°T relative flow with a speed of (70.3 ± 7.1) cms^{-1}. ARIES II therefore aligns within 9°T of this relative current

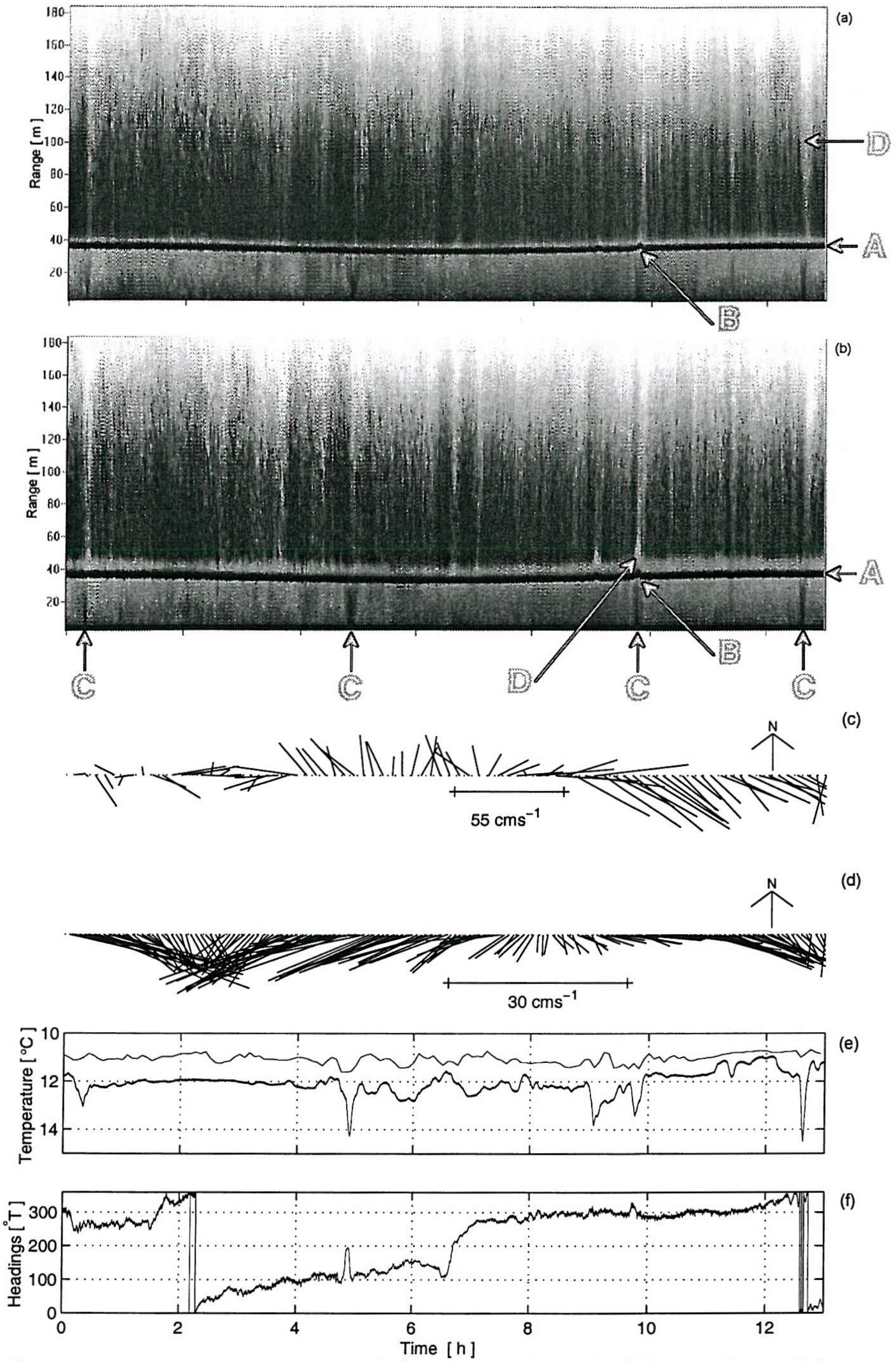

Fig. 7.1: *Long-period sonographs: (a) Forward and (b) starboard beams. Features with high scattering are shown in black. Currents: (c) at 30 m and (d) at 55 m. Temperature with vertical scale increasing downwards: (e) at 55 m (thin solid line) and at 36.1 m (thick solid line). The latter is Fig. 5.2c, repeated here for correlating with sonographs. (f) Headings, showing the direction in which the forward sonar beam is pointing and is therefore contrary to the current direction. The start of ARIES II records is 07:07:00 GMT. The corresponding starting times for the current meter records are, in respective order, 07:12:30 GMT (30 m) and 07:07:30 GMT (55 m), both displayed with a time scale consistent with that for ARIES II. Mean wind speed from the DERA-ship is,* $\mathcal{U}_{10} = (15.9 \pm 2.1)$ *ms*$^{-1}$ *from* $(298 \pm 19)^{\circ}T$.

direction (see also section 5.3.2).

Beyond the range of the sea surface, scattering is from targets detected in the water, below the sea surface and along the sea surface itself where the most common scatterers are near-surface bubbles created by breaking waves. Variations of scattering intensity with time reflect changes in the sea surface roughness and bubble production under different wind conditions and breaking activity (i.e. frequency of occurrence and spatial distribution). Other factors include changes in beam orientation as the instrument aligns in response to currents, and variations caused by the presence of sub-surface scatterers which attenuate the sound reaching up the surface. Variations in acoustic intensity with range arise from the distribution of scatterers in the beams and by the attenuation of sound with range. There is also a reduction in scattering at ranges immediately after the sea surface return. It appears to result from the inclination angle of the beam pattern (i.e. 20° above the horizontal) in which a side-band shows insufficient power to reveal the structure of targets.

7.2 Rain squalls and biological scatterers

Acoustic features labelled A in Fig. 7.2a,b are qualitatively similar to those reported by Thorpe and Hall (1983) and Thorpe *et al.* (1985) for the effect of passing rain showers on sonographs, but no confirmation of precipitation (i.e. drizzle or heavy rain) was reported in the ARIES II deployment site (see section 4.2). These zones of enhanced scattering are not associated with internal waves (e.g. a raw voltage fluctuation detected in Fig. 7.2e occurs at the centre of the temperature fluctuation in Fig. 7.2f), and neither reflect changes in the orientation of sonar beams because headings remained roughly uniform (Fig. 7.2g), showing alignment consistent with the direction of currents (Fig. 7.2d). There are several causes that may contribute to enhance the near-surface scattering when rain-drops impact onto the water surface. Rain-drops generate both capillary ripples which add small-scale roughness to the sea surface, and tangential stresses that increase gravity waves (Poon *et al.*, 1992; Yang *et al.*, 1997; Contreras *et al.*, 2003). A large number of micro-bubbles are generated by secondary splashes after large rain-drops, flattened by air drag, strike the water surface (e.g. those with diameters $> 2200\ \mu$m), thus providing an additional source of near-surface scattering (Nystuen and Medwin, 1995; Thoroddsen *et al.*, 2003).

A general decrease in the scattering intensity with time, as observed in Fig. 7.2a,b, is probably associated with a reduction in the wind speed. Acoustic signatures of swimming marine organisms and breaking waves occur in the two beams; they are illustrated in Fig. 7.2a,b (marked B and C respectively) and particularly in Fig. 7.2e where the maximal raw voltage ($\approx$3.5 V) is evident at a mean range of 15 m from the

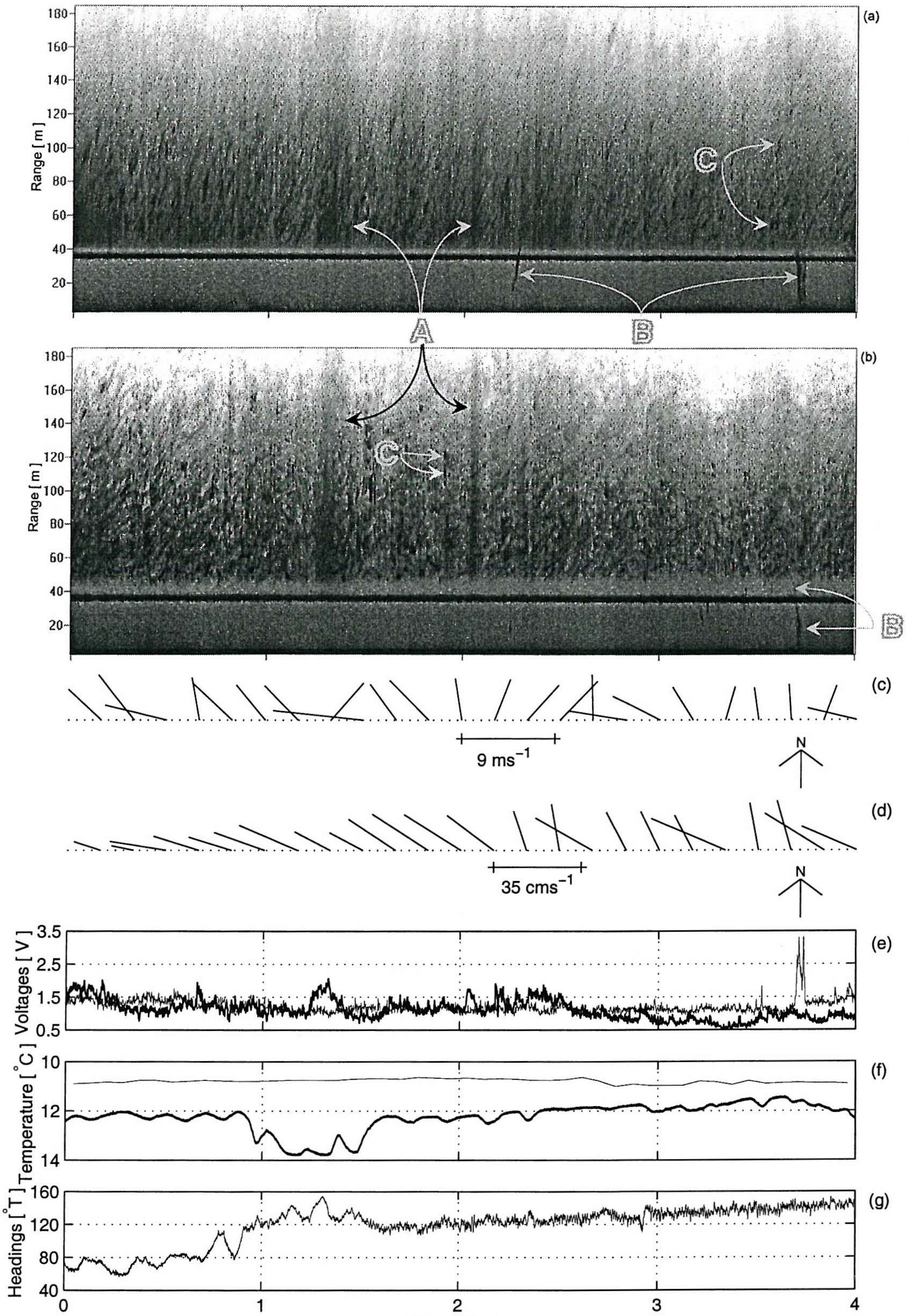

Fig. 7.2: *Similar to Fig. 7.1, but wind (from the meteorological buoy), currents (at 30 m), temperature and headings are shown in (c), (d), (f) and (g), respectively. Mean raw voltages for (a) are shown in (e) at the following ranges: (80 ± 40) m (thick solid line) and (15 ± 10) m (thin solid line), both with a resolution of 23.4 cm and 5.5 s. The ARIES II records start at 17:15 GMT on 23th August 1995.*

forward beam. (It is worth noticing that the maximal output of the acoustic signal is of about 10 V, and although only 1% of the signal is roughly recovered at a 15 m range its variations are very important). Biological scatterers ascending to near the sea surface (range increases with time) at a speed of about 23 $\mathrm{cms^{-1}}$ or 20 m in 87 s are observed at 2.2 h (19:30 GMT) into Fig. 7.2a, suggesting small fish migrating and meet planktonic organisms to feed on grounds. The enlargement in Fig. 7.3 shows in addition biological targets, but approaching rapidly towards the two beams (range decreases with time) below the water surface (label A) and along the sea surface (label C). Targets remaining stationary (hovering without motion) are labelled B. The mean speed of targets, estimated at a range of 27 m, is of about (21.6 ± 15.1) $\mathrm{cms^{-1}}$ which is larger than the vertical speeds ascribed to day-night diel migrations (see section 2.1.5) and consistent with reported fish speeds (e.g. Greer Walker *et al.*, 1978). The estimated speeds are also of the same order of magnitude as currents at 30 m, which for Fig. 7.3 are (35.2 ± 0.1) $\mathrm{cms^{-1}}$ towards (334 ± 24)°T.

7.3 Rain squalls and the damping of surface waves

Fig. 7.4 shows the effects of rainfall in calming down the sea surface. Signatures of breaking waves occur like flecks in Fig. 7.4a,b (labels A) where the number of breaking events tends to decrease after rain showers (labels B) have elapsed, between 40 and 50 min into the record. The generation of near-surface bubbles is thus reduced and the scattered sound lacks structure in Fig. 7.4a,b, which can also be observed in raw voltages (Fig. 7.4e) averaged at a range of 80 m from the starboard beam. This tendency is explained as follows. Rain itself is known to cause normal stresses that increase the dissipation of surface waves within the rain region (e.g. Yang *et al.*, 1997). Although rain-generated capillary ripples contribute to enhance the surface roughness (e.g. the hyperbolic targets labelled D), the net effect is the damping of surface waves, particularly at low winds. Following Yang *et al.* (1997), the normal stress induced by rain is proportional to the vertical component of the impact velocity of rain-drops and to rain intensity. Since the former is constant, the normal stress is then determined solely by the rain intensity, that is independent of wind speed. Hence these rain squalls captured by ARIES II are probably a signature of heavy rain. Furthermore, the loss of structure in both sonographs is also in part because there is no significant contribution from wind to generate ripples and to induce new breaking waves or flecks.

The region of near-surface enhanced scattering labelled C in Fig. 7.4a,b is coincident with the arrival of a packet of ISWs (Fig. 7.4f), where the leading wave is detected by ARIES II about 9 min before its arrival at the current meter mooring. As stated in section 2.3, internal waves may form regions of increased scattering beyond the range of

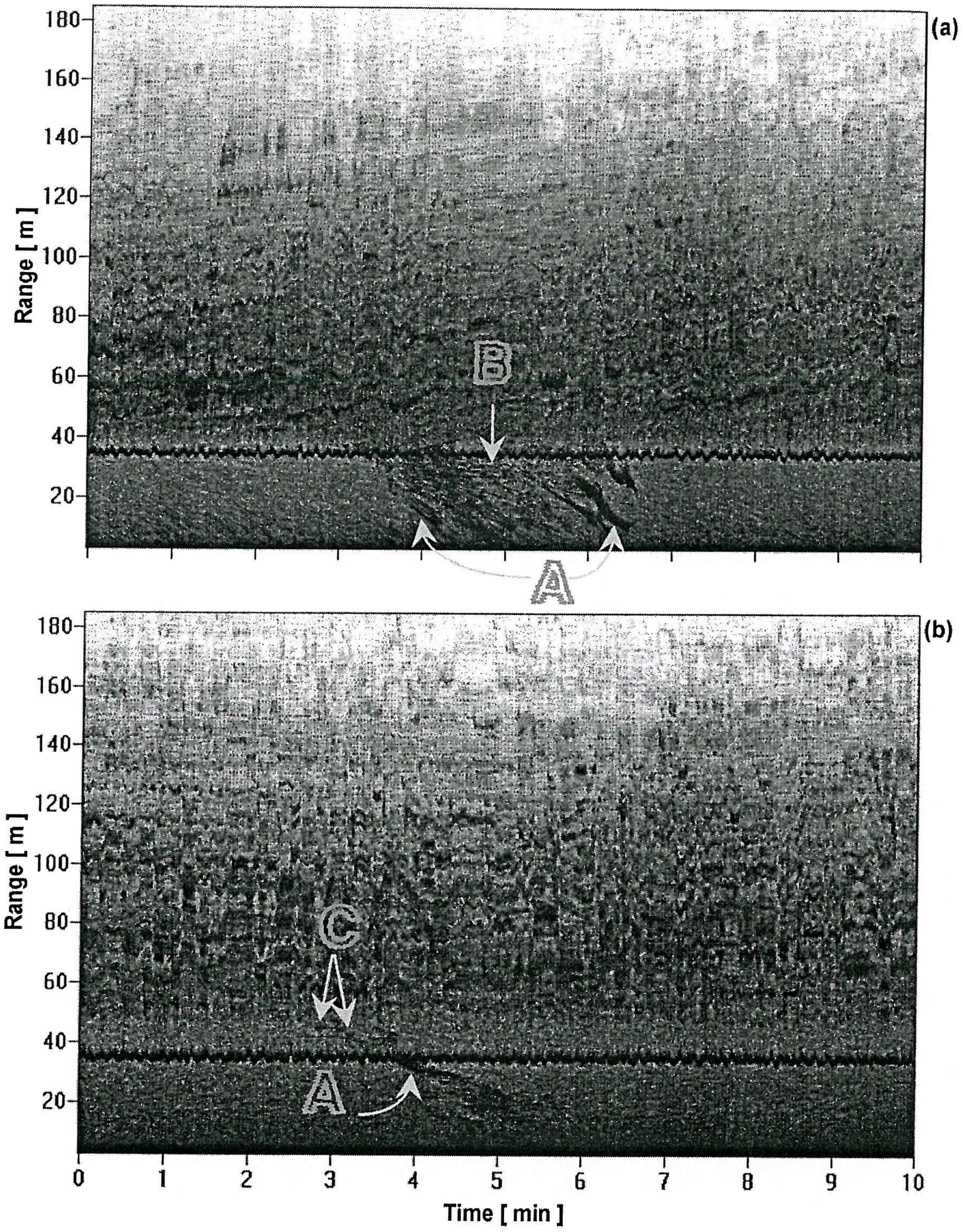

Fig. 7.3: Enlargement of Fig. 7.2a,b illustrating biological scatterers swimming near the sea surface. The sonographs start at 20:53 GMT.

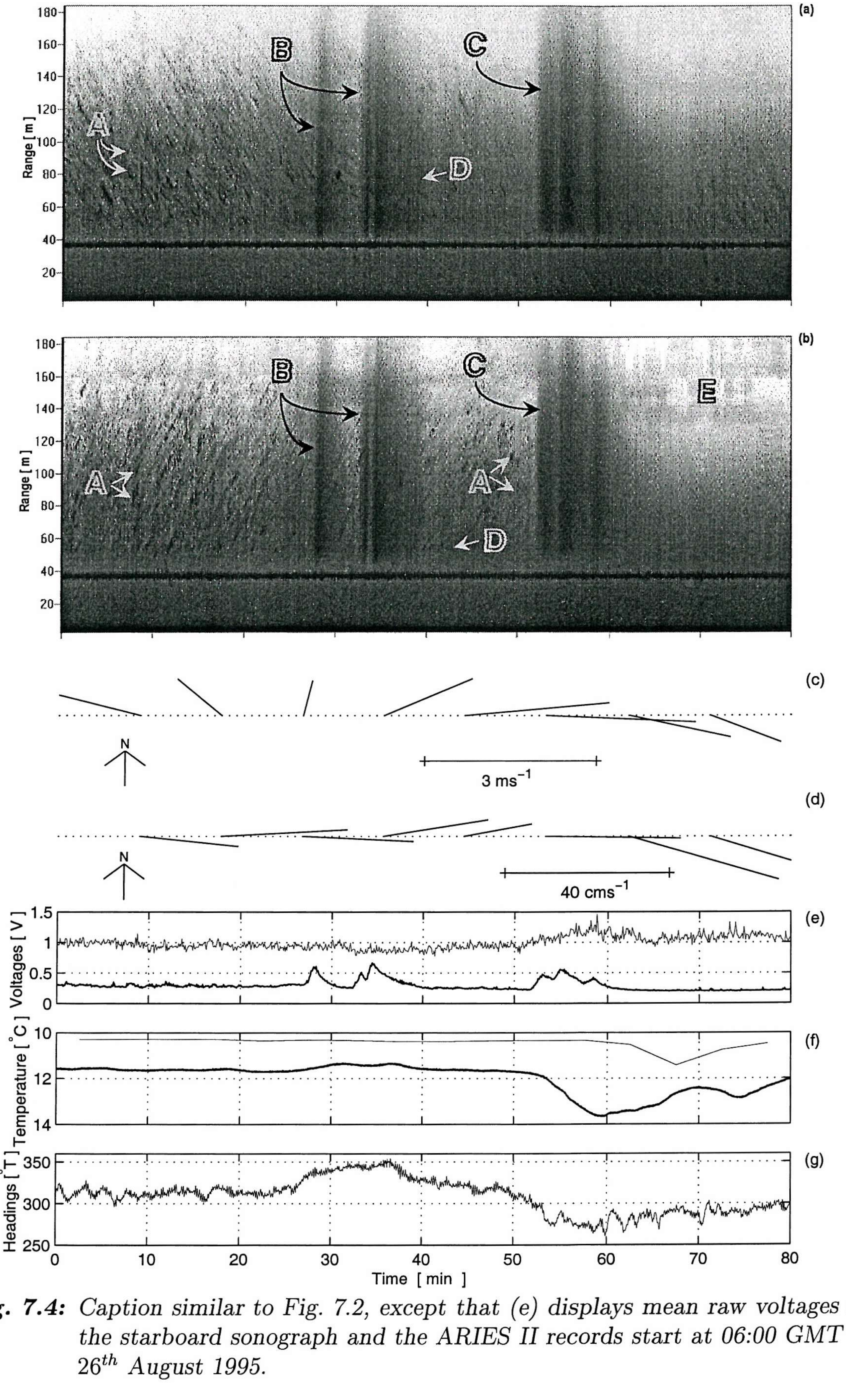

Fig. 7.4: *Caption similar to Fig. 7.2, except that (e) displays mean raw voltages for the starboard sonograph and the ARIES II records start at 06:00 GMT on* 26th *August 1995.*

the sea surface which are characterised by an abrupt decline in the acoustic signal at far range. This is not the case here since the acoustic signal is similar to the signatures of rain squalls (e.g. Fig. 7.4e), and it is possible that the internal wave signature is being masked by the rain effects. The important point, however, is that sonographs are not enough to prove the identity of rain beyond doubt. To do this, auxiliary temperature measurements, field confirmation using rain gauges or underwater instrumentation (i.e. through acoustic mini-drifting buoys; see Nystuen and Selsor, 1997) would be required.

Given the low wind conditions in which ARIES II was operating, Fig. 7.4a,b may additionally show secondary reflections between the surface and the sea bed at far range. Thus, reflections from ARIES II and the buoyancy sphere would appear at ranges less than 100 m, whilst second reflections between the surface and the bottom and back again, at ranges of about 180 m. These reflections, however, are not clearly observed in the sonographs. Although the reflection at roughly 149 m range in the starboard sonograph represents an echo from the sea bed itself (see label E in Fig. 7.4b), it is not observed in the forward sonograph. Therefore the reduction in the acoustical signal marked E, between 140 m and 160 m, is probably a distortion caused by the movement of the toroidal buoy.

7.4 Internal waves and biological scatterers

Typical acoustic signatures of internal waves consist largely of zones of enhanced scattering located beneath the sea surface and starting at very short range from sonar beams (e.g. Fig. 6.2, label C; Fig. 7.5, label A), and either scattering bands (e.g. Fig. 6.2, label H) or patches (e.g. Fig. 7.5, label B) showing an intensification in the near-surface scattering that accompanies the forward flank of wave troughs at ranges greater than that of the sea surface (see also section 2.3). However, these signatures by themselves do not draw a definitive distinction from those ascribed to rain squalls or biological scatterers detected outside the internal wave troughs (e.g. label C in Fig. 7.5). Consequently their description requires extra support from other sensors.

Fig. 7.5e shows temperature fluctuations at ARIES II depth, between 10 and 20 min and about 60 min into the record, indicating internal waves of depression with amplitudes estimated to be of about 7 m and 14 m respectively. The zone of enhanced scattering marked B (Fig. 7.5a and d) is therefore occurring over the wave trough; it is possible that the interaction between the wave-induced near-surface flows and surface waves (see section 2.3.1) results in a high concentration of bubbles, as suggested by the acoustic signatures of breaking waves shown in Fig. 7.5a (label D). In the starboard sonograph, this zone appears to be obscured by biological scatterers inducing a higher scattering below the sea surface than in the forward sonograph (not shown). Although

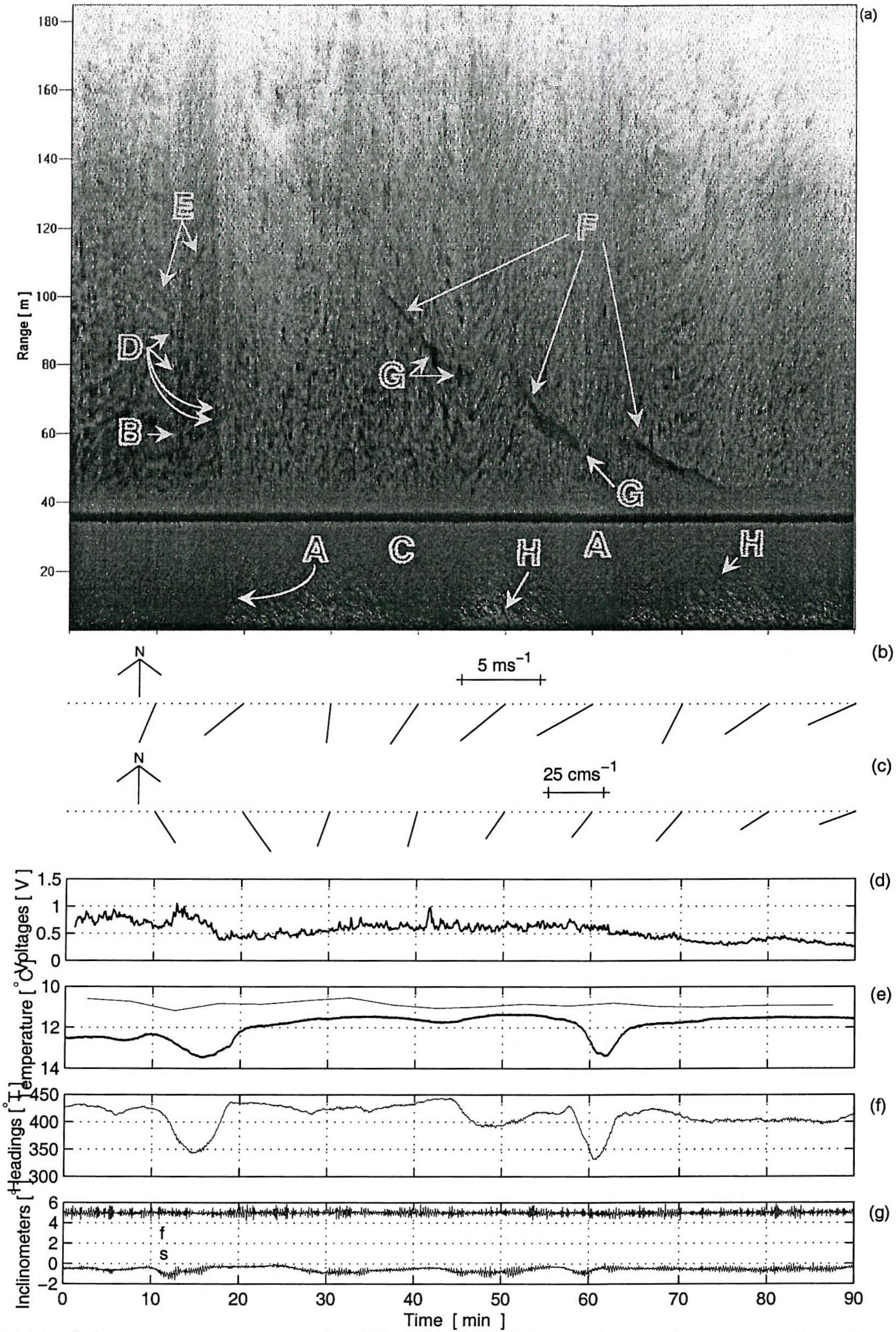

Fig. 7.5: *(a) Forward sonograph; (b) Wind at 10 m above the sea surface from the meteorological buoy; (c) Currents at 30 m; (d) Mean raw voltages at a range of (80 ± 40) m from the forward sonar beam; (e) temperature increasing downwards, at 55 m (thin solid line) and at 36.1 m (thick solid line); (f) Headings; and (g) Inclinometers where pitching is referred to as 'f' and rolling as 's'. Records start at 13:00 GMT on 18th August 1995.*

the signatures labelled A are not clear enough to indicate whether biological scatterers are swimming around or remaining stationary in the internal wave flow, Fig. 7.5a shows scattererers, between 20 and 50 min, both approaching the forward beam at ranges roughly less than 18 m and receding quickly at larger ranges. Other biological scatterers are visible as transient targets (label H).

The enhanced zones A and B are enforced further as signatures indicating the presence of internal waves by Fig. 7.5f which shows ARIES II turning anticlockwise, from 68°T to 344°T in 5 min and from 70°T to 333°T in 3 min, implying current pulses towards 164°T and 153°T respectively. The latter rapid rotation has perhaps caused the absence of a near-surface acoustic signature in the forward sonograph at 60 min. Several acoustic features appearing to change direction are also shown in the forward sonograph (e.g. those marked E), but it is in reality the streamlined instrument that has modified its orientation and therefore the features' view direction. There is no clear evidence of internal waves at 55 m depth (Fig. 7.5e), and the current meter resolution at 30 m (Fig. 7.5c) does not allow a reliable estimation of the relative current. Hence the angle between the forward beam and the direction of the internal wave is unknown. The pressure fluctuations measured by ARIES II during the propagation of these waves are of 0.1 m.

Fig. 7.5a is particularly interesting because of the unusual acoustic features approaching the forward beam (label F), although some of the features show the characteristic signature of breaking waves (label G). After an exhaustive search of ship's navigation tracks in both the deck and scientific log books for Challenger 121A/SES 3B (Sherwin and Simpson, 1996, see also section 4.2), no evidence of cruise activities were found during the date stated in Fig. 7.5. The DERA-ship Colonel Templar was also working in the Malin-Hebrides area, but we do not have her cruise track for the preceding date. Ship wakes are known to leave an extensive (e.g. 80 m wide in range) and relatively persistent (e.g. 5 min) acoustic patch (e.g. Thorpe and Hall, 1983, Fig. 8a) formed by bubbles generated by the ship's propellers. The patch does not cross the range of the sea surface and the bubble distribution within the wake varies in density and width, probably caused by the passage of the ship though the surface waves. When the ship is stationary, the noise caused by the engine and propeller is registered by the sonars as a continuous vertical line of strong scattering that extends to far ranges. These characteristics are not at all shared by the features marked F, although wind conditions in Fig. 7.5 are similar to those in Thorpe and Hall (1983). In addition, the temperature signal of internal waves gives confidence in that these features are not a ship's wake, but are probably biological in origin. Acoustic features between 65 and 80 min into Fig. 7.5a are approaching the forward beam over the backward flank of the internal wave trough, until they remain stationary after the wave has passed by. The features are apparently affected by divergent surface currents, leading to the exclusion of the targets from the wave trough. It is probable that these are swimming scatterers which have failed to catch the internal wave to be transported in the direction of wave propagation. Perhaps this short-duration wave is not an appropriated transport mechanism for biological scatterers.

7.5 Internal waves and the sea surface roughness

Fig. 7.6 (i.e. label A) displays another example of the zone of enhanced scattering at ranges beyond the sea surface specified earlier to be caused by non-linear internal waves. There are linear features moving away from the sonar beam (Fig. 7.6a) and approaching the starboard beam (Fig. 7.6b), but at much lower local speed, during the first 17 min of the records. What strikes the naked eye is the apparent change in orientation of the linear features labelled B. However, it is actually the streamlined instrument that has changed orientation, from 50°T to 273°T in about 3 min (implying the onset of an eastward flow) and from about 260°T to 40°T between 28 and 30 min into Fig. 7.6e. Subsequently the initial view direction of features observed in the first 17 min (Fig. 7.6a) is roughly returned to after the internal wave has passed by. The episodic intensification of near-surface scattering over the internal wave trough is obscuring the linear character of features, which have been identified as bubble bands delineating convergent surface flows of Langmuir circulation (see section 7.8). It is believed that the spacing of bubble bands decreases between the forward flank of the wave and the centre of the wave trough, thereby concentrating near-surface bubbles and increasing acoustic returns. Furthermore, it is unclear to what extent the breaking of surface waves produces additional bubbles or whether the pattern of bubble bands breaks down and regenerates during the propagation of the internal wave. Signatures of breaking waves are more evident following the internal wave propagation (label D in Fig. 7.6a,b).

The vertical lines marked C in Fig. 7.6a coincide with the maximum voltages for the forward beam, at 19 min and 28 min into Fig. 7.6c respectively. These lines appear to indicate the convergence and divergence zones of the internal wave, that is the zones of minimum (negative straining) and maximum (positive straining) surface current gradients.

Wave-induced fluctuations for the 30 m current meter and ARIES II are, in respective order, 93°T and 280°T (i.e. towards 100°T), but the estimated relative current is (30.1 ± 6.0) cms^{-1} towards (61 ± 1)°T. The amplitude of the internal wave of depression shown in Fig. 7.6d is of about 27 m, whilst the pressure fluctuation associated with the wave is of about 0.25 m.

Wave groups are clearly observed in Fig. 7.6f; they apparently increase and decrease

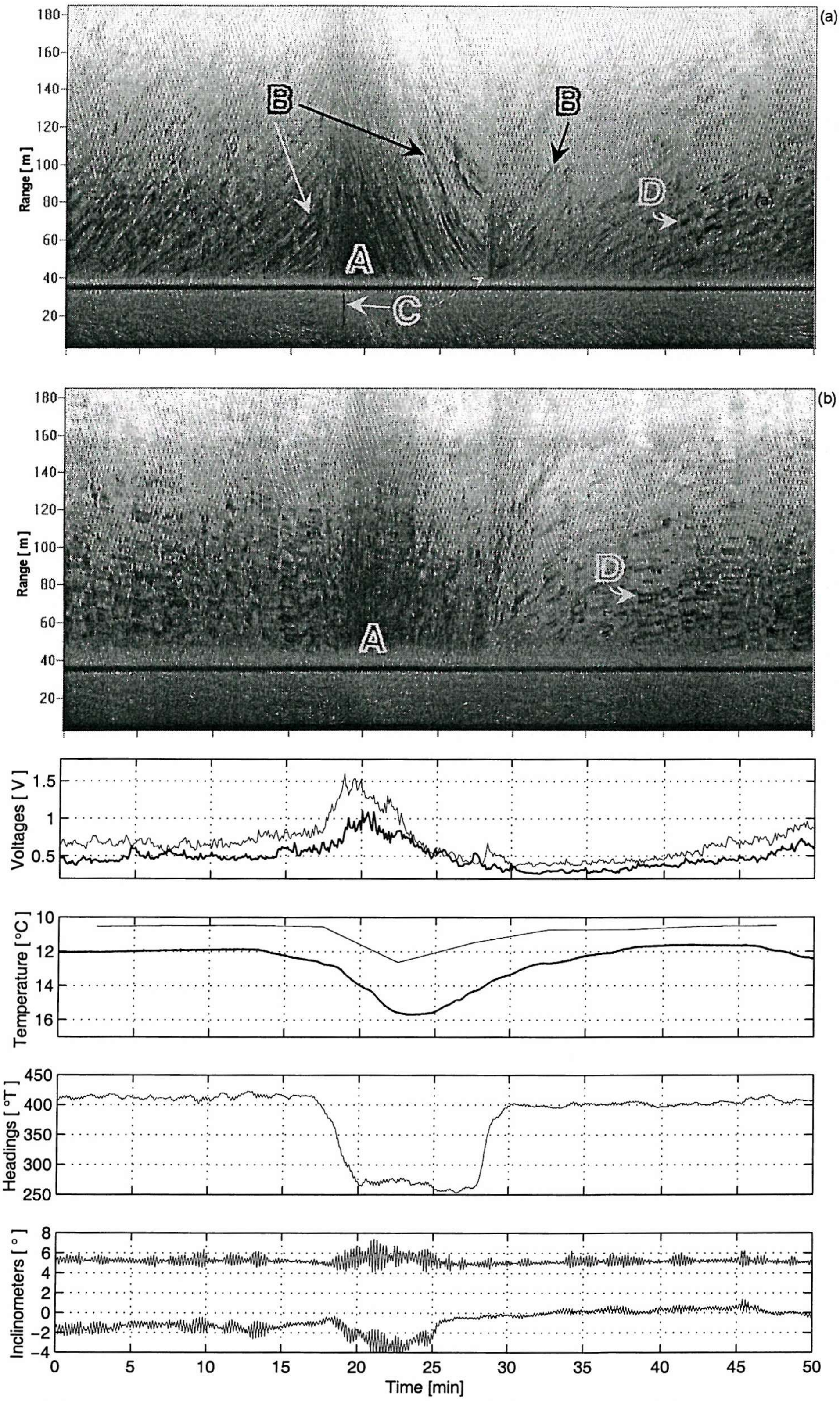

Fig. 7.6: *(a) Forward sonograph; (b) Starboard Sonograph; (c) Mean raw voltages at* (80 ± 40) *m range for the forward (thin solid line) and the starboard (thick solid line) beams; (d) Temperature; (e) Headings, with the vertical scale rolled over 360° T for convenience; and (f) Inclinometers. Other details as in Fig. 7.5. Mean wind and (30 m) current conditions are, in respective order,* $\mathcal{U}_{10} = (5.2 \pm 0.1)$ *ms*$^{-1}$ *from* $(266 \pm 10)°T$ *and* (16.9 ± 4.0) *cms*$^{-1}$ *towards* $(188 \pm 54)°T$*. Records start at 17:00 GMT on* 20^{th} *August 1995.*

Tab. 7.1: *Estimations of wave period and amplitude for Fig. 7.7. Here T_s and T_z denote the wave period at the sea surface range (Fig. 7.7a) and the zero-up crossing period from the pressure record (Fig. 7.7b) respectively, and c_g is the group speed (see section 2.3.1). The wave direction could not be estimated with any confidence.*

Label	T_s	T_z	Δp	$\mathbb{A}$	c_g
	(s)	(s)	(x10^3 Pa)	(m)	(ms^{-1})
A	-	10.0	1.5	0.60	7.5
B	11.5	11.8	2.5	0.68	8.8
C	12.2	12.0	3.0	0.78	9.0
D	-	13.3	2.0	0.44	10.0

amplitude in the internal wave trough. This is worth pursuing and an 8 min enlargement of Fig. 7.6 is shown in Fig. 7.7. It seems that the roughness of sea surface has been increased under the action of internal wave-induced flows (Fig. 7.7a, label B). However, the zone of increased roughness is in phase with the wave groups detected in the pressure record (Fig. 7.7b) and have an estimated period of about 12 s (Table 7.1). In addition, the phase speed of the internal wave is 73.6 cms^{-1} (which has been estimated using equations (2.15) and (2.18) with $\varrho = 0.9987$ and $\gamma = 0.3273$, the latter with $h_1 = 36$ m and $h_2 = 110$ m), that is one order of magnitude less than the estimated group speed of surface waves. Consequently, the Phillip's resonance condition (section 2.3.1) is not satisfied and both the increase in wave amplitude and the enhancement of surface roughness over the forward flank of the internal wave are unlikely to be caused by the straining of surface waves by internal wave flows. The scale in Fig. 7.7a, on the other hand, is not enough to determine whether high-frequency waves (e.g. 3-4 s) are superposed on the wave groups at the range of the sea surface (see also section 6.2.1).

Signatures of biological scatterers are also observed in the wave trough (Fig. 7.7a, label E). Targets may appear stationary or approaching the forward beam at close range, and migrating towards the sea surface. This is indicative of non-passive targets, probably small fish. An enlargement is displayed in Fig. 7.8. At short range, targets show a predominant banding character (label A), often persisting in the forward beam longer than in the starboard beam. Most of the banding in sonographs is approaching the forward sonar. The starboard sonar generally has little directional bias (label D), although at larger ranges the trend is an increasing of range with time (e.g. label E). The banding seems to imply individuals are being carried down beam (label A), near to

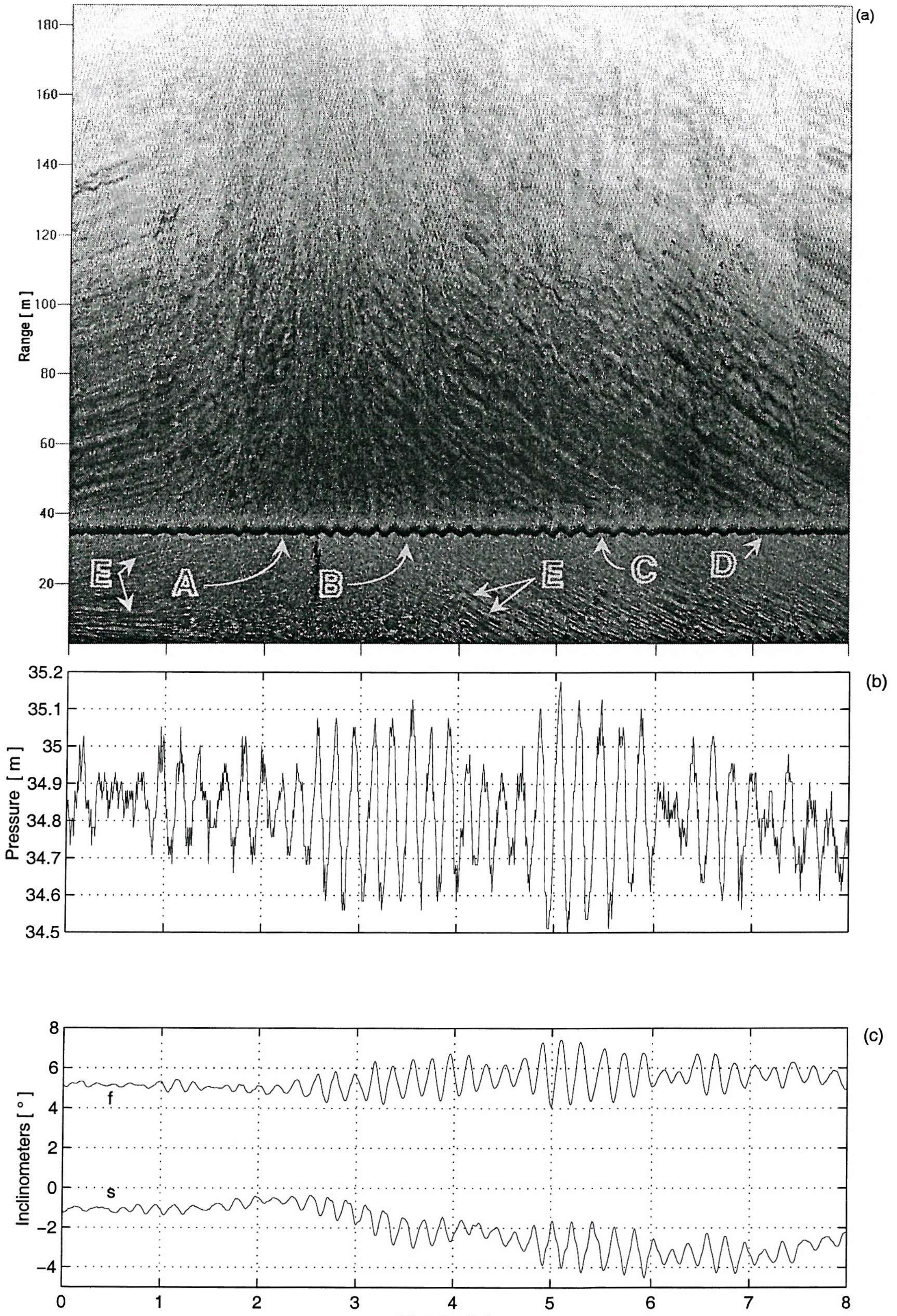

Fig. 7.7: *Enlargement of Fig. 7.6. (a) Forward sonograph; (b) Pressure at transducers level; and (c) Inclinometers. Other details as in Fig. 7.5. Records start at 17:16 GMT.*

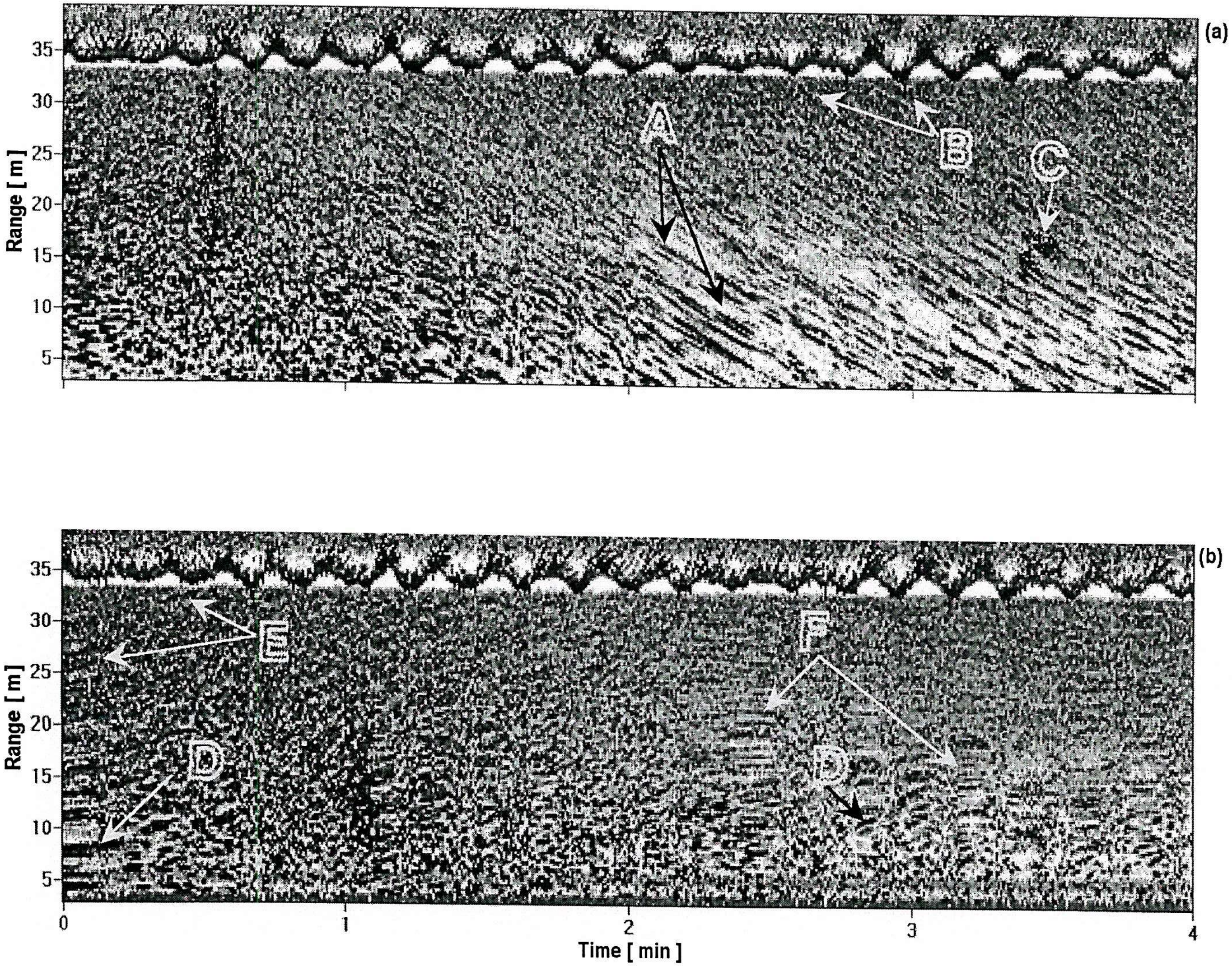

Fig. 7.8: *Normalised enlargement of Fig. 7.7 starting at 17:18 GMT. (a) Forward sonograph; and (b) Starboard sonograph. The amplitude of wave groups is of about 0.9 m. Shading darkens with increasing acoustic returns.*

sonar depth, but more diffuse populations are occasionally present (label C). Targets also appear far from the forward sonar (label B), perhaps migrating down from the sea surface (label B), whilst targets marked F in the starboard sonar suggest a pattern caused by port-starboard tilts when ARIES II is veering (see for example Fig. 7.6e,f).

7.6 The hyperbolic acoustic signature of surface waves

A series of curvilinear streaks accompanying wave groups, clearly marked at the sea surface range above ARIES II, are shown in Fig. 7.9a (label A). The rate of change of the range of the streaks with time, measured directly from the forward and starboard sonograph (although the latter not shown) and averaging over at least three dominant streaks, is consistent with the phase speed of swell (Table 7.2). Hence the streaks travel at phase speed following the hyperbolic paths described in section 6.4. The hyperbola overlaid in Fig. 7.9a (label G) fits the shape of the streaks quite well. These near-vertical curvilinear streaks are generally formed by many short, less steeply inclined, higher-frequency streaks which generally identify individual breaking events, like that labelled B in Fig. 7.9a. Thus, the acoustic signature of low-frequency waves appears to result from specular reflection of high-frequency waves superposed on or over swell waves.

High-frequency waves, typically with periods in the range (2-4) s, are better observed at ranges slightly beyond the sea surface (label C, and also label F in Fig. 7.9c) and during moderated wind conditions, particularly in between different wave groups (Fig. 7.9b, label D). At high wind speeds the direction of high-frequency waves is generally difficult to estimate, whilst at low wind speeds it is the propagation direction of swell that becomes difficult to discriminate. Label E in Fig. 7.9c constitutes an exception. It followed a period of rain squalls (see Fig. 7.4 for reference) and the source of scattering is perhaps associated with the remnants of bubbles created by the impact of rain-drops on the surface. On the other hand, the enhancement in the scattering of targets occurring close to the crests of wave-groups suggests the influence or amplification of high-frequency waves (label F) riding on the swell crests, although no clear signatures of breaking waves are perceptible in the prevailing low-wind conditions.

Fig. 7.9c also shows that the slope of the streaks decreases with time (label G) and meets the surface echoes on the tilted surfaces of swell. Since surface waves appear to propagate towards the forward beam (no evidence of propagation was observed in the starboard beam, see Table 7.2), then scattering comes from the backward face of wave crests, the region near the node where the mean wave profile is most nearly normal to the direction of the forward beam.

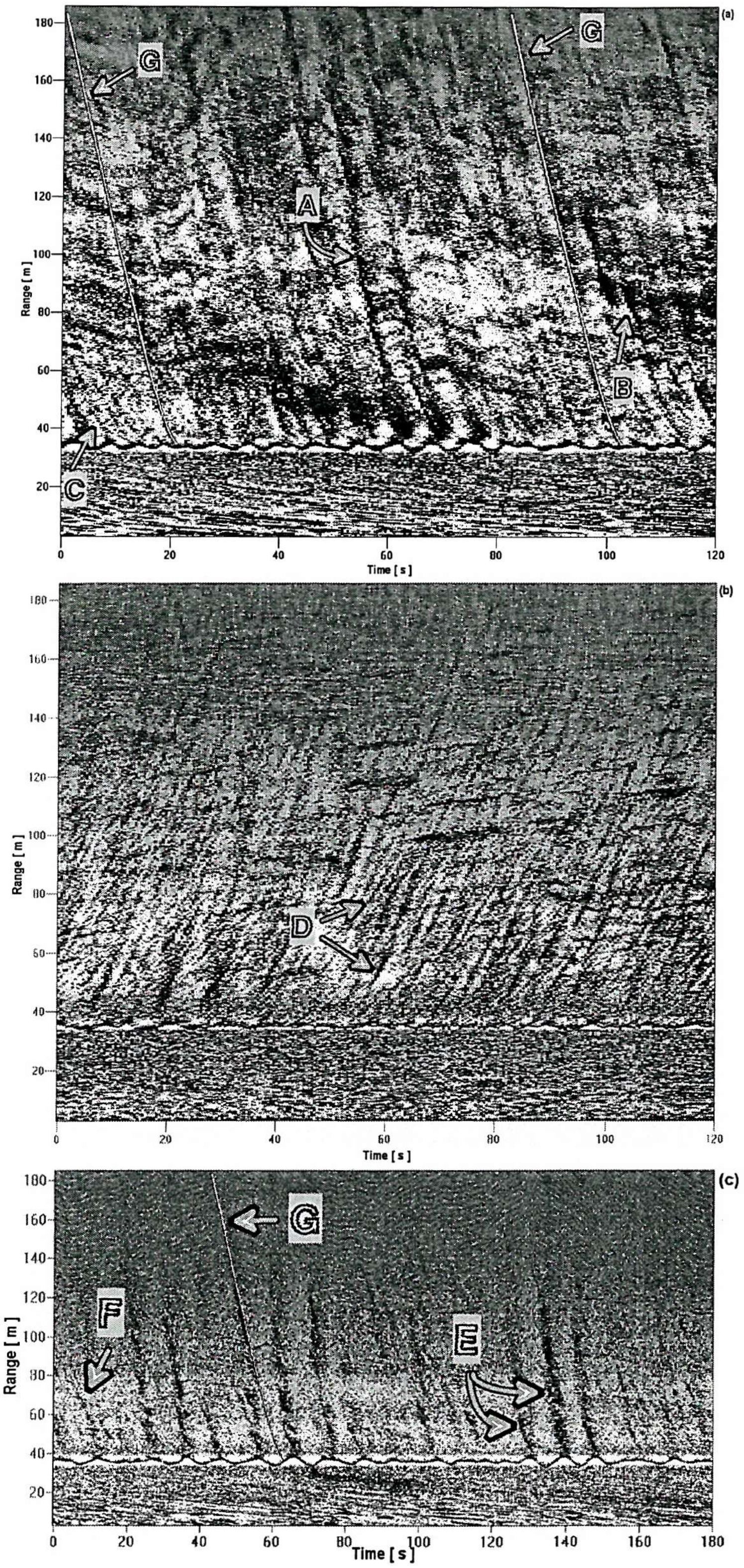

Fig. 7.9: *High-resolution normalised acoustic signatures of surface waves under different wind conditions. (a) forward sonograph on 24th August 1995 starting at 09:22 GMT, $\mathcal{U}_{10} = 11.5$ ms^{-1} from 343°T; (b) Starboard sonograph on 22th August 1995 at 05:35 GMT, $\mathcal{U}_{10} = 5.9$ ms^{-1} from 342°T; and (c) Forward sonograph on 26th August 1995 starting at 07:09 GMT, $\mathcal{U}_{10} = 2.2$ ms^{-1} from 145°T. Labels described in text.*

Tab. 7.2: *Surface wave characteristics for Fig. 7.9. Here Θ denotes direction and the sub-indexes a, hf, and sw indicate, in respective order, ARIES II, high-frequency surface waves and swell. Periods for high-frequency waves are obtained from sonographs, whilst swell periods represent the zero-up crossing period derived from the respective pressure records. The mean phase speed, c (ms^{-1}), and the local wave direction, ψ (°), for each sonograph are found from (6.10) and (6.11), respectively. The wave direction data are derived from the direction of the forward beam, Θ_a (°T), and ψ. Columns without data indicate that no reliable estimations could be found.*

Fig.				Sonograph					Sonograph		
	Θ_a (°T)	T_{hf} (s)	c_{hf} (ms^{-1})	c_{hf} (ms^{-1})	ψ_{hf} (°)	Θ_{hf} (°T)	T_{sw} (s)	c_{sw} (ms^{-1})	c_{sw} (ms^{-1})	ψ_{sw} (°)	Θ_{sw} (°T)
7.9a	238±25	2.5	3.9	3.4±0.8	237±4	115±29	9.2	14.3	13.3±4.5	219±7	97±18
7.9b	350±5	2.3	3.6	3.3±0.4	136±7	126±12	10.0	15.6	-	-	-
7.9c	287±7	-	-	-	-	-	10.6	16.5	-14.9±3.0	0	107±7

7.7 The acoustic signatures of breaking waves

Classical signatures of a breaking wave are illustrated in Fig. 7.10 where breaking wave crests have been labelled A and B, with the plumes of bubbles receding from the sonar as **a** and **b** (notice the two simultaneous breaking events along the same surface wave front at A); labels C and D indicate 'vertical' streaks caused by surface waves at short and far ranges, respectively. Both breaking wave signatures are detected as isolated short-range quasi-vertical lines of strong scattering. A 3 min average centred at the time of the breaking wave labelled B shows the direction of the acoustic beam to be (91 ± 1)°T and that of the wind from (301 ± 2)°T, which is 30° to the right of the beam. Whether the wave crest responsible for B is in a direction normal to the acoustic beam (section 2.2.3) is difficult to assess because the direction of propagation of swell and also the period and propagation of high-frequency waves could not be obtained with any confidence from an enlargement of a portion of Fig. 7.10, one centred at 19 min into the record which displays the breaking wave B (not shown). As already reported by Thorpe *et al.* (1998), wind speed probably limits the presence of scattering streaks in sonographs. The streaks travel with speeds comparable to the deep-water phase speeds of wind-sea and swell. Here, it is suggested that high-frequency waves generated by the wind propagate downwind (i.e. 121°T) with crests not normal enough to the acoustic beam so as to form patterns of staggered lines like those observed by Thorpe and Hall (1983). Although the situation depicted in Fig. 7.10 (e.g. scarce breaking waves) is different to the conditions described by Thorpe and Hall (1983), there appears to be a

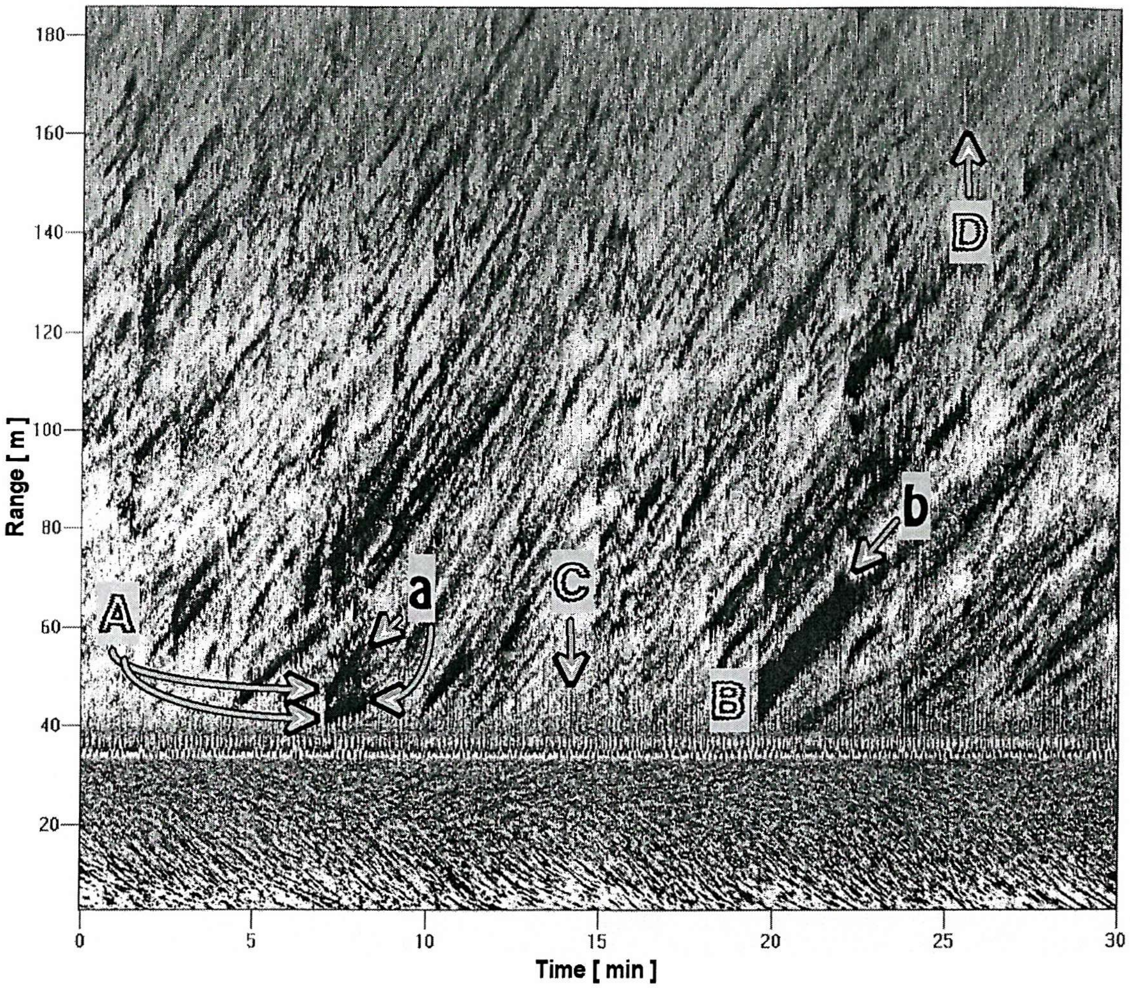

Fig. 7.10: *Normalised sonograph showing classical signatures of breaking waves and plumes of bubbles possibly elongated in the wave direction. Features in black indicate high concentration of scatterers (e.g. bubbles) or zones of highest acoustic returns. The horizontal wavy line of strong scattering at about 37 m corresponds to the range of the water surface. Wind speed is* $\mathcal{U}_{10} = (9.9 \pm 0.9)$ *ms*$^{-1}$ *from* $(290 \pm 9)^{\circ}T$ *and a mean flow at a depth of 30 m is* (16.7 ± 6.1) *cm*$^{-1}$*, remarkably towards* $(289 \pm 16)^{\circ}T$*. The mean zero crossing period, estimated from 5 min pressure records, is* (9.9 ± 0.6) *s and the ratio* $\frac{\mathcal{U}_{10}}{c}$ *is about 0.6 (see section 2.1.3).*

reasonable consistency. The breaking crest B (Fig. 7.10) is, however, associated with the first wave of a group consisting of six single waves with a period of 9 s and a height of about 1.3 m.

Characteristics of the huge single breaking event B are obtained from Fig. 7.10 (see section 2.2.2): $\frac{\lambda_b}{t_b} \sim \frac{14\text{ m}}{3\text{ s}} \sim 4.7\text{ ms}^{-1}$, $t_p \sim 3.5$ min (i.e. $O(70T)$!) and $\frac{d_p}{\ell} \sim \frac{990\text{ m}}{30\text{ m}} \sim 30$!. Then, in this particular case, d_b is about six times the length of the dominant swell!. Bubbles formed immediately after breaking are advected following the orbital wave motion. However, since the momentum transferred to the surrounding water is diffused rapidly, then the drifting of bubbles adjust to that of the mean current in roughly 2-3 wave periods after breaking (Thorpe and Hall, 1983). Hence the velocity of a mean current can be estimated from measurements of the drift of bubble plumes in sonographs. In particular, the above plume, b, moves 30 m away from the acoustic source in 210 s, that is at about 14.3 cms^{-1}. The drift of the sea surface can be divided in the Lagrangian drift caused by the dominant wave motion and the Eulerian wind-driven current caused by the wind stress. For a uniform train of waves in deep water, the Lagrangian drift is given by $\frac{2\pi^3 H^2}{gT^3}$ whilst the Eulerian drift by $\frac{0.0127\mathcal{U}_{10}}{(\sin\varphi)^{\frac{1}{2}}}$ (the latter based upon field observations and valid for $\varphi > 10°$ and $\mathcal{U}_{10} > 6$ ms^{-1}) where H is the wave height and φ is the latitude (e.g. Bowden, 1983). Then for $H = 1.3$ m, $T = 9$ s, $\mathcal{U}_{10} = 9.9$ ms^{-1} and $\varphi = 56.4575°$ (the latitude of ARIES II as described in chapter 4), the Lagrangian drift is of only 1.5 cms^{-1} but the wind-driven current is notably of 13.8 cms^{-1}. We can therefore provide a possible explanation for a wave breaking out from the centre of a wave group. The consistency in the preceding speeds suggest that the drift of the plume results from a surface current driven by the wind. It is receding from the acoustic source, probably in the direction of the mean wind (towards 110°T) and in opposition to the mean flow (289°T) measured at 30 m water depth. The latter might perhaps be associated with the breaking of the first wave in a group of six because, as stated above, the speeds of the plume (14.3 cms^{-1}), the Eulerian sea surface drift (13.8 cms^{-1}) and the mean flow (16.7 cms^{-1}) are all of the same order of magnitude. Swell can propagate in any direction onshore and although it is unlikely that a component of the group speed opposite to a mean (tidal) flow be responsible for the breaking wave B, perhaps, shear has contributed to the breaking and dispersion of this huge plume of bubbles. The latter is suggested from Fig. 7.10, where the presence of sloping scatterers beneath the range of the water surface, which are approaching the sonar beam, if dominantly passive, might be evidence of shear. On the other hand, the phase speed of the breaking crest B is 4.7 ms^{-1}, the period is 3 s and the bubble plume b remains in the sonograph for about 3.5 min. It appears therefore that high-frequency waves riding on swell are associated with the breaking wave B and that the plume of bubbles is receding from the sonograph in a direction close to that of the wind. Following Rapp and Melville (1990), the origin of the plume of bubbles b might come from an horizontal vortex with forward motion highly reduced after 3.5 min (see section 2.2.3).

An example of a wave group formed by 8 individual waves that is breaking at its centre is shown in Fig. 7.11, between 40 and 140 s into the record. Whilst the maximal wave amplitude of the group estimated from the pressure record is of about 4.6 m (T_z = 12.5 s, Δp = 1.9 x 10^4 Pa), the corresponding height determined directly from the sonograph is roughly 10.4 m, which represents a good agreement. Bubble plumes at A are situated on the wave crests and over the wave flanks, suggesting that the plumes, in time, are being left behind by the group. Further, the presence of zones of enhanced scattering at C and high-frequency waves superposed on swell at D are indicative of bubble production not caused by the overturning of low-frequency waves. Moreover, headings (Fig. 7.11d) show that the clockwise rotation of the streamlined instrument, between 290°T and 64°T, is associated with the propagation of a 22 m non-linear internal wave of depression, reinforcing that the breaking of the wave group is caused by the amplification of high-frequency waves near the crests of the group itself. The internal wave amplitude was obtained from the corresponding temperature record which varies from 11.8°C at 06:50 GMT to 15.1°C at 06:56 GMT (not shown). Unfortunately, the acoustic returns at ranges beyond 100 m are greatly reduced and as consequence the angle between the direction of swell and the relative current could not be determined for Fig. 7.11. The bubble cloud occurring beneath the wave crest (label B) indicates horizontal forward advection induced by water particles of surface waves, its shape bears a resemblance to billow-like clouds detected in inverted echo-sounders (see section 2.1.3). Thereby the implied penetration depth of the bubble cloud, $\mathcal{D}_\theta$, is 3.5 m (with $\mathcal{U}_{10}$ = 14.5 ms^{-1} and $\Delta\theta$ = 0.5 K, obtained from the meteorological buoy), that is 34% of the estimated wave height.

The most noticeable features of breaking waves are illustrated in Fig. 7.12a. The tilted dark lines at A and B mark the position of breaking crests which create, just after breaking, a pattern of several individual near-surface bubble plumes persisting for about 3 min (label C), although their acoustic signal is interrupted by a rapid anticlockwise rotation of the instrument at D (Fig. 7.12d). Since the strong acoustic intensity of the plumes is indicative of a high concentration of bubbles, this pattern appears to imply convergent flows of longitudinal vortices aligned normal of the breaking crest, resembling the formation of a pattern of foam bands left behind by waves breaking on a beach. The latter also lying normal to the advancing wave crest, but lasting only for a few seconds. It is uncertain, however, whether high or low air bubble concentrations are found beneath foam patches (Bortkovskii, 1999). In addition, the wave amplitude, phase speed and direction of propagation for the wave group at A are roughly 0.67 m,

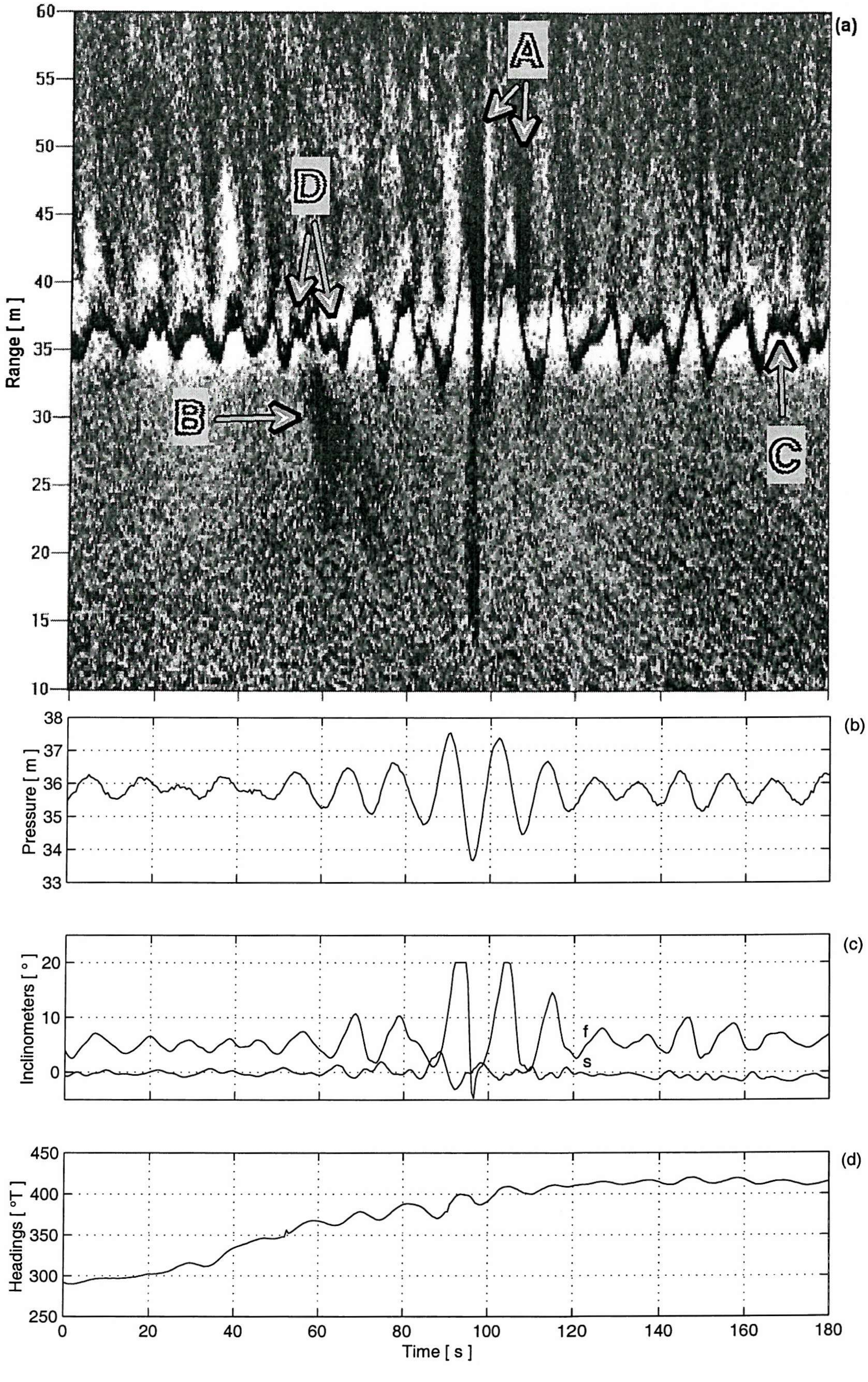

Fig. 7.11: *(a) Normalised forward sonograph; (b) Pressure at transducers level; (c) Inclinometers and (d) Headings. Wind speed is* $\mathcal{U}_{10} = 14.5$ *ms*$^{-1}$ *from 348°T. Records start at 06:54 GMT.*

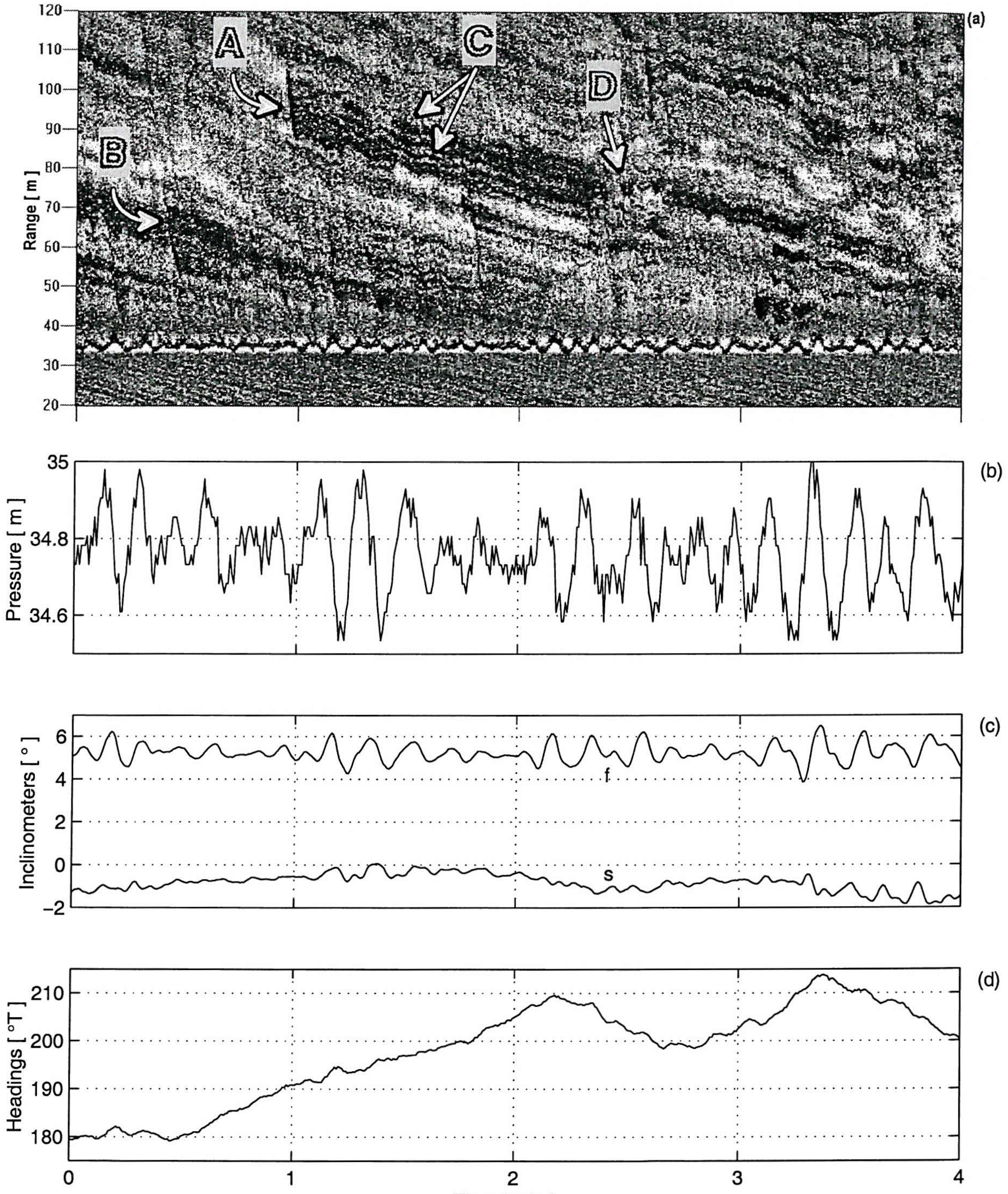

Fig. 7.12: *Idem to Fig. 7.11 except that, (a) corresponds to the starboard sonograph, $\mathcal{U}_{10} = (11.4 \pm 0.2)\ ms^{-1}$ from $(291 \pm 2)^{\circ} T$ and records start at 07:46 GMT. No signatures of breaking waves were captured in the corresponding forward sonograph.*

15.0 ms^{-1} and (66 ± 5)°T respectively (from linear theory $c = 17.8$ ms^{-1} for $T_z = 11.4$ s). The rotation of the instrument, between 0.5 min and 2.2 min into Fig. 7.12d, is associated with a 20 m solitary-like wave of depression with an estimated relative current speed and direction of (37.1 ± 1.9) cms^{-1} and (142 ± 7)°T. No correlation is observed between the directions ascribed to the wave group and internal wave, however Crombie *et al.* (1978) have found that non-linear wave interactions may produce high-frequency waves travelling against the wind direction. The direction of the starboard beam at the time of the breaking wave labelled A is (285 ± 5)°T, which is 6°T in opposition to the wind and 37° against the direction of the relative current. It is therefore possible that the interaction of internal wave flows with high-frequency waves travelling in the direction of starboard beam (e.g wave crests normal to the beam direction) has produced the breaking waves at A and B (see sections 2.2.2 and 2.3.1).

7.8 The acoustic signatures of Langmuir circulation

Dark linear features in Fig. 7.13, indicating a high concentration of bubbles, are interpreted as bubble bands lying along the lines of convergence created by Langmuir circulations (section 2.1.4). They are plotted with a different intensity scale, unquantified because the sonars are un-calibrated. At low wind speeds the linear features are discontinuous (i.e. fragmented), probably reflecting an insufficient supply of bubbles, but tend to persist for more time as the wind speed increases. At high wind speeds the bands appear to increasingly undulate in phase at all ranges (for example between 20 and 40 s into Fig. 7.13a), an effect produced by the oscillations of the heading of the sonar over the appearance of features seen in the sonographs (section 6.4.4). Adjacent bands are also observed to merge. Perhaps this is a mechanism in which a steady pattern of LC is to be produced. The characteristics of bubble bands observed in Fig. 7.13 are consistent with other shapes identified and reported in the sonar literature (sections 2.1.4 and 2.4.2): Y-junctions (label B) and inverted Y-junctions (label E), bands spaced with different scales (labels A and D), and the presence of breaking waves (label C). The average distance between neighbouring bubble bands increases with wind speed (Table 7.3), and the lateral advection is probably dominated by tidal currents. Although bubble bands are poorly aligned with the wind direction, they generally tend to be closely aligned to the wind after averaging longer sonograph records (Thorpe *et al.*, 1998). Possible causes for the misalignment of LC are outlined in section 2.4.2.

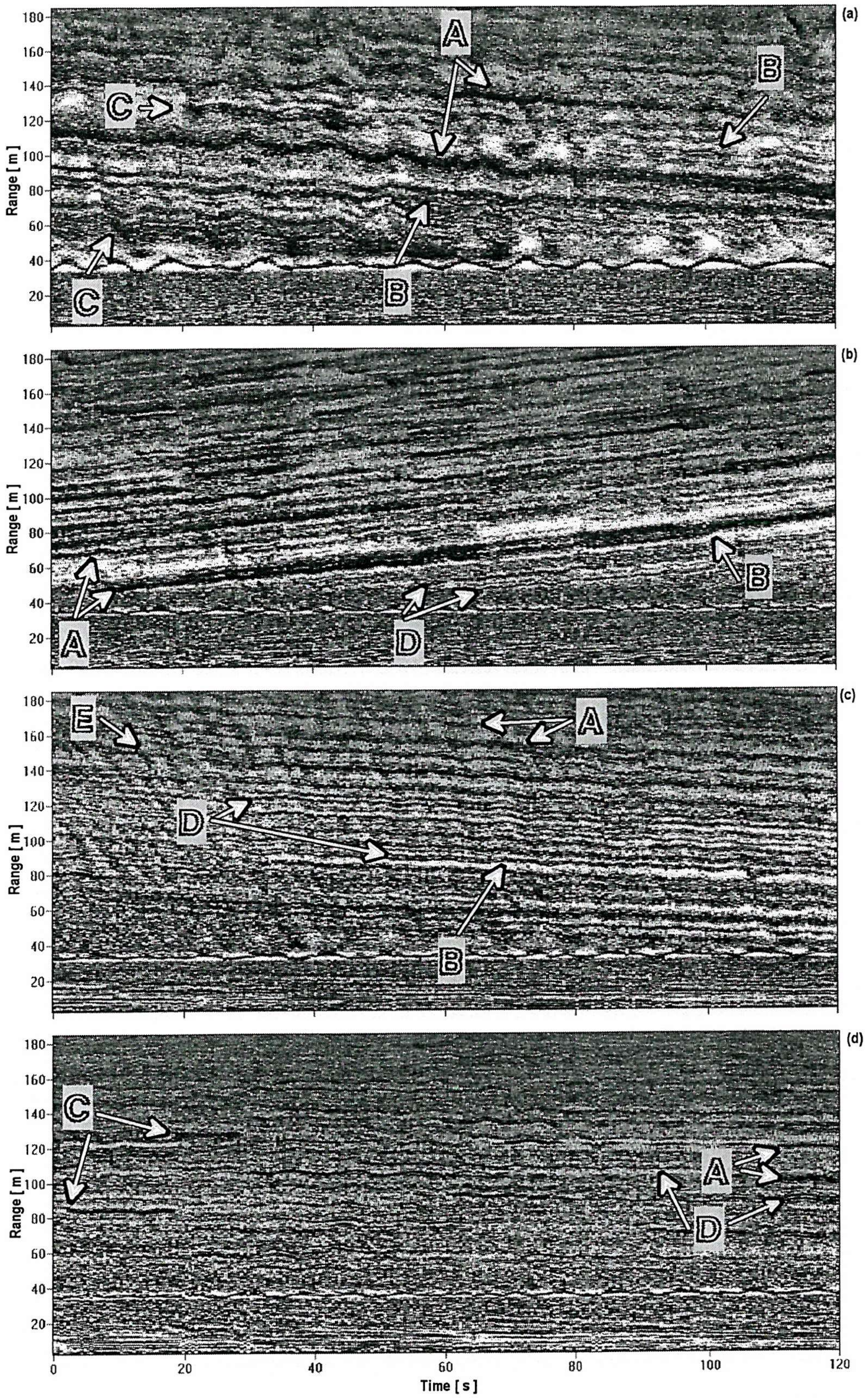

Fig. 7.13: *Bubble bands under different wind conditions. (a)* $\mathcal{U}_{10} = 14.2$ *ms*$^{-1}$ *from* 67°*T on 25th August 1995 at 06:10 GMT; (b)* $\mathcal{U}_{10} = 7.8$ *ms*$^{-1}$ *from* 277°*T on 22nd August 1995 at 19:22 GMT; (c)* $\mathcal{U}_{10} = 5.5$ *ms*$^{-1}$ *from* 296°*T on 13th August 1995 at 13:38 GMT; (d)* $\mathcal{U}_{10} = 3.8$ *ms*$^{-1}$ *from* 258°*T on 17th August 1995 at 11:33 GMT.*

Tab. 7.3: *The variations of the scales of bubble bands and the errors in the estimations of V for Fig. 7.13 according to equations (6.18) and (6.23-6.25). Here θ_{wi} and θ_{ar} denote the wind direction and the orientation of ARIES II, respectively. The variation of beam heading, $\dot{\eth}$, is typically of $0(10^{-3})$ rads^{-1} and it is neglected for practical purposes. The estimations of $\mathcal{S}$ and V are derived from averages, each over four measurements of linear features seen in sonographs at a mean range of 120 m. The root mean square of ARIES II alignment with flows is not included in σ_T^2, but the standard deviation of θ reflect changes in the slope of features and the variation of mean headings.*

$\mathcal{U}_{10}$ (ms^{-1})	θ_{wi} (°T)	θ_{ar} (°T)	$\mathcal{S}$ (m)	V (cms^{-1})	θ (°T)	σ_T^2 (cm^{2}s^{-2})
14.2	67	267 ± 4	8.4 ± 1.6	-4.4 ± 3.1	9 ± 5	9
7.8	277	54 ± 3	6.0 ± 0.5	-4.5 ± 3.8	315 ± 11	15
5.5	296	109 ± 2	5.7 ± 1.3	1.5 ± 1.1	206 ± 7	4
3.8	258	270 ± 3	4.4 ± 0.4	-2.7 ± 1.8	323 ± 30	6

7.9 Applications

ARIES II (i.e. acoustic imagery and environmental sensors) is a valuable apparatus to measuring simultaneously several different organised motions occurring near the sea surface, which are particularly difficult to discriminate utilising conventional instrumentation. Thereby, the current section focuses on two deliverables of the possible uses of the streamlined instrument to draw on knowledge of the upper ocean boundary layer.

7.9.1 The straining of internal waves

In order to take advantage of the high-resolution pressure and temperature measurements provided by ARIES II, a proposal was put forward in section 2.3.3 for the internal wave straining estimated via a compressible Boussinesq equation, that is from pressure variations recorded as ISWs of depression are passing by.

Fig. 7.14a and 7.15a display the horizontal strain at the mean ARIES II depth as inferred from equation (2.24). Pressure measurements are referred to the level of sonar transducers, that is at a depth different from the temperature sensor (see section 4.1). However, this is not important for the straining estimations since calculations are done from variations of pressure with time and not with depth. The unperturbed pressure

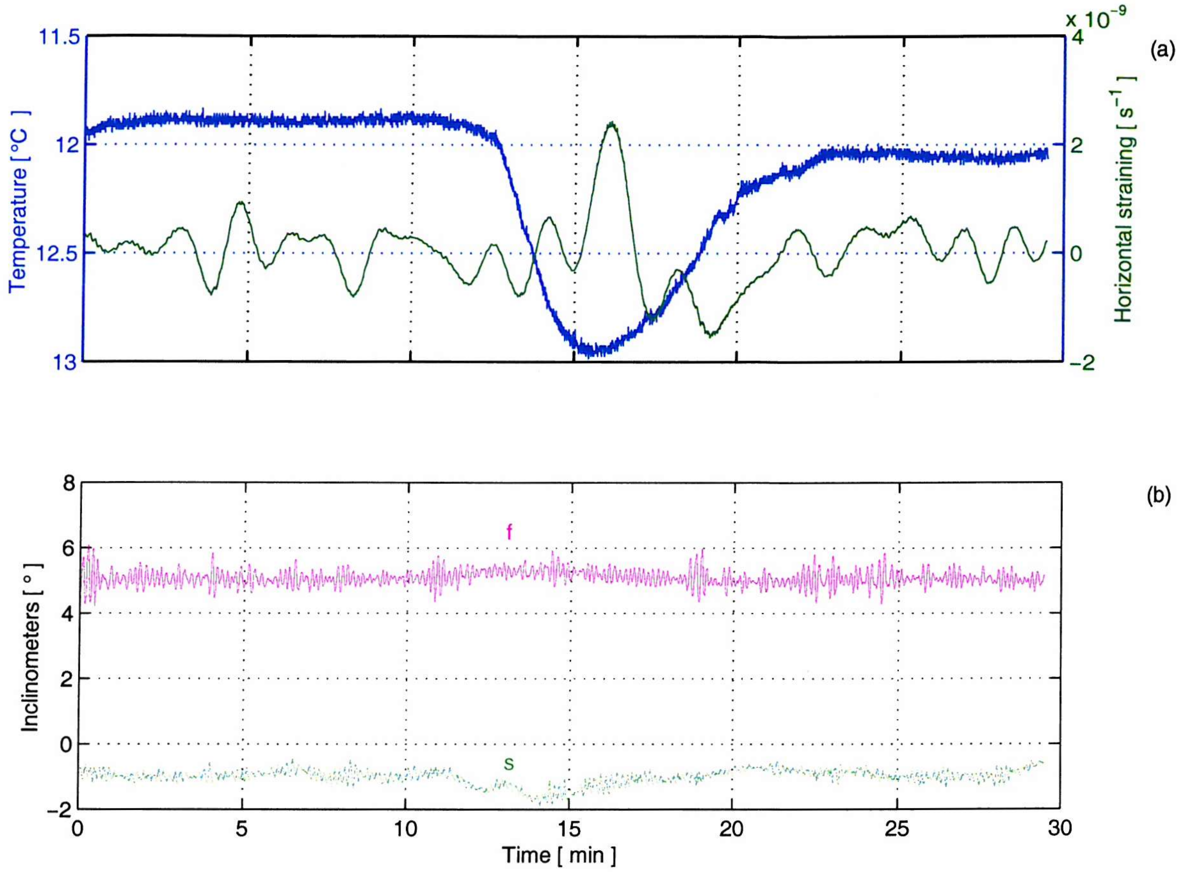

Fig. 7.14: *The straining rate within a non-linear internal wave. (a) Temperature (thick solid line), increasing downwards, and horizontal straining (thin solid line) at the level of sonar transducers; (b) Inclinometers, with labels as defined in Fig. 5.2. The vertical excursion of ARIES II produced by the internal wave is of about 0.1 m. The record starts at 12:25 GMT on 15th August 1995.*

is estimated by low-pass filtering the instantaneous pressure record with a cut-off frequency of 3.333 x 10^{-3} Hz. The pressure variations are calculated by subtracting each low-passed pressure from the instantaneous pressure record, whilst pressure variations with time are estimated using centred finite-differences. To reveal the internal wave straining, a band-pass filter (1.111−5.555) x 10^{-3} Hz is applied to attenuate contributions from instrumental noise, swell and wave-groups, and tidal and inertial signals.

Surface horizontal straining calculated using expressions for a two-layer fluid (e.g. equation (2.16)) or numerical simulations of the Korteweg-deVries equation (e.g. Liu *et al.*, 1998) show two well-defined maximal values (e.g. Fig. 2.9b). The first one corresponds to the internal wave convergence zone ($\frac{\partial u'}{\partial x} < 0$), indicating that u' decreases in the flow direction (e.g. Fig. 2.9a). The second one stands for the divergence zone of the internal wave ($\frac{\partial u'}{\partial x} > 0$). The horizontal straining shown in Fig. 7.14a and 7.15b is

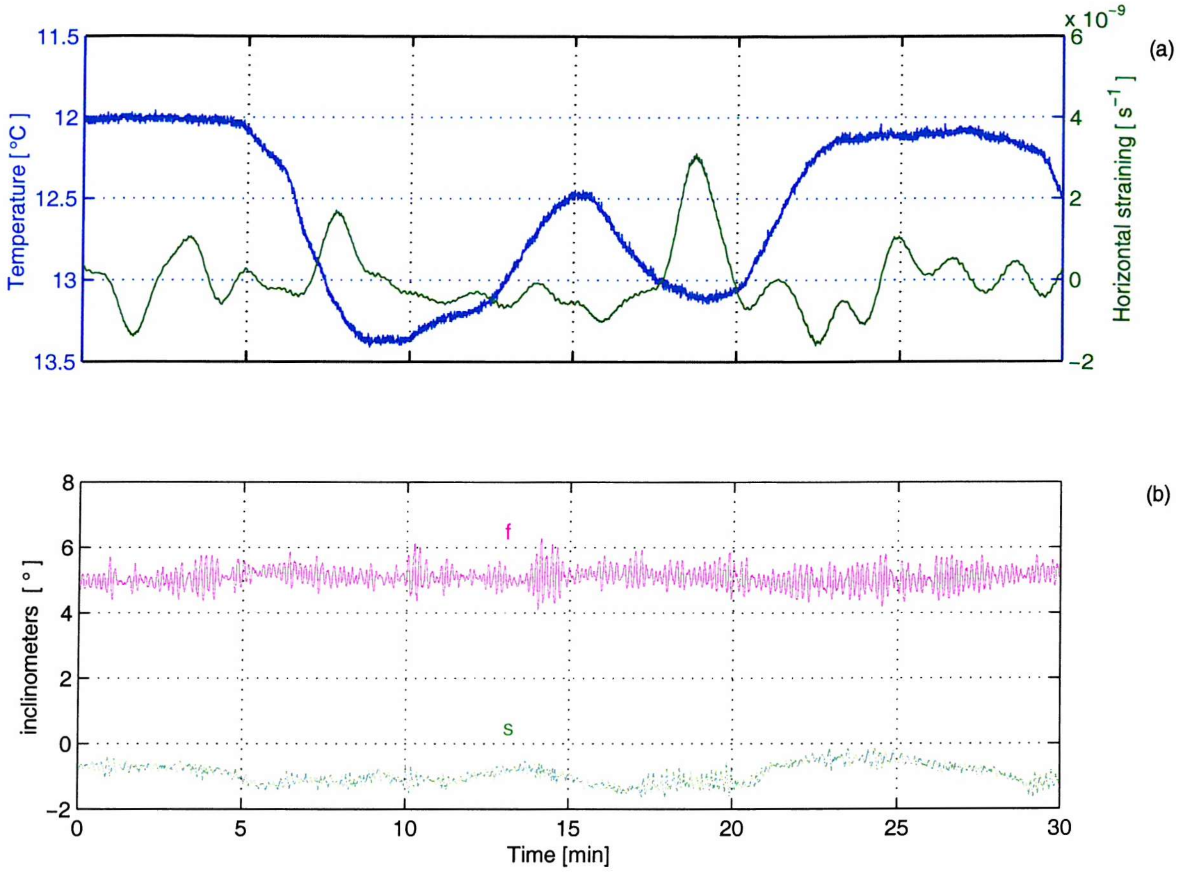

Fig. 7.15: *As for Fig. 7.14, but starting at 12:55 GMT on the same day.*

inconsistent with the ideal notion of strain within the internal wave trough, although the temperature begins to increase when the straining is negative, both maintaining the same slope. It appears, in addition, that there is a lack of detailed *in situ* field measurements of the internal wave straining. Consequently, a comparison with theoretical calculations may not necessarily have to agree with Fig. 7.14a and 7.15a and other factors should be taking into account, for example, the modal structure of the waves and mixing (see also section 2.3.1). Thus, the relative gradual slope of the temperature signal during the passage of ISWs suggests the effect of mixing, provoked perhaps by vertical shear in the direction of wave propagation which in turn may induce changes in the velocity field inside the wave trough.

Another issue worth to mention regards the magnitude of the straining. Reported values for the surface strain based upon a 10 m wave amplitude are of the order of 10^{-3} s^{-1} in water depths of about 70 m (Liu, 1988) and of the order of 10^{-2} s^{-1} in a 60 m upper layer depth (Liu *et al.*, 1998). These relatively high straining values are associated with dissipation and shoaling effects on the wave propagation. The straining estimated here from observations is of about 10^{-9} s^{-1} and reflects, on the one side, the inclusion of the sound speed in equation (2.24). However, what is important is that by using a different constant, the shape of the straining curve will not change. For example, a magnitude of the order of 10^{-6} s^{-1} for the straining is expected if the factor $(\rho_1 h_1 g)^{-1}$ is utilised in equation (2.24). The estimated straining, on the order hand, has a reference mean depth of 34.6 m and relatively larger values are expected near the surface depending upon the local vertical mode structure of the non-linear internal waves. Furthermore, numerical noise in the referred to above straining estimation is discarded because all computations were done in double precision (64 bits), and the relative accuracy for floating point numbers in the author's computer is of $O(10^{-16})$.

A detailed physical interpretation of the inferred internal wave straining requires further consistency tests with straining derived from the KdV equation (e.g. Grimshaw *et al.*, 2003), which is not treated here. However, the pressure measurements are robust themselves and demonstrate the capability of ARIES II for detecting the wave strain.

7.9.2 On the distortion of bubble bands by internal waves

Fig. 7.6a,b display the coexistence of Langmuir circulation with non-linear internal waves, whilst Fig. 7.16 draws attention towards the response of Langmuir circulation to perturbations caused by the waves. The fact that the wind speed speed and direction remained constant for the full 50 min period (see caption in Fig. 7.6), seems to suggest that the variations in the dimensions of bubble bands are indeed associated with the propagation of the internal wave. Before and after the passage of the wave trough, the bubble bands tend to be orientated between the direction of wind and the direction of the current at 30 m (Fig. 7.16a), that is 34°T and 24°T within the wind and current on average, respectively. The near-surface lateral drift (Fig. 7.16b) is not totally consistent with either the current component or the relative current component normal to the orientation ascribed to the bands, nevertheless the velocity component of biological scatterers tends to follow the variations of the current component. Thereby biological targets appear to be passive tracers of the 30 m current speed. Within the wave trough (i.e. 15-35 min into the record), the bands become closely aligned to the wind or current, and the lateral drift is consistent with either the current component or the relative current component. The latter seems to suggest that residual rotary currents may contribute to the distortion of bubble bands. In addition, the spacing of bubble bands is (13±1) m before the internal wave arrives (Fig.7.16c), but it decreases to about 9 m over the forward flank of the wave trough, at 20 min into the record. Hence the reduction is of the order of 30%. A comparison with equation (2.31) is done afterwards. It is estimated that the amplitude and direction of propagation of the internal wave are, 27 m and (61±1)°T (i.e. an unusual direction, but both ARIES II and the current

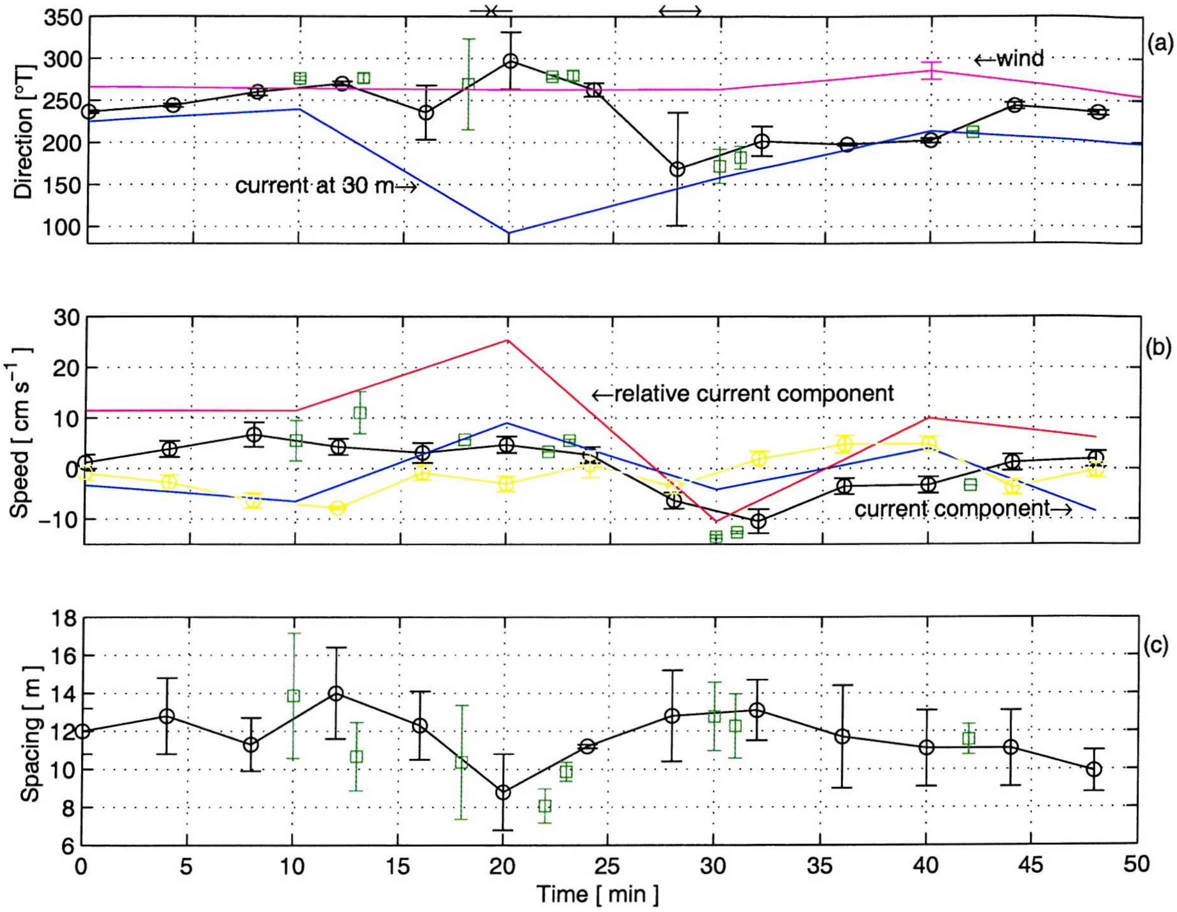

Fig. 7.16: *Measurements of bubble band dimensions corresponding to Fig. 7.6, which is part of Fig. 4.4b. (a) Wind (magenta) and 30 m current direction (blue), and band orientation (black) obtained from equation (6.23); (b) The speed of the relative current (red), the current (blue) and biological scatterers (yellow, with measurements carried out at a range of 8 ± 5 m from the sonar beam) components normal to bubble bands respectively, and the lateral drift speed of the bands (black) from equation (6.24); and (c) The spacing of bubble bands (black) according to equation (6.18). These data are based upon measurements effectuated over 4 min (◯) and 2 min (□) sonographs. The arrows shown on top of (a) mark, respectively, the internal wave convergence and divergence zones, at 19 min and about 28 min into the record.*

meter indicate the onset of an eastward flow at the arrival of the wave trough. It should be said, however, that a direction of propagation of $(129 \pm 1)^\circ$T was estimated by Small *et al.* (1999) from a comparison of SAR images on 20 and 21 August 1995 at 11:36 GMT. In addition, Inall *et al.* (2000, 2001) report a propagation of $(130 \pm 5)^\circ$T on 21 August 1995 at about 18:15 GMT from X-band radar images. Consequently, the preceding direction of propagation on 20 August 1995 at about 17:23 GMT might be wrong.), respectively. From equation (2.19), $L_b \approx 98$ m with $\gamma = \frac{34.6}{111.4}$. Considering $\Lambda\varkappa \approx \frac{\Lambda}{L_b}$, an approximation to $\mathcal{S}_{iw}$ gives 3 m, implying a reduction of 77%. These values indicate a poor agreement. After 20 min into Fig. 6.3c, the spacing increases up to (11 ± 1) m once the wave has passed by. Consequently, the spacing of bubble bands recovers in a few tens of minutes.

Although the variation in $\mathcal{X}$ and N with time was found to be insignificant, the distortion of bubble bands appears to be predominantly passive (Fig. 7.17b). Non-passive advection is correlated with negative horizontal straining (Fig. 7.17a). For example, the measurements of the speed of biological scatterers normal to the orientation of bubble bands shown in Fig. 7.16b, indicate a correlation with straining at 24 and 28 min into the record. This suggests that both bubble bands and biological targets are similarly affected by the straining in the flow. Variations in $\mathcal{X}_p$ (Fig. 7.17c) are dominated by the variations in α, where negative values indicate bubble bands oriented to the right of the internal wave direction (see Fig. 7.16a). The physical implications of these results are beyond the scope of the current work, but demonstrate the potential of ARIES II to obtain quantitative information of simultaneous UOBL processes.

7.10 Summary

Here a brief summary of the features reported, which are new and un-reported elsewhere or greater detail is given, is listed as follows:

- The surface tide.
- The scattering bands that propagate in the direction of solitary-type internal waves along the sea surface.
- The zones of enhanced scattering located either along or beneath the sea surface which mark, in respective order, the presence of high bubble concentrations (e.g. resulting from breaking waves or the clustering of bubble bands) and biological scatterers over internal wave troughs.
- The simultaneous occurrence of near-surface acoustic signatures of rain showers and internal waves, of Langmuir circulation and internal waves, and biological scatterers and internal waves.

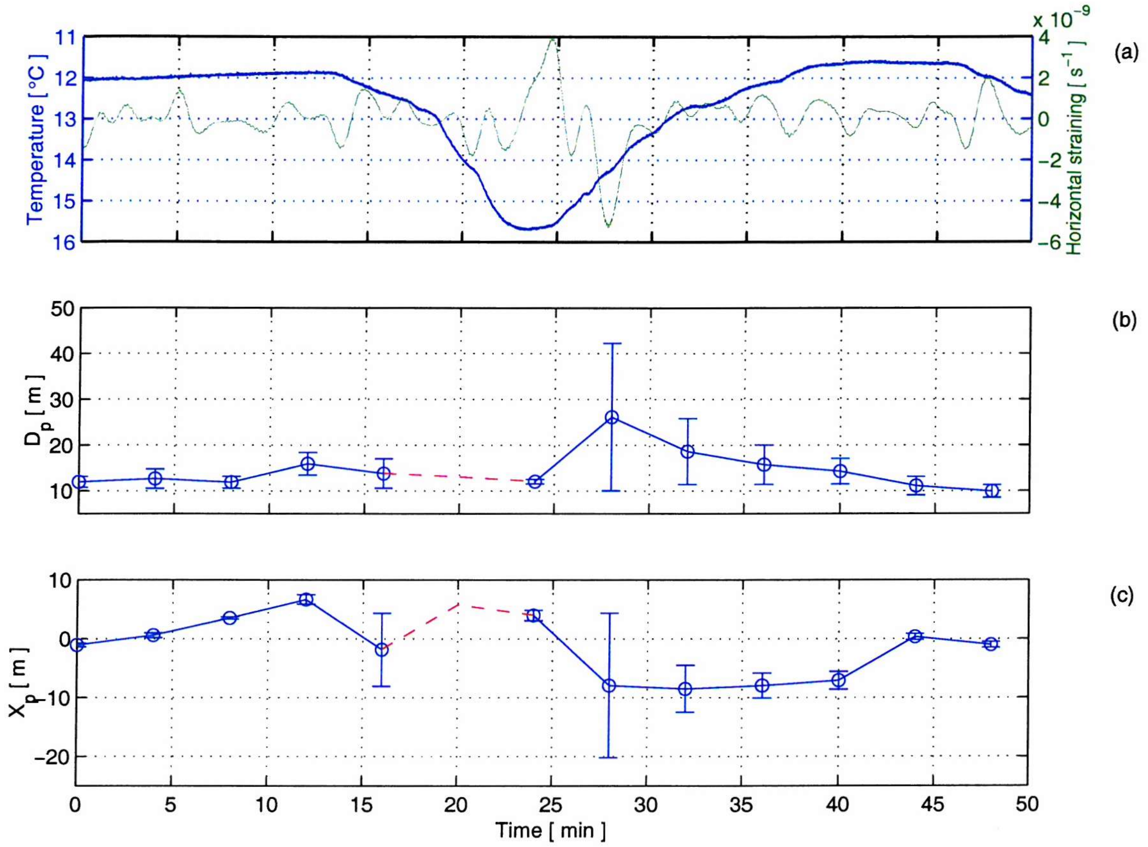

Fig. 7.17: *(a) Temperature (thick solid line, as for Fig. 7.6d), increasing downwards, and horizontal straining (thin solid line) at the level of sonar transducers; (b) The distance of passive advection from equation (6.26); and (c) the projection of the spacing of bubble bands along the direction of the internal wave from equation (6.28). The dotted lines indicate unreliable data at 20 min, with variations of ±306 m and ±91 m for (b) and (c), respectively. These values are associated with the standard deviation in the orientation of bubble bands. The vertical excursion of the instrument caused by the wave is of about 0.2 m.*

- The apparent increase in the sea surface roughness over the forward flank of internal wave troughs, which is coincident with the propagation of groups of surface waves in the wave troughs.
- The apparent increase in the sea surface range caused by the knocking-down of the mooring line by internal wave-induced flows.
- The vertical acoustic lines marking the convergence and divergence zones of internal waves.
- A breaking wave group at the range of the sea surface.
- The novel acoustic signatures of breaking waves at ranges beyond the sea surface.

- The non-passive advection of bubble bands associated with horizontal straining.

8. SUMMARY AND CONCLUSIONS

The current thesis reports on the development of an autonomous recording inverted echo sounder, ARIES II. This novel apparatus has been operating in the Malin-Hebrides Shelf, a site known for active fishing and intense non-linear internal wave activity, to observe the dynamics of near-surface processes in the deep ocean. ARIES II has achieved both remote measurements in this hostile environment and captured the simultaneous occurrence of several different small-scale processes in high-resolution acoustic images, as the processes respond to various wind forcing conditions. Observations of near-surface processes are complicated by the energetic motions of the upper ocean which disturb the function of the instrument. Therefore the objective undertaken here is a discourse on the performance of ARIES II, the errors and uncertainties which have an effect on both its alignment to relative flows and the appearance of features captured in sonographs, and to demonstrate its capability to detecting acoustic signatures of near-surface organised motions. The organisation of both bubble clouds into bands roughly aligned to the wind direction by surface convergent flows and streaks advancing roughly at the phase speed of surface waves, has motivated the derivation of simple specific formulations to obtain quantitative data from acoustic images. These images have revealed complicated patterns of Langmuir circulation and solitary-type internal waves of depression, surface breaking waves and rain squalls, and biological activity. Some selection has been made of portions of data illustrating particularly striking phenomena.

8.1 Instrumentation

It is through understanding of instrumental pitfalls that it is possible to make significant progress in detecting the variety of phenomena that constitute the upper ocean boundary layer. Several instrumental pitfalls have been identified which may affect the function of ARIES II in the field and have some influence in the quantification of upper ocean processes. Thus there is some uncertainty about the quality of the measurements provided by the compass because it is un-calibrated, and also because magnetic interference with the stainless steel frame was discovered after the deployment of ARIES II. Although these inconvenient issues are perhaps minimised by filtering or averaging data, they require attention to remove any doubt in the reliability of headings for future uses of this instrument. Other issues include the possible effects of: (1) an uneven weight distribution on the position of the pivot point of ARIES II; and those related to (2) slightly convex-concave surfaces covering the streamlined instrument on the generation of significant lift forces. The first issue is only important in no-flow conditions (e.g. $\leq 2\text{cms}^{-1}$), a rare situation observed during the period of measurements. Comparisons between headings and transverse tilts, and between angles of attack and transverse tilts did not yield conclusive results for the second issue. Consequently, the role of the asymmetric sides of ARIES II in driving vortex shedding from the fin and transverse vibrations of the frame requires future numerical modelling. Under these circumstances, it is assumed that the preceding issues have a negligible effect on the quantification of small-scale upper ocean processes.

8.2 Performance

There are a number of clear results. One of them regards the response of ARIES II to fluid motions, which can be observed in the inclinometers. Thereby the instrument tends to a mean rolling of $O(-0.5^\circ)$ as it rotates slowly to change orientation either clockwise or anticlockwise. The natural position of ARIES II is 5.1° up to fore and 1.0° up to starboard (see section 3.2 for reference), with variations caused mainly by internal waves, currents and groups of surface waves. Maximal rolling attributed to tidal flows is 2.5° down to starboard, whilst wave groups are capable of inducing a pitch attitude of the order of $\pm 10^\circ$ during high wind conditions. Non-linear internal waves produce the rolling of the instrument up to 10° down to starboard. These maximal tilts are about 37% less than the tilt angle predicted from design conditions (section 5.5).

One advantage of making high-resolution measurements is that the time scale can be referenced to the same clock as other low-resolution observations using conventional instrumentation. Thus the observations presented in the current thesis have demonstrated that an important source of difficulty deals with the orientation of the streamlined instrument with mean and internal wave-induced flows. The rms of the scatter of the alignment of ARIES II with currents is of about 30°T, whilst that corresponding to internal waves is roughly 40°T. These values are in excess of the mean alignment between the surface convergences associated with Langmuir circulation and the mean wind direction, which is of 20°T. The best possible alignment obtained was with mean flows. For $\mathcal{U}_{10} > 7\ \text{ms}^{-1}$ the rms scatter of points is 23°T; it improves to 19°T for current speeds in the range (40-75) cms^{-1}. Moreover, the streamlined instrument appears able to align within 6°T for lower speeds. It is believed that the root cause of yawing is the poor resolution of current meters, and to a lesser degree, on the dynamics of the study site and instrumental imperfections. In order to provide quantitative information, the above leads to select particular periods where the orientation of the streamlined instrument is consistent with either the direction of the relative current or the direction of the 30 m current meter at the onset of eastward flows. Further, these results draw attention to additional deployment of both ARIES II and conventional instrumentation with the same sampling rates to provide a better assessment of the yawing motion.

By using simple methods (sections 5.5 and 5.6), it is estimated that maximal vertical excursions caused by the knocking-down of ARIES II at the level of both the instrument attachment point at its base frame and at the anchor attachment point to the mooring line, are 0.3 m and 1.3 m respectively. These models underestimate observations from the ARIES II site.

The generation of acoustic images has been done assuming a constant speed of sound. Consequently, there are a number of factors that affect the estimation of the range of reflecting targets and their appearance in the acoustic images. By using a simple geometrical approach, it is estimated that the maximal error in the range of the sea surface produced when variations of temperature in the water column are ignored, as internal waves registered by ARIES II propagate in the thermocline, is -0.5 m. The effects of refraction and reflection of sound rays on the range of near-surface targets appear unimportant. It should be say, however, that the two acoustic beam patterns are not known because sonars are un-calibrated.

It has been found that the instrument heading and the orbital speeds of surface waves are the main factors that produce distortions in the acoustic features observed in sonographs. Oscillations in the heading cause fluctuations in the range of acoustic signatures associated with Langmuir circulation. The fluctuations are in phase at all ranges and are easy to identify because they increase with range and as bubble bands become more aligned to the beam direction. The near-surface orbital motions driven by surface waves also lead to changes in the range of bubble bands by displacing the bubble clouds confined within the bands. In this case the range fluctuations advance in phase with range at the phase speed of surface waves, but these do not increase with range. Specific formulations describing these distortions have been developed (sections 6.4.3 and 6.4.4).

Groups of surface waves and internal waves induce motions on the sonar beams. Groups of waves, for example, may drive fluctuations in the tilt of the forward beam which in turn produces a change in the vertical inclination of the starboard beam and a migration of its intersection along the sea surface (the opposite effect is associated with internal waves). The maximal beam migration produced by both groups of waves and internal waves is roughly 6 m.

A key component to the interpretation of acoustic images is the ability to extract quantitative data to provide insights into the relevant physics of near-surface processes. Thus two sets of geometrical equations based upon the concept of plane wave have been derived. The first set allows to estimate the phase speed, direction of propagation and wavelength of both low-frequency and high-frequency surface waves. The second set can be utilised to estimate the lateral drift speed, orientation and spacing of bubble bands. This set in particular is applied to assess the changes in the dimensions of bubble bands for a period before a non-linear internal wave arrives, as it passes and afterwards. A simple test has also been developed to determine to what extent the changes in the dimensions of the bands are caused solely by the wave. It is suggested that these changes reflect the distortion of Langmuir circulation by internal waves.

8.3 Observations

A spectral analysis of the environmental sensors has demonstrated that ARIES II responds to the fluid motions produced by wind-sea and swell at the spectral bands, in respective order, (0.1882-0.3106) Hz and (0.0938-0.1016) Hz, and to wave groups at a spectral frequency of 0.0078 Hz. The pressure sensor has also revealed the modulation of the tide, whilst the propagation of non-linear internal waves of depression has been clearly observed through the temperature sensor.

Both long-period and short-period sonographs have provided detailed documentation of locally dominant near-surface processes occurring in the Malin-Hebrides shelf. It has been demonstrated that the sonographs contain signals generated by the tide, solitary-type internal waves, rain squalls, Langmuir circulation, wave groups, breaking surface waves, bubble plumes and biological activity. Side-scan sonar data have also provided evidence of the simultaneous occurrence of rain squalls and internal waves, Langmuir circulation, surface and internal waves, and biological scatterers and internal waves. Novel acoustic signatures are related to: the surface tide, a scattering band over the forward flank of an internal wave trough from which the direction of propagation can be inferred, an intensification of surface scattering also over this flank which is believed to have been caused by breaking waves and/or bubble bands clustered together, the apparent increase in the roughness of the sea surface over internal wave troughs which is associated with the propagation of groups of surface waves, vertical acoustic lines which appear to mark the convergence and divergence zones of internal waves, the presence of biological scatterers over wave troughs near to sonar depth from which the velocity field can potentially be estimated, the knocking-down of the mooring line, the breaking of surface waves, and the hyperbolic signature of high-frequency waves.

Acoustic images have revealed the occurrence of complicated patterns of bubble bands. There is a hierarchy of coexisting scales with mean spacings typically of the order of (3-9) m. Bubble bands appear to merge with larger bands, whilst apparently pairs of bands merge with each other to form new bands between older ones. The orientation of bubble bands appears locally misaligned with the wind direction, although by averaging 1 h or 2 h records the bands are aligned within 10°T of the direction of wind. This thesis has demonstrated that non-linear internal waves represent a potential cause of misalignment within the wave trough, where in particular, an abrupt change of 95°T in the band orientation is correlated with horizontal straining (section 7.9.2). It is unclear, however, to what extent magnetic interference and un-calibrated compass might adversely affect the estimated band orientations. Whilst the spacing of bubble bands tends to decrease at the internal convergence zones, the enhanced acoustic intensity of targets observed over wave troughs is indicative of a larger presence of bubbles per unit area, perhaps by the clustering of bubble bands. However, an increase in the breaking frequency of surface waves, the breaking up of Langmuir circulation or a combination of both are valid causes as well.

8.4 Concluding remarks

The main conclusions of this thesis are given as follows:

- Both sonar transducers and the compass do need to be calibrated (e.g. the bubble size distributions could be determined), in order to avoid uncertainty about the reliability of measurements that can be obtained from acoustic images.
- Additional fieldwork, numerical modelling and laboratory tests are required to estimate the drag coefficient of ARIES II and to study the role of vortex shedding on the rolling of the instrument. Furthermore, a current meter and ARIES II should be installed in the same mooring line, and sampling at a similar rate in order to examine yawing motion. Under internal wave conditions, a larger fin may help to damping out yaw and roll.
- ARIES II is a stable working framework which remains generally 5.1° up to fore and 1.0° up to starboard (see section 3.2). Maximal pitching and rolling caused by surface wave groups (during high wind conditions) and non-linear internal waves (during spring tides) are both of about 10°. The maximal vertical excursion caused by internal waves was 1.7 m during spring tides.
- The alignment of ARIES II into mean currents has a rms scatter of 34°T for low winds ($\mathcal{U}_{10} \leq 7$ ms^{-1}) and 23°T for high winds. The rms scatter of points improves to 19°T for current speeds in the range $(40 - 75)$ cms^{-1}. There are

also short-time periods coincident with current speeds less than 36 cms^{-1} and a combination of low or high winds where the instrument aligns within $(6 \pm 4)^\circ$T.

- The best estimation of the direction of propagation of non-linear internal waves based upon low-resolution current meters is $(146 \pm 45)^\circ$T. It corresponds to neap tides. The rms scatter of the measurements for the alignment of ARIES II with internal-wave induced flows are 45°T during spring tides and 84°T during neap tides. At the time of the passage of the waves, the corresponding rms between the orientation of ARIES II and the direction of the 30 m current meter are 40°T and 42°T for spring and neap tides respectively.

- Therefore, error bars associated with uncertainties which attach to the yawing of ARIES II are, $(27 \pm 7)^\circ$T with mean currents, and 45°T and 84°T with internal wave-induced flows during spring and neap tides, respectively. The yawing of ARIES II is attributed to the poor sampling rate of currents rather than instrumental imperfections (e.g. an asymmetrical streamlined profile) or dynamics (e.g. the presence of rotary currents).

- ARIES II was operating continuously and unattended in a zone remote from shore. It has proven conclusively to be a valuable tool, providing remotely from underwater, large amounts of vivid high-resolution acoustic images of near-surface processes occurring in the deep ocean.

- The observations presented indicate the presence of many characteristics of Langmuir circulation, non-linear internal waves, rain squalls and breaking surface waves, which are difficult to observe visually and directly using conventional instrumentation.

- Novel acoustic signatures of upper ocean processes are comprised of (1) the surface tide (Fig. 7.1); (2) zones of enhanced surface and subsurface scattering over the troughs of non-linear internal waves of depression (Fig. 6.2, 7.6, 7.1 and 7.8); (3) the apparent increase in the roughness of the sea surface (Fig. 7.7); (4) vertical acoustic lines marking the convergence and divergence zones of internal waves (Fig. 7.8); (5) the knocking-down of the mooring line at the range of the sea surface (Fig. 7.1); (6) the breaking of surface waves (Fig. 7.11 and 7.12); (7) the hyperbolic scattering bands which meet just the sea surface echoes (Fig. 7.9); and (8) the concurrence of rain squalls, internal waves, Langmuir circulation, surface waves and biological scatterers (Fig. 7.4, 7.5 and 7.6).

- There is a need for better accounts of events (e.g. rain, surface manifestations of Langmuir circulation and internal waves) occurred during scientific cruises in ship log books to give a better support to the description of sonographs.

- Observations of many sonographs have revealed that acoustic features are mostly distorted by the instrument heading and by the orbital motions of surface waves. Specific formulations have been developed to describe these cases.
- Variations in the pitch (roll) angle appear not to change the intersection of the forward (starboard) beam with the surface or the range of targets.
- It has been found that the scattering of surface waves probably comes from the backward face of wave crests.
- ARIES II has demonstrated capacity to fill a gap regarding the apparent lack of direct detailed measurements of the straining within wave troughs of solitary-type internal waves of depression.
- A very important finding of this thesis does consist in the ability to provide estimates of the dimensions of surface waves and Langmuir circulation using a streamlined instrument equipped with dual-beam orthogonal side-scan sonars, which leads onto the potential to investigate plausible interactions among various small-scale processes, for instance, the misalignment of bubble bands caused by internal waves. However, possible effects of both un-calibrated compass and magnetic interference on the estimation of the orientation of bubble bands remains as an un-resolved issue.
- The fundamental contributions of the current work are the detailed analysis of the performance of ARIES II, and the close inspection of uncertainties, assumptions and errors associated with the interpretation and quantification of turbulent phenomena captured in acoustic imagery.

8.5 Future lines of research

Although ARIES II has provided vivid examples of upper ocean processes, this thesis has touched on only few aspects of the turbulence occurring near the sea surface and therefore much work remains to be done.

From a technical point of view, it is necessary the development of specific software to: (1) extract the wavy line at the range from the sea surface from acoustic images; (2) correct the range fluctuations of linear features using the formulation derived in section 6.4.4; (3) detect and estimate the frequency of occurrence of surface breaking waves; (4) detect the hyperbolic tracks of surface waves in order to improve the estimation of the direction of propagation; and (5) apply techniques for the recognition of patterns to provide comparisons of the dimensions of bubble bands with those obtained by overlapping tracing paper on sonographs. Such a techniques would particularly refine the detection of fragmented bubble bands and coexisting scales of Langmuir circulation, and definitely would improve the estimation of the spacing of bubble bands.

From a physical point of view, there are several interesting lines of research to pursue. (1) Acoustic signatures of both high-frequency and low-frequency surface waves can be utilised to study the effect of the waves on the roughness of the sea surface, which is a parameter that affects the estimation of the drag coefficient (section 2.2.1). Since the relevant dimensions are the wind speed, and the phase speed, wavelength and wave height of surface waves, then a dependence from the compass is avoided. (2) The scattering provided by acoustic images, may perhaps be utilised to obtain large scale signals from small-scale observations along the sea surface. The scattering, however, depends from the view direction of the sonar beams. (3) An important assumption and weakness in the Craik-Leibovich instability mechanism is that the Stokes drift is assumed parallel to the direction of the wind stress. It is possible to follow the evolution of the dimensions of bubble bands in the absence of internal waves and therefore to test the orientation of the bands against the direction of the mean wind and the direction of both wind-sea and swell. (4) Since results show that the speed of biological targets is of the same order of magnitude as the speed of the 30 m currents, then it might be possible to estimate, within certain error bar, the velocity field within internal wave troughs. Vertical speeds could be evaluated from, $\frac{\partial T}{\partial t} \; / \; < \frac{\partial T}{\partial z} >$. (5) Section 4.3.1 presented evidence of an internal wave packet with two waves of roughly the same amplitude. If one of the waves is not part of the packet, then it might be that an isolated wave is just crossing the packet. On the other hand, if the two waves belong to the same packet, then this may imply a highly non-linear evolution in the packet propagation. A numerical model based upon the KdV equation with the effects of wave refraction and spherical spreading included, could be used for examining this behaviour. (6) Results shown in section 7.9.2 illustrate the effect of non-passive advection of bubble bands by non-linear internal waves. Possible causes to investigate are the regeneration of bands in zones of abrupt changes in orientation (breaking of the circulation), the active interaction of bubble bands, internal and surface waves, the instability of the bubble band pattern and external forcing. Further measurements in the deep ocean will be required to compare, contrast and validate results obtained from sonographs and numerical modelling.

REFERENCES

Aleksandrov, A. P. and Vaindruk, E. S. (1974). Measurement of the parameters of an aerated sea layer as a method of remote investigation of near-surface vertical turbulence. In R. Ozmidov, editor, *The Investigation of the Variability of Hydrophysical Fields in the Ocean*, pages 122–128. Nauka Publishing Office, Moscow. (In Russian. A translation with code RUSSIA LP 4-3-80 can be obtained from the National Oceanography Library. E-mail: nol@soc.soton.ac.uk).

Aleksandrov, A. P., Vaindruk, E. S., and Dedikov, V. N. (1975). Acoustic method for remote measurement of speed in the surface layer of the sea. In *USSR and Eastern Europe Scientific Abstracts*, number 360 in U.S. Joint Publications Research Service, page 35. (Abstract).

Alford, M. H. and Pinkel, R. (2000). Observations of overturning in the thermocline: The context of ocean mixing. *J. Phys. Oceanogr.*, **30**, 805–832.

Apel, J. R. (1987). *Principles of Ocean Physics*. Academic Press.

Apel, J. R. (1995). Linear and nonlinear internal waves in coastal and marginal seas. In M. Ikeda and F. W. Dobson, editors, *Oceanographic Applications of Remote Sensing*, pages 57–78. CRC Press.

Apel, J. R., Holbrook, J. R., Liu, A. K., and Tsai, J. J. (1985). The Sulu Sea experiment. *J. Phys. Oceanogr.*, **15**, 1625–1651.

Apel, J. R., Gasparovic, R. F., Thompson, D. R., and Gotwols, B. L. (1988). Signatures of surface wave/internal wave interactions: Experiments and theory. *Dyn. Atmos. Oceans*, **12**, 89–106.

Apel, J. R., Ostrovsky, L. A., and Stepanyants, Y. A. (1995). Internal solitons in the ocean. Report MERCJRA 0695, The Johns Hopkins University. 66 pp.

Ashjian, C. J., Smith, S., Flagg, C. N., and Wilson, C. (1998). Patterns and occurrence of diel vertical migration of zooplankton biomass in the mid-atlantic bight described by an acoustic Doppler current profiler. *Cont. Shelf Res.*, **18**, 831–858.

Assaf, G., Gerard, R., and Gordon, A. L. (1971). Some mechanisms of oceanic mixing revealed in aereal photographs. *J. Geophys. Res.*, **76**, 6550–6572.

Bagg, M. and Thomas, J. O. (1984). The detection of internal waves in the North Atlantic using real aperture airbone radar. *Int. J. Rem. Sens.*, **5**, 961–974.

Baldwin, D. R. and Thorpe, S. A. (1996). Sidescan sonar study of water motions at the edge of the surf zone. Final Report December 1996, University of Southampton, Southampton Oceanography Centre.

Barstow, S. F. (1983). The ecology of Langmuir circulation: A review. *Marine Environ. Res.*, **9**, 211–236.

Bees, M. A. (1998). Planktonic communities and chaotic advection in dynamical models of Langmuir circulation. *Appl. Scien. Res.*, **59**, 141–158.

Bees, M. A., Mezic, I., and McGlade, J. (1998). Planktonic interactions and chaotic advection in Langmuir circulation. *Maths. Comput. Simul.*, **44**, 527–544.

Benjamin, T. B. (1966). Internal waves of finite amplitude and permanent form. *J. Fluid Mech.*, **25**, 241–270.

Bhaskaran, R. and Leibovich, S. (2002). Eulerian and lagrangian Langmuir circulation patterns. *Phys. Fluids*, **14**, 2557–2571.

Bogucki, D. J. and Redekopp, L. G. (1999). A mechanism for sediment resuspension by internal solitary waves. *Geophys. Res. Lett.*, **26**, 1317–1320.

Bogucki, D. J., Dickey, T., and Redekopp, L. G. (1997). Sediment resuspension and mixing by resonantly generated internal solitary waves. *J. Phys. Oceanogr.*, **27**, 1181–1196.

Bortkovskii, R. S. (1999). On the subsurface two-phase layer structure within patches of foam. In M. L. Banner, editor, *The Wind-Driven Air-Sea Interface Electromagnetic and Acoustic Sensing, Wave Dynamics and Turbulent Fluxes*, pages 171–178. The University of New South Wales.

Bowden, K. F. (1983). *Physical Oceanography of Coastal Waters*. Ellis Horwood Limited.

Brown, A. B. and Scott, J. C. (1987). Observation of ocean internal waves using echosounders. *Acoust. Lett.*, **11**, 108–114.

Buckingham, M. J., Berkhout, B. V., and Glegg, S. A. L. (1992). Imaging the ocean with ambient noise. *Nature*, **356**, 327–329.

Burrows, M., Thorpe, S. A., and Meldrum, D. T. (1999). Dispersion over the Hebridean and Shetland shelves and slopes. *Cont. Shelf Res.*, **19**, 49–55.

Chini, G. P. and Leibovich, S. (1998). Langmuir circulation dynamics above a deformable thermocline. In *1998 Ocean Sciences Meeting*, volume **79** of *Eos, Transactions, American Geophysical Union*, page OS149. American Geophysical Union.

Clamond, D. (1999). Steady finite amplitude waves on a horizontal seabed of arbitrary depth. *J. Fluid Mech.*, **398**, 45–60.

Cochrane, N. A., Sameoto, D., Herman, A. W., and Neilson, J. (1991). Multiple-Frequency acoustic backscattering and zooplankton aggregations in the inner Scotian Shelf Basin. *Can. J. Fish. Aquat. Sci.*, **48**, 340–355.

Colbo, K. and Li, M. (1999). Parameterizing particle dispersion in Langmuir circulation. *J. Geophys. Res.*, **104**, 26,059–26,068.

Contreras, R. F., Plant, W. J., Keller, W. C., Hayes, K., and Nystuen, J. (2003). Effects of rain on Ku-band backscatter from the ocean. *J. Geophys. Res.*, **108(C5)**, art. 3165.

Cowles, T. J., Desiderio, R. A., and Carr, M.-E. (1998). Small-scale planktonic structure: persistence and trophic consequences. *Oceanography*, **11**, 4–9.

Cox, S. M. (1997). Onset of Langmuir circulation when shear flow and Stokes drift are not parallel. *Fluid Dyn. Res.*, **19**, 149–167.

Cox, S. M. and Leibovich, S. (1997). Large-scale three-dimensional Langmuir circulation. *Phys. Fluids*, **9**, 2851–2863.

Craik, A. D. D. (1977). The generation of Langmuir circulations by an instability mechanism. *J. Fluid Mech.*, **81**, 209–223.

Crombie, D. D., Hasselmann, K., and Sell, W. (1978). High-frequency radar observations of sea waves travelling in opposition to the wind. *Boundary-Layer Meteorol.*, **13**, 45–54.

da Silva, J. C. B., Ermakov, S. A., Robinson, I. S., Jeans, D. R. G., and Kijashko, S. V. (1998). Role of surface films in ERS SAR signatures of internal waves on the shelf. 1. short-period internal waves. *J. Geophys. Res.*, **C4**, 8009–8031.

Dahl, P. H. and Jessup, A. T. (1995). On bubble clouds produced by breaking events: An event analysis of ocean acoustic measurements. *J. Geophys. Res.*, **100**, 5007–5020.

Deane, G. B. (1999). Acoustic hot-spots and breaking wave noise in the surf zone. *J. Acoust. Soc. Am.*, **105**, 3151–3167.

Deane, G. B. and Stokes, M. D. (2002). Scale dependence of bubble creation mechanisms in breaking waves. *Nature*, **418**, 839–844.

Donato, A. N., Peregrine, D. H., and Stocker, J. R. (1999). The focusing of surface waves by internal waves. *J. Fluid Mech.*, **384**, 27–58.

Donelan, M., Longuet-Higgins, M. S., and Turner, J. S. (1972). Surface wave motion induced by wind. *Science*, **87**, 119–123.

Drazin, P. G. (1983). *Solitons.* Cambridge University Press.

Dunne, A. G. (1987). *Admiralty Manual of Navigation: Volume I.* Her Majesty's Stationery Office.

Dyke, P. P. G. and Barstow, S. F. (1983). The importance of Langmuir circulations to the ecology of the mixed layer. In Sündermann/Lenz, editor, *North Sea Dynamics*, pages 486–497. Springer-Verlag, Berlin.

Etling, D. and Brown, R. A. (1993). Roll vortices in the planetary boundary layer: a review. *Boundary-Layer Meteorol.*, **65**, 215–248.

Evans, G. T. and Taylor, F. J. R. (1980). Phytoplankton accumulation in Langmuir cells. *Limnol. Oceanogr.*, **25**, 840–845.

Faller, A. J. (1964). The angle of windrows in the ocean. *Tellus*, **16**, 363–370.

Faller, A. J. (1971). Oceanic turbulence and the Langmuir circulations. *Ann. Rev. Ecol. Syst.*, **2**, 201–236.

Farmer, D. M. (1997). Observing the ocean side of the air-sea interface. *Oceanography*, **10**, 106–110.

Farmer, D. M. and Armi, L. (1999). The generation and trapping of solitary waves over topography. *Science*, **283**, 188–190.

Farmer, D. M. and Li, M. (1994). Oil dispersion by turbulence and coherent circulations. *Ocean Engng.*, **21**, 575–586.

Farmer, D. M. and Li, M. (1995). Patterns of bubble clouds organized by Langmuir circulation. *J. Phys. Oceanogr.*, **25**, 1426–1440.

Farmer, D. M. and Smith, J. D. (1980). Tidal interaction of stratified flow with a sill in Knight Inlet. *Deep-Sea Res.*, **27A**, 239–254.

Fedorov, K. N. and Ginsberg, A. I. (1986). Phenomena on the sea surface observed visually. *Oceanology*, **26**, 5–14.

Filatov, N. N., Ryanzhin, S. V., and Zaytsev, L. V. (1980). Features of turbulence, Langmuir circulation and internal waves in a lake. *Izv. Atmos. Oceanic Phys.*, **16**, 694–698.

Fisher, J. and Visbeck, M. (1993). Seasonal variation of the daily zooplankton migration in the Greenland Sea. *Deep-Sea Res.*, **40**, 1547–1557.

Flagg, C. N. and Smith, S. L. (1989). On the use of acoustic Doppler current profiler to measure zooplankton abundance. *Deep-Sea Res.*, **36**, 455–474.

Flemming, B. W. (1982). Causes and effects of sonograph distortion and some graphical methods for their manual correction. In W. G. A. Russell-Cargill, editor, *Recent Developments in Side Scan Sonar Thechniques*, pages 103–138. Central Acoustics Laboratory, University of Cape Town.

Franks, P. J. S. (1995). Thin layers of phytoplankton: a model of formation by near-inertial wave shear. *Deep-Sea Res.*, **42**, 75–91.

García-Górriz, E. G., Font, J., and Candela, J. (1997). Data quality control for vessel mounted acoustic Doppler current profiler. Application for the western Mediterranean Sea. *Sci. Mar.*, **61**, 417–430.

Gargett, A. E. and Hughes, B. A. (1972). On the interaction of surface and internal waves. *J. Fluid Mech.*, **52**, 179–191.

Garratt, J. R. (1992). *The atmospheric boundary layer*. Cambridge University Press.

Garrett, C. (1996). Processes in the surface mixed layer of the ocean. *Dyn. Atmos. Oceans*, **23**, 19–34.

Garrett, C. and Munk, W. (1979). Internal waves in the ocean. *Ann. Rev. Fluid Mech.*, **11**, 339–369.

Gasparovic, R. F. and Apel, J. R. (1988). An overview of the SAR internal wave signature experiment. *J. Geophys. Res.*, **93**, 12,304–12,316.

Gasparovic, R. F., Apel, J. R., and Kasischke, E. S. (1988). An overview of the SAR internal wave surface experiment. *J. Geophys. Res.*, **93**, 12,304–12,316.

Gasparovic, R. F., Thompson, D. R., and Apel, J. R. (1989). Synthetic aperture radar imaging of ship-generated internal waves. *APL Tech. Dig.*, **10**, 326–330.

Geernaert, G. L., Hansen, F., Courtney, M., and Herbers, T. (1993). Directional attributes of the ocean surface wind stress vector. *J. Geophys. Res.*, **98**, 16,571–16,582.

Gemmrich, J. R. and Farmer, D. M. (1999). Near-Surface turbulence and thermal structure in a wind-driven sea. *J. Phys. Oceanogr.*, **29**, 480–499.

Gerkema, T. and Zimmerman, J. T. F. (1995). Generation of nonlinear internal tides ans solitary waves. *J. Phys. Oceanogr.*, **25**, 1081–1094.

Gnanadesikan, A. and Weller, R. A. (1995). Structure and instability of the Ekman spiral in the presence of surface gravity waves. *J. Phys. Oceanogr.*, **25**, 3148–3171.

Graham, A. and Hall, A. J. (1997). The horizontal distribution of bubbles in a shallow sea. *Cont. Shelf Res.*, **17**, 1051–1082.

Green, T. and Houk, D. F. (1979). The mixing of rain with near-surface water. *J. Fluid Mech.*, **90**, 569–588.

Greer Walker, M., Harden Jones, F. R., and Arnold, G. P. (1978). The movements of plaice (*pleuronectes platessa l.* tracked in the open sea). *J. Cons. int. Explor. Mer*, **38**, 58–86.

Grimshaw, R., Pelinovsky, E., and Talipova, T. (2003). Damping of large-amplitude solitary waves. *Wave Motion*, **37**, 351–364.

Guizen, K., Barthelélemy, E., and Inall, M. E. (1999). Internal tide generation at a shelf break by an oblique barotropic tide: Observations and analytical modelling. *J. Geophys. Res.*, **104**, 15,655–15,668.

Hall, A. J. (1986). ARIES Technical Report. IOS Internal Document No. 253, 77pp.

Hallock, Z. R., Small, J., George, J., Field, R. L., and Scott, J. C. (2000). Shoreward propagation of internal waves at the Malin Shelf edge. *Cont. Shelf Res.*, **20**, 2045–2057.

Haury, L. R. and Shulenberger, E. (1998). Surface nutrient enrichment in the California Current off Southern California: description and possible causes. *Deep-Sea Res. II*, **45**, 1577–1601.

Haury, L. R., Briscoe, M. G., and Orr, M. H. (1979). Tidally generated internal wave packets in Massachusetts Bay. *Science*, **278**, 312–317.

Haury, L. R., Wiebe, P. H., Orr, M. H., and Briscoe, M. G. (1983). Tidally generated high-frequency internal wave packets and their effects on plankton in Massachusetts Bay. *J. Mar. Res.*, **41**, 65–112.

Henyey, F. S. (1999). Exact solitary wave solutions in shallow water. In *Dynamics of the Oceanic Internal Gravity Waves, II*, Proceedings ‘Aha Hulik‘oa, pages 89–93. University of Hawaii.

Henyey, F. S. and Hoering, A. (1997). Energetics of borelike internal waves. *J. Geophys. Res.*, **C2**, 3323–3330.

Heywood, K. J., Scrope-Howe, S., and Barton, E. D. (1991). Estimation of zooplankton abundance from shipborne ADCP backscatter. *Deep-Sea Res.*, **38**, 677–691.

Holliday, D. V., Pieper, R. E., Greenlaw, C. F., and Dawson, J. K. (1998). Acoustical sensing of small-scale vertical structures in zooplankton assemblages. *Oceanography*, **11**, 18–23.

Holligan, P. M., Pingree, R. D., and Mardell, G. T. (1985). Ocean solitons, nutrient pulses and phytoplankton. *Nature*, **314**, 348–350.

Holt, J. T. and Thorpe, S. A. (1997). The propagation of high frequency internal waves in the Celtic Sea. *Deep-Sea Res.*, **44**, 2087–2116.

Horikawa, K. (1988). *Nearshore Dynamics and Coastal Processes*. University of Tokyo Press.

Hughes, B. A. (1978). The effect of internal waves on surface wind waves, 2. Theoretical analysis. *J. Geophys. Res.*, **83**, 455–465.

Hughes, B. A. and Dawson, T. W. (1988). Joint Canada-U.S. ocean wave investigation project: an overview of the Georgia Strait Experiment. *J. Geophys. Res.*, **93**, 12,219–12,334.

Hussain, A. K. M. F. (1986). Coherent structures and turbulence. *J. Fluid Mech.*, **173**, 303–356.

Huthance, J. M. (1986). The Rockall slope current and shelf-edge processes. *Proc. R. Soc. Edin.*, **B 88**, 83–101.

Inall, M. E., Rippeth, T. P., and Sherwin, T. J. (2000). Impact of nonlinear waves on the dissipation of internal tidal energy at a shelf break. *J. Geophys. Res.*, **105**, 8687–8705.

Inall, M. E., Shapiro, G. I., and Sherwin, T. J. (2001). Mass transport by non-linear internal waves on the Malin Shelf. *Cont. Shelf Res.*, **21**, 1449–1472.

Kamykowski, D. (1979). Possible interactions between phytoplankton and semidiurnal internal tides. *J. Mar. Res.*, **32**, 67–89.

Kantha, L. H. and Clayson, C. A. (2000). *Small Scale Processes in Geophysical Fluid Flows*. Academic Press.

Kanwisher, J. (1963). On the exchange of gases between the atmosphere and the sea. *Deep-Sea Res.*, **10**, 195–207.

Kao, T. W., Pan, F.-S., and Renouard, D. (1985). Internal solitons on the pycnocline: generation, propagation, and shoaling and breaking over a slope. *J. Fluid Mech.*, **159**, 19–53.

Kenney, B. C. (1977). *An Experimental Investigation of the Fluctuating Currents Responsible for the Generation of Windrows*. Ph. D. dissertation, Unversity of Waterloo. 163 pp.

Keulegan, G. H. (1953). Characteristics of internal solitary waves. *J. Res. Nat. Bur.*

Stand., **51**, 133–140.

Kinder, T. H. (1984). Net mass-transport by internal waves near the Strait of Gibraltar. *Geophys. Res. Lett.*, **11**, 987–990.

Kinsman, B. (1965). *Wind waves.* Prentice-Hall Inc.

Lamb, K. G. (1997). Particle transport by nonbreaking, solitary internal waves. *J. Geophys. Res.*, **102**, 18,641–18,600.

Lamb, K. G. (2003). Shoaling solitary internal waves: on a criterion for the formation of waves with trapped cores. *J. Fluid Mech.*, **478**, 81–100.

Lande, R. and Yentsch, C. S. (1988). Internal waves, primary production and the compensation depth of marine phytoplankton. *J. Plankton. Res.*, **10**, 565–571.

Langmuir, I. (1938). Surface motion of water induced by wind. *Science*, **87**, 119–123.

Ledbetter, M. (1979). Langmuir circulations and plankton patchiness. *Ecol. Modelling*, **7**, 289–310.

Lee, O. S. (1961). Effect of an internal wave on sound in the ocean. *J. Acoust. Soc. Am.*, **33**, 677–680.

Leibovich, S. (1977). Convective instability of stably stratified water in the ocean. *J. Fluid Mech.*, **82**, 561–585.

Leibovich, S. (1983). The form and dynamics of Langmuir circulations. *Ann. Rev. Fluid Mech.*, **15**, 391–427.

Leibovich, S. and Lumley, J. L. (1982). Interaction of turbulence and Langmuir cells in vertical transport of oil droplets. In H. Tennekes, editor, *First International Conference on Meteorology and Air/Sea Interaction of the Coast Zone*, pages 271–276. American Meteorological Society, Boston.

Leibovich, S. and Paolucci, S. (1980). The Langmuir circulation instability as a mixing mechanism in the upper ocean. *J. Phys. Oceanogr.*, **10**, 186–207.

Leibovich, S. and Tandon, A. (1993). Three-dimensional circulation instability in a stratified layer. *J. Geophys. Res.*, **C9**, 501–516.

Leibovich, S., Lele, S. K., and Moroz, I. M. (1989). Nonlinear dynamics in Langmuir circulations and in thermosolutal convection. *J. Fluid Mech.*, **198**, 471–511.

Leighton, T. G. (1994). *The Acoustic Bubble.* Academic Press.

Lennert-Cody, C. E. and Franks, P. J. S. (1999). Plankton patchiness in high-frequency internal waves. *Mar. Ecol. Prog. Ser.*, **186**, 59–66.

Lesieur, M. (1997). *Turbulence in Fluids.* Kluwer Academic Publishers.

Levine, M. D., Paulson, C. A., Briscoe, M. G., Weller, R. A., and Peters, H. (1983). Internal waves in JASIN. *Phil. Trans. R. Soc. Lond. A*, **308**, 389–405.

Li, M. and Garrett, C. (1993). Cell merging and the jet/downwelling ratio in Langmuir circulation. *J. Mar. Res.*, **51**, 737–769.

Liu, A. K. (1988). Analysis of nonlinear internal waves in the New York Bight. *J. Geophys. Res.*, **93**, 12,317–12,329.

Liu, A. K., Martin, S., and Kwok, R. (1997). Tracking of ice edges and ice floes by wavelet analysis of SAR images. *J. Atmos. Oceanic Technol.*, **14**, 1187–1198.

Liu, A. K., Chang, Y. S., Hsu, M.-K., and Liang, N. K. (1998). Evolution of nonlinear internal waves in the East and South China Seas. *J. Geophys. Res.*, **103**, 7995–8008.

Liu, G. R., Li, W., Zhang, X. M., and Varadan, V. K. (2003). Shape identification of underwater objects using backscattered frequency signals. *J. Acoust. Soc. Am.*, **113**, 3146–3154.

Loder, J. W. and Hamilton, J. M. (1991). Degradation of some mechanical current-meter measurements by high-frequency mooring or wave motion. *IEEE J. Oceanic Eng.*, **16**, 343–349.

Long, R. R. (1956). Solitary waves in one- and two-fluid systems. *Tellus*, **5**, 460–471.

Longuet-Higgins, M. S. (1983). On the joint distribution of wave period and amplitudes in a random wave field. *Proc. Roy. Soc. Lond. A*, **389**, 241–258.

Longuet-Higgins, M. S. and Fox, M. J. H. (1977). Theory of the almost-highest wave: the inner solution. *J. Fluid Mech.*, **80**, 721–741.

Mackenzie, K. V. (1981). Nine-term equation for sound speed in the oceans. *J. Acoust. Soc. Am.*, **70**, 807–812.

Malinen, T., Horppila, J., and Liljendahl-Nurminen, A. (2001). Langmuir circulations disturb the low-oxygen refuge of phantom midge larvae. *Limnol. Oceanogr.*, **46**, 689–692.

McWilliams, J. C., Sullivan, P. P., and Moeng, C. (1997). Langmuir turbulence in the ocean. *J. Fluid Mech.*, **334**, 1–30.

Medwin, H. and Breitz, N. D. (1989). Ambient and transient bubble spectral densities in quiescent seas and under spilling breakers. *J. Geophys. Res.*, **94**, 12,751–12,759.

Medwin, H. and Clay, C. S. (1998). *Fundamentals of Acoustic Oceanography*. Academic Press.

Melville, W. K. (1996). The role of surface-wave breaking in air-sea interaction. *Annu. Rev. Fluid. Mech.*, **28**, 279–321.

Melville, W. K., Shear, R., and Veron, F. (1998). Laboratory measurements of the generation and evolution of Langmuir circulations. *J. Fluid Mech.*, **364**, 31–58.

Melville, W. K., Veron, F., and White, C. J. (2002). The velocity field under breaking waves: coherent structures and turbulence. *J. Fluid Mech.*, **454**, 203–233.

Métais, O. (1997). Numerical simulation of geophysical turbulence. *Sci. Mar.*, **61**, 75–91, Supl. 1.

Nadaoka, K., Hino, M., and Koyano, Y. (1989). Structure of the turbulent flow field under breaking waves in the surf zone. *J. Fluid Mech.*, **204**, 359–387.

Nystuen, J. A. and Medwin, H. (1995). Underwater sound produced by rainfall: secondary splashes of aerosols. *J. Acoust. Soc. Am.*, **97**, 1606–1613.

Nystuen, J. A. and Selsor, H. D. (1997). Weather classification using passive acoustic drifters. *J. Acoust. Soc. Am.*, **14**, 656–666.

Oikonomou, E. K. (1997). *Stationary Phase Internal Waves Generated by Flow along Sloping Topography*. Ph. D. dissertation, Unversity of Southampton. 192 pp.

Orr, M. H., Haury, L. R., Wiebe, P. H., and Briscoe, M. G. (2000). Backscatter of high-frequency (200 kHz) acoustic wavefields from ocean turbulence. *J. Acoust. Soc. Am.*, **108**, 1595–1601.

Osborn, T. (1998). Finestructure, microstructure, and thin layers. *Oceanography*, **11**, 36–48.

Osborn, T., Farmer, D. M., Vagle, S., Thorpe, S. A., and Curé, M. (1992). Measurements of bubble plumes and turbulence from a submarine. *Atmos.-Ocean*, **30**, 419–440.

Osborne, A. R. and Burch, T. L. (1980). Internal solitons in the Andaman Sea. *Science*, **208**, 451–460.

Ostrovsky, L. A. and Stepanyants, Y. A. (1989). Do internal solitons exist in the ocean? *Revs. Geophys.*, **27**, 293–310.

Packwood, A. R. (1995). ARIES II, Concept Designs and Initial Layout Drawings.

Department of Mechanical Engineering, University of Surrey.

Pedersen, B. and Trevorrow, M. V. (1999). Continuous monitoring of fish in a shallow channel using a fixed horizontal sonar. *J. Acoust. Soc. Am.*, **105**, 3126–3135.

Pedlosky, J. (1987). *Geophysical Fluid Dynamics*. Springer-Verlag.

Peregrine, D. H. (1991). Breaking water waves. In A. R. Osborne, editor, *Nonlinear Topics in Ocean Physics*, pages 499–526. North Holland.

Peters, A. S. and Stoker, J. J. (1960). Solitary waves in liquids having non-constant density. *Comm. Pure Appl. Maths.*, **13**, 115–164.

Phillips, O. M. (1973). On the interaction of internal and surface waves. *Phys. Atmos. Ocean*, **9**, 954–961.

Phillips, W. R. C. (2001). On an instability to Langmuir circulations and the role of Prandtl and Richardson numbers. *J. Fluid Mech.*, **442**, 335–358.

Phillips, W. R. C. (2002). Langmuir circulations beneath growing or decaying surface waves. *J. Fluid Mech.*, **469**, 317–342.

Pingree, R. D. (1984). Some applications of the remote sensing to studies in the Bay of Biscay, Celtic Sea and English Channel. In J. C. J. Nihoul, editor, *Remote Sensing of Shelf Sea Hydrodynamics*, pages 287–315. Elsevier Science Publishers B. V.

Pingree, R. D. and Mardell, G. T. (1981). Slope turbulence, internal waves and phytoplankton growth at the Celtic Sea shelf-break. *Phil. Trans. R. Soc. Lond. A*, **302**, 663–682.

Pingree, R. D. and New, A. L. (1995). Structure, seasonal development and sunglint spatial coherence of the internal tide on the Celtic and Armorican shelves and in the Bay of Biscay. *Deep-Sea Res.*, **42**, 245–284.

Pingree, R. D., Mardell, G. T., and New, A. L. (1986). Propagation of internal tides from the upper slopes of the Bay of Biscay. *Nature*, **321**, 154–158.

Pinkel, R. (1979). Observations of strongly nonlinear internal motion in the open sea using range-gated Doppler sonar. *J. Phys. Oceanogr.*, **9**, 675–686.

Pinkel, R. (1981). On the use of Doppler sonar for internal wave measurements. *Deep-Sea Res.*, **28A**, 269–289.

Pinkel, R. (1983). Doppler sonar observations of internal waves: wavefield structure. *J. Phys. Oceanogr.*, **13**, 804–815.

Pinkel, R. (2000). Internal solitary waves in the warm pool of the western equatorial pacific. *J. Phys. Oceanogr.*, **30**, 2906–2926.

Pinkel, R. and Smith, J. A. (1987). Open ocean surface-wave measurement using Doppler sonar. *J. Geophys. Res.*, **92**, 12,967–12,973.

Pinkel, R. and Smith, J. A. (1992). Repeat sequence coding for improved precision of Doppler sonar and sodar. *J. Atmos. Oceanic Technol.*, **9**, 149–163.

Pinkel, R., Merrifield, M., Smith, J. A., and Ramm, H. (1996). Sea surface and mixed layer studies. In M. A. Donelan, W. H. Hui, and W. J. Plant, editors, *The Air-Sea Interface: Radio and Acoustic Sensing, Turbulence and Wave Dynamics*, pages 599–606. The Rosenstiel School of Marine and Atmospheric Science, University of Miami.

Pistek, P. and Violette, P. L. (1999). Observations of the supression of tide-generated nonlinear internal wave packets in the Strait of Gibraltar. *J. Mar. Syst.*, **20**, 113–128.

Plueddemann, A. J. and Pinkel, R. (1989). Characterization of the pattern of diel migrations using Doppler sonar. *Deep-Sea Res.*, **36**, 509–530.

Plueddemann, A. J. and Weller, R. A. (1999). Structure and evolution of the oceanic surface boundary layer during the Surface Waves Processes Program. *J. Mar. Syst.*, **21**, 85–102.

Plueddemann, A. J., Smith, J. A., Farmer, D. M., Weller, R. A., Crawford, W. R., Pinkel, R., Vagle, S., and Gnanadesidan, A. (1996). Structure and variability of Langmuir circulation during the surface waves processes program. *J. Geophys. Res.*, **101**, 3525–3543.

Pollard, R. T. (1977). Observations and theories of Langmuir circulations and their role in near surface mixing. In M. Angel, editor, *A Voyage of Discovery: G. Deacon 70th Anniversary Volume*, pages 235–251. Pergamon.

Polonichko, V. (1997). Generation of Langmuir circulation for nonaligned wind stress and stokes drift. *J. Geophys. Res.*, **102**, 15,773–15,780.

Poon, Y.-K., Tang, S., and Wu, J. (1992). Interactions between wind and waves. *J. Phys. Oceanogr.*, **22**, 977–987.

Price, J. F., R. A, W., and Pinkel, R. (1986). Diurnal cycling: Observations and models of the upper ocean response to diurnal heating, cooling, and wind mixing. *J. Geophys. Res.*, **91**, 8411–8427.

Proni, J. R. and Apel, J. R. (1975). On the use of high-frequency acoustics for the study of internal waves and microstructure. *J. Geophys. Res.*, **80**, 1147–1151.

Proni, J. R., Ostapoff, F., and Sellers, R. L. (1978). Acoustic observations of high-frequency, near-surface internal wave groups in the deep ocean during GATE. *Deep-Sea Res.*, **25**, 299–307.

Rapp, R. J. and Melville, W. K. (1990). Laboratory measurements of deep-water breaking waves. *Phil. Trans. R. Soc. Lond. A*, **A331**, 731–800.

Rippeth, T. P. and Inall, M. E. (2002). Observations of the internal tide and associated mixing across the Malin Shelf. *J. Geophys. Res.*, **107**, 3:1–15.

Robinson, S. K. (1991). Coherent motions in the turbulent boundary layer. *Ann. Rev. Fluid Mech.*, **23**, 601–639.

Ryanzhin, S. V. (1980). On the energy and the depth of penetration of Langmuir circulation. *Izv. All Union Geogr. Soc.*, **112**, 46–54.

Sandstrom, H. and Elliot, J. A. (1984). Internal tide and solitons on the Scotian Shelf: A nutrient pump and work. *J. Geophys. Res.*, **89**, 6415–6426.

Segur, H. and Hammack, J. L. (1982). Soliton models of long internal waves. *J. Fluid Mech.*, **118**, 285–304.

Seim, H. E. and Gregg, M. C. (1994). Detailed observations of naturally occurring shear instability. *J. Geophys. Res.*, **99**, 10,049–10,073.

Sene, K. J., Hunt, J. C. R., and Thomas, K. N. H. (1994). The role of coherent structure in bubble transport by turbulent shear flows. *J. Fluid Mech.*, **259**, 219–240.

Sherwin, T. J. (1988a). Analysis of an internal tide observed on the Malin shelf, North of Ireland. *J. Phys. Oceanogr.*, **18**, 1035–1050.

Sherwin, T. J. (1988b). Measurements of current speed using an Aanderaa RCM4 current meter in the presence of surface waves. *Cont. Shelf Res.*, **8**, 131–144.

Sherwin, T. J. and Simpson, J. H. (1996). Cruise report Challenger 121/LOIS-SES 3, August/September 1995. UCES Report U96-1, University of Wales, Bangor.

Simpson, J. H. (1998a). The Celtic Seas coastal segment (19,E). In A. R. Robinson and K. H. Brink, editors, *The Sea, Vol. 11, The Global Coastal Ocean: Regional Studies and Syntheses*, pages 659–698. John Willey & Sons, Inc.

Simpson, J. H. (1998b). Tidal processes in shelf seas. In K. H. Brink and A. R. Robinson, editors, *The Sea, Vol. 10, The Global Coastal Ocean: Processes and Methods*, pages 113–150. John Willey & Sons, Inc.

Skyllingstad, E. D., Smyth, W. D., and Crawford, G. B. (2000). Resonant wind-driven mixing in the ocean boundary layer. *J. Phys. Oceanogr.*, **30**, 1866–1890.

Small, J. (2001). A nonlinear model of the shoaling and refraction of interfacial solitary waves in the ocean Part. I: Development of the model and investigations of the shoaling effect. *J. Phys. Oceanogr.*, **31**, 3163–3183.

Small, J., Hallock, Z., Pavey, G., and Scott, J. (1999). Observations of large amplitude internal waves at the Malin Shelf edge during SESAME 1995. *Cont. Shelf Res.*, **19**, 1389–1436.

Smith, J. A. (1992). Observed growth of Langmuir circulation. *J. Geophys. Res.*, **97**, 5651–5664.

Smith, J. A. (1998). Evolution of Langmuir circulation during a storm. *J. Geophys. Res.*, **103**, 12,649–12,668. (http://jerry.ucsd.edu).

Smith, J. A. (2001). Observations and theories of Langmuir circulation: a story of mixing. In J. L. Lumley, editor, *Fluid Mechanics and the Enviroment Dynamical Approaches*, pages 295–314. Springer.

Smith, J. A. and Largier, L. (1995). Observations of nearshore circulation: rip currents. *J. Geophys. Res.*, **100**, 10,967–10,975.

Smith, J. A. and Pinkel, R. (1987). Observations of waves and Langmuir circulation with Doppler sonars. In *Dynamics of the Oceanic Surface Mixed Layer*, Proceedings ‘Aha Hulik‘oa, pages 95–118. University of Hawaii.

Smith, J. A., Pinkel, R., and Weller, R. A. (1987). Velocity structure in the mixed layer during MILDEX. *J. Phys. Oceanogr.*, **17**, 425–439.

Spindel, R. C., Porter, R. P., and Schwoerer, J. A. (1978). Acoustic phase tracking of ocean moorings. *IEEE. J. Oceanic Eng.*, **OE-3**, 27–31.

Stanton, T. K., Chu, D., Wiebe, P. H., Martin, L. V., and Eastwood, R. L. (1998). Sound scattering by several zooplankton groups. I. Experimental determination of dominant scattering mechanisms. *J. Acoust. Soc. Am.*, **103**, 225–253.

Stanton, T. K., Chu, D., Wiebe, P. H., Eastwood, R. L., and Warren, J. D. (2000). Acoustic scattering by benthic and planktonic shelled animals. *J. Acoust. Soc. Am.*, pages 535–550.

Stanton, T. P. and Ostrovsky, L. A. (1998). Observations of highly nonlinear internal solitons over the Continental Shelf. *Geophys. Res. Lett.*, **25**, 2695–2698.

Stommel, H. (1949). Trajectories of small bodies sinking slowly through convection cells. *J. Mar. Res.*, **8**, 24–29.

Sutcliffe, W. H., Sheldon, R. W., Prakash, A., and Gordon, D. C. (1971). Relations between wind speed, Langmuir circulation and particle concentration in the ocean.

Deep-Sea Res., **18**, 639–643.

Szczucka, J. and Klusek, Z. (1996). Migration patterns of acoustic scatterers in the southern Baltic Sea. *Oceanologia*, **38**, 61–79.

Tandon, A. and Leibovich, S. (1995a). Secondary instabilities in Langmuir circulations. *J. Phys. Oceanogr.*, **25**, 1206–1217.

Tandon, A. and Leibovich, S. (1995b). Simulations of three-dimensional Langmuir circulation in water of constant density. *J. Geophys. Res.*, **100**, 22,613–22,623.

Teixeira, M. A. C. and Belcher, S. E. (2002). On the distortion of turbulence by a progressive surface wave. *J. Fluid Mech.*, **458**, 229–267.

Thompson, D. R. (1985). Intensity modulations in Synthetic Aperture Radar Images of ocean surface currents and the wave/current interaction process. *APL Tech. Dig.*, **6**, 346–353.

Thompson, D. R. and Gasparovic, R. F. (1986). Intensity modulation in SAR images of internal waves. *Nature*, **320**, 345–348.

Thoroddsen, S. T., Etoh, T. G., and Takehara, K. (2003). Air entrapment under an impacting drop. *J. Fluid Mech.*, **478**, 125–134.

Thorpe, S. A. (1968). On the shape of progressive internal waves. *Phil. Trans. R. Soc. Lond. A*, **263**, 563–614.

Thorpe, S. A. (1982). On the clouds of bubbles formed by breaking wind-waves in deep water, and their role in air-sea grans transfer. *Phil. Trans. R. Soc. Lond. A*, **304**, 155–210.

Thorpe, S. A. (1984). The effect of Langmuir circulation on the distribution of submerged bubbles caused by breaking wind waves. *J. Fluid Mech.*, **142**, 151–170.

Thorpe, S. A. (1986a). Bubble clouds: a review of their detection by sonar, of related models, and of how K_v may be determined. In E. C. Monahan and G. H. Niocaill, editors, *Oceanic Whitecaps and Their Role in Air-Sea Exchange Processes*, pages 57–68. D. Reidel Publishing Company.

Thorpe, S. A. (1986b). Measurements with an automatically recording inverted echo sounder; ARIES and the bubble clouds. *J. Phys. Oceanogr.*, **16**, 1462–1478.

Thorpe, S. A. (1988). The dynamics of the boundary layers of the deep ocean. *Sci. Prog. Oxf.*, **72**, 189–206.

Thorpe, S. A. (1992a). The break-up of Langmuir circulation and the instability of an array of vortices. *J. Phys. Oceanogr.*, **22**, 350–360.

Thorpe, S. A. (1992b). Bubble clouds and the dynamics of the upper ocean. *Q. J. R. Meteorol. Soc.*, **118**, 1–22.

Thorpe, S. A. (1995a). Dynamical processes of transfer at the sea surface. *Progress in Oceanography*, **35**, 315–352. Pergamon.

Thorpe, S. A. (1995b). On the meandering and dispersion of a plume of floating particles caused by Langmuir circulation and a mean current. *J. Phys. Oceanogr.*, **25**, 685–690.

Thorpe, S. A. (1997). Interactions between internal waves and boundary layer vortices. *J. Phys. Oceanogr.*, **27**, 62–71.

Thorpe, S. A. (1998). Turbulence in the stratified and rotating world ocean. *Theoret. Comput. Fluid Dyn.*, **11**, 171–181.

Thorpe, S. A. and Baldwin, D. R. (1995). NERC final report - construction of autonomous sonar (SIDAL Funding). Interim Report GST/02/830, University of Southampton, Southampton Oceanography Centre.

Thorpe, S. A. and Curé, M. S. (1994). One-dimensional dispersion in a lake infered from sonar observations. In K. Bevan, P. Chatwin, and J. Millbank, editors, *Mixing and Transport in the Enviroment*, pages 17–28. John Willey & Sons Ltd.

Thorpe, S. A. and Hall, A. J. (1982). Observations of the thermal structure of Langmuir circulations. *J. Fluid Mech.*, **114**, 237–250.

Thorpe, S. A. and Hall, A. J. (1983). The characteristics of breaking waves, bubble clouds, and near-surface currents observed using side-scan sonar. *Cont. Shelf Res.*, **1**, 353–384.

Thorpe, S. A. and Hall, A. J. (1987). Bubble clouds and temperature anomalies in the upper ocean. *Nature*, **328**, 48–51.

Thorpe, S. A. and Hall, A. J. (1993). Nearshore side-scan sonar studies. *J. Atmos. Oceanic Technol.*, **10**, 778–783.

Thorpe, S. A. and Humphries, P. N. (1980). Bubbles and breaking waves. *Nature*, **283**, 463–465.

Thorpe, S. A. and Stubbs, A. R. (1979). Bubbles in a freshwater lake. *Nature*, **279**, 403–405.

Thorpe, S. A., Hall, A. J., Packwood, A. R., and Stubbs, A. R. (1985). The use of a towed side-scan sonar to investigate processes near the sea surface. *Cont. Shelf Res.*, **4**, 597–607.

Thorpe, S. A., Belloul, M. B., and Hall, A. J. (1987). Internal waves and whitecaps. *Nature*, **330**, 740–742.

Thorpe, S. A., Curé, M. S., Graham, A., and Hall, A. J. (1994). Sonar observations of Langmuir circulation and estimation of dispersion of floating particles. *J. Atmos. Oceanic Technol.*, **11**, 1273–1294.

Thorpe, S. A., Graham, A., and Hall, A. (1996). Wave and dispersion studies in shallow water using side-scan sonar. In C. Pattiaratchi, editor, *Mixing in Estuaries and Coastal Seas*, pages 110–114. Coastal and Estuarine Studies. American Geophysical Union.

Thorpe, S. A., Ulloa, M. J., Baldwin, D., and Hall, A. J. (1998). An autonomously recording inverted echo sounder: ARIES II. *J. Atmos. Oceanic Technol.*, **15**, 1346–1360.

Thorpe, S. A., Osborn, T. R., Jackson, J. F. E., Hall, A. J., and Lueck, R. G. (2003). Measurements of turbulence in the upper-ocean mixing layer using Autosub. *J. Phys. Oceanogr.*, **33**, 122–145.

Trenberth, K. E., Large, W. G., and Olson, J. G. (1990). The mean annual cycle in global ocean wind stress. *J. Phys. Oceanogr.*, **20**, 1742–1760.

Trevorrow, M. V. (1998). Observations of internal solitary waves near Oregon coast with an inverted echo sounder. *J. Geophys. Res.*, **103**, 7671–7680.

Tricker, R. A. R. (1964). *Bores, Breakers, Waves and Wakes.* American Elsevier Publishing Company, Inc.

Tritton, D. J. (1988). *Physical Fluid Dynamics.* Oxford Science Publications.

Tucker, M. J. and Stubbs, A. R. (1963). Underwater acoustics as a tool in oceanography. In V. M. Alberts, editor, *Underwater Acoustics*, pages 301–319. Pennsylvania State University Publication, Plenum Press.

Ulloa, M. J. (1998). Non-linear internal waves observed by ARIES II at the Malin shelf break. In *UK Oceanography '98*, Challenger Society for Marine Science Conference, page 57. Challenger Society for Marine Science.

Ulloa, M. J. and Thorpe, S. A. (1998). Acoustic observations of the distortion of bubble bands by internal waves at the shelf break. In *1998 Ocean Sciences Meeting*, volume **79** of *Eos, Transactions, American Geophysical Union*, page OS148. American Geophysical Union.

Valdez, V. (1960). Internal waves on an echo-sounder record. *Deep-Sea Res.*, **7**, 148–151.

Wallace, B. B. and Hamilton, D. P. (1999). The effect of variations in irradiance on buoyancy regulation in *microcystis aeruginosa*. *Limnol. Oceanogr.*, **44**, 273–281.

Weller, R. A. and Plueddemann, A. J. (1996). Observations of the vertical structure of the oceanic boundary layer. *J. Geophys. Res.*, **101**, 8789–8806.

Weller, R. A., Dean, J. P., Marra, J., Price, J. F., Frances, F. A., and Boardman, D. C. (1985). Three-dimensional flow in the upper ocean. *Science*, **227**, 1552–1556.

Wesson, J. C. and Gregg, M. C. (1994). Mixing at Camarinal Sill in the Strait of Gibraltar. *J. Geophys. Res.*, **99**, 9847–9878.

Wiseman, W. J., Mooers, C. N. K., and Forristal, G. Z. (1983). Ocean current processes. *Ocean Sci. Engng.*, **8**, 367–459.

Woodcock, A. H. (1993). Winds, subsurface pelagic *sargassum* and Langmuir circulations. *J. Exp. Mar. Biol. Ecol.*, **170**, 117–125.

Woolf, D. K. (1997). Bubbles and their role in gas exchange. In P. S. Liss and R. A. Duce, editors, *The Sea Surface and Global Change*, pages 173–205. Cambridge University Press.

Wu, J. (1994). The sea surface is aerodynamically rough even under light winds. *Boundary-Layer Meteorol.*, **69**, 149–158.

Xing, J. and Davies, A. M. (1996). A numerical model of the long term flow along the Malin-Hebrides shelf. *J. Mar. Syst.*, **8**, 191–218.

Xing, J. and Davies, A. M. (1998). A three-dimensional model of internal tides on the Malin-Hebrides shelf and shelf edge. *J. Geophys. Res.*, **103**, 27,821–27,847.

Yang, Z., Tang, S., and Wu, J. (1997). An experimental study of rain effects on fine structures of wind waves. *J. Phys. Oceanogr.*, **27**, 419–430.

Yelland, M. J. and Taylor, P. G. (1996). Wind stress measurements from the open ocean. *J. Phys. Oceanogr.*, **26**, 541–558.

Zedel, L. and Farmer, D. M. (1991). Organized structures in subsurface bubble clouds: Langmuir circulation in the open ocean. *J. Geophys. Res.*, **96**, 8889–8900.

Zedel, L., Crawford, G. B., and Gordon, L. (1996). On the determination of wind direction using an upward looking acoustic Doppler current profiler. *J. Geophys. Res.*, **101**, 12,163–12,176.

Zedel, L., Gordon, L., and Osterthus, S. (1999). Ocean ambient sound instrument system: Acoustic estimation of wind speed and direction from a subsurface package. *J. Atmos. Oceanic Technol.*, **16**, 1118–1126.